INSIGHTS INTO MIDDLE CRUSTAL PROCESSES IN MAGMATIC ARCS, COAST MOUNTAINS, BRITISH COLUMBIA

A Thesis

Presented to the Faculty of the Graduate School

of Cornell University

In Partial Fulfillment of the Requirements for the Degree of

Doctor of Philosophy

by

Gabriela Viviana Depine

August 2009

INSIGHTS INTO MIDDLE CRUSTAL PROCESSES IN MAGMATIC ARCS, COAST MOUNTAINS, BRITISH COLUMBIA

Gabriela Viviana Depine, Ph.D.

Cornell University 2009

This thesis explores processes occurring in the middle and lower crust of magmatic arc-settings. This study is based on observations on the Coast Mountains of British Columbia, Canada, at ~53° N la titude. The rocks exposed at the surface in this area represent the roots of a Mesozoic to early Tertiary magmatic arc.

Transpressional deformation occurred synchronously with magmatism and metamorphism from the Late Cretaceous to the Early Eocene. Between 61 and 50 Ma, the entire Canadian Cordillera tracks a period of extension and exhumation of high-grade metamorphic rocks, synchronous with intensified magmatism.

The thermal state of the crust during this time period was explored using numerical models. The models attempt to reproduce a geotherm that explains observations found in the field, such as abundance of amphibolitic migmatites, widespread magmatism, granulite facies metamorphism, and high-temperature low-pressure metamorphism. The resulting geotherm is isothermal from the pluton emplacement depth to the Moho. The temperature of the profile is buffered by the solidus temperature of the country-rock. The upper crust is characterized by a steep temperature gradient of ~50℃/km.

The structure and petrology of three plutons was analyzed to better understand pluton emplacement processes. Two of the plutons, the Kitlope

and Quottoon plutons; are characterized by steep foliations and intruded during transpression. The third pluton, the Chief Matthew's pluton; intruded as a sub-horizontal sill during extension. The transposition of the foliation from vertical to horizontal is explained by the development of melt-filled tension gashes oriented perpendicular to the sub-vertical foliation. Melt migration results in melt accumulation in the gashes. This process coupled with a change from regional transtension caused development of flat foliation localized around the Chief Mathew's pluton.

The exhumation path and cooling history of the three plutons was also explored. Petrology, geothermobarometry, geochemistry, and cooling ages were analyzed to determine that: 1) exhumation of ~6 km of rock occurred between the emplacement of the Quottoon and Chief Matthew's plutons at a rate of ~2-3 mm/yr; 2) the rocks cooled at a rate of ~50℃/Ma; 3) the area cooled below the biotite closure temperature by 51 Ma. An exhumation model integrating the studied area with the rest of the Canadian Cordillera is also proposed.

BIOGRAPHICAL SKETCH

Gabriela Depine was born and raised in Buenos Aires, Argentina. During her time in school (Colegio San Gabriel) she discovered her love and respect for nature. For five consecutive summers from the age of eleven to fifteen she went camping in Patagonia with friends as part of a program sponsored by her school. By the age of 16 she climbed four major peaks in the Patagonian Andes. When she graduated from high-school it was very clear to her that she wanted to stay close to nature and decided to study geology.

She deeply enjoyed her time at the Universidad de Buenos Aires. One of the field trips organized by her university was shared with Cornellian Sue Kay's Andean field trip. At this time is when she developed connections with Cornell University and, after graduation, she moved to the US to pursue a PhD in geology.

Dedicado a mis padres Silvia y Santos. Por el apoyo constante e incondicional. Por estar siempre, y por mostrarme y mantenerme enfocada acerca de lo que importa en la vida.

ACKNOWLEDGMENTS

My understanding of geology has evolved significantly over my years at Cornell University. I would like to thank the EAS department for providing me with the opportunity to join and interact with its members.

My work is the result of team work, for which I would like to thank Chris Andronicos, my committee chair, for the interactions, patience, support, and unforgettable shared moments in the field. My thinking has been greatly challenged while working with him, and he made the impossible, turned me into a (quasi) structural geologist!

I would also like to thank Jason Phipps-Morgan for the confidence and unconditional advice. It has been a pleasure working with him, and also very challenging. He gets the honor of have turned me into a (nearly-quasi) numerical modeler!

Sue Kay has also been an important part of my learning experience at Cornell, as a member of my committee. But most important she showed me and walked me through a door of opportunities with her support from the very beginning, for which I am deeply thankful.

I would also like to thank Mike Thompson. As my outsider committee member, the interactions with him provided me with perspective. His class in thermodynamics has been one of the best courses I have taken at Cornell and what I learned there was fundamental for my future research.

The faculty from EAS have provided me with advice and very interesting geological discussions throughout the years. In particular, Rick Allmendinger and Terry Jordan have made me feel welcomed from the very beginning, and their advice and support have been encouraging and is greatly

appreciated. I would also like to thank John Hunt for his help and availability with the electron microprobe.

Researchers from the BATHOLITHS project have improved my understanding of the Coast Mountains with several discussions during conferences and workshops. In particular, Margi Rusmore, James Girardi, Linc Hollister, and Kelly Russell have directly imprinted my work.

There are also people from outside Cornell that deserve to be recognized here. My research has an important field component which requires interaction and help from people. I am greatly thankful for the hospitality and interactions of the people from mainly Terrace, but also Kitimat, and Prince Rupert. In the field my research was improved by discussions with Julie Chang, Sean Long, Jeremy Deans, Dave Wolf, and my ‘grandavdisor’ Linc Hollister. Linc was also very helpful in providing the funding for a boat campaign across Gardner Canal. The logistics of the campaigns were possible thanks to the help and good vibes provided by Captain Don Wilson and helicopter pilot Craig Kendel.

My fellow graduate students also supported and helped me throughout my years at Cornell. And I really appreciate having them around for scientific/ life drama discussions. The later is my favorite type, though. In particular Adam Goss, Katie Tamulonis, Greg Kirkpatrick, Chao Shi, Jack Loveless, Jacob Moore, Joey Rosario, Peter Nester, Adrienne Long, and Brian Ruskin, have greatly improved my experience at Cornell by going far and beyond.

My parents and sisters, as always, are the pillar of my life. And I would like to thank them for being here for me even though they are there.

The research was funded by NSF EAR 0738827 grant to Professor Chris Andronicos.

TABLE OF CONTENTS

LIST OF FIGURES

LIST OF TABLES

LIST OF ABBREVIATIONS

Als	Aluminosilicate
An	Anorthite
And	Andalusite
BIO	Biotite
BC	British Columbia
CHL, CHLR	Chlorite
CHTD	Chloritoid
cm	Centimeter
cor	Corundum
CORD	Cordierite
Cpx	Clinopyroxene
E	East
FSP	Feldspar
Grt	Garnet
Hbl	Hornblende
HREE	Heavy rare-earth elements
ILM	Ilmenite
Kfs	Potassium Feldspar
Km	Kilometer
Ky	Kyanite
L, LIQ	Liquid
Ma	Million Years
mm	Millimeter
Ms	Muscovite

N	North
NW	Northwest
NE	Northeast
Opx	Orthopyroxene
OSUM0	Osmulite
P	Pressure
Pl, PLG	Plagioclase
PHNG	Phengite
QTZ	Quartz
REE	Rare-earth elements
V	Vapor
S	South
SE	Southeast
Sil, Sill	Sillimanite
SPIN	Spinel
STAU	Staurolite
SW	Southwest
T	Temperature
t	Time
W	West
yr	year
zo	Zoicite

INTRODUCTION

The motivation for the thesis is to contribute to our understanding of the geologic processes that lead to the formation of continental crust. The formation and differentiation of continental crust is thought to largely result from the differentiation of mantle derived melts into more silica rich compositions representative of the continental crust (Rudnick 1995). Several different tectonic environments have been suggested as sites for this crustal distillation including continental arcs (Rudnick 1995, Hollister and Andronicos 2006, Ducea and Saleeby 1998, Kay and Kay 1988), rifts and extensional provenances (Dewey 1988, Costa and Rey 1995), collisional orogenic belts (Karlstorm and Bowring 1993, Condie 1990), and mantle plume settings (Hill et al 1992, Condie 2003). In this thesis I have focused my work on the Coast Mountains of British Columbia, Canada (Figure 1), which represent one of the largest recent sites for crustal growth in the world (Hollister and Andronicos 2006).

The crust of western British Columbia today has a seismic velocity structure similar to that of the average andesitic continental crust (Holbrook et al 1999, Hollister and Andronicos 2006). The formation and differentiation of the crust of British Columbia occurred during terrane accretion and calc-alkaline magmatism during the Mesozoic and Early Tertiary (Coney et al 1980, Hollister and Andronicos 2006, Johnston and Canil 2007). Today the Coast Mountains are composed of rocks that represent the middle and upper crust of a continental magmatic arc formed during terrane collision and subduction along the continental margin (Figure 2). This belt of magmatic and metamorphic rocks extends for more than a 1000 km, from southeast Alaska

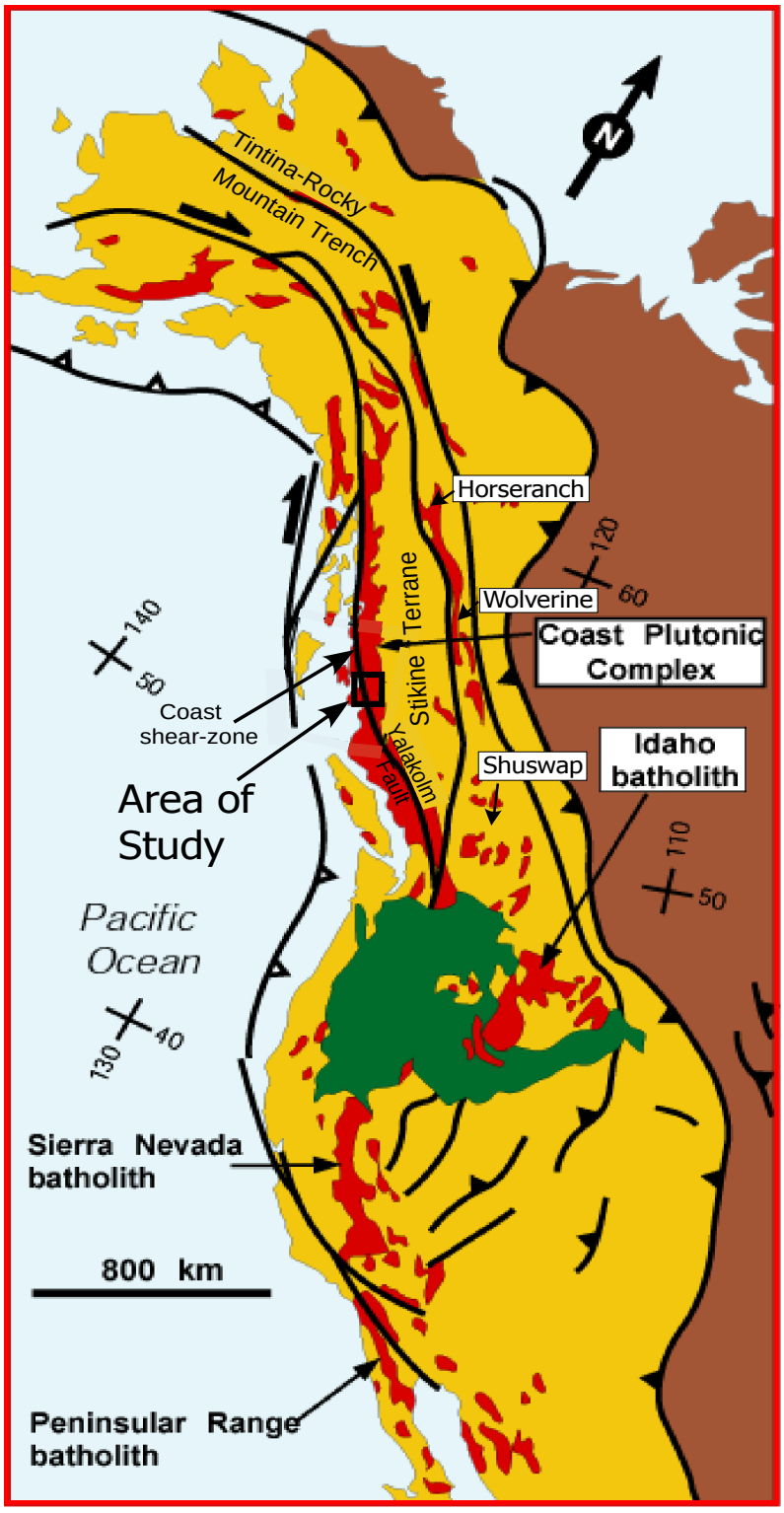

Figure 1: Map of western North America. The yellow area is the North American Cordillera. The red areas represent Mesozoic batholith complexes. Green marks the Columbia River and Snake River plain flood-basalts. Major faults are shown. Map modified from Chardon et al 1999.

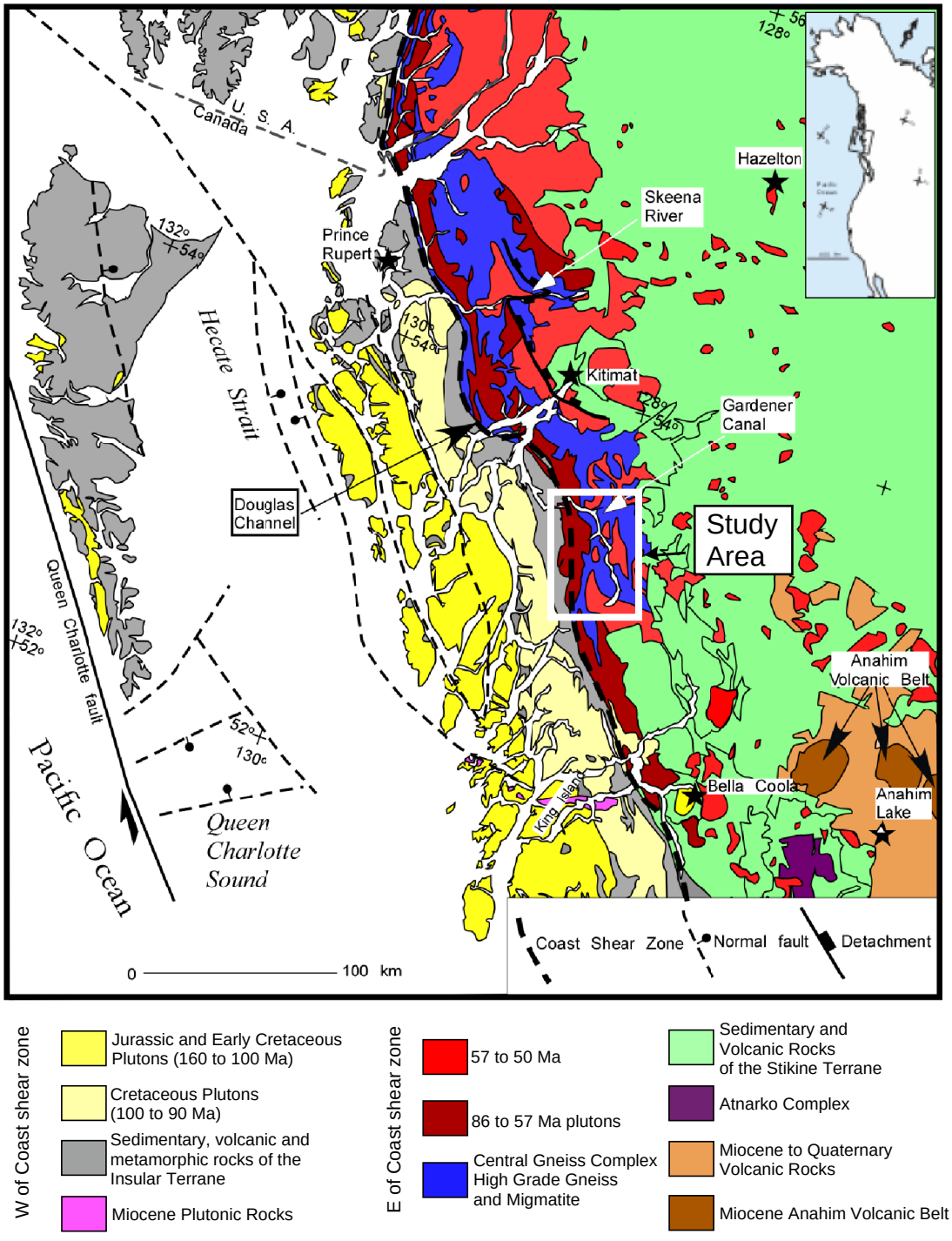

Figure 2: Simplified geologic map of the Coast Mountains between 52° and 56°. Modified form Hollister and Andronicos 2006.

to northwestern Washington. This unique exposure of the middle crust of a magmatic arc provides a window into the middle crust and lower crust and gives important constraints on the processes of mid-crustal melt transport and pluton emplacement, crustal differentiation, magma/rock interactions, migmatization, and deformation mechanisms of rocks during metamorphism and magma transport.

The temperature structure of arc crust plays a fundamental role on its evolution. The thermal profile of the crust affects the generation and migration of melts, the rheology of the rocks and their ability to deform and flow, and the occurrence of metamorphic reactions. These fundamental problems are the focus of chapter 1 (Published as Depine et al 2008). This chapter models numerically the effects of migrating melt through the crust, resulting in a quasi-steady state geotherm that we believe characterizes magmatic arcs. The calculated thermal profile produces an isothermal geotherm from the depth of pluton emplacement in the upper middle crust, through the lower crust to the Moho. The most important constraints on the shape of the quasi-steady state geotherm are the temperature at the Moho and the solidus temperature of the crustal rocks. The modeled geotherm reproduces many of the features observed in the Coast Mountains and other mountain belts, including uniformly high temperatures of ~800℃ in upper amphibolite an d granulite facies regardless of peak pressure, the presence of wide spread low-pressure, high-temperature metamorphic terranes, and a weak lower and middle crust susceptible to orogenic flow and collapse. The implications of this thermal structure of the crust set the thermal context for the processes evaluated in the subsequent two chapters.

Deformation processes within magmatic arcs have been among the most hotly debated topics in the structural geology and tectonics (c.f. Patterson et al 1991), and have persisted since nearly the beginning of geology as a science (Hutton 1794). Key questions related to the role of deformation in arcs are the interaction of far field effects like relative plate motions with near field effects like magma buoyancy, and how these interactions affect strain partitioning. The role of inherited zones of weakness in the crust and upper mantle strongly influences these processes, as does the thermal and rheological state of the lithosphere when deformation occurs. Chapter 2 of this thesis focuses on three plutonic bodies in the Gardner Canal area that were emplaced in less than 10 Ma and developed distinctly different structures that appear to reflect changes in the arc related to both near-field and far-field processes. The Kitlope pluton on the southern edge of the study area intruded as east-west trending near vertical sheets that reflect partitioning of dextral transpressive strain at 61 Ma. The Quottoon pluton was emplaced at ~60 Ma along the Coast shear-zone, a ~1200 km zone shear-zone that cuts the Coast Mountains, reflecting the effects of crustal anisotropy and convergent tectonics on controlling pluton geometry. The Chief Mathew's pluton was emplaced as sub horizontal sills reflecting a switch from a dominantly convergent to an extensional deformation regime after 60 Ma.

Chapter 3 was motivated by another fundamental question in geological sciences: how are high grade metamorphic rocks produced and exhumed during orogenesis? Uplift and exhumation of metamorphic terranes has been linked to crustal shortening (Hollister 1982, Hollister 1993), crustal extension (e.g. Armstrong 1982), and transpression zones (e.g. Leloup et al 1995). The development of the theory of plate tectonics placed emphasis on tectonic

deformation driven by relative horizontal motions as being primarily responsible for uplift and erosion of metamorphic rocks (e.g. England and Houseman 1988). Recent studies (Molnar and Lyon-Caen 1988, Jones et al 1996, England and Molnar 1997, Flesch et al 2000) have emphasized that horizontal displacements of plates coupled with lateral variations in gravitational potential energy are needed to explain the patterns of deformation observed in many mountain belts. Furthermore, the interaction of erosion at the surface of the earth with tectonic deformation is now recognized to be a fundamental driver of exhumation in currently active mountain belts (Beaumont et al 2001, Koons et al 2002). Chapter 3 studies aspects of the exhumation of the high grade metamorphic rocks, and pressure-temperature-path followed by the plutons and their host rocks. The study is based on quantitative petrology, cooling ages and geochemistry. At the end of this chapter a model for the exhumation of the whole Canadian Cordillera is proposed.

The overall tectonic history of the Coast Mountains based on the results of this study and others is that convergent margin tectonics and crustal thickening occurred between 110 and 70 Ma across the Coast Mountains. After crustal thickening, the Coast Mountains were affected by synorogenic extension and extrusion of high-grade rocks between 57 and 48 Ma. This stage overlaps the final stages of arc magmatism that resulted in the evolution and development of the continental crust that is observed today.

The work presented in this thesis is mainly based on fieldwork performed at Gardner Canal and Kitlope Lake areas. Two field campaigns to the areas were performed. The field work was conducted by helicopter, boat, and 4-wheel drive trucks, given that most of the places we visited were

remote. The field campaigns provided the fundamental data on which this thesis is based including: geological maps; samples for chemistry, radiometric ages, micro-structural, and petrological analyses; and structural measurements needed for tectonic analysis.

REFERENCES

Armstrong, R.L., 1982. Cordilleran metamorphic core complexes - from Arizona to southern Canada. Annual Reviews of Earth and Planetary Sciences, 10: 129-154.

Beaumont, C., Jamieson, R.A., Nguyen, M.H. and Lee, B., 2001. Himalayan tectonics explained by extrusion of a low-viscosity crustal channel coupled to focused surface denudation. Nature, 414, 738–742.

Condie, K.C., 1990. Growth and accretion of continental crust: Inferences based on Laurentia. Chemical Geology, 83, 183-194.

Condie, K.C., 2003. Supercontinets, superplumes, and continental growth: the Neoproterozic record. Geological Society of London, Special Publication 206: 1-21.

Coney, P.J., Jones, D.L. and Monger, J.W.H., 1980. Cordilleran suspect terranes. Nature, 288: 329-333.

Costa, S. and Rey, P., 1995. Lower crustal rejuvenation and crustal growth during post-thickening collapse: Insights from a crustal cross section through a metamorphic core complex. Geology, 23: 905-908.

Depine, G.V., Andronicos, C.L. and Phipps-Morgan, J., 2008. Near-isothermal conditions in the middle and lower crust induced by melt migration. Nature 452: 80-83.

Dewey, J.F., 1988. Extensional collapse of orogens. Tectonics, 7, 1123-1139.

Ducea, M. and Saleeby Jason, B., 1998. A case for delamination of the deep batholithic crust beneath the Sierra Nevada, California. International Geology Review: 78-93.

England, P.C. and Houseman, G.A. (1988). The mechanics of the Tibetan plateau, Phil. Transactions of the Royal Society of London, A-326: 301-320.

England, P.C., and Molnar, P., 1997. Active deformation of Asia: from kinematics to dynamics. Science, 278: 647–650.

Flesch, M., Holt, W.E., Haines, A.J. and Shen-Tu, B., 2000. Dynamics of the Pacific–North American plate boundary in the Western United States. Science, 287: 834–836.

Hill, R.I., Campbell, I.H., Davies, G.F., and Griffiths, R.W., 1992. Mantle Plumes and Continental Tectonics. Science, 256: 186-193.

Holbrook, W.S., Lizarralde, D., McGeary, S., Bangs, N. and Diebold, J., 1999. Structure and composition of the Aleutian island arc and implications for continental crustal growth. Geology, 27: 31-34.

Hollister, L.S., 1982. Metamorphic evidence for rapid (2mm/yr) uplift of a portion of the Central Gneiss Complex, Coast Mountains, British Columbia. Canadian Mineralogist, 20: 319-332.

Hollister, L.S.,1993, The role of melt in the uplift and exhumation of orogenic belts. Chemical Geology, 108: 31-48.

Hollister, L.S. and Andronicos, C.L., 2006. Formation of new continental crust in Western British Columbia during transpression and transtension. Earth and Planetary Science Letters, 249(1-2): 29-38.

Hutton, J., 1794. Observation on Granite, reprinted 1973, Hafner Press, New York.

Johnston, S.T., and Canil, D., 2007. Crustal Architecture of SW Yukon, norther Cordillera: Implications for crustal growth in a convergent margin orogen. Tectonics, 26, TC1006.

Jones, H., Unruh, J.R. and Sonder, L.J. 1996. The role of gravitational potential energy in active deformation in the southwestern United States. Nature, 381: 37–41.

Karlstrom, K.E. and Bowring, S.A., 1993. Proterozoic Orogenic history of Arizona. In: Reed Jr., J.C., Bickford, M.E., Houston, R.S., Link, P.K.,

Rankin, D.W., Sims, P.K. and Van Schmus, W.R., (Eds.), Precambrian: Conterminous U.S. The Geology of North America C-2, Geological Society of America: 188–211.

Kay, S.M. and Kay, R.W., 1988. Crustal recycling and the Aleutian arc. Geochemica et Cosmochimica Acta, 52: 1351-1359.

Koons, P.O., Zeitler, P.K., Chamberlain, C.P., Craw, D. and Meltzer, A.S., 2002. Mechanical links between erosion and metamorphism in Nanga Parbat, Pakistan Himalaya. American Journal of Science, 302: 749–773.

Leloup, P.H., Lacassin, R., Tapponnier, P., Schaerer, U., Zhong, D., Liu, X., Zhang, L., Ji, S. and Trinh, P.T., 1995. The Ailao Shan-Red River shear zone (Yunnan, China), Tertiary transform boundary of Indo-China. Tectonophysics, 251: 3–84.

Molnar, P. and Lyon-Caen, H., 1988. Some simple physical aspects of the support, structure, and evolution of mountain belts. Geological Society of America Special Paper, 218: 179–207.

Paterson, S.R., Vernon, R.H., and Fowler, T.K., 1991. Aureole tectonics. In Contact Metamorphism, Kerrick, D.M. (ed.), Mineralogical Society of America, Reviews in Mineralogy, 26: 673-722.

Rudnick, R.L., 1995. Making continental crust. Nature, 378: 571-578.

CHAPTER 1

NEAR ISOTHERMAL CONDITIONS IN THE MIDDLE AND LOWER CRUST INDUCED BY MELT MIGRATION

The thermal structure of the crust plays a fundamental role strongly influencing deformation, metamorphism and plutonism (Thompson 1999, Gerbi et al 2006, Sandiford et al 1991). Models for the geothermal gradient in stable crust predict a steady increase of temperature with depth. This thermal structure is incompatible with observations from high-temperature metamorphic terranes exhumed in orogens (Thompson 1999, Patiño-Douce et al 1990, Hollister 1982, De Yoreo et al 1991). Global compilations (Pattison et al 2003) of peak conditions in high-temperature metamorphic terranes define relatively narrow ranges of peak temperatures over a wide range in pressure, for both isothermal decompression and isobaric cooling paths. Here we develop simple 1-d thermal models that include the effects of melt migration. These models show that long-lived plutonism results in a quasi-steady-state geotherm with: 1) a rapid temperature increase in the upper crust and nearly isothermal conditions in the middle and lower crust; 2) upward advection of heat by melt that generates granulite facies metamorphism, and 3) widespread andalusite-sillimanite metamorphism in the upper crust. Once the quasi-steady-state thermal profile is reached, the middle and lower crust are greatly weakened due to high temperatures and anatectic conditions, thus setting the stage for gravitational collapse (Molnar and Lyon-Caen 1988), exhumation and isothermal decompression after the onset of plutonism. Near-isothermal

---

**Originally published as:* Depine, G.V., Andronicos, C., Phipps-Morgan, J., 2008. Near isothermal conditions in the middle and lower crust induced by melt migration. Nature, 452: 80-83.

conditions in the middle and lower crust result from the thermal buffering effect of dehydration melting reactions that, in part, control the shape of the geotherm.

Pressure-temperature (P-T) estimates in andalusite-sillimanite metamorphic belts and middle crustal granulite terranes predict unreasonably hot geothermal gradients if one assumes a purely conductive geotherm, steadily increasing with depth (Figure 1.1D). Here, we demonstrate the shape of a more realistic geotherm in crust undergoing extensive partial melting and high temperature metamorphism. The abundance of plutons and batholiths associated with migmatites and granulites in these terranes suggest that heat transport by pervasive flow of magma through the crust plays a significant role in shaping the metamorphic geotherm (Gerbi et al 2006, De Yoreo et al 1991, Leitch and Weinberg 2002, and references therein). Decompression melting caused by post-thickening crustal extension has often been called upon to explain the low-pressure high-temperature metamorphism found in some of these terrains (Thompson 1999). In contrast, field studies of terranes with isobaric cooling P-T paths demonstrate that migmatite formation, granulites, and plutonism formed *prior to* exhumation and uplift (Harley 1989). Concentration of radioactive elements during crustal thickening can, given enough time, cause melting of mica rich lithologies (Patiño-Douce et al 1990, Huerta et al 1996). However, additional heat sources are required to induce large degrees of anatexis in amphibolite bulk compositions (Thompson 1999, Sandiford et al 1991, De Yoreo et al 1991), the likely crustal protolith of calc-alkaline plutonic suites (Thompson 1999, López and Castro 2001). Mechanisms that have been proposed in the literature to increase the mantle

Figure 1.1: 1-D numerical models showing evolution of predicted crustal geotherms through time as a function of mantle heat flux, melt focusing, and lower crustal solidus relations. Bold lines represent geotherms every 3 Ma, starting at the initial steadily-increasing with depth geotherm perturbed at 55 km with a temperature of 1250℃. The thin dashed li nes represent the solidus curve in A-D and other metamorphic reactions in D. Dots represent P-T estimates of worldwide granulites corrected for retrograde exchange (Pattison et al 2003). Three examples are shown: A) A model for a mantle heat flux of 120 mWm^{-2} and amphibolite dehydration melting curve. The quasi-steady-state is reached after 37.7 Ma. B) A model including melt focusing by a factor of two with a mantle heat flux of 47.5 mWm^{-2}, the quasi-steady-state is reached after 25.5 Ma. C) A model using the hornblende + quartz +/- plagioclase dehydration melting curve as the solidus for the crust. In this case focusing of the melt by a factor of two with a mantle heat flux of 65 mWm^{-2} is also required for the 'hot' threshold geotherm. The quasi-steady-state is arrived after 25.7 Ma. We note that this model best fits P-T estimates from worldwide granulite terranes. D) Comparison between geotherms predicted from surface heat flow measurements and calculated melt-enhanced geotherm from model 1. The grey field includes the general region of andalusite-sillimanite type metamorphism (Pattison and Tracy 1991). Note that simply conductive geotherms extrapolated from surface heat flow measurements do not intersect conditions recorded by most granulites or andalusite-sillimanite metamorphic belts. Also plotted are reaction curves relevant for granulite facies metamorphism (Pattison et al 2003).

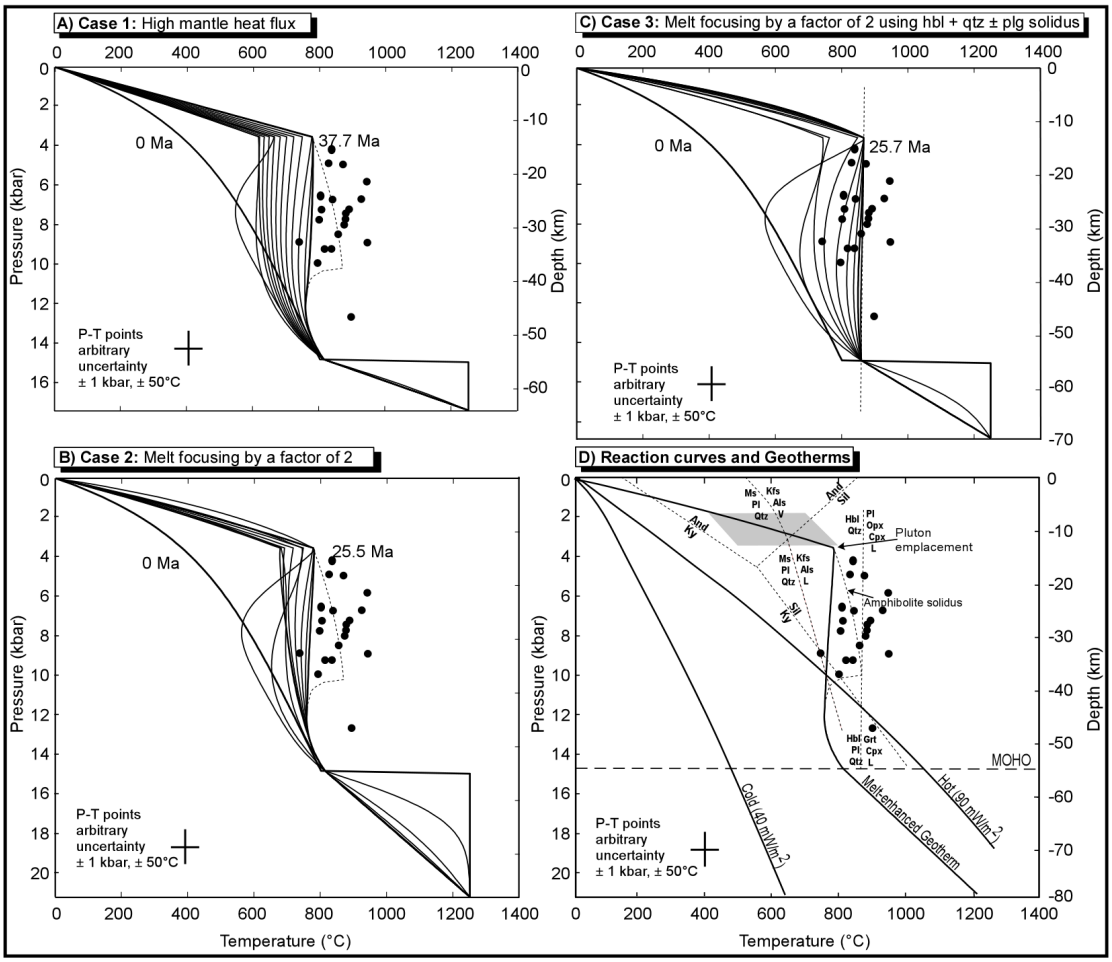
A) Case 1: High mantle heat flux
0 Ma
37.7 Ma
P-T points
arbitrary
uncertainty
± 1 kbar, ± 50°C
Pressure (kbar)
Depth (km)
C) Case 3: Melt focusing by a factor of 2 using hbl + qtz ± plg solidus
0 Ma
25.7 Ma
P-T points
arbitrary
uncertainty
± 1 kbar, ± 50°C
B) Case 2: Melt focusing by a factor of 2
0 Ma
25.5 Ma
P-T points
arbitrary
uncertainty
± 1 kbar, ± 50°C
Temperature (°C)
D) Reaction curves and Geotherms
Ms Kfs Pl Qtz
And Sil
Hbl Qtz
Pl Opx Cpx L
Pluton emplacement
Ms Kfs Pl Qtz L
Amphibolite solidus
And Ky
Sil Ky
Hbl Grt Pl Cpx Qtz L
MOHO
Cold (40 mW/m-2)
Melt-enhanced Geotherm
Hot (90 mW/m-2)
P-T points
arbitrary
uncertainty
± 1 kbar, ± 50°C
Pressure (kbar)
Depth (km)
Temperature (°C)

heat flux in granulite terranes include: 1) mantle plume activity (Chardon et al 2002, Gibson and Stevens 1998), 2) post-thickening extensional collapse and/or erosional thinning (Thompson 1999, Thompson et al 2001), 3) pre-thickening extension (De Yoreo et al 1991), 4) lower crustal delamination (Kay and Kay 1993), or 5) subduction of an active spreading ridge (Brown 1998).

In this paper we model the thermal structure of thickened crust undergoing partial melting, which results in a melt-transport-elevated geotherm that fits many observed features of granulite-migmatite terranes. The results are applicable to continental arcs and collisional orogens. These models place constraints on the heat flux across the Moho that is necessary to trigger granulite metamorphism and anatexis in the absence of changes in crustal thickness due to erosion, crustal thickening, extension or addition of mantle derived melts to the crust. The models do not depend on crustal rheology; melt transport mechanism or the detailed nature of deformation. We focus on crustally derived magmas without inclusion of melts or fluids that may be introduced by subduction zone processes. Although these processes are of importance, we choose to keep our models as simple as possible to emphasize interaction between melt migration, melting in the crust, and upward heat transport across the Moho. The shape of the melt-enhanced geotherm is found to strongly depend upon the shape of the solidus curve for a specific composition, because equilibrium melting reactions buffer temperature until exhaustion of one (or more) of the melting phases. The models assume a fluid-absent amphibolite middle and lower crust (Figure 1.1, Hollister and Andronicos 2006), mica-rich lithologies or fluid-present reactions would melt at lower temperatures.

Our models are constrained in particular by observations from the central gneiss complex (CGC) of western British Columbia (Hollister 1982, Hollister and Andronicos 2006, Hollister et al 2004, Andronicos et al 2003, Kenah and Hollister 1983). The CGC is characterized by an amphibolitic lower crust (Hollister 1982, Kenah and Hollister 1983), with widespread migmatitic gneiss and granulite intruded by calc-alkaline plutons (Hollister 1982) that were emplaced at middle crustal levels (~10 to 25 km deep), and which represent two magmatic pulses related to distinct tectonic episodes between 85-65 and 60-52 Ma (Hollister and Andronicos 2006). During the first event, plutons were emplaced during transpressional to convergent tectonics associated with thickening of the crust to at least 55 km. Both events are characterized by high grade metamorphism and widespread migmatites. However, the second event is characterized by an additional magmatic flare-up of voluminous igneous plutons (Andronicos et al 2003) that intruded during ongoing regional granulite-facies metamorphism (Kenah and Hollister 1983). Large-scale crustal extension dominated tectonics during the magmatic flare up, so that rocks followed a ‘clockwise’ isothermal P-T-t path (Hollister 1982).

The 1-D numerical models generate predicted crustal thermal profiles for varying crustal melt fluxes and heat conduction across the Moho. Each simulation assumes that heat transfer is by conduction and by melt transport. The models solve the following advection-diffusion-melting equation:

$$\rho\, c_p\, \partial T/\partial t + \rho c_p\, W\, \partial T/\partial y = \kappa\, \partial^2 T/\partial y^2 + \rho H(y) - \rho\, \Delta H\, \partial F/\partial t.$$

Model parameters are listed in Table 1.1. Boundary conditions are surface T= 0℃ and basal T= 1250℃. The maximum dep th of the profile is varied to simulate different long-term basal mantle heat fluxes. Therefore, geotherms have a simple physical meaning from the top of the profile to the

Table 1: Constants and values used in models

κ	Thermal conductivity	2.5 W ℃ $^{-1}$ m^{-3}
ρ	Density	2700 kg m^{-3}
cp	Heat capacity	1170 J Kg^{-1} ℃ $^{-1}$ (Hollister et al 2004)
ΔH	Latent heat	320 kJ kg^{-1}
W	Velocity of flow	Function of melt fraction: $\partial F/\partial t$
H	Radioactive heat production	$H = H_o\, e^{-y/10000}$ (Turcotte and Schubert 2002)
T	Temperature	
t	Time	
y	Depth	

(H_o = 3.4 x 10^{-10} W kg^{-1} calculated for 80 Ma ago)

Moho; but, below the Moho, the curve is a gradient representing specific mantle heat fluxes across the Moho that does not reflect the shape of the convective mantle geotherm. The larger the gradient, the higher the mantle heat flux, and the sooner the model arrives to the steady-state equilibrium.

The model starts with 55 km thick crust and a near-surface geothermal gradient of 35℃km $^{-1}$, similar to the surface heat flow measured in modern arcs(Furukawa et al 1998). An initial temperature at the crust-mantle interface of 1250℃ (Figure 1.1) is equivalent to positioning asthenosphere directly at the base of the crust. This could result from delamination, asthenospheric upwelling by steepening of a slab, impingement of a mantle plume or initiation of rifting. Our model does not depend on which process actually occurs. The outcome is rapid cooling of the uppermost mantle until the mantle heat flux achieves a quasi-steady state value determined by the thickness of the mantle 'lid', which simulates the formation of a dynamically maintained layer of mantle lithosphere. Transfer of heat from the mantle to the crust triggers melting in the lower crust. The Moho evolves from 1250℃ to the cr ustal solidus temperature due to thermal-buffering of melting. In amphibolite, melt is assumed to accumulate to a threshold of 10 vol.%, at which point the melt migrates to 13 km, advecting upward heat in the crust-derived melts. Crust below 13 km is displaced downwards to replace the ascending melt, as a simple mass balance.

Two end-member scenarios occur, depending on the heat input from the mantle (Figure 1.1 and 1.2A). In the first scenario, the depth to the 1250^{o}C isotherm (bottom of the model) was chosen to produce a mantle heat flux of ~120 mWm^{-2} at the quasi-steady state (Figure 1.1A). With these conditions a pluton forms at 13 km within 5 Ma of the tectonic perturbation and starts

diffusing heat downward into the colder lower crust. After 35 Ma, the model arrives at the quasi-steady-state profile. The needed mantle heat input is equivalent to that from intruding 0.93 km of basalt per Ma for 35 Ma (i.e. 32.5 km of basaltic underplating). This scenario would require extraordinarily hot mantle heat fluxes and/or volumes of basaltic underplating that are not often found in orogens.

For a mantle heat input lower than 120 mWm^{-2} extensive crustal melting does not occur and granulites in the middle crust are not generated in realistic geological time scales (<35 Ma, Figure 1.2A). In order to generate extensive crustal melting and granulite formation under conditions of reduced mantle heat input, we found that focusing of crustal melt into the column is needed to produce partial melting and high temperature metamorphism that results in our second end member scenario. To simulate melt focusing, more melt is migrated from the model base to accumulate in a mid-crustal pluton than is generated in the 1-d crustal column. This is equivalent to bringing melt laterally from adjacent regions at the base of the crust. For common mantle heat fluxes in orogens (<100mWm^{-2}) and geologically reasonable time spans (<35 Ma), we found that melt must be focused by a factor of at least 1.3 (Figure 1.2A). As an example, if melt is focused by a factor of two, a quasi-steady state is predicted to occur after 25.5 Ma for a mantle heat flux of 47.5 mWm^{-2} (Figure 1.1B). Therefore, melt focusing can greatly lower the requirement of a high heat flux across the Moho (Figure 1.2A), indicating that this scenario is geologically more permissive.

The results of these models reproduce geotherms that pass at the lower temperature end of P-T data compiled from many granulite terranes (Figure 1.1). This is likely due to the limitations of our models, which assume

Figure 1.2: Comparison between mantle heat fluxes and the time to the onset of the quasi-steady-state melt-enhanced geotherm. A) Results using the amphibolite solidus curve. Each curve represents different melt focusing factors. The top curve has no melt focusing and represents the first end-member discussed in the text, where extremely high mantle inputs (<120 mW m^{-2}) are required. The following curves represent the second case scenario discussed in the text, where melt focusing leads to geotherms that match P-T estimates from the lower temperature end of granulite terranes. B) Results using the hornblende + quartz +/- plagioclase melting curve, which matches P-T estimates from many granulite terranes. In this case higher mantle heat fluxes are required as well as a longer time span (minimum 20 Ma) in order to generate the melt-enhanced geotherm. As seen in Figure 1.1C, these conditions better match P-T data from granulite terranes.

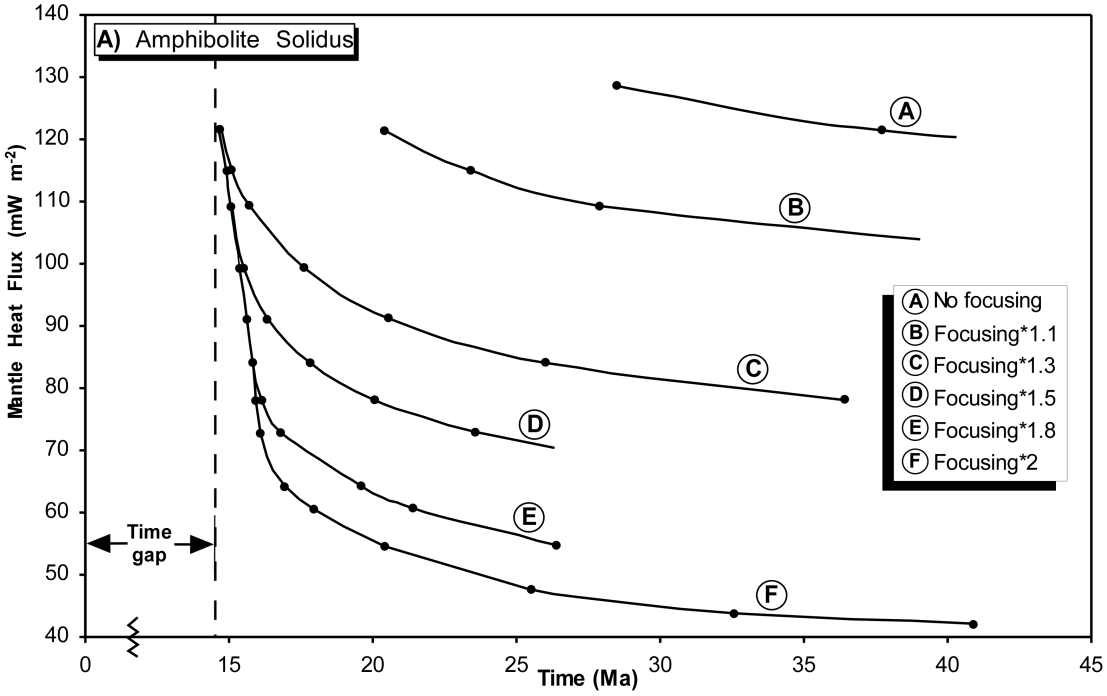
A) Amphibolite Solidus
Mantle Heat Flux (mW m-2)
Time (Ma)
Time gap
A No focusing
B Focusing*1.1
C Focusing*1.3
D Focusing*1.5
E Focusing*1.8
F Focusing*2

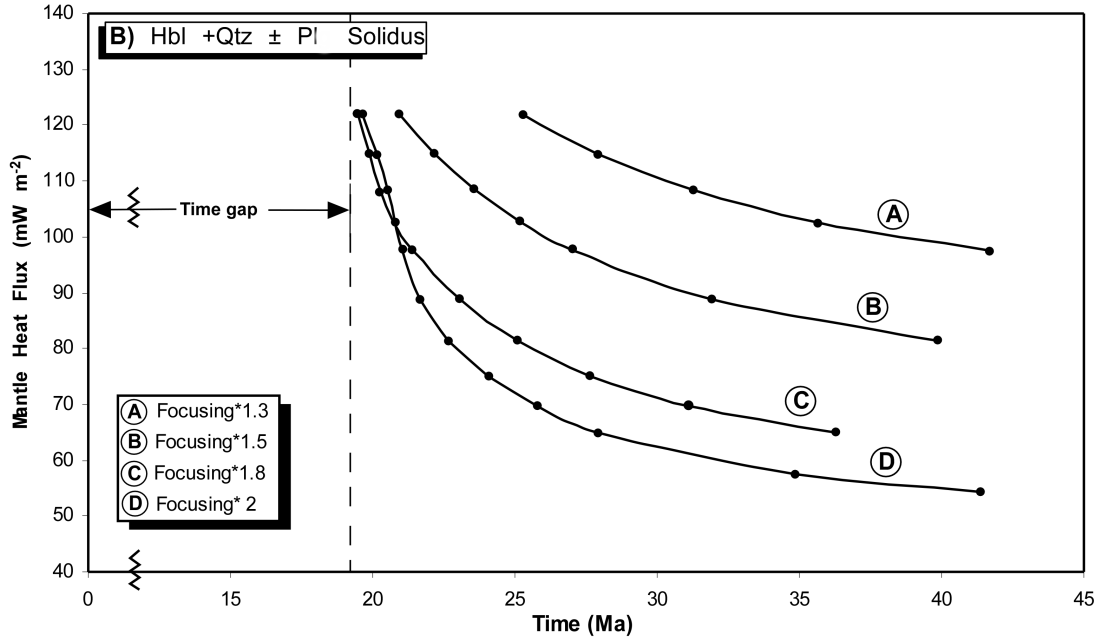
B) Hbl +Qtz ± Pl Solidus
Mantle Heat Flux (mW m-2)
Time (Ma)
Time gap
A Focusing*1.3
B Focusing*1.5
C Focusing*1.8
D Focusing* 2

melting is continuous in a fixed composition and that no phases are exhausted. In nature, melting would change mineral composition and exhaust one or more phases in the rocks incrementally changing the solidus to higher temperatures, which would relax the constraint of thermal buffering during melting. In Figure 1.1C, we investigate melting of hornblende + quartz ± plagioclase, which occurs at higher T than the amphibolite solidus in fig. 1D. P-T estimates from natural (Figure 1.1C) granulite terranes overlap this geotherm, but some record temperatures up to 200^{o} C hotter. This geotherm requires focusing of melt by a factor of 1.5 (Figure 1.2B). For example, a minimum mantle heat flux of 65 mWm^{-2} is required when focusing by a factor of 2. The time to get to the quasi-steady-state geotherm using this solidus curve takes longer (> 20Ma) than when using the amphibolite solidus curve (> 15Ma, compare Figure 1.2A with Figure 1.2B). Clearly granulite terranes that record these conditions have undergone extraordinary processes to result in such high crustal temperatures.

A possible mechanism for melt focusing is crustal flow (Hollister and Andronicos 2006, Andronicos et al 2003, Beaumont et al 2001, Rabinowicz and Vigneresse 2004). Many tectonic environments are thought to result in melt focusing, including spreading at mid-ocean ridges (Morgan 1987), continental arcs (Hollister and Andronicos 2006), extensional tectonic settings (MacCready et al 1997), mantle plumes (Morgan 1987), and transpressive fault zones (Brown and Solar 1998). Strike-slip shear-zones can also act as corridors for melt focusing in ductile environments (Hutton 1988). Orogen parallel transport is a common feature in modern convergent margins, where 31% of convergent margins have oblique convergence sufficient to generate transcurrent displacements (Patchett and Chase 2002). Note that our thermal

modelling can also capture the thermal effects of focused additions of basaltic magmas into a batholith, where the amount of focusing would reflect the ratio of basalt to calc-alkaline melts into the batholith. For simplicity, we have assumed that no basalt is added.

The models show that the thermal evolution in granulite crustal environments was profoundly shaped by melt migration and pluton construction. These results are similar to previous studies which concluded that partial melting in the crust and granulite facies metamorphism requires elevated mantle heat fluxes and pervasive melt migration through the crust (Thompson 1999, De Yoreo et al 1991, Leitch and Weinberg 2002, Hodges et al 1988). Our models highlight the important roles of heat transport by melt migration, and of thermal buffering by crustal anatexis as originally suggested by studies of metamorphism in the Himalaya (Hodges et al 1988), and modelled by Stüwe (1995). Extreme conditions in large hot orogens typified by granulite facies metamorphism, low-pressure high-temperature metamorphic belts and calc-alkaline batholiths are therefore likely to result from large fluxes of magma through the crustal column.

The required processes of basaltic underplating, asthenospheric impingement and melt focusing remain cryptic in the geologic record, yet our models imply they may be common in orogenic settings, as has been inferred from numerous studies of high temperature metamorphic terranes (Thompson 1999, Leitch and Weinberg 2002, Harley 1989, MacCready et al 1997). The models show the predicted shape of the resultant geotherms which have the following implications for metamorphic and tectonic process. The quasi-steady state profiles (Figure 1.1D) have very steep surface geothermal gradients of more than 50℃/km consistent with the generation of andalusite-sillimanite

metamorphic terranes and consistent with observations of peak conditions in many contact aureoles (Pattison and Tracy 1991). Melt migration and pluton construction cause the entire middle and lower crust to reach temperatures of ~800℃ and the lowest 12 km of the crust to be part ially molten. These conditions are similar to those estimated for many high-grade metamorphic terranes (Pattison et al 2003, Harley 1989). Our models show that linear extrapolation of geothermal gradients is only applicable to the upper portions of the crust in active tectonic settings and that the middle and lower crust experience near isothermal conditions buffered by the melting temperatures of the crustal rocks. Melt-laden middle and lower crust produce conditions that favor orogenic instability, and may be a necessary precondition for late orogenic extensional collapse and/or lower crustal flow. For terranes where collapse occurs, exhumation would follow the pressure peak and be nearly-isothermal because the entire middle and lower crust is hot. Thus exceptionally fast exhumation rates are not necessary for nearly-isothermal decompression. Slowly exhumed orogens that stay at high temperatures for long time periods (>10s of Ma, Shaw et al 2005) can also be explained by exhumation along a quasi-steady-state melt-enhanced geotherm. For terranes that do not collapse, isobaric heating and cooling paths would be followed.

REFERENCES

Andronicos, C.L., Chardon, D.H., Hollister, L.S., Gehrels, G.E. and Woodsworth, G.J., 2003. Strain partitioning in an obliquely convergent orogen, plutonism, and synorogenic collapse: Coast Mountains Batholith, British Columbia, Canada. Tectonics, 22: 1-24.

Beaumont, C., Jamieson, R.A., Nguyen, M.H. and Lee, B., 2001. Himalayan tectonics explained by extrusion of a low-viscosity crustal channel coupled to focused surface denudation. Nature, 414: 738-742.

Brown, M., 1998. Ridge-trench interactions and high-T–low-P metamorphism, with particular reference to the Cretaceous evolution of the Japanese Islands. In Treloar, P.J., and O'Brien, P.J. (eds.), What drives metamorphism and metamorphic reactions? Geological Society of London Special Publication, 138: 137–169.

Brown, M. and Solar, G.S., 1998. Shear-zone systems and melts; feedback relations and self-organization in orogenic belts. Journal of Structural Geology, 20: 211-227.

Chardon, D., Peucat, J.J., Jayananda, M., Choukroune, P. and Fanning, C.M., 2002. Archean granite-greenstone tectonics at Kolar (South India); interplay of diapirism and bulk inhomogeneous contraction during juvenile magmatic accretion. Tectonics 21, doi:10.1029/2001TC901032.

De Yoreo, J.J., Lux, D.R. and Guidotti, C.V., 1991. Thermal modelling in low-pressure/high-temperature metamorphic belts. Tectonophysics, 188: 209-238.

Furukawa, Y., Shinjoe, H. and Nishimura, S., 1998. Heat flow in the southwest Japan arc and its implication for thermal processes under arcs. Geophysical Research Letters, 25: 1087-1090.

Gerbi, C.C., Johnson, S.E. and Koons, P.O., 2006. Controls on low-pressure anatexis. Journal of Metamorphic Geology, 24: 107-118.

Gibson, R.L. and Stevens, G., 1998. Regional metamorphism due to anorogenic intracratonic magmatism. In Treloar, P.J., and O'Brien, P.J. (eds.), What drives metamorphism and metamorphic reactions? Geological Society of London Special Publication, 138: 121-135.

Harley, S.L., 1989. The origins of granulites: a metamorphic perspective. Geological Magazine, 126: 215-247.

Hodges, K.V., Le Fort, P. and Pecher, A., 1988. Possible thermal buffering by crustal anatexis collisional orogens: Thermobarometric evidence from Nepalese Himalaya. Geology, 16: 707-710.

Hollister, L.S., 1982. Metamorphic evidence for rapid (2 mm/yr) uplift of a portion of the Central Gneiss Complex, Coast Mountains, B.C. Canadian Mineralogist, 20: 319-332.

Hollister, L.S. and Andronicos, C.L., 2006. Formation of new continental crust in western British Columbia during transpression and transtension. Earth and Planetary Science Letters, 249: 29-38.

Hollister, L.S., Hargraves, R.B., James, T.S. and Renne, P.R., 2004. The paleomagnetic effects of reheating the Ecstall pluton, British Columbia. Earth and Planetary Science Letters, 221: 397-407.

Huerta, A.D., Royden, L.H. and Hodges, K.V., 1996. The interdependence of deformational and thermal processes in mountain belts. Science, 273: 637-639.

Hutton, D.H.W., 1988. Igneous emplacement in a shear-zone termination: The biotite granite at Strontian, Scotland. Geological Society of America Bulletin, 100: 1392-1399.

Kay, R.W. and Mahlburg-Kay, S., 1993. Delamination and delamination magmatism. Tectonophysics, 219, 177-189.

Kenah, C. and Hollister, L.S. 1983. Anatexis in the Central Gneiss Complex, British Columbia. In Migmatites, Melting and Metamorphism; Proceedings of Meeting on High Grade Metamorphism, Migmatites and Melting of the Geochemical Group of the Mineralogical Society of

the University of Glasgow, edited by M. P. Atherton and C. D. Gribble: 142–162, Shiva, Nantwich, U.K.

MacCready, T., Snoke, A.W., Wright, J.E. and Howard, K.A., 1997. Mid-crustal flow during Tertiary extension in the Ruby Mountains core complex, Nevada. Geological Society of America Bulletin, 109: 1576-1594.

Molnar, P. and Lyon-Caen, H., 1988. Some simple physical aspects of the support, structure, and evolution of mountain belts. Geological Society of America Special Paper, 218: 179-207.

Morgan, J.P., 1987. Melt migration beneath mid-ocean spreading centers. Geophysical Research Letters, 14: 1238-1241.

Leitch, A.M. and Weinberg, R.F., 2002. Modelling granite migration by mesoscale pervasive flow. Earth and Planetary Science Letters, 200, 131.

López, S. and Castro, A., 2001. Determination of the fluid-absent solidus and supersolidus phase relationships of MORB-derived amphibolites in the range 4-14 kbar. American Mineralogist, 86: 1396-1403.

Patchett, P.J. and Chase, C.G., 2002. Role of transform continental margins in major crustal growth episodes. Geology, 30: 39-42.

Patiño-Douce, A.E., Humphreys, E.D. and Johnston, A.D., 1990. Anatexis and metamorphism in tectonically thickened continental crust exemplified by the Sevier hinterland, western North America. Earth and Planetary Science Letters, 97: 290-315.

Pattison, D.R.M. and Tracy, R.J., 1991. Phase equilibria and thermobarometry of metapelites. In Kerrick, D.M. (ed.), Contact Metamorphism, Mineralogical Society of America Reviews in Mineralogy, 26: 105-206.

Pattison, D.R.M., Chacko, T., Farquhar, J. and McFarlane, C.R.M., 2003. Temperatures of granulite-facies metamorphism; constraints from experimental phase equilibria and thermobarometry corrected for retrograde exchange. Journal of Petrology, 44: 867-900.

Rabinowicz, M. and Vigneresse, J.L., 2004. Melt segregation under compaction and shear channeling; application to granitic magma segregation in a continental crust. Journal of Geophysical Research, 109: B04407.1-B04407.20.

Sandiford, M., Martin, N., Zhou, S. and Fraser, G., 1991. Mechanical consequences of granite emplacement during high-T, low-P metamorphism and the origin of "anticlockwise" PT paths. Earth and Planetary Science Letters, 107: 164-172.

Shaw, C.A., Heizler, M.T. and Karlstrom, K.E., 2005. 40Ar/39Ar thermochronologic record of 1.45-1.35 Ga intracontinental tectonism in the southern Rocky Mountains: Interplay of conductive and advective heating with intracontinental deformation. In Karlstrom, K.E. and Keller, G.R. (eds.), The Rocky Mountain Region; an Evolving Lithosphere; Tectonics, Geochemistry, and Geophysics, American Geophysical Union, Washington DC: 163-184.

Stüwe, K., 1995. Thermal buffering effects at the solidus. Implications for the equilibration of partially melted metamorphic rocks. Tectonophysics, 248: 39-51.

Thompson, A.B., 1999. Some time-space relationships for crustal melting and granitic intrusion at various depths. In Castro, A., Fernández, C. and Vigneresse, J.L. (eds.), Understanding Granites: Integrating New and Classical Techniques, Geological Society of London Special Publication, 158: 7–25.

Thompson, A.B., Schulmann, K., Jezek, J. and Tolar, V., 2001. Thermally softened continental extensional zones (arcs and rifts) as precursors to thickened orogenic belts. Tectonophysics, 332: 115-141.

Turcotte, D.L. and Schubert, G., 1992. Geodynamics. Cambridge University Press, Cambridge.

CHAPTER 2

RESPONSE OF SYNOROGENIC PLUTONS IN THE MIDDLE CRUST OF CONTINENTAL MAGMATIC ARCS TO REGIONAL TECTONIC CHANGES: AN EXAMPLE FROM THE COAST MOUNTAINS OF BRITISH COLUMBIA

I. Abstract

The Coast Mountains of British Columbia, Canada, record an increase in magmatic activity, acceleration in the exhumation rate, and a change from transpression to extension between ~60 and 52 Ma. We studied three mid-crustal plutons located at the southern termination of the central gneiss complex that intruded during this time period. We derive conclusions about the role of preexisting structures on melt migration, pluton emplacement mechanisms, and strain partitioning during changing tectonic conditions. The study is based on structural analysis of fabrics developed in the plutons and country-rocks. The Quottoon and Kitlope plutons (~60 Ma) have nearly-vertical foliations and lineations consistent with vertical flow of magmas during N-S shortening with a flattening component to strain, in a transpressional regime. The Chief Matthew's pluton (~57 Ma) intruded with sub-horizontal foliation and radially distributed lineations consistent with sub-vertical flattening, during extension. The change in orientations of the structures represents an almost orthogonal rotation of the shortening direction in the area. We envision the initiation of the transposition of the foliation by the development of melt-filled tension fractures perpendicular to the foliation. These structures locally change the orientation of the incremental strain axis and attract melt, trigger horizontal flow, and eventually form sub-horizontal plutons, like the Chief

Matthew's pluton. The Coast shear-zone is present in the study area and acted as the conduit that focused and fed the melts that formed the sub-vertical plutons. The space for the intrusion of plutons in an overall compressional environment is created by partitioning the deformation around the plutons into domains of flattening, simple-shear, and constrictional strain. Patterns of deformation around the plutons are strongly three dimensional and reflect the interaction of magma transport and regional deformation.

II. Introduction

The formation and emplacement of plutons is the principal mechanism by which continental crust differentiates and evolves (Paterson and Fowler 1993, Brown and Solar 1998). It is also one of the least understood geological processes because "pluton formation" cannot be studied as an active process except by geophysical remote sensing. Laboratory experiments cannot easily simulate pluton emplacement because they lack the complexity of nature (Cruden 1988, Paterson and Fowler 1993); moreover, it is impossible to reproduce the geological strain rates that govern the segregation and emplacement of melts (Paterson and Fowler 1993). Numerical models give insight into the problem, but still make assumptions that may not be justified in nature (Bittner and Schmeling 1995). Therefore, field observations of exhumed middle crustal plutons are one of the best approaches to constrain the processes that control pluton emplacement.

Several studies (e.g. Hollister and Crawford 1986, Karlstrom 1989) have pointed out that magma generation, migration and emplacement occurs synchronously with regional tectonic deformation in orogenic belts. Furthermore, many studies have concluded that there are feedbacks between

metamorphism, plutonism and deformation (Hollister 1993, Karlstrom and Williams 1993, Chardon 2003, Andronicos et al 2003). Pluton emplacement occurs in a variety of tectonic environments including contractional orogenic belts, raising the question of how space is made for plutons in dominantly compressive stress fields. Many plutons have been correlated with shear-zones and regional scale deformation, pointing to a close association between deformation and pluton generation and emplacement (Hutton 1987, Karlstrom and Bowring 1993, Kirby et al 1995, Ingram and Hutton 1994), although some have questioned this correlation (Paterson and Schmidt 1999).

The Coast Mountains of British Columbia have proven to be an outstanding natural laboratory to study orogenic processes, including pluton emplacement (Hollister and Andronicos 2006). For instance, interactions between deformation and plutonism (Hollister and Crawford 1986, Ingram and Hutton 1994) and plutonism and metamorphism (Hollister 1982, Hollister 1993) have been well documented. The processes that control pluton emplacement have also been extensively studied (Klepeis et al 1998, Andronicos et al 2003, Chardon et al 1999, Chardon 2003). This paper presents detailed field studies of plutons in the Coast plutonic complex of British Columbia, Canada (Figure 2.1), that provide significant insight into the structure of a relatively unstudied segment of the Coast Mountains batholith. Our analysis is focused on field relationships between the plutons and their country-rocks, the geometry of the bodies in relationship to the inferred tectonic regime at the time of emplacement, and the role of shear-zones and preexistent structures in emplacement of the magmas. Our results document the complex kinematic patterns that develop during plutonism and highlight the role of magma emplacement in controlling the architecture of the middle crust.

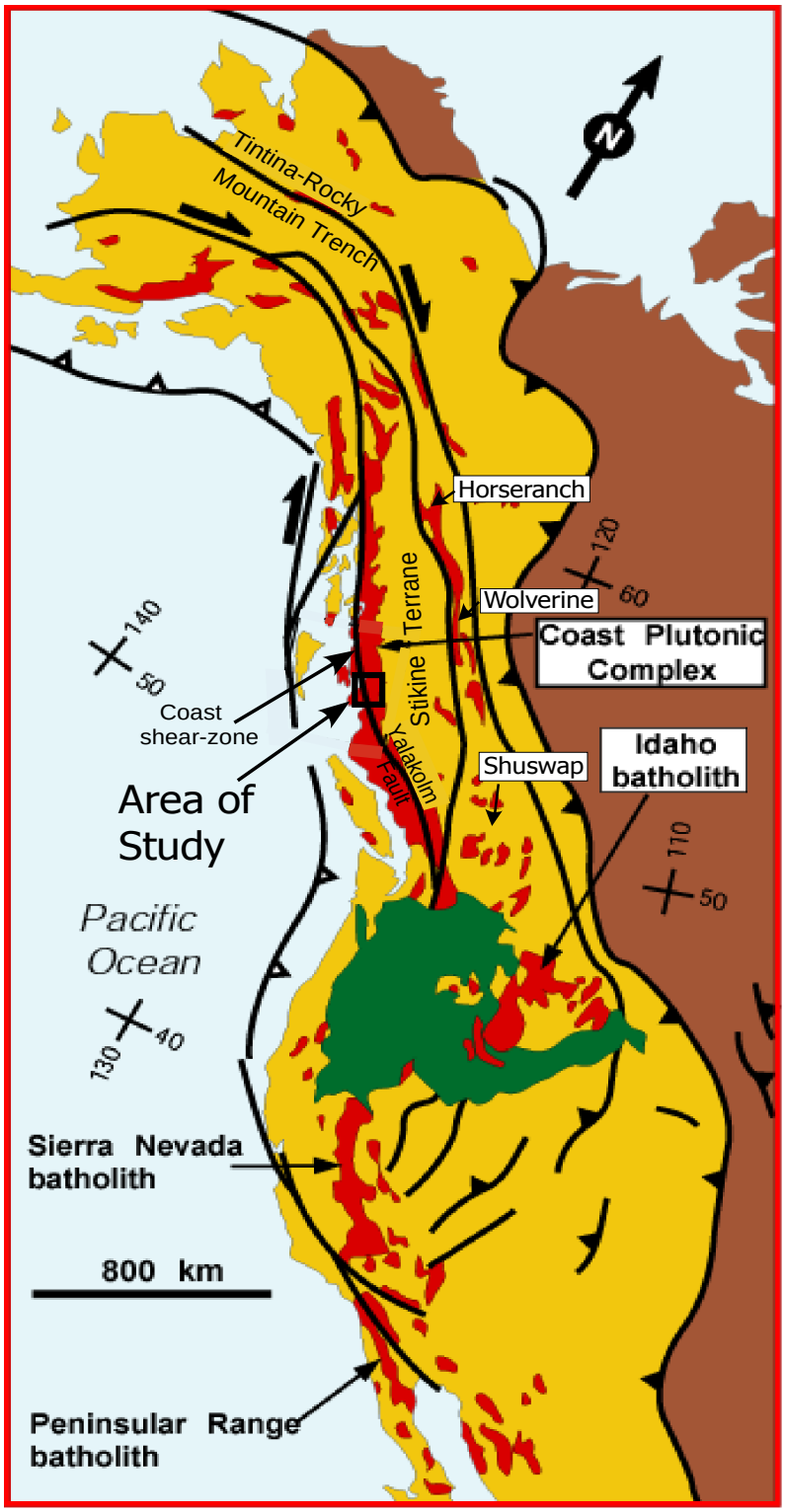

Figure 2.1: Map of western North America. The yellow area is the North American Cordillera. The red areas represent Mesozoic batholith complexes. Green marks the Columbia River and Snake River plain flood-basalts. Major faults are shown. Map modified from Chardon et al 1999.

III. Tectonic overview of the Coast Mountains of British Columbia

The Coast Mountains are located on the western side of the Canadian Cordillera. They track the complete tectonic evolution of an orogen from its formation by subduction and collision to its exhumation and uplift (Hollister 1982, Hollister and Andronicos 2006). The rocks that constitute the orogenic belt today are metamorphic and igneous rocks and extend for more than a thousand kilometers along the North American margin (Hollister and Andronicos 2006). The quality and extent of these outcrops make the Coast Mountains an excellent place to study middle crustal processes during orogenesis and pluton emplacement.

During the Mesozoic a series of elongated terrains (e.g. Stikine, Wrangell and Alexander) collided along the western Canadian Cordillera (Johnston 2001). The final terrains to collide compose the Insular Superterrane (Alexander, Wrangelia, and Taku terranes, and Gravina belt). The timing of the final docking of the terranes is still a subject of discussion, but most evidence points to assembly during the middle Cretaceous (Rubin and Saleeby 1992, Crawford et al 1987) followed by large magnitude right lateral coastwise displacements (Irving et al 1996, Enkin 2006). The magnitude of coastwise displacement is not well constrained, but conservative estimates suggest ~1000 km (Butler et al 2002), whereas paleomagnetic data suggest as much as 3000 km of displacement (Enkin 2006).

The localization of transpression from the amalgamation of terranes resulted in two orogen parallel belts of high-grade metamorphic rocks and associated arc-related plutons, the Omineca and the Coast belts. The two belts are separated by the interior plateau of British Columbia. However, the

timing of much of their deformation, metamorphism and plutonism is synchronous suggesting tectonic linkage between these two belts.

During the Late Cretaceous and early Tertiary (~90 Ma to ~50 Ma) the sense of shear across regional scale, northwest striking, strike-slip faults was dextral and focused within several crustal scale shear-zones (Struik 1992, Andronicos et al 2003, Figure 2.1). These include the Tintina- Northern Rocky Mountain Trench and Pinchi faults along the eastern side of the Interior plateau, and the Fraser and Yalakolm faults in southern British Columbia (Gabrielse 1985, Price and Carmichael 1986, Struik 1992, Umhoefer and Klienspehn 1995). The Coast shear-zone in the Coast belt has a complex kinematic history with right lateral transpression (Andronicos et al 1999; McClelland and Mattinson 2000) followed by reverse and normal dip-slip displacements (Ingram and Hutton 1994, Klepeis et al 1998, Rusmore et al 2005).

The crust was significantly thickened by the contractional to transpressional deformation that occurred during this time interval (90-50 Ma) (Hutchison 1982, Crawford et al 1987, Thomas and Sinha 1999, Hollister and Andronicos 2006). In the Coast Mountains, magmatism and amphibolite to granulite grade metamorphism was focused east of the Coast shear-zone during this time interval (Hollister and Andronicos 1997). At ~60 Ma the magmatic flux increased resulting in a magmatic flare-up that lasted until 50 Ma, when a large volume of plutons was emplaced within the Coast Mountains, and regions to the east. This event was accompanied by fast exhumation of several metamorphic core complexes within the Omineca belt, including the Wolverine complex (Struik 1992); the Shuswap Complex (Parrish et al 1988); the Horseranch Range (Plint et al 1992). The Coast Mountains

batholith was also exhumed at this time (Hollister 1982, Hollister 1993, Andronicos et al 2003).

The Coast shear-zone is the most prominent structure in the Coast Mountains because it separates rocks with contrasting magmatic, metamorphic and structural histories (Crawford and Hollister 1982, Figure 2.2). West of the Coast shear-zone amphibolite facies rocks cooled rapidly following pluton emplacement (Crawford et al 1979 and 1987). These rocks were reheated to the greenschist facies (~250 to 300℃) in the interval 65-50 Ma due to uplift of hot rocks on the east side of the Coast shear-zone (Hollister et al 2004). East of the Coast shear-zone rocks record their thermal peak at this time (Hollister 1993).

The metamorphic rocks, east of the Coast shear-zone, that host the late Cretaceous and early Tertiary plutons are referred to as the central gneiss complex (Hutchison 1982, Hollister and Andronicos 2000, Figure 2.2). The central gneiss complex is a high-grade metamorphic terrane and extends from southeastern Alaska to the Kitlope Lake area, south of Gardner Canal. The central gneiss complex is characterized by peak temperatures of >700℃, peak pressures of >8 kbar, and a clockwise P-T path marked by isothermal decompression and cooling ages for hornblende and biotite of <52 Ma (Hollister 1982, Hollister and Andronicos 2000, Andronicos et al 2003, Rusmore et al 2005). These features suggest that rocks that extend for more than a thousand kilometers along strike, all experienced a metamorphic event in the upper amphibolite to granulite facies, in the late Cretaceous to early Tertiary during extensive intrusion of plutons (Andronicos et al 2003, Johnston and Canil, 2007, Rusmore et al 2005).

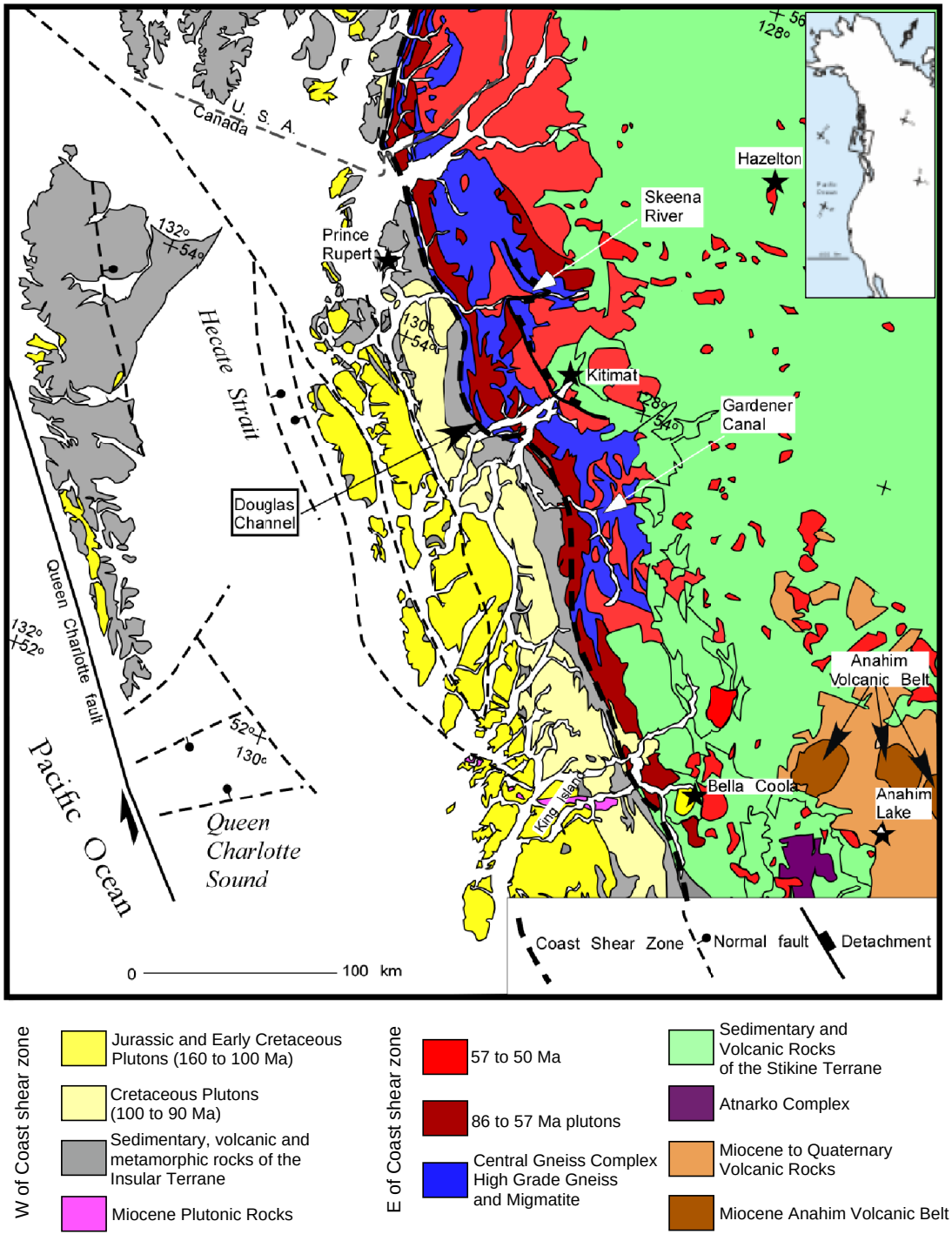

Figure 2.2: Simplified geologic map of the Coast Mountains between 52° and 56°. Modified form Hollister and Andronicos 2006.

One of the most studied batholiths east of the Coast shear-zone is the Quottoon pluton, which is the southernmost extension of the “Great tonalite sill” (Brew and Ford 1981, Ingram and Hutton 1994, Figure 2.2). The Great tonalite sill is an orogen-parallel batholith which extends from southeast Alaska to British Columbia. It intrudes the northeastern side of the Coast shear zone for nearly a 1200 km with an average width of <25 km (Thomas and Sinha 1999). The batholith is composed of physically and chemically distinct steep tabular plutons emplaced in close spatial association during the deformation of the Coast-shear zone prior to the complete crystallization of the magmas (Ingram and Hutton 1994, Thomas and Sinha 1999, Andronicos et al 1999). This batholith intruded late kinematically during active NE-SW directed contraction (Ingram and Hutton 1994, McClelland et al 1992, Klepeis et al 1998, Andronicos et al 1999).

The Gamsby Complex (Figure 2.2) bounds the central gneiss complex to the east. Mt. Gamsby records Jurassic deformation and superimposition of deformation (Hamblock 2006). An early flat foliation associated with recumbent folds is overprinted by vertical NW-SE trending vertical folds. The last deformation is linked to the intrusion of a tonalite with a zircon age of 155.3 ± 2.7 Ma (Table 2.1). The older deformation is estimated to be older, based on a 188.1 ± 3.3 Ma quartz diorite postdating the recumbent folds (Hamblock 2006). The final structural pattern encountered at Mt. Gamsby are folded domains of flat and steep foliations, which are preserved because no younger deformation occurred in the area.

In this paper we focus on the structure of southern termination of the central gneiss complex and analyze the plutons that intruded in the area during the early Tertiary magmatic flare-up. We also show a detailed

Table 2.1: Zircon crystallization ages present in the area

Pluton	Age (Ma)	Error (Ma)
Quottoon	59.5	1.6
Chief Matthew's	58.2	0.9
Chief Matthew's	55.6	0.9
Kitlope	61.1	1.2
Diorite Gamsby	188.1	3.3
Tonalite Gamsby	155.3	2.7
Dike Gamsby	52.0	2.8
Orthogneiss	96.8	2.1
Orthogneiss	125.4	3.3

description of the kinematics during plutons emplacement and the deformation in the country-rocks.

IV. Structure of the southern termination of the central gneiss complex

Gardner Canal is a fjord formed during the last Cenozoic glaciation in Coastal British Columbia (Figure 2.3). The Canal extends for ~110 kilometers from the Kitlope Lake to Douglas Channel, and provides access to a transect through the central gneiss complex and the associated plutonic bodies. Curved segments and numerous bays of Gardner Canal provide access to across strike and strike parallel sections of the structure of the area. A regional map of the area was originally completed by Roddick (1970) as part of the Coast Mountains mapping project. In this work we provide a more detailed analysis of the structure at Gardner Canal focused on the kinematics and finite strain pattern recorded in this segment of the orogen. The work is based on detailed mapping of a ~40 kilometer transect from Europa Bay to Queen Point. Kitlope Lake is located at the southern termination of Gardner Canal (Figure 2.3). Two different mountain ranges were studied in detail on ridges above each side of the Kitlope Lake.

The rocks at Gardner Canal and Kitlope Lake are upper amphibolite facies orthogneiss and amphibolite interlayered with rare paragneiss. The protoliths of the amphibolite and paragneiss are supracrustal and may, at least locally, correlate with rocks of the Stikine terrane. The rocks are deformed profoundly with protoliths varying from coarse-grained plutonic rocks to mixed metasedimentary rocks. These rocks are often cross-cut by pegmatitic and aplitic dikes that intruded prior to the last deformation phase. Less common are layers of paragneiss, which are easily spotted in the field by their

Figure 2.3: Geologic map of the southern termination of the central gneiss complex. The map shows areas and points of references mentioned in the text. Also shown are the sample locations mentioned in the text.

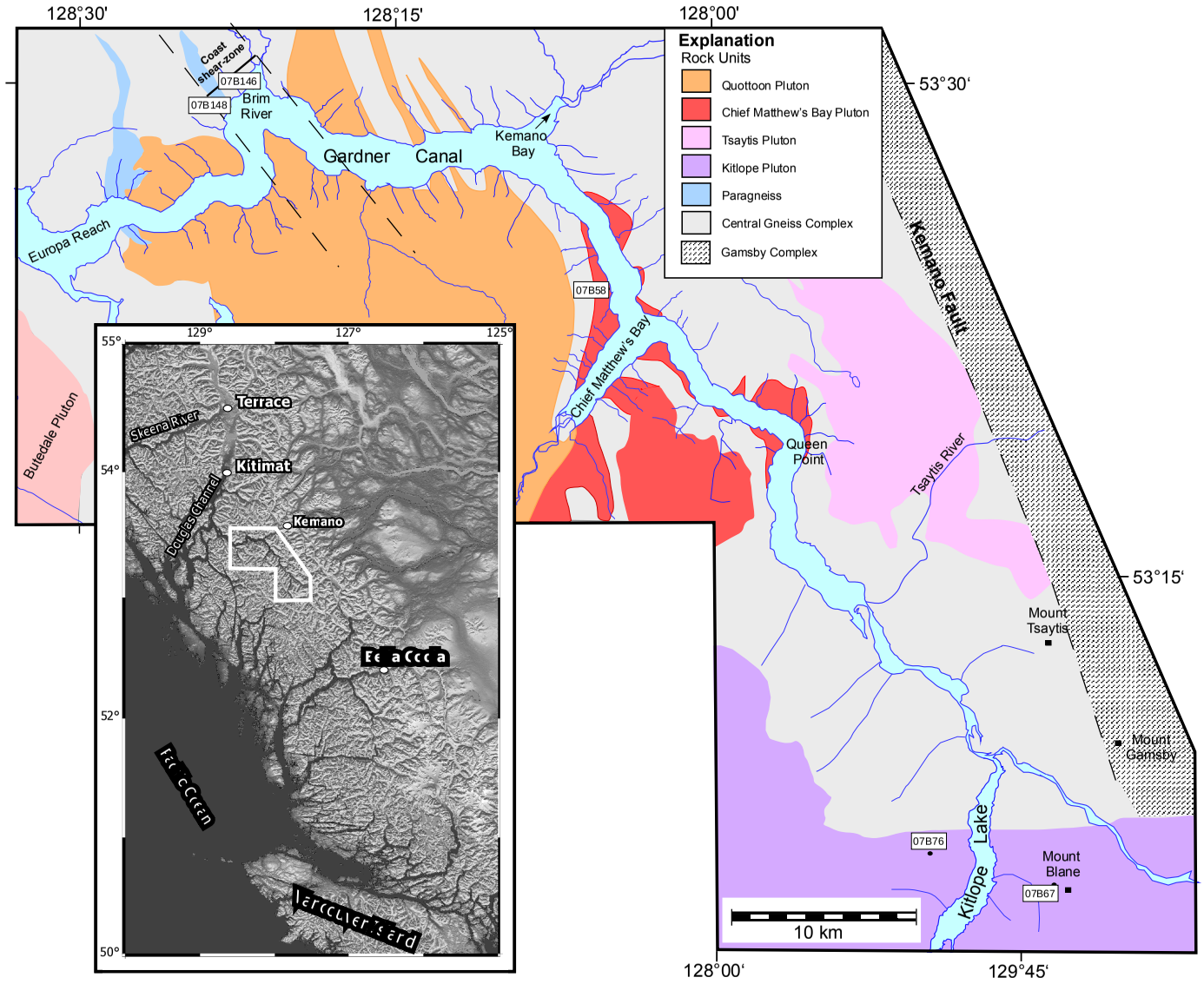
128°30'
128°15'
128°00'
53°30'
53°15'
128°00'
129°45'
Explanation
Rock Units
Quottoon Pluton
Chief Matthew's Bay Pluton
Tsaytis Pluton
Kitlope Pluton
Paragneiss
Central Gneiss Complex
Gamsby Complex
Coast shear-zone
07B146
07B148
Brim River
Gardner Canal
Kemano Bay
Europa Reach
Butedale Pluton
07B58
Chief Matthew's Bay
Kemano Fault
Queen Point
Tsaytis River
Mount Tsaytis
Mount Gamsby
Mount Blane
07B67
07B76
Kitlope Lake
10 km
129°
127°
125°
55°
54°
52°
50°
Terrace
Skeena River
Kitimat
Douglas Channel
Kemano

characteristic rusty weathering. Another type of rock found in the area is calc-silicate, which weathers a characteristic green color due to the abundance of epidote and diopside in the rocks.

Three main plutonic bodies are present in the area: 1) A granodiorite correlated to the Quottoon pluton; 2) a granodiorite named in this paper the Chief Matthew's Pluton; and 3) a granodiorite called the Kitlope Pluton in the south (Figure 2.3). There are nine localities with radiometric zircon ages in the area (Table 2.1, Gehrels et al in revision). One zircon age corresponds to the Quottoon pluton, and is 59.5 ± 1.6 Ma. Two ages correspond to the Chief Matthew's pluton and are 55.6 ± 0.9 and 58.2 ± 0.9 Ma. The Kitlope Pluton has an age of 61.1 ± 1.2 Ma. Other two ages are of orthogneiss of the central gneiss complex and are 96.8 ± 2.1 and 125.4 ± 3.3 Ma. The final three ages correspond to the Gamsby complex, and are a quartz diorite of 188.1 ± 3.3 Ma, a tonalite of 155.3 ± 2.7 Ma, and a younger dike of 52 ± 2.8 Ma. Even though the average age difference between the Quottoon, Kitlope, and Chief Matthew's plutons is only ~4 Ma, the tectonic strains and orientations which dominated the individual intrusions and the kinematics are very different as will be shown below.

For this reason, the structure of the termination of the central gneiss complex is described with emphasis on these three main plutons and the deformation of the country-rocks around them. This integrated study is useful given that the country-rocks record information that has been erased from the pluton given its molten character. Moreover, the deformation of the country-rocks is the key to unravel the mechanisms by which a pluton makes room for its intrusion.

IV.A. Kitlope Pluton (~61 Ma) and country-rocks

The Kitlope pluton is a granodiorite that intruded into the central gneiss complex. The northern contact of the pluton is nearly vertical and strikes E-W (Figure 2.3-2.4). The intrusion consists of discrete sheets of granodiorite interrupted by (rare) screens of orthogneiss and amphibolite, similar in many ways to the Quottoon pluton to the north. However, the Kitlope pluton is not as intensely deformed, and has many regions which preserve pristine magmatic fabrics.

The pluton varies from foliated to non-foliated (S_K) with the strongest solid-state foliations occurring near its contacts and near country rock screens. In many places the foliation is concordant with country rock fabrics, but in some places the pluton crosscuts fabrics attesting to deformation prior to the intrusion of the pluton. Fabrics within the pluton show a complete transition from solid-state foliation near the contacts to magmatic foliation in the interior. Foliations vary from N-S along its western side to E-W with consistent steep to subvertical dips towards the eastern side of the Kitlope Lake, at Mt. Blane (Figure 2.4).

Mineral lineations (L_K) within the pluton are defined by oriented biotite and hornblende. On the west side of Kitlope Lake, mineral orientations are variable, but generally steeply plunging (Figure 2.4). This variability is also found in the country-rocks, where the lineations are also defined by elongate minerals such as hornblende and biotite. At Mt. Blane, on the east side of Kitlope Lake, the lineations define a girdle parallel to the foliation plane with a west plunging maximum (Figure 2.4).

On the west side of the Kitlope Lake, the foliation is folded into open folds defined by screens of country rocks. These folds (F_K) have steeply

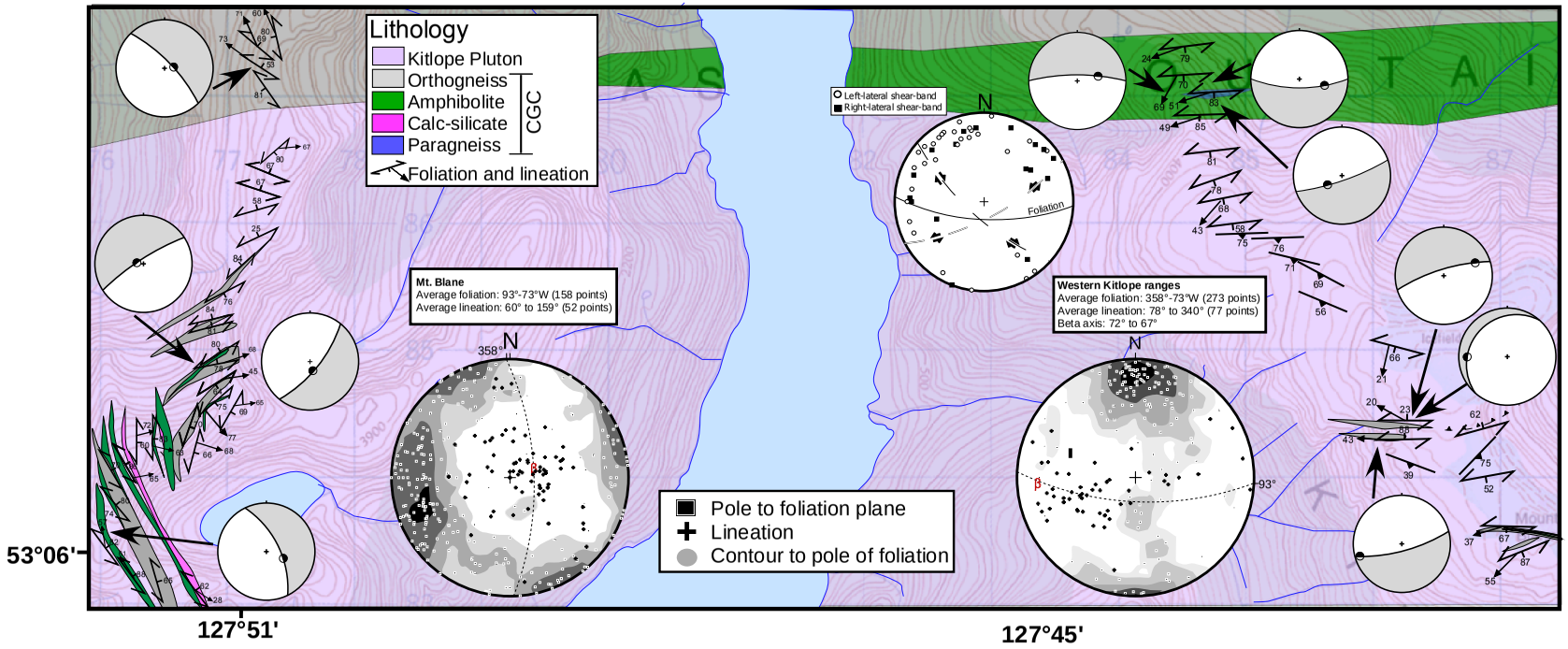

Figure 2.4: Geologic map and stereonets summarizing the structure of the Kitlope Lake area.

plunging hinges sub-parallel to the mineral lineation in this area (Figure 2.4). The approximate orientation for the fold axial plane is E-W, which is consistent with the general E-W striking foliation seen in the pluton at Mt. Blane farther to the east.

The northern contact of the pluton on the west side of Kitlope Lake is characterized by the presence of an intrusive breccia, made up of two phases of the Kitlope pluton (Figure 2.5a). Within the country rocks to the north of the breccia the foliation is northwest striking. South of the breccia, the foliation within the pluton strikes ~E-W with steep dips similar to the orientations to the east at Mt. Blane. In contrast to the contact on the west side of Kitlope Lake, the contact at Mt. Blane is sharp and concordant between the country rocks and the pluton. At the contact with the country rocks, the pluton has well developed solid state foliation which decreases in intensity to a magmatic alignment of feldspar in the interior of the pluton. This transition occurs within 500 m of the contact.

Kinematics

At Mt. Blane, shear-bands were recognized in the pluton by offsets in dikes and country-rock screens, or by the deflection of the foliation (Figure 2.5b). Two populations of strike-slip shear-bands were recognized which had a conjugate geometry. When plotted in stereographic projection, the acute angle made by the intersection of right-lateral and left-later shear-bands is bisected by the average foliation plane for the area (Figure 2.4). This observation is consistent with formation of the shear-bands at the same time as the formation of the foliation. This geometry is consistent with N-S shortening across the

Figure 2.5: Mesoscale and Microscale pictures of structures found in the rocks of study. (a) Agmatite breccia located at the contact of the Kitlope pluton with the country-rocks to the north, at the western margin of the Kitlope Lake. The fragments and the matrix belong to the Kitlope pluton. (b) Reverse shear-band in the Kitlope pluton cutting mafic dike and also the deflection in the foliation in the orthogneiss. The shear-band is filed with melt. (c) Melt filling tension gashes perpendicular to the nearly-vertical foliation of the Quottoon pluton. (d) Folded boudins in amphibolite at locality 2. The boudin necks were reactivated as reverse shear-bands filled with melt during folding and intrusion of the Quottoon pluton. The fold asymmetry is consistent with top to the NE sense of shear. (e) Photomicrograph of plagioclase with mechanical twinning and bulging boundaries with quartz. Interlobate grain-boundary between quartz grains. (f) Photomicrograph of tiled plagioclase indicates magmatic flow during crystallization. (g) Isoclinal to tight folds in amphibolite at the contact with the Chief Matthew's pluton at locality 3. The axial plane of the folds is parallel to the contact with the pluton. (h) NW-dipping shear-bands in amphibolite at the contact with the base of Chief Matthew's pluton at locality 5. (i) L-tectonite in orthogneiss at locality 5. (j) Macrocale chocolate-tablet boudinage in country-rock at locality 6. (k) Country-rock at the base of the Chief Matthew's pluton showing melt present deformation. The horizontal foliation is being boudinaged, with leucosome parallel to the foliation and filling boudin necks.

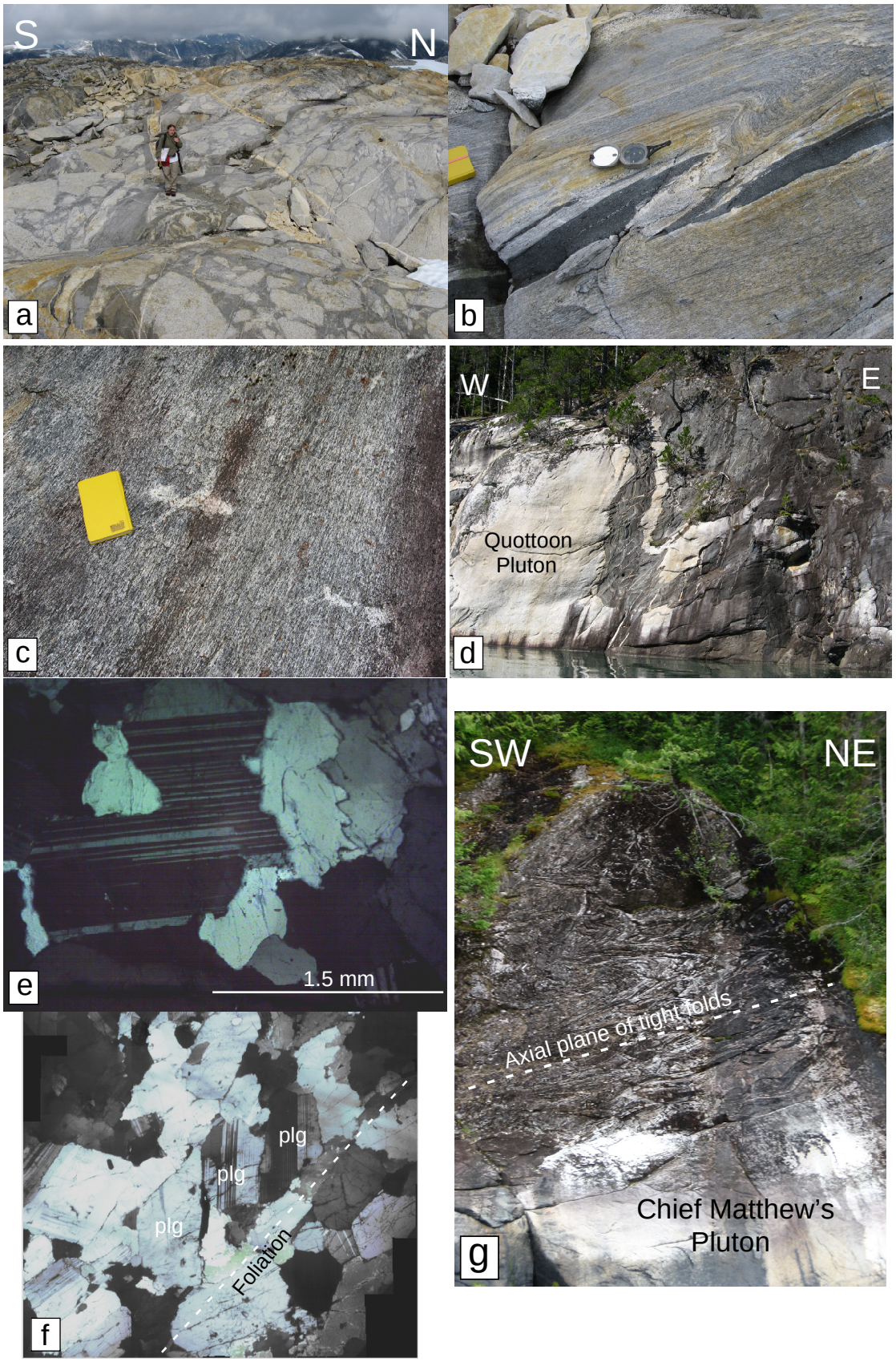
S
N
a
b
c
W
E
Quottoon
Pluton
d
e
1.5 mm
SW
NE
Axial plane of tight folds
Chief Matthew's
Pluton
g
plg
plg
plg
Foliation
f

Figure 2.5 (Continued)

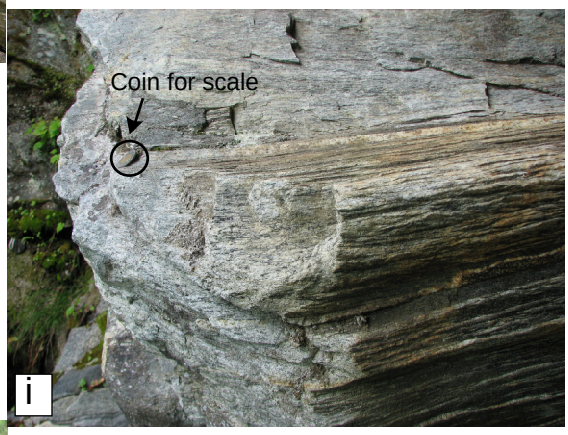

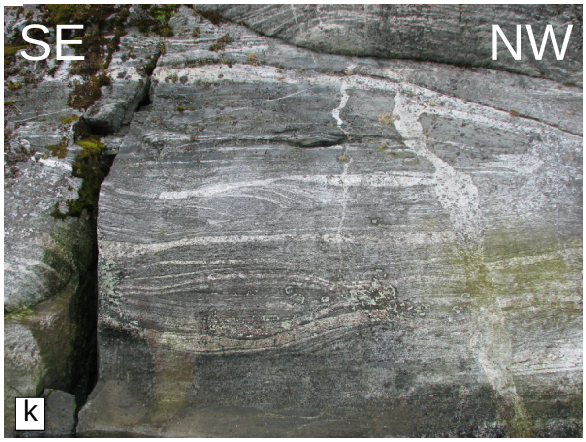

pluton country rock contact. The larger number of left-lateral shear-bands point to a greater left-lateral component to the deformation.

Microscale kinematic indicators and asymmetric folds consistently show south-side up shear. This is consistent with the pluton being up relative to the country rocks (Figure 2.4).

To summarize (Table 2.2), the Kitlope pluton has a steeply dipping east-west contact along its northern margin. Kinematic indicators and the orientation of the foliations are consistent with N-S shortening and south-side up shear, indicating an upward movement of the pluton during emplacement. The western margin of the pluton contains folded country rock screens which have east-west axial surfaces and steeply plunging hinges, consistent with N-S shortening and vertical stretching.

IV.B. Quottoon pluton (~60 Ma) and country-rocks

The Quottoon pluton is found in the area between Brim River and Kemano Bay. The pluton is a granodiorite characterized by interleaved tabular plutonic bodies with steep dips and abundant country-rock screens. The number of country-rock screens gradually increases towards the east until the plutonic rock ceases to appear at Kemano Bay (Figure 2.6-2.7). Migmatites are common east of Brim River within the country rock screens. The migmatites are characterized by patches of felsic minerals with course grained hornblende. The patches disrupt the fabrics of the host gneiss and have igneous textures. The migmatites are texturally and mineralogically similar to migmatites found along the Skeena River to the north (Kenah and Hollister 1983, Lappin and Hollister 1980), which are interpreted to have developed as a result of hornblende dehydration melting. Many of the patches are present

Table 2.2: Deformation events

Event	Location		Associated Structures	Intrusior	Regime	Time
D1	Gardner Canal		Steep and flat fabrics Boudinage			>125 Ma
D2	From Brim River to South of Kemano Bay	S_2	NW-SE foliation steeply dipping to the SW	Quottoon Pluton	Horizontal Flattening	~60 Ma
		F_2	folds with axial planes // to S2			
		L_2	Lineation radially distributed Top to the NE reverse shear			
	Kitlope Lake	S_k	~Vertical E-W foliation	Kitlope Pluton		
		L_k	~Vertical lineation			
		F_k	folds with E-W axial plane			
	Europa Reach	S_{ER}	Steep NW-SE foliation			
		L_{ER}	S-plunging shallow lineation dextral shear-sense			
D3	From South of Kemano Bay to South of Queen Point including Chief matthew's Bay	S_3	NW-SE foliation shallowly dipping to the SW	Chief Matthew's Pluton	Subvertical Flattening	~58 Ma
		L_3	Lineation radially distributed in foliation plane with 2 orthogonal maxima			

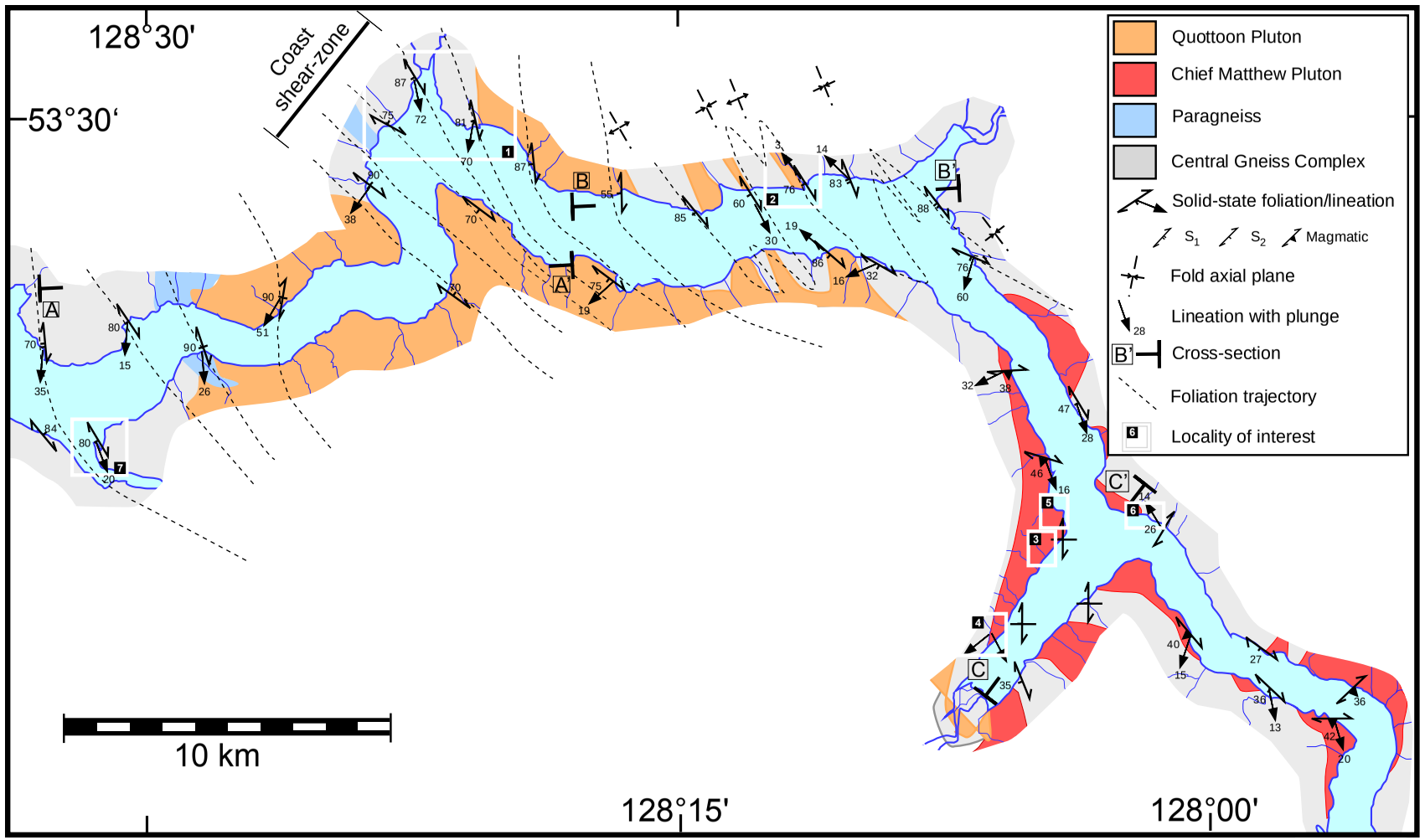

Figure 2.6: Map of the area of Gardner Canal, showing variations of foliation and lineation in the study area.

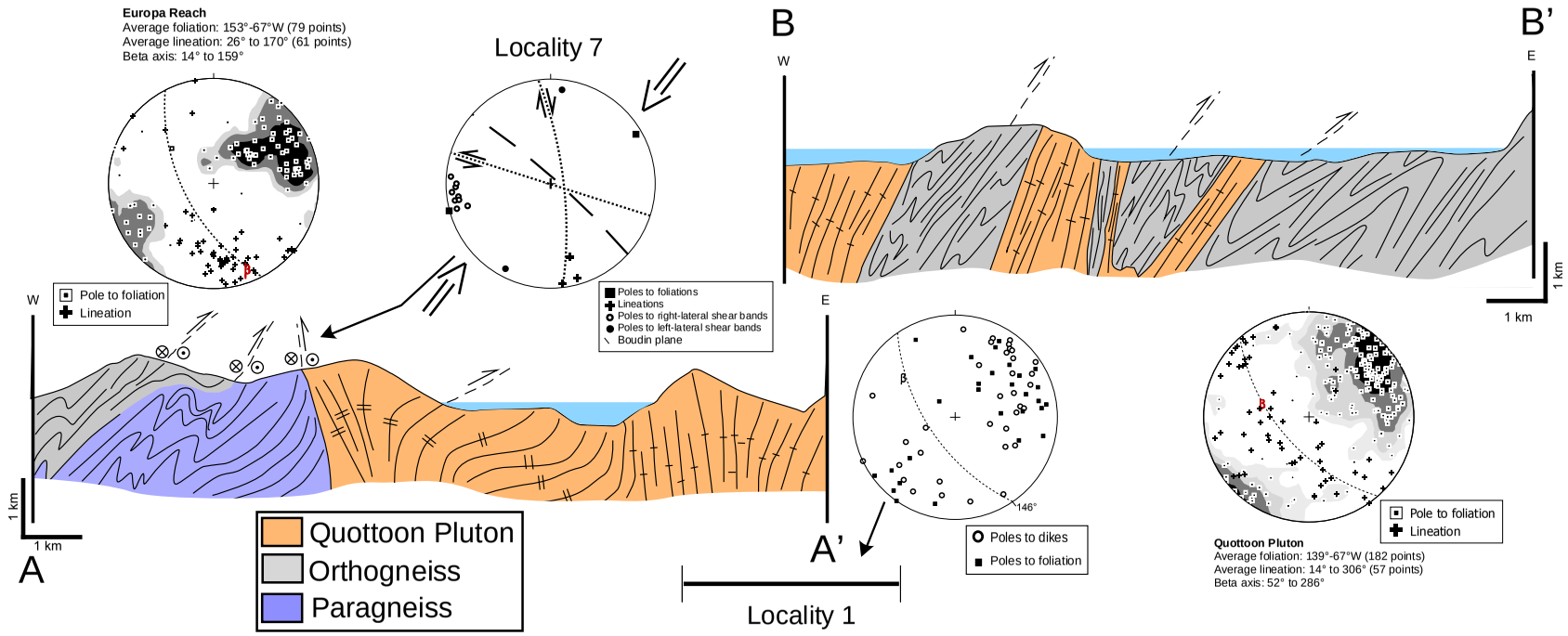

Figure 2.7: Cross-section and stereonets of the region from Europa Reach to Kemano Bay (see figure 2.4 for exact location).

as tabular gashes at high angles to the stretching lineation in the rock suggesting they were melts filling tensile fractures (Figure 2.5c).

The country rocks that host the Quottoon Pluton are intensely folded and contain evidence for at least two episodes of deformation (Table 2.2). At the margins of the Quottoon pluton asymmetric northeast vergent folds (F_2) are common. The axial planes to the folds dip steeply to the southwest and the fold axis trend northwest-southeast with shallow plunges. Spatially, the folds become tighter as the Quottoon pluton is approached from the east. These folds fold an earlier gneissic foliation (S_1). This gneissic foliation appears to have had shallow dips prior to folding. This foliation records an episode of intense boudinage prior to folding (F_2) as indicated by the ubiquitous presence of folded boundins in the area between Brim River and Kemano Bay (Figure 5d). Locally at the margins of the Quottoon pluton the boudin necks were reactivated during folding (F_2) into reverse shear-bands filled with leucosome. The Quottoon pluton is also folded at the contact into cuspate/lobate folds. The geometry of the folds indicates that the pluton was less competent than the country rock suggesting that it was not completely crystallized during folding. We refer to the early gneissic fabric as S_1, and the axial planar cleavage as S_2. However, it is likely based on regional relationships that S_1 is a transposition fabric (see for example Hamblock 2006).

A well-developed mineral lineation (L_2) is defined by aligned hornblende and biotite. The lineation defines a girdle parallel to the S_2 foliation plane (Figure 2.7). Several outcrops within the Quottoon pluton and orthogneiss contain a very strong lineation so that it was difficult to define a foliation. These domains of strong linear fabric were found at the fold hinges within the country rocks, and within a particularly mylonitized section of the Quottoon pluton.

Boudins also occur parallel to the fold axis of F_2 folds. These observations taken together indicate stretching parallel to the fold axis during F_2 at the macroscale. However, the distribution of stretching lineation on a girdle parallel to S_2 is consistent with flattening at the bulk scale (eg. Gapais et al 1987).

Within the Quottoon pluton there is a single well-developed foliation, which strikes northwest-southeast with steep western dips (Figure 2.7), parallel to the axial planar cleavage within host rocks. The foliation within the pluton is defined by the alignment of biotite, hornblende and tabular plagioclase grains. Microscopically the fabric is defined by aligned laths of plagioclase with interlobate grain boundaries with bulging microtexture (Figure 2.5e). Chessboard extinction in quartz is widespread. Plagioclase also contains abundant mechanical twins, some of which include bent twinning. These textures are consistent with deformation at temperatures close to the solidus of the rock, and are similar to those described for the Quottoon pluton farther north (Ingram and Hutton 1994, Andronicos et al 1999).

Going from east to west across the pluton, there is a strain gradient as indicated by an increase in the intensity of fabrics and changes in microstructure. For instance, quartz fills cracks in plagioclase located on the west. Quartz grains within the crack fillings have core and mantle microstructure, typical of deformation in regime 2 of Hirth and Tullis (1992). The cracks are oriented perpendicular to the lineation within the rock and are associated with the presence of sericite and epidote, consistent with alteration in the presence of fluids. This change in microstructure indicates that the strain gradient is associated with a decrease in temperature from west to east across the pluton. Similar textures and structures were interpreted by Ingram and

Hutton (1994) to indicate that this deformation occurred as the pluton solidified.

Kinematics

Kinematic indicators were recorded when found in the field; they include shear-bands, fold asymmetry, and sigma clasts. The kinematic interpretations were made on outcrop faces oriented parallel to the lineation and perpendicular to the foliation following the recommendations of Simpson and Schmidt (1983). Kinematic indicators were also studied at the microscopic scale in oriented thin sections.

We used the asymmetry of F_2 folds found from Brim River to Kemano Bay to infer large scale fold vergence. The fold asymmetry throughout the entire area between Brim River and Kemano Bay indicates northeast vergence. At Brim River (Locality 1, Figure 2.6-2.7), a series of folded pegmatitic dikes within plutonic rock also have asymmetry consistent with northeast vergence (Figure 2.7). The fact that the dikes are folded with the foliation indicates that the dikes are pre-tectonic with respect to the F_2 folds. The folded boudins were also used for kinematic indicators (Locality 2, Figure 2.6-2.5d). The boudin necks have been reactivated as reverse shear bands during folding, which indicates top to the northeast sense of shear, consistent with the fold asymmetry.

In summary (Table 2.2), the Quottoon pluton intruded at ~60 Ma. It contains a foliation which parallels the axial planar cleavage to F_2 folds in the country rocks. The foliation strikes northwest-southeast and dips steeply southwest. Lineations are radially distributed within the S_2 foliation plane, consistent with a large flattening component to the strain. The parallelism of

the foliation in the Quottoon pluton with the axial planar cleavage in the country rocks suggests these fabrics formed synchronously. This is supported by the cuspate lobate folds at the contact between the Quottoon pluton and its country rocks at Brim River. The northeast vergent folds and geometry of sheared boudin necks are consistent with top to the northeast reverse shear during F_2 folding. Overprinting relationships indicate at least one phase of deformation (D_1) in the country-rocks prior to the intrusion of the Quottoon pluton. This older fabric contains extensive boudins and likely had a shallow dip prior to folding.

IV.C. Chief Matthew's Bay Pluton (~57 Ma) and country-rocks

The Chief Matthew's pluton is a gently-dipping tabular pluton that extends from south of Kemano bay to Queen Point, including Chief Matthew's Bay (Figure 2.3-2.6). The pluton consists of several discrete granodioritic sills that altogether account for a thickness of ~6 km (Figure 2.8). The pluton usually contains hornblende and biotite as mafic minerals. However, there are sectors of the pluton that are more felsic and are characterized by the absence of hornblende and the presence of larger grains of microcline up to 2.5 cm in length.

At the microscopic scale, plagioclase is subhedral with tabular shape. It is common for the grains to be normally zoned and twinned. Quartz is anhedral and located in the interstices of other minerals indicating that it formed late in the crystallization sequence. Biotite is subhedral and has a pleochroism that varies from yellow to dark brown. Hornblende is subhedral with pleochroism that goes from light-green to dark-green and is associated

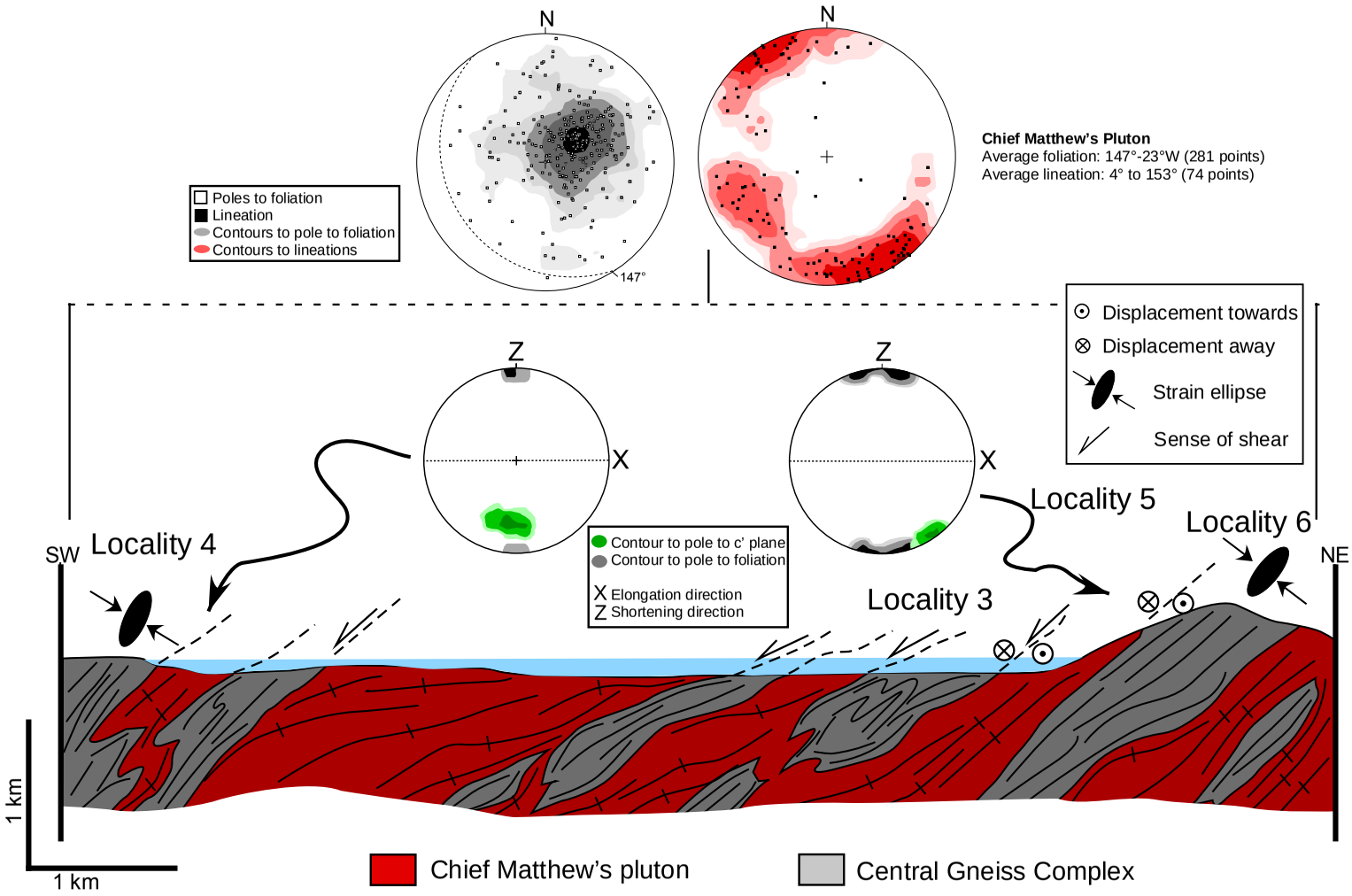

Figure 2.8: Cross-section and stereonets summarizing the structure across Chief Matthew's Bay (see figure 2.6 for exact location).

with biotite and titanite. K-feldspar is not very abundant, except in the hornblende absent sectors mentioned above.

The pluton has both magmatic and solid state foliations. Modifications to the original magmatic texture of the rock are found most obviously in quartz, which has chessboard extinction, bulging edges, and subgrains. Feldspar has a relatively pristine igneous texture with only deformation twinning. However, plagioclase grains are imbricated (Figure 2.5f), attesting to flow during crystallization. Shear-bands are widespread in outcrop and thin section, indicating shear during intrusion of the magma. Solid state deformation is not widespread throughout the pluton and is most common near the margins of the sills. The magmatic foliation within the pluton parallels foliations in the country rocks. Throughout the sill complex foliations strike northwest-southeast and dip gently southwest (Figure 2.8).

In the country rocks that host the pluton, a new foliation (S_3) is developed that overprints S_1 and S_2 (Table 2.2). This foliation is associated with F_3 folds which are tight to isoclinal with axial planes parallel to the contacts with the sills (Locality 3, Figure 2.6-2.5). Within screens of gneiss interior to the sills the foliation is completely transposed and is parallel to contacts with sills. The S_3 fabric is associated with intense boudinage. The boudin necks are filled with leucosome and granodiorite indicating deformation as the sills intruded. The geometry of the F_3 folds is consistent with folding across the pluton/country rock contact.

The lineation (L_3) is best developed in the country rocks and is defined by alignment of elongate minerals including biotite and hornblende, elongate mafic enclaves, and tabular feldspars. Two different lineations were found and are nearly perpendicular. The most common lineation trends northwest-

southeast and plunges shallowly. A second lineation is also present within the plane of shear bands. This lineation plunges moderately to shallowly to the southwest. The two lineations together define a girdle parallel to the mean foliation plane within the sill complex (Figure 2.8).

Kinematics

The two most common kinematic indicators within the Chief Matthew's pluton are asymmetric shear-bands (C') and asymmetrically tiled feldspars at the microscopic scale (Figure 2.5f). These structures and their kinematics are described in detail here.

At the southern tip of the Chief Matthew's Bay, the top of the Chief Mathew's pluton is exposed (Locality 4, Figure 2.6-2.8). The shear-bands in this area strike NW-SE and dip ~30° to the SW. The sense of shear across the shear bands is top down to the southwest. As described above the lineation within the shear-bands plunge to the SW while the lineation within the foliation plunge to the NW. The geometry of the shear bands coupled with the shear bands and foliation indicate two directions of stretching.

Mutually cross-cutting relationships show that deformation was synchronous with plutonism at this location and that both stretching directions developed during plutonism. For instance, an apophysis of the pluton cross-cuts the foliation, but is also folded with the axial surface parallel to the local foliation suggesting intrusion during and across the foliation plane. Furthermore the shear bands offset the apophysis of granite and also have granitic material concentrated into the shear plane, again indicating shearing while melt is present. These relationships indicate that intrusion of the granite

occurred during foliation development and folding as well as shear-band development.

Along the northeast side of Chief Mathew's bay, near its intersection with Gardner Canal (Locality 5, Figure 2.6-2.8), the bottom of one of the sills that makes up the Chief Mathew's pluton is exposed. Shear-bands in this area strike northeast and dip to the northwest. The sense of shear is top-down to the northwest. The contact between the country rocks and the pluton is concordant with both the shear-bands and the foliation (Figure 2.5h). Unlike the top of the pluton at the top of Chief Mathews's Bay, the intersection of the foliation plane and the shear bands is normal to the stretching lineation, indicating that the foliation and shear bands are kinematically compatible (Passchier and Trouw 1996). The shear bands have a monoclinic symmetry consistent with non-coaxial deformation (Figure 2.8). L-tectonites are also found in this area, and their lineation plunges parallel to the lineation found in L-S tectonites, which are cut by the shear-bands (Figure 2.5i). The geometry of the shear-bands and L-tectonites suggests strong northwest directed extension along this contact of the pluton.

On the northeastern side of Gardner Canal opposite Chief Mathew's Bay, the base of the sill complex is exposed (Locality 6, Figure 2.6). In this area shear-bands form anastomosing networks which interlink to form chocolate tablet boudinage of the foliation (Figure 2.5j). The geometry of the shear bands and boudins suggests a large coaxial component to the deformation. Since the average lineation and enveloping surface of the boudins are gently dipping, the shortening direction inferred to be subvertical in this area. This inference is confirmed by the presence of extensive dike and

vein arrays that also define chocolate tablet boudinage with two perpendicular directions of stretching.

At the microscopic scale, samples of the pluton contain fabrics which indicate magmatic flow within the pluton. These fabrics are defined by networks of tabular feldspar with interstial quartz and mafic phases. The feldspars are relatively undeformed. However, the feldspars are tiled and form proto C/S fabrics, which suggest a non-coaxial component to the magmatic flow (Gapais 1989) throughout the pluton. Shear-sense determined from shear-bands and magmatic fabrics are plotted in Figure 2.9. An interesting feature of the kinematics within the Chief Mathew's pluton is that the shear-sense is highly variable throughout the pluton. However, along the axis of Gardner Canal, the dominant flow direction appears to be northwest-southeast. In contrast, at the margins of the pluton, flow is northeast-southwest on average.

In summary, the Chief Matthew's Pluton intruded during formation of a new foliation (S_3, Table 2.2). The strain within the sill complex is highly variable. At the outcrop scale, shear-bands indicate domains of both non-coaxial and coaxial deformation. Asymmetric magmatic flow fabrics also show highly variable magmatic flow directions. Lineations are radially distributed within the foliation plane with northwest-southeast and northeast-southwest maxima. Overall, the geometry of the structures is consistent with intrusion of the sills during subvertical shortening and both orogen-parallel and orogen-perpendicular stretching. This overall pattern of deformation is consistent with tectonic extension during emplacement of the sill complex.

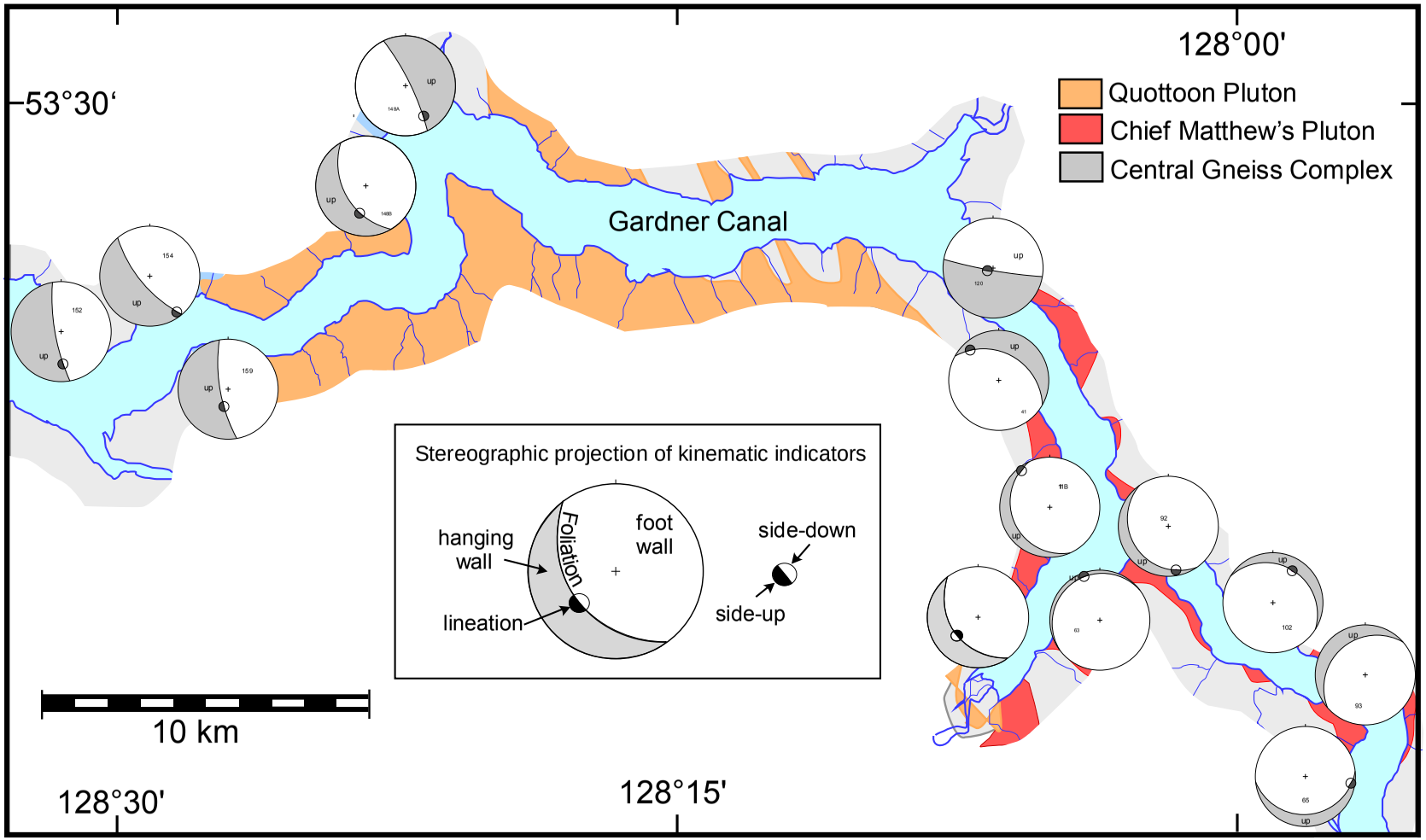

Figure 2.9: Kinematic indicators for Gardner canal. The data includes outcrop-scale and micro-scale. Kinematic indicators obtained on individual oriented samples.

IV.D. Europa Reach (west of the Quottoon pluton)

The rocks at Europa reach (Figure 2.3-2.6) are amphibolite and orthogneiss metamorphosed in the epidote amphibolite facies. The orthogneiss and amphibolite are characterized by abundant epidote and microcline. Garnet is present in the amphibolites as well as clinopyroxene. No migmatites were recognized in the area. Microscopically, the rocks show equigranular texture, with polygonal grains with boundaries at 120°. Some biotite grains, which trace the foliation of the rock, are enclosed in larger felsic grains. These textures indicate deformation at high temperatures and recovery after the end of deformation. No orthopyroxene is found in the rocks in the area which constrains the temperature to be below ~750℃.

The foliations (S_{2ER}) strike northwest-southeast and dip steeply southwest. The mineral lineations are clustered with shallow plunges to the south (Figure 2.7), consistent with strike-slip deformation. Some outcrops are isoclinally folded (F_{2ER}) with axial surfaces that parallel the northwest-southeast foliation. Fold hinges plunge shallowly to the southeast, subparallel to the mineral lineations. Parallel to the foliation, layers of calc-silicate rock rich in epidote and diopside are stretched into boudins. The intersection of two sets of conjugate shear-bands is bisected by the foliation plane (Locality 7, Figure 2.6). The fact that conjugate shear-bands develop indicate coaxial shortening normal to the foliation (Platt and Vissers 1980). All these structural elements together, point to a general northwest-southeast stretching direction and northeast-southwest shortening direction. However, dextral shear-bands dominate, which indicate dextral deformation with small flattening.

Kinematics

C' shear-bands cross-cutting the foliation are common west of the Quottoon pluton. Although conjugate pairs of shear-bands are common (Figure 2.7), dextral shear-bands are better developed and strike north-south with steep dips to the east. The sinistral set is less developed and strikes northwest-southeast and is sub-vertical. The dominance of dextral shear-bands together with the shallow lineation indicates a large dextral component to the deformation. Micro-structural analyses performed on oriented thin-sections documented sigma clasts, c/s fabrics and c'structures and confirm a dextral sense of shear (Figure 2.9).

A summary for the area west of the Quottoon pluton is that epidote amphibolite grade rocks contain a northwest-southeast foliation (S_{2ER}), and gently south plunging lineation (L_{2ER}). The sense of shear for the deformation is dextral based on shear-bands and micro-structural analysis.

IV.E. Strain Estimated By Autocorrelation Function

The structural analysis at Gardner Canal was complemented with results obtained using the autocorrelation function (ACF) technique (Heilbronner 1992), which uses a Fast Fourier Transform to estimate how well an image, in this case an oriented thin section, correlates with itself. This technique is powerful when applied to plutonic rocks and rocks of the central gneiss complex since conventional strain analysis techniques are impossible or hard to apply in these lithologies. The ACF is a function of grain size, shape and orientation of individual grains and density of mafic versus felsic minerals. The orientation of the mineral grains can be seen in the general shape of the ACF. Foliated rocks show elongated patterns parallel to the foliation, while

non-foliated rocks show isotropic patterns (Figure 2.10). Strain can be calculated by taking the ratio of the maximum and minimum axes of the ellipse representing a thresholded gray-level contour in the ACF. For consistency, we picked the ellipse representing the 96th gray-level in the image (Figure 2.11). The calculated value is a measure of deformation intensity, and a minimum estimate of the true strain.

In general, the sizes of the strain ellipses obtained using the autocorrelation function for the area of Gardner Canal are a function of the rock type. Country rocks show strain ellipses that are consistently smaller than the rocks of the Quottoon pluton (Figure 2.11a-b). Smaller ellipses can be correlated with smaller grain size of the rocks, which may indicate grain size reduction. This observation suggests that the plutonic rocks may be less deformed than the country rocks, again pointing to an intrusion of the Quottoon and Chief Matthew's plutons late in the deformation history of the area. All the thin sections were cut in the X-Z plane of strain. The ellipses in Figure 2.10 have been normalized to show the same minimum diameter. The ellipses are oriented with the long axis parallel to the orientation of the foliation for each sample. The general value for strain obtained for the plutonic rocks of Chief Matthew's pluton is 1.25, and for the Quottoon pluton 1.7. The position of the Coast shear-zone at Brim River is highlighted by the NW-SE orientation of the strain ellipses, towards the east and west the orientations change to different angles. The variable orientation of the ACF ellipses for the Chief Matthew' pluton is consistent with horizontal flow during sub-vertical flattening and radial stretching during pluton emplacement.

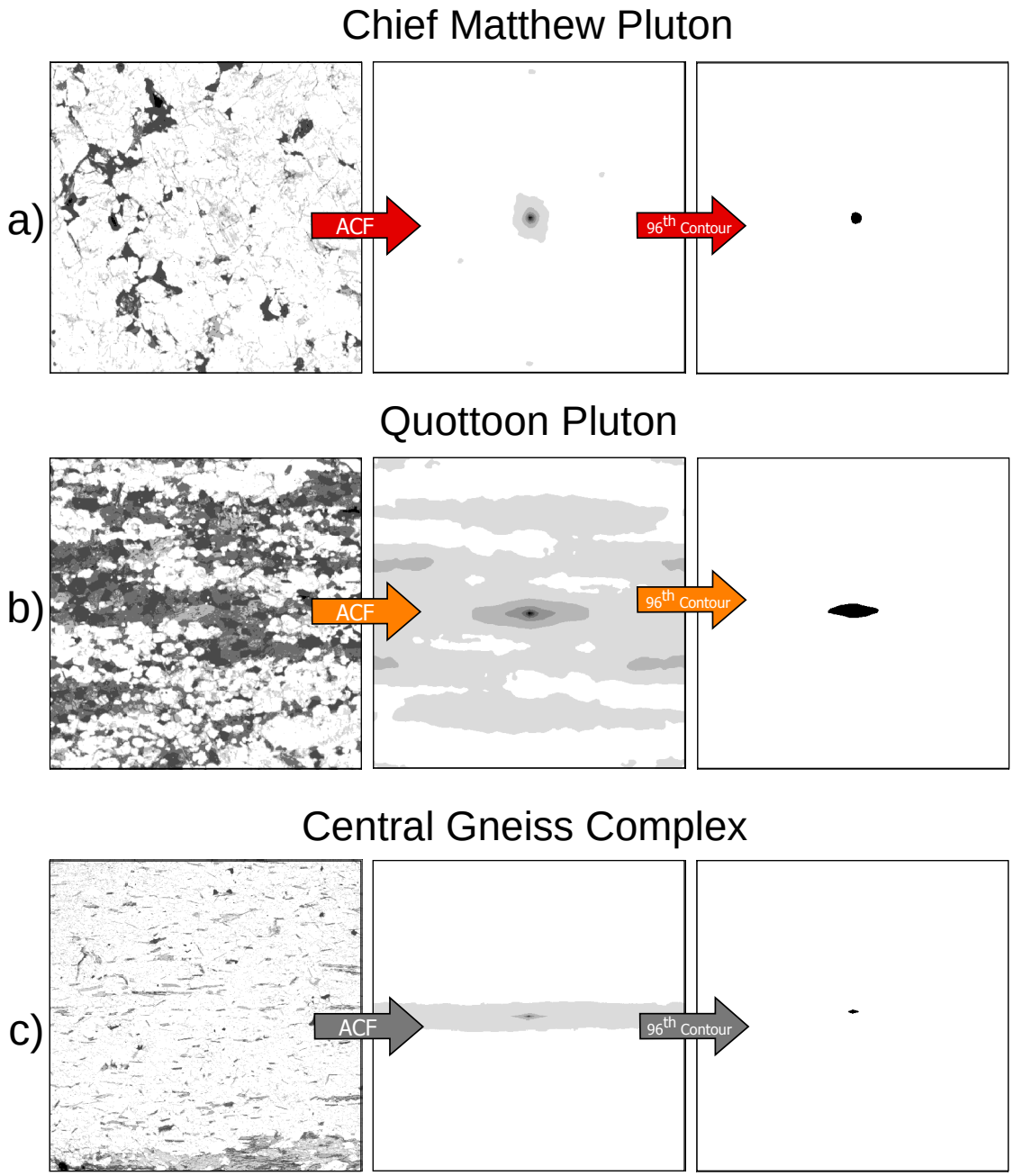

Figure 2.10: Examples of processing thin-sections of rocks with the autocorrelation function. The first image is a black and white scan of a thin-section; the second image is the autocorrelation function of the thin-section; the third image is the previous image filtered by selecting only the grey colors greater than the 96th grey contour, that can be correlated to the strain ellipse. The examples show the effect of a foliation and grain size on the resulting ellipse. a) plutonic rock; b) amphibolite gneiss; and c) biotite gneiss.

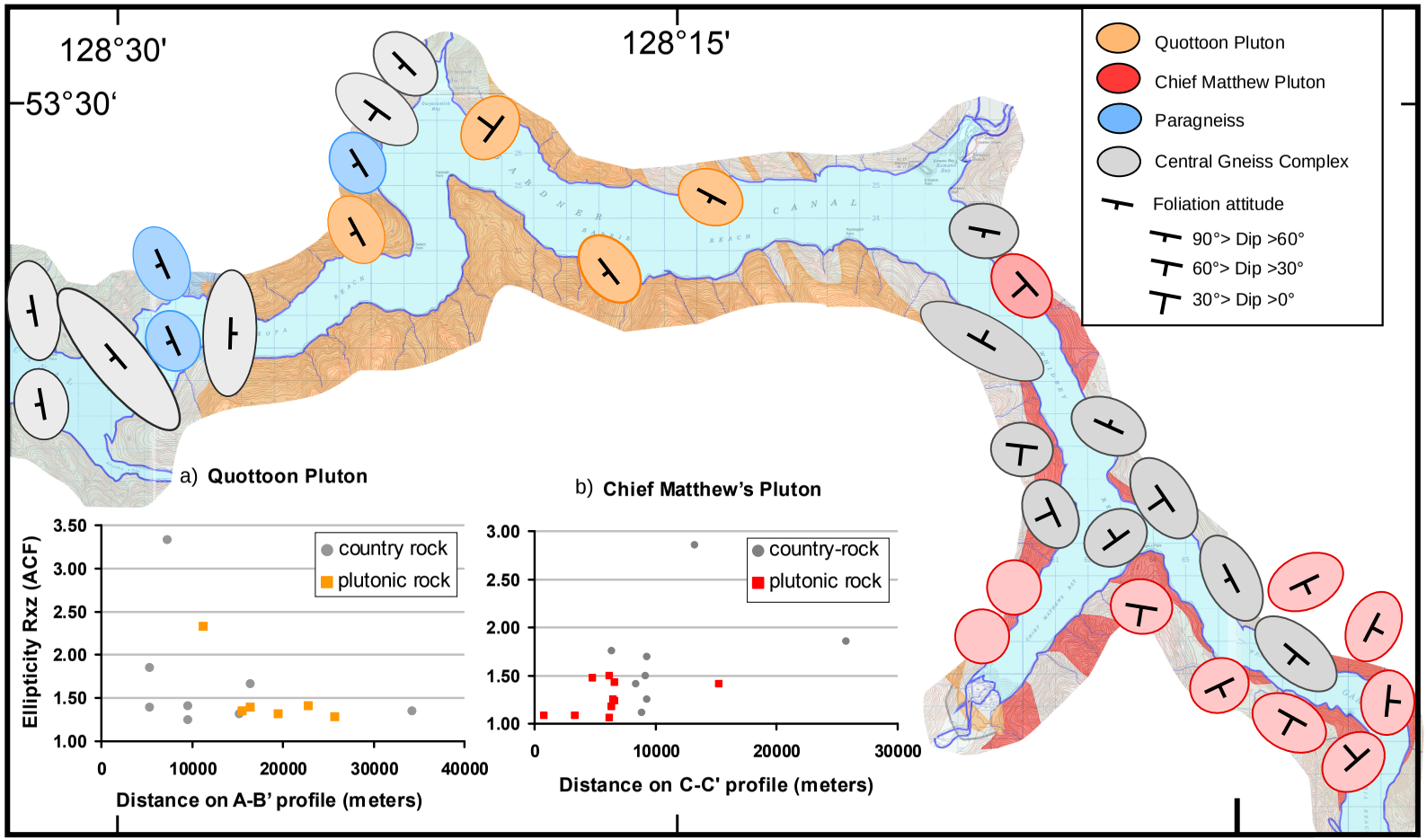

Figure 2.11: Strain ellipses calculated using the autocorrelation function for individual rocks at Gardner Canal. The size of the ellipses has been normalized to the average measured size to ease comparison of orientations and shapes. The ellipses are oriented with respect to the foliations of the rocks. The two graphs compare the ellipticity of the individual strain ellipses along the cross-sections. Ellipses were plotted with the long axis parallel to the strike of teh local foliation.

At Europa Reach the most prominent calculated strain ellipse shows an orientation for the stretching and shortening directions which matches the one derived by the shear-band analysis, and the ellipticity is 3.33.

V. Discussion

V.A. Coast shear-zone

The Coast shear-zone is the largest structure in the Coast Mountains (Brew and Ford 1978, Ingram and Hutton 1994). It is a crustal scale shear-zone that extends for more than 1200 km (Rusmore et al 2001) from Alaska to British Columbia. The minimum age of this structure is given by the age of the Quottoon pluton, which intruded post-kinematically during the waning stages of the structure (Crawford et al 1987, Ingran and Hutton 1994, Klepeis et al 1998, Thomas and Sinha 1999, Andronicos et al 1999, Rusmore et al 2001). The Coast shear-zone was developed after the accretion of terranes (Chardon et al 1999); however the possibility of it being a reactivated major suture between terranes can not be discarded (Hollister and Andronicos 1997). The structure has been reactivated several times, and left-lateral, dextral and down-dip movements have been described for different time periods.

Along strike (NW-SE), the Coast shear-zone is characterized by steep foliations, which usually dip to the NE, and are associated with nearly vertical lineations (Ingram and Hutton 1994, Klepeis et al 1998, Crawford et al 1987, McClelland et al 1992, Rusmore et al 2001, Andronicos et al 1999). In map view, the Coast shear-zone changes its width along strike and can be as wide as 15 km in some places, and as narrow as 5 km in others.

At Gardner Canal, the Coast shear-zone was previously recognized east of Brim River by Rusmore et al (2001), based on the presence of

protomylonitic fabrics in the Quottoon pluton, and the presence of reverse shear-bands that strike NW and dip to the NE. We agree with this inferred position for the Coast shear-zone but found no evidence for NE dip in this area. As described above, the Quottoon Pluton is characterized by a steeply southwest dipping solid-state foliation and steeply plunging lineation. Another discrepancy from other localities is that the Coast shear-zone is usually associated with east-side-up reverse shear-sense. At Gardner Canal, even though we infer reverse kinematics for the Coast shear-zone, the fold geometry consistently indicates a southwest-side-up geometry.

West of the proposed position for the Coast shear-zone, at Europa Reach, the rocks are characterized by abundant metamorphic epidote, microcline, garnet and clinopyroxene. The rocks east of Brim River do not have epidote, which indicates that they cooled down at lower pressures than the stability field of epidote. Also, migmatitic rocks are east of Brim River and are absent west of the Quottoon pluton at Europa Reach. We interpret these observations as a contrast in cooling history east and west of the Quottoon pluton. To the west, the rocks cooled earlier and stayed in the epidote stability field; this is consistent with the rocks belonging to the Western metamorphic belt. At the same time, the rocks east of the western boundary of the Quottoon pluton stayed hot and cooled later when the orogen was being exhumed. We take this contrast in metamorphic history as evidence for the presence of a major structural break in the area. We infer that this structural break is the Coast shear-zone.

The dextral kinematics found at Europa Reach could record an older deformation event than those described to the east of the Coast shear-zone, an event possibly related to the intrusion of the Butedale pluton at 84 Ma

(Gehrels et al in revision). Alternatively, the dextral kinematics could be related to deformation in the Coast shear-zone, as seen at the Skeena River (Andronicos et al 1999).

The southern continuation of the Coast shear-zone is cryptic. The western side of the Kitlope Pluton contains foliations that strike north-south and steeply dip to the east with steeply plunging lineations. These orientations may indicate a strain gradient on the western side of the Kitlope pluton consistent with the presence of the Coast shear-zone. This is a possible explanation for the change in foliation orientation between Mt. Blane and the ridges west of Kitlope Lake. If this is the case, the southern termination of the central gneiss complex would be controlled by a bend in the Coast shear-zone, and the Coast shear-zone could have been a first-order control on exhumation of the high-grade rocks. Also, if the Coast shear-zone was a first-order controller of the intrusion of the Kitlope Pluton, a bend on the structure would explain why the orientation of the Kitlope Pluton is so different than the orientation of the Quottoon pluton, given their similar ages.

Alternatively, the different orientation of the plutons could be due to strain partitioning related to plate motions. A last possibility would be that the orientation is entirely related to changes in the strain-field produced by the intrusion of the pluton itself. In this case the differences in orientation would be entirely caused by pluton related deformation. The last section of the paper will develop these ideas further.

V.B. Kinematics of pluton emplacement

The Quottoon, Chief Matthew's, and Kitlope plutons are part of a large magmatic event that took place east of the Coast shear-zone from 65 to 50 Ma

(Gehrels et al in revision). This event postdates more than 60 Ma of magmatic activity in the area, based on the abundance of orthogneiss with Late Jurassic ages. Long-lived magmatism throughout the crust modifies its thermal state. The geothermal gradient becomes isothermal from the depths were plutons intrude (~15-20 km) to the Moho, as demonstrated by numerical models (Depine et al 2008). The temperature is buffered by the solidus temperature of the country-rocks that predominate in the crust. The dominant lithology in the central gneiss complex and at Gardner Canal is amphibolite, which has a solidus temperature of ~750℃. This temperature wil l induce partial melting of a variety of lithologies in the crust with lower solidus temperatures. We argue that the plutons at Gardner Canal were emplaced in crust that was at homogeneously high temperatures east of the Coast shear-zone. Supporting evidence for this conclusion is the widespread presence of migmatitic amphibolite and orthogneiss.

An implication of such a hot crust is that most of the deformation will be focused in the central gneiss complex, which represents the weak deformable block of the orogen. This narrow belt is soft due to thermal and deformational softening.

A combination of the presence of migmatites; grain-size reduction (Thompson et al 1997); mineral transformation; and increasing temperature is responsible for decreasing strength of crustal rocks. Eventually, after a large enough melt fraction forms (~7-10% Rosenberg and Handy 2005, Brown 2007), the melt will start migrating through the solid matrix. The transition from melt migration by granular flow throughout the crust to pluton emplacement is given by focusing the melt. One proposed region for melt focusing is crustal-scale shear-zones (Hollister and Crawford 1986, Ingram and Hutton 1994,

Brown and Solar 1998). The Quottoon pluton is intimately related with the Coast shear-zone (Ingram and Hutton, 1994, Klepeis et al 1998, Andronicos et al 1999, Rusmore et al 2001).

We interpret the vertical structures associated to the Quottoon pluton as the feeder area for the other plutons east of the Coast shear-zone, like the Chief Matthew's pluton. Melt ascends through the Coast shear-zone due to pressure gradients, creating a feedback between deformation and magmatism (Lissenberg and van Staal 2006). The Kitlope pluton is also characterized by vertical foliations and lineations that point to a vertical movement for the magmas, also indicating that the Kitlope pluton represents a vertical conduit for magma ascent.

At Gardner Canal, the Quottoon intruded during horizontal shortening at ~60 Ma, as indicated by the flattening fabrics described above (Figure 2.12a). Because plutons are assembled by large increments of magmatic additions (Petford et al 2000, Brown and McClelland 2000), syntectonic intrusions usually record progressive deformation. The progressive deformation indicated by the Quottoon pluton is top to the east reverse shear-sense as shown by the kinematic indicators and fold geometry.

By ~57 Ma when the Chief Matthew's pluton intruded, the deformation appears to have reversed from horizontal shortening to horizontal extension (Figure 2.12d). The change in the orientation of the plutons has been explained in two different ways, by far-field or near-field reasons. The first mechanism is near-field to the plutonic system so that the rotation in the shortening direction only depends on forces related to the emplacement of the pluton. In general, the mechanisms by which plutons switch from vertical to sub-horizontal shape are related to buoyancy and to stalling of magma at the

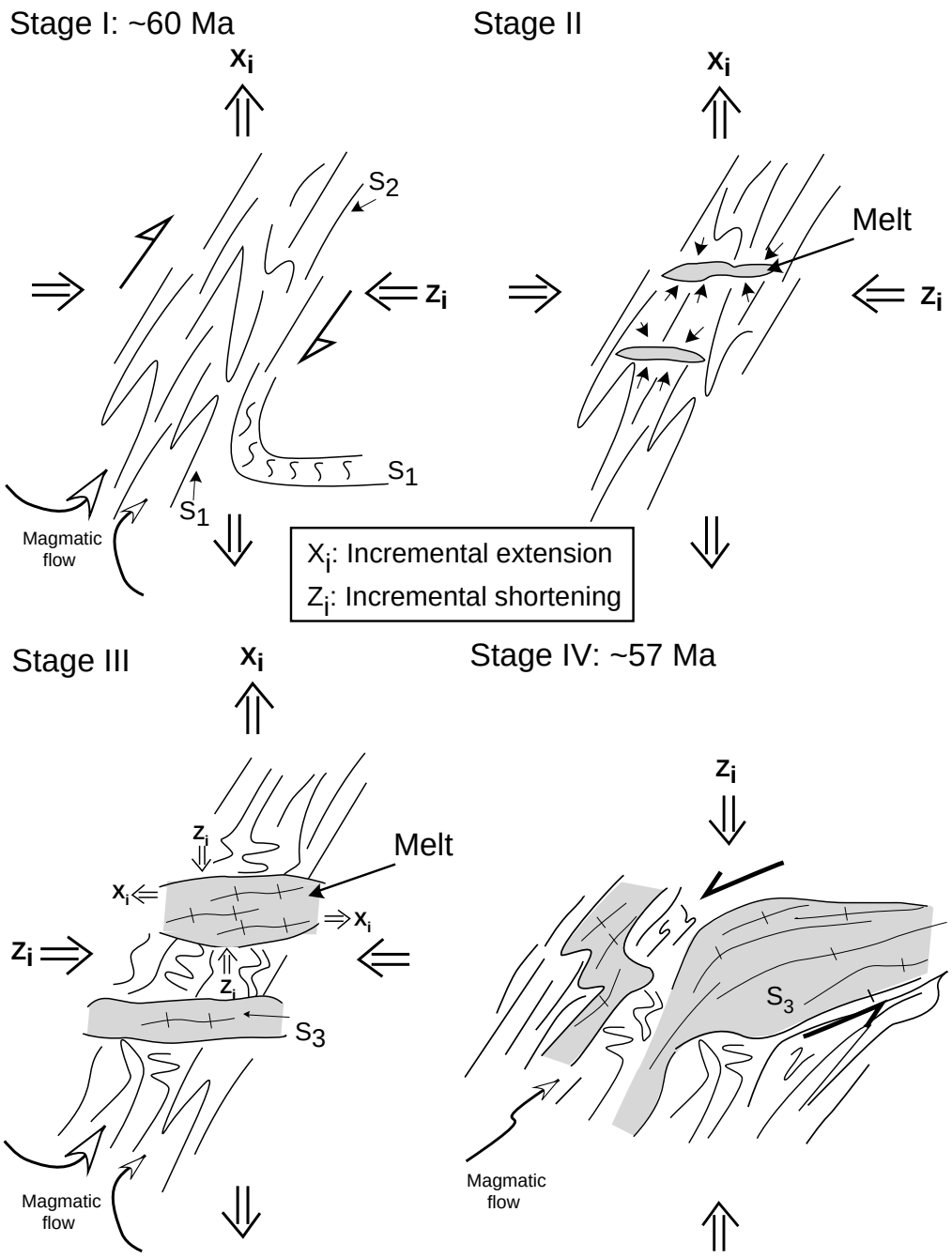

Figure 2.12: Sketch of cross-sections of model that shows the transposition of foliation from vertical to horizontal as induced by melt. Stage 1: Vertical foliation (S2) developed during transpression overprints a previous vertical and flat foliation (S1). Stage 2: Incipient melt-filled tension gashes form perpendicular to the previous foliation. Stage 3: Continuation of flow of melt into the fractures locally changes the strain axes. Stage 4: The melt accumulations become large, and form a pluton characterized by horizontal flow and subhorizontal foliation (S3).

brittle/ductile transition (Brown and Solar 1998). We can rule out this mechanism since the rocks at Gardner Canal are well below the brittle-ductile transition, and the amphibolitic migmatites that host the plutons are denser than the plutonic rocks.

Another possible mechanism is extensional hydro-fracturing in the adjacent country-rock during transpression (Wagner et al 2006). This near-field explanation is valid at Gardner Canal based on field observations where the Quottoon pluton develops melt filled tensile fractures oriented perpendicular to the foliation and lineation (Figure 2.5c). This orientation for the melt is parallel to the incremental shortening direction during horizontal shortening (Figure 2.12b). Once formed, a sub-horizontal melt filled gash in a material will cause a reorientation of the local incremental strain axis since the melt/solid interfaces cannot sustain shear stress. As magma is added to the gash, inflation leads to a larger area where the incremental strains are reoriented (Figure 2.12c). The magmas that form the Chief Matthew's pluton could have used this type of anisotropy to produce large pathways for sub-horizontal flow producing the sill complex. This mechanism can explain the horizontal geometry for the Chief Matthew's pluton as well as produce apparent vertical shortening around the sill complex. Inflation of the sills produces the flattening fabrics seen at the tops and bottoms of the sills and horizontal flow of magma produces the asymmetric fabrics seen throughout the sill complex (Figure 2.5f, 2.5h and 2.12c-d).

On the other hand, the change in the direction of the shortening can be explained extrinsically by a change in regional stresses. The Chief Matthew's pluton shows horizontal foliations and horizontal lineations, which become stable during subvertical flattening and radial stretching which are consistent

with the intrusion of the pluton in extensional or transtensional regime with an angle of divergence greater than 20° (Teyssier and Tikoff 1999). There are also other plutons in the Coast Mountains with a subhorizontal geometry at about the same time (i.e. Khyex sill complex (67-63 Ma), Kasiks sill complex (53 Ma), Tsaytis pluton (56 Ma); Andronicos et al 2003, Crawford et al 1999, Van de Heyden 1989). These plutons have been argued to have intruded during regional tectonic extension. The Tsaytis pluton is a gently to moderately dipping tonalite (Van de Heyden 1989). We believe that it can be linked to the Chief Matthew's pluton given the similar age, structure, cooling history and areal proximity. The Kasiks sill complex is also associated with crustal scale detachment which unambiguously points to tectonic extension in the area. We do not have evidence for a crustal scale-detachment at Gardner Canal. However, we do not think that the model presented above is exclusive of regional tectonic extension.

Independent of the cause of the transposition of the foliation between 60 and 58 Ma, there is agreement (Paterson and Fowler 1993, Hollister and Crawford 1986) that when plutons intrude they affect the near-field stresses of the country-rocks. The rocks around the Chief Matthew's pluton preserve several synplutonic structures that exemplify this fact. The extensional shear-bands described in the country-rock with different orientations, the isoclinal folds, the chocolate-tablet boudinage, and the areas with extreme stretching are all structures that indicate that the deformation was strongly partitioned with different orientations in the country rock to create room for the intrusion and inflation of the pluton. The almost perpendicular orientations for the shear-bands indicate that overall the pluton was intruding during vertical flattening,

but the deformation was being partitioned into domains of flattening, stretching and simple-shear.

The orientation of the Coast shear-zone and fabrics in the Quottoon pluton strongly overprinted a previous fabric in the area, which is characterized by alternating regions of steep and flat structures. These fabrics can be correlated to what it is found to the east at Mt. Gamsby (Hamblock 2006). Different to the strong overprinting relationships surrounding the intrusion of the Quottoon pluton, the rocks associated with the intrusion of the Chief Matthew's pluton follow the overall pluton shape and foliation. Flat foliations are widespread. Melt related to the intrusion of the pluton crosscuts the flat foliation and also flows parallel to it at the contact with the Chief Matthew's pluton (Figure 2.5k). We interpret this relationship as the Chief Matthew's pluton sometimes reusing and reactivating the pre-existent flat foliation that was already present in the area.

V.C. Using plutons to infer tectonic plate regimes

In this paper we have studied three different plutons that were emplaced during a time span of ~5 Ma. However, each pluton shows a different finite strain pattern. The emplacement of plutons will interfere with the tectonic strain present in an area, causing a "tectonic surge" in the surroundings of the pluton (Hollister and Crawford 1986). This means that pluton emplacement changes the strain-field close to a pluton, and if several intrusions occur in an area, the regional strain-field is also affected. So, the question that remains is how much can we infer about the far-field strain of an area based on the study of plutons?

Relevant to this analysis, three different regional models, based on plate reconstructions, have been proposed for the North American margin for the Late Cretaceous and Paleogene. The first one relies on a change in the convergence angle of the Kula-Pacific plate from orthogonal to more oblique at ~55 Ma (Lonsdale 1988) that would have triggered the collapse of the orogen, exhumation of high grade rocks, and the increase in magmatism by releasing tectonic stresses (Andronicos et al 2003, Struik 1999). Another model proposes the existence of an extra, now-fully subducted plate called the Resurrection plate (Haeussler et al 2003) that would have generated extension due to the subduction of buoyant young oceanic crust, and a magmatic flare-up possibly related to a slab-window. The third model, based on paleomagnetic data, is referred to as the Baja-BC hypothesis, which states that a large segment of western North America was translated more than 3000 km northward in the middle Cretaceous and finally docked to the present position at ~50 Ma (Beck 1976, Irving et al 1985). The Coast shear-zone is proposed to have been the strike-slip surface by some authors (Irving et al 1996, Hollister and Andronicos 1997). This model is not exclusive of the first one.

If we assume that the orientation of the plutons is purely an expression of the relative convergence direction between the Kula and Pacific Plates, then following the first two regional models, for plutons older than ~57 Ma we should expect to find kinematics reflecting NE-SW shortening, and plutons younger than ~56 Ma should indicate extension. Also, if we consider the third regional model, plutons older than ~50 Ma and associated to the Coast shear-zone (e.g. Quottoon and Kitlope plutons) should show evidence of large dextral displacement.

The Quottoon Pluton at Gardner Canal shows NE-SW shortening, which would be consistent with the pluton intruding during dextral transpression (Figure 2.13). However, the kinematic indicators show top to the east reverse sense of shear, which indicate that the intrusion of the Quottoon pluton was late in the area, after the strike-slip displacement ended, as was proposed for the Quottoon pluton at the Skeena River (Andronicos et al 1999). The dextral kinematic indicators found west of the Coast shear-zone in Gardner Canal could be the evidence for dextral displacements either previous or by partitioning of the strain during the intrusion of the Quottoon pluton. The Kitlope pluton shows a preferred N-S shortening direction which also matches the regional orientation for compression during dextral transpression (Figure 2.13).

The Chief Matthew' pluton is characterized by vertical flattening, and it is linked to extension. This pluton matches regional models. Crawford et al (1999) also reported the transition from compression to extension at 59 Ma for the central gneiss complex, based on studies on the Khyex sill complex located south of Portland Inlet. Other areas of interest in the Canadian Cordillera are located at the Omineca belt, which is characterized by a series of high grade metamorphic ranges, bounded by normal faults, which were exhumed during the Eocene during an increase in magmatic activity (Struik 1992). The switch from a contractional regime to extensional is also reported at ~58 Ma (Parrish et al 1988, Parrish 1995, Vanderhaeghe et al 2003).

These observations indicate that far-field tectonic stresses were also contributing to the intrusion and flow of plutons.

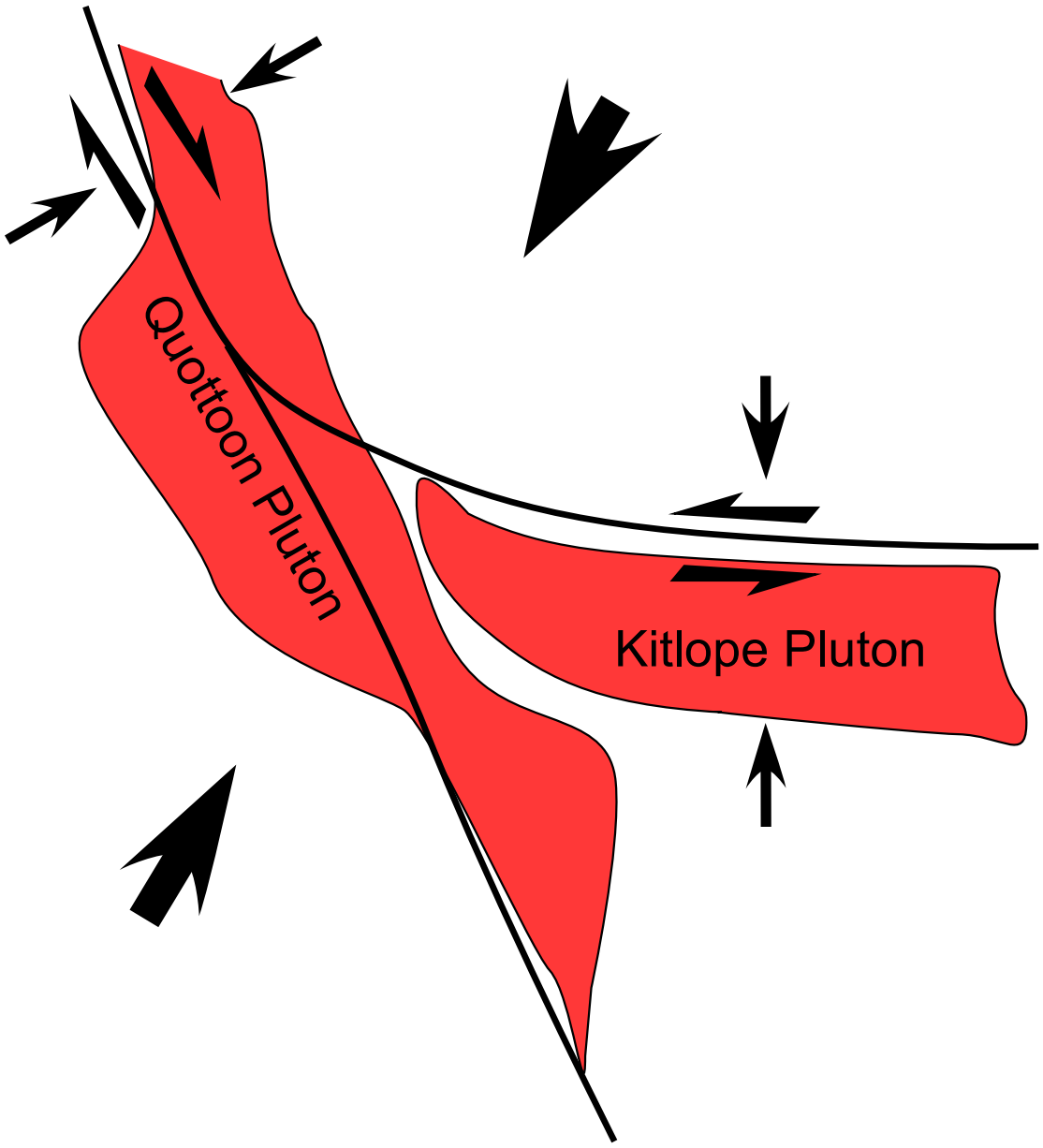

Figure 2.13: Schematic map view showing the orientations of the Quottoon and Kitlope plutons. Both pluton orientations are consistent with a dextral transpressional regime, consistent with partitioning of dextral transpressive strain.

VI. Conclusions

The structural analysis of three different middle-crustal plutons in the Coast Mountain of British Columbia provided insight into strain partitioning, pluton emplacement mechanisms and the role of melt during orogenesis. Plutonism accompanied both the build-up stage of the mountain belt and also occurred during its final exhumation.

The plutons in this study are the Kitlope pluton (61 Ma), the Quottoon pluton (60 Ma) and the Chief Matthew's pluton (57 Ma). These plutons are important because they overlap the time when a transition from compression to extension is tracked in several metamorphic core-complexes in the Canadian Cordillera and northwestern USA.

We found that there is a change from horizontal to vertical shortening between the emplacement of the Quottoon pluton and the Chief Matthew's pluton. The transposition in the deformation occurred between 60 and 57 Ma. This timing is in agreement with what other authors inferred based on studies in different areas (Parrish et al 1988, 1995, Vanderhaeghe et al 2003, Crawford et al 1999). The regional-scale synchronicity in deformation and mode suggests that the rocks are responding either to stresses related to plate convergence, or to an intrinsic mechanism that would have affected the whole orogen (for example, the coherent loss of the lower crust and/or crustal collapse, as it will be discussed in chapter 3 of this thesis).

The deformation of the country-rocks accompanying intrusion of first the Quottoon pluton and later the Chief Matthew's pluton records an almost orthogonal transposition of the foliation. We present a model where horizontal tensile melt fractures develop perpendicular to the foliation consistent with the orientation of the regional strain. The presence of melt in this orientation

encourages more melt to accumulate. The larger accumulations locally change the orientation of local strain axes. The final stage occurs when big volumes of melt accumulate after large sub-horizontal displacements and form plutons.

Finally, the detailed analysis of the well exposed Chief Matthew's pluton led to some important conclusions about mechanisms of pluton emplacement. Plutons reuse preexisting foliations to flow if possible. The strain produced by the intrusion and inflation of the pluton is partitioned into different domains in the country-rocks. These domains present folds with axial planes parallel to the pluton; chocolate-tablet boudinage; and shear-bands formed by simple-shear. Altogether, the different domains form a radial orientation of the finite stretching direction, as well as the orientation of the lineations with respect to the foliation, which indicates radial flow of the magma during intrusion and vertical flattening linked to sill inflation.

REFERENCES

Andronicos, C.L., Hollister, L.S., Davidson, C. and Chardon, D. 1999. Kinematics and tectonic significance of transpressive structures within the Coast Plutonic Complex, British Columbia. Journal of Structural Geology, 21: 229–243.

Andronicos, C.L., Chardon, D.H., Hollister, L.S., Gehrels, G.E., and Woodsworth, G.J., 2003. Strain partitioning in an obliquely convergent orogen, plutonism, and synorogenic collapse: Coast Mountains Batholith, British Columbia, Canada. Tectonics, 22(2): 1012.

Beck, M.E., 1976. Discordant paleomagnetic pole positions as evidence of regional shear in the western Cordillera of North America. American Journal of Science, 276: 694-712.

Bittner, D. and Schmeling, H. 1995. Numerical modelling of melting processes and induced diapirism in the lower crust. Geophysical Journal International, 123(1):59–70.

Brew, D.A. and Ford, A.B., 1978. Megalineament in southeastern Alaska marks southwest edge of coast Range batholithic complex. Canadian Journal of Earth Sciences, 15: 1763–1772.

Brew, D.A. and Ford, A.B., 1981. The Coast Plutonic Complex sill, southeastern Alaska. In Albert, N.R.D. and Hudson, T., eds., The United States Geological Survey in Alaska: Accomplishments during 1979: US Geological Survey Circular, 823-B: B96-B99.

Brown, E.H. and McClelland, W.C., 2000. Pluton emplacement by sheeting and vertical ballooning in part of the southeast Coast Plutonic Complex, British Columbia. Geological Society of America Bulletin, 112(5): 708-719.

Brown, M. 2007. Crustal melting and melt extraction, ascent and emplacement in orogens: mechanisms and consequences. Journal of the Geological Society of London, 164: 709-730.

Brown, M. and Solar, G.S., 1998. Granite ascent and emplacement during contractional deformation in convergent orogens. Journal of Structural Geology, 20(9-10): 1365-1393.

Butler, R.F., Gehrels, G. E., Baldwin, S. L. and Davidson, C., 2002. Paleomagnetism and geochronology of the Ecstall pluton in the Coast Mountains of British Columbia: Evidence for local deformation rather than large-scale transport. Journal of Geophysical Research, 107(B1).

Chardon, D., Andronicos, C.L. and Hollister, L.S., 1999. Large-scale transpressive shear zone patterns and displacements within magmatic arcs: The Coast Plutonic Complex, British Columbia, Tectonics, 18: 278–292.

Chardon, D., 2003. Strain partitioning and batholith emplacement at the root of a transpressive magmatic arc. Journal of Structural Geology, 25(1): 91-107.

Crawford, M.L., Klepeis, K.A., Gehrels, G. and Isachsen, C., 1999. Batholith emplacement at mid-crustal levels and its exhumation within an obliquely convergent margin: The influence of granite emplacement on tectonics. Tectonophysics, 312: 57–78.

Crawford, M.L. and Hollister, L.S., 1982. Contrast of metamorphic and structural histories across the work channel lineament, coast plutonic complex, British Columbia. Journal of Geophysical Research, 87(B5): 3849-3860.

Crawford, M.L., Kraus, D.W. and Hollister, L.S. 1979. Petrological and fluid inclusion study of calc-silicate rocks, Prince Rupert, British Columbia. American Journal of Science, 9: 1135-1159.

Crawford, M.L., Hollister, L.S. and Woodsworth, G.J. 1987. Crustal deformation and regional metamorphism across a terrain boundary, Coast Plutonic Complex, British Columbia. Tectonics, 6: 343–361.

Cruden, A.R., 1988. Deformation around a rising diapir modeled by creeping flow past a sphere. Tectonics, 7(5): 1091–1101.

Depine, G.V., Andronicos, C.L. and Phipps-Morgan, J., 2008. Near-isothermal conditions in the middle and lower crust induced by melt migration. Nature 452: 80-83.

Enkin, R.J. 2006. Paleomagnetism and the case for Baja British Columbia. In Haggart J.W., Monger J.W.H., Enkin R.J. eds. Paleogeography of the North American Cordillera: Evidence for and against Large-Scale Displacements. Geological Association of Canada Special Paper 46: 233–253.

Gabrielse, H., 1985. Major dextral transcurrent displacements along the Northern Rocky Mountain Trench and related lineaments in north-central British Columbia. Geological Society of America Bulletin, 96: 1-14.

Gapais, D., 1989. Shear structures within deformed granites: Mechanical and thermal indicators. Geology,17(12): 1144-1147.

Gapais, D., Bale, P., Choukroune, P., Cobbold, P.R., Mahjoub, Y. and Marquer, D., 1987. Bulk kinematics from shear zone patterns: some field examples. Journal of Structural Geology, 9(5-6): 635-646.

Hamblock, J.M. 2006. Understanding the composition, origin, and evolution of the continental crust: Case studies in the southern Rio Grande rift, New Mexico, United States of Americaand the Coast Plutonic Complex, British Columbia, Canada. Doctorate dissertation, ETD Collection for University of Texas, El Paso. Paper AAI3242135.

Haeussler, P.J., Bradley, D.C., Wells, R.E. and Miller, M.L. 2003. Life and death of the Resurrection plate: Evidence for its existence and subduction in the northeastern Pacific in Paleocene–Eocene time. Geological Society of America Bulletin, 115(7): 867-880.

Heilbronner, R. 1992. The autocorrelation function: an image processing tool for fabric analysis. Tectonophysics, 212 (3-4): 351-370.

Hirth, G. and Tullis, J. 1992. Dislocation creep regimes in quartz aggregates. Journal of Structural Geology, 14(2): 145-159.

Hollister, L.S., 1982. Metamorphic evidence for rapid (2 mm/yr) uplift of a portion of the Central Gneiss Complex, Coast Mountains, B.C. The Canadian Mineralogist, 20(3): 319-332.

Hollister, L.S. and Crawford, M.L., 1986. Melt-enhanced deformation: A major tectonic process. Geology, 14(7): 558-561.

Hollister, L.S., 1993. The role of melt in the uplift and exhumation of orogenic belts. Chemical geology, 108(1-4): 31-48.

Hollister, L.S. and Andronicos, C.L., 1997. A candidate for the Baja British Columbia Fault system in the Coast Plutonic Complex. Geological Society of America Today 7, pp. 1–7.

Hollister, L.S. and Andronicos, C.L. 2000. The Central Gneiss Complex, Coast Orogen, British Columbia. Special Paper Geological Society of America, 343: 45–59.

Hollister, L.S., Hargraves, R.B., James, T.S. and Renne, P.R., 2004. The paleomagnetic effects of reheating the Ecstall pluton, British Columbia. Earth and Planetary Science Letters, 221 (1-4): 397-407.

Hollister, L.S. and Andronicos, C.L., 2006. Formation of new continental crust in Western British Columbia during transpression and transtension. Earth and Planetary Science Letters, 249(1-2): 29-38.

Hutchinson, W.W. 1982. Geology of the Prince Rupert–Skeena map area, British Columbia. Geological Survey of Canada Memoir 394: 1–116.

Hutton, D.H.W. 1987. Strike-slip terranes and a model for the evolution of the British and Irish Caledonides. Geological Magazine, 124(5): 405-425.

Ingram, G.M., and Hutton, D.H.W., 1994. The Great Tonalite Sill: Emplacement into a contractional shear zone and implications for Late Cretaceous to early Eocene tectonics in southeastern Alaska and British Columbia. Geological Society of America Bulletin, 106(5): 715-728.

Irving, E., Wynne, P.J., Thorkelson, D.J. and Schiarizza, P. 1996. Large (1000 to 4000 km) northward movements of tectonic domains in the northern Cordillera, 83 to 45 Ma. Journal of Geophysical Research, 101: 901–916.

Irving, E., Woodsworth, G.J., Wynne, P.J. and Morrison, A., 1985. Paleomagnetic evidence for displacement from the south of the Coast Plutonic Complex, British Columbia. Canadian Journal of Earth Science, 22(4): 584-598.

Johnston, S.T. 2001. The Great Alaskan Terrane Wreck: reconciliation of paleomagnetic and geological data in the northern Cordillera. Earth and Planetary Science Letters, 193(3-4): 259-272.

Johnston, S.T., and Canil, D., 2007. Crustal Architecture of SW Yukon, norther Cordillera: Implications for crustal growth in a convergent margin orogen. Tectonics, 26: TC1006.

Karlstrom, K.E., 1989. Toward a syntectonic paradigm for granitoids. Eos Transactions of the American Geophysical Union, 70(32), 762.

Karlstrom, K.E. and Bowring, S.A., 1993. Proterozoic Orogenic history of Arizona. In: Reed Jr., J.C., Bickford, M.E., Houston, R.S., Link, P.K., Rankin, D.W., Sims, P.K. and Van Schmus, W.R., Editors, 1993. Precambrian: Conterminous U.S. The Geology of North America C-2, Geological Society of America, Boulder, Colorado: 188–211.

Kalstrom, K.E. and Williams, M.L., 1993. The case for simultaneous deformation, metamorphism and plutonism: an example from Proterozoic rocks in central Arizona. Journal of Structural Geology, 17 (1): 59-81.

Kenah, C. and Hollister, L.S. 1983. Anatexis in the Central Gneiss Complex, British Columbia. In Migmatites, Melting and Metamorphism; Proceedings of Meeting on High Grade Metamorphism, Migmatites and Melting of the Geochemical Group of the Mineralogical Society of the University of Glasgow, edited by M.P. Atherton and C.D. Gribble: 142–162, Shiva, Nantwich, United Kingdom.

Kirby, E., Karlstrom, K.E., Andronicos, C.L., and Dallmeyer, R.D., 1995. Tectonic setting of the Sandia pluton; an orogenic 1.4 Ga granite in New Mexico: Tectonics, 14:185.

Klepeis, K.A., Crawford, M.L. and Gehrels, G., 1998. Structural history of the crustal-scale Coast shear zone north of Portland Canal, southeast Alaska and British Columbia. Journal of Structural Geology, 20: 883-904.

Klepeis, K.A. and Crawford, M.L., 1999. High-temperature arc-parallel normal faulting and transtension at the roots of an obliquely convergent orogen. Geology, 27(1): 7-10.

Lappin, A.R. and Hollister, L.S. 1980. Partial melting in the Central Gneiss Complex near Prince Rupert, British Columbia. American Journal of Science, 280: 518–545.

Lissenberg, C.J. and van Staal, C.R., 2006. Feedback between deformation and magmatism in the Lloyds River Fault Zone: An example of episodic fault reactivation in an accretionary setting, Newfoundland Appalachians. Tectonics, 25: TC4004.

Lonsdale, P. 1988. Paleogene history of the Kula plate: Offshore evidence and onshore implications. Geological Society America Bulletin, 100: 733–754.

McClelland, W.C., Gehrels, G., Samson, S.D. and Patchett, P.J. 1992. Structural and geochronologic relations along the western flank of the Coast Mountains batholith: Stikine River to Cape Fanshaw, central SE Alaska. Journal of Structural Geology 14: 475–489.

McClelland, W.C. and Mattinson, J.M. 2000. Cretaceous-Tertiary evolution of the western Coast Mountains, central southeastern Alaska. In Stowell, H.H. and McClelland, W.C., eds., Tectonics of the Coast Mountains, Southeastern Alaska and British Columbia: Boulder, Colorado, Geological Society of America Special Paper 343: 159-182.

Parrish, R.R., Carr, S.D. and Parkinson, D.L. 1988. Eocene Extensional Tectonics and Geochronology of the southern Omineca Belt, British Columbia and Washington. Tectonics, 7: 181–212.

Parrish, R., 1995. Thermal evolution of the southeastern Canadian Cordillera. Canadian Journal of Earth Sciences, 32: 1618-1642.

Paterson, S.R. and Fowler Jr, T.K., 1993. Re-examining pluton emplacement processes. Journal of Structural Geology, 15(2):191-206.

Paterson, S.R. and Schmidt, K.L., 1999. Is there a close spatial relationship between faults and plutons? Journal of Structural Geology, 21(8-9): 1131-1142.

Passchier, C.W. and Trouw, R.A.J., 1996. Microtectonics, 289, Springer-Verlag, New York.

Petford, N., Cruden, A.R., McCaffrey, K.J.W. and Vigneresse, J.-L., 2000. Granite magma formation, transport and emplacement in the Earth's crust. Nature, 408: 669-673.

Platt, J.P. and Vissers, R.L.M. 1980. Extensional structures in anisotropic Rocks. Journal of Structural Geology, 2(4): 397-410.

Plint, H.E., Erdmer, P., Reynolds, P.H. and Grist, A.M. 1992. Eocene tectonics in the Omineca Belt, northern British Columbia, Canada: Field, 40Ar/39Ar, and fission track data from the Horseranch Range. Geological Society of America Bulletin, 104: 106–116.

Price, R.A. and Carmichael, D.M. 1986. Geometric test for late Cretaceous–Paleogene intracontinental transform faulting in the Canadian Cordillera. Geology 14: 468–471.

Roddick, J.A., 1970. Douglas Channel-Hecate Strait Map Area. British Columbia: Geological Survey of Canada Paper, Paper 70-41.

Rosenberg, C.L. and Handy, M.R. 2005. Experimental deformation of partially melted granite revisited: implications for the continental crust. Journal of Metamorphic Geology, 23(1): 19-28.

Rubin, C.M. and Saleeby, J.B., 1992. Tectonic history of the eastern edge of the Alexander Terrane, Southeast Alaska. Tectonics, 11(3): 586–602.

Rusmore, M.E., Gehrels, G., Woodsworth, G.J., 2001. Southern continuation of the Coast shear zone and Paleocene strain partitioning in British Columbia–southeast Alaska. Geological Society America Bulletin, 113(8): 961-975.

Rusmore, M.E., Woodsworth, G.J. and Gehrels, G.E. 2005. Two-stage exhumation of midcrustal arc rocks, Coast Mountains, British Columbia. Tectonics, 24: TC5013.

Simpson, C. and Schmidt, S.H. 1983. An evaluation of criteria to deduce the sense of movement in sheared rocks. Geological Society of America Bulletin 94: 1281–1288.

Struik, L.C. 1992. Intersecting intracontinental Tertiary transform fault systems in the North American Cordillera. Canadian Journal of Earth Science, 30: 1262–1274.

Teyssier, C. and Tikoff, B. 1999. Fabric stability in oblique convergence and divergente. Journal of Structural Geology, 21(8-9): 969-974.

Thomas, J.B. and Sinha, A.K. 1999. Field, geochemical, and isotopic evidence for magma mixing and assimilation and fractional crystallization processes in the Quottoon igneous complex, northwestern British Columbia and southeastern Alaska. Canadian Journal of Earth Science, 36: 819–831.

Thompson, A.B., Schulman, K. and Jezek, J., 1997. Extrusion tectonics and elevation of lower crustal metamorphic rocks in convergent orogens. Geology, 25(6): 491-494.

Umhoefer, P.J., and Kleinspehn, K.L., 1995. Mesoscale and regional kinematics of the northwestern Yalakom fault system: Major Paleogene dextral faulting in British Columbia, Canada. Tectonics, 14(1): 78–94.

Vanderhaeghe, O., Teyssier, C., McDougall, I. and Dunlap, W.J. 2003. Cooling and exhumation of the Shuswap Metamorphic Core Complex constrained by 40Ar/39Ar thermochronology. Geological Society Society of America Bulletin, 115(2): 200-216.

Van der Heyden, P., 1989. U-Pb and K-Ar geochronometry of the Coast Plutonic complex, 53°N to 54°N, British Columbia, and implications for the Insular-Intermontane Superterrane boundary. Doctoral thesis, University of British Columbia, Canada.

Wagner, R., Rosenberg, C.L., Handy, M.R., Möbus, C. and Albertz, M., 2006. Fracture-driven intrusion and upwelling of a mid-crustal pluton fed from a transpressive shear zone—The Rieserferner Pluton (Eastern Alps). Geological Society of America Bulletin, 118(1-2): 219-237.

CHAPTER 3

METAMORPHIC CONSTRAINTS ON THE P-T PATH OF A CALC-ALKALINE BATHOLITH COMPLEX, CENTRAL GNEISS COMPLEX, BRITISH COLUMBIA

I. Abstract

The southern termination of the central gneiss complex located at Gardner Canal and the Kitlope Lake, Coast Mountains in British Columbia, is characterized by long-lived upper amphibolite facies metamorphism at constant temperatures of ~750℃. Magmatism was sync hronous with metamorphism as indicated by the abundant plutons. Peak pressures of 0.75-0.65 GPa were achieved synchronously with the intrusion of steep Kitlope (61 Ma) and Quottoon (60 Ma) plutons. An isothermal decompression of ~0.2 GPa occurred in the area accompanied with the intrusion of the sub-horizontal Chief Matthew's pluton at 57 Ma, at a rate of 2-3 mm/yr. Based on cooling ages, the area experienced cooling at a rate ~50℃/ Ma; cooling was probably synchronous with exhumation. All the rocks cooled below the biotite closure temperature by 51 Ma. The plutons in the area are intruded contemporaneous with a transpressive to extensional change in deformation along the Canadian Cordillera from being transpressive to extensional. The timing and exhumation rate found in the southern termination of the central gneiss complex is comparable to what is found along the Coast Mountains and also in metamorphic core-complexes in the Omineca belt to the east. We propose an orogen-scale tectonic model for the evolution of the metamorphic core-complexes in the Canadian Cordillera in order to explain mechanisms of

exhumation of ~25 km of crust. The model requires a thermally weakened lower-middle crust, as well as a release of the compressional forces at the plate boundary. Exhumation is triggered by the vertical collapse of the rigid upper crust in the interior plateau. This results in extrusion of material towards both sides of the plateau. The crustal scale strike-slip faults play a major role during exhumation both assisting it and also acting as thermal/rheological barriers to lateral extrusion. Deformation, while partially focused at detachment faults, is mainly distributed in the flowing lower and middle crust.

II. Introduction

Metamorphism, intrusion of melt, the presence or absence of fluids, and preexisting crustal structures are all important ingredients in focusing and distributing deformation in orogens. Orogens can fail and exhume when the rheology of different sectors of the crust changes because of changes in these parameters. Alternatively, orogens can exhume when stresses at the plate margins are reduced, so that a thick crust becomes gravitationally unstable. Moreover, all these effects can simultaneously act to lead to exhumation of an orogen. Exhumation would then be a dynamic interactive process whose complexity can result from the feedback between the above processes.

In this paper we use the Coast Mountains in British Columbia to study exhumation linked processes. This orogen formed during the Jurassic and Cretaceous. After ~100 Ma the orogen was exhumed in the Early Eocene. The objective of this paper is to examine this orogen to learn how rocks are exhumed, learn the P-T path followed by the rocks, and determine possible triggers for uplift and exhumation. Unfortunately, a calculation of stored gravitational potential energy in ancient orogens like this is ambiguous.

However, we will attempt to come up with a regional model that accounts for the observations in the central gneiss complex and other regions of the Canadian cordillera.

First, we describe the petrology of the rocks and present pressure and temperature calculations using mineral thermobarometry, petrogenetic grids, and phase diagrams calculated for specific bulk compositions. We also include cooling ages to unravel cooling rates of the rocks and to better constrain the timing of events. Finally, we show trace element geochemical data and use it to track changes in the source area of plutons of different ages and correlate them to variations in total crustal thickness.

III. Tectonic framework of the Coast Mountains

The Coast Mountains are located in northwestern North America. They are a >1500 km long belt that stretches from Washington State to southeast Alaska (Figure 3.1). Today the crustal thickness beneath the Coast Mountains is at most 32 km (Cook et al 1992, Morozov et al 2001, Hollister and Andronicos 2006). The rocks at the surface vary in metamorphic grade from green-schist to granulite facies. The areas that expose the highest grade rocks are arguably the largest and best exposed middle-crustal sections of a Phanerozoic magmatic arc in the world.

The northwestern margin of North America is made up of a series of elongated terranes (Coney et al 1980). Their provenance and final docking into present positions is still under debate (Beck 1976, Irving et al 1985). Episodic accretion of terranes generated cycles of increasing magmatic activity and thickening and thinning of the crust throughout the Jurassic and Cretaceous (Armstrong 1988, Monger et al 1982).

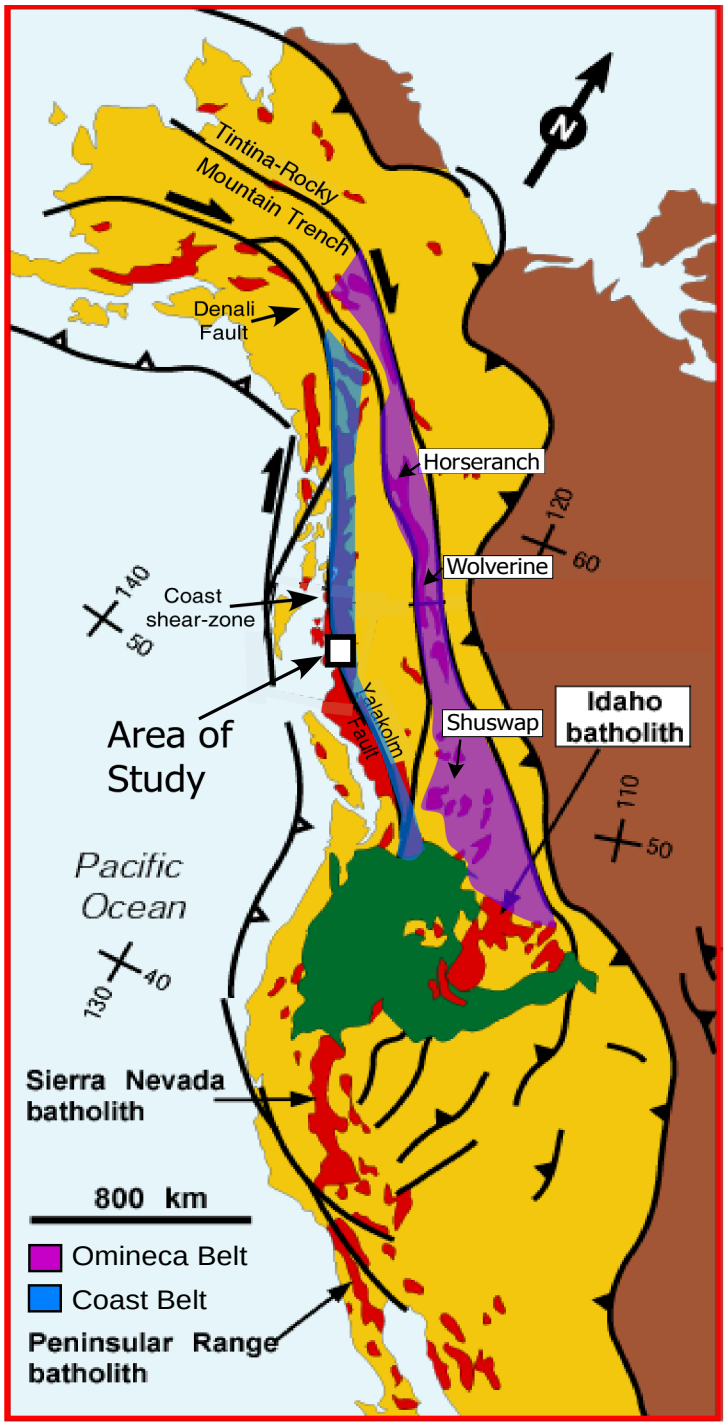

Figure 3.1: Map of western North America showing major faults, metamorphic core-complexes and batholith provinces. The yellow area is the Cordillera; the brown area is the cratonic part of North America; the red areas are Mesozoic bathiloths; and the green areas are the Columbia River and Snake Plain flood basalts. Also highlighted are the Coast and Omineca belts as defined by Armstrong (1988) with the internal plateau located in between. The map has been modified after Chardon et al (1999).

The subject of this paper is the last cycle of thickening in the Late Cretaceous and subsequent unroofing of ~15 km of the crust in the Eocene.

Plate movement reconstructions (Debiche et al 1987), paleomagnetic data (Bogue et al 1995), geologic discontinuities (Crawford and Hollister 1982) and kinematics of shear-zones (Andronicos et al 1999) in the Coast Mountains point to an important component of translation from 85 to 60 Ma (Irving et al 1996, Hollister and Andronicos 2006). The translation has been attributed to the most prominent crustal-scale structure in the belt, the Coast-shear zone (Hollister and Andronicos 1997). The presence of a fold and thrust belt and widespread folding of the rocks indicating SW-NE shortening at the same time interval, indicate that a component of compression was also important. This attests to transpression as the tectonic regime for this time. The crust was thickened to about 55 km during this time period (Hollister and Andronicos 2006), as evidenced by the metamorphic pressures of ~0.8 GPa determined for rocks that are at the surface today. This would require ~25 km of burial (Hollister 1982). Also, the geochemistry of some of the plutons indicates crustal sources melting of >45 km (Thomas and Sinha 1999).

During the Early Eocene (~55 to 48 Ma) the Coast Mountains experinced 1) rapid exhumation (Hollister 1982, Andronicos et al 2003, Rusmore et al 2005, Gehrels et al in revision); 2) an increase in magmatic flux (Hollister and Andronicos 2006, Ducea and Barton 2007, Gehrels et al in revision); and 3) crustal extension (Heah 1991, Crawford et al 1999, Andronicos et al 2003, Rusmore et al 2005, Hollister and Andronicos 2006). Possible explanations that have been suggested in the literature for these events are: 1) A change in the motion of the tectonic plates (Lonsdale, 1988; Andronicos et al 2003); 2) gravitational collapse of continental crust (Parrish et

al 1988); or 3) subduction of an active spreading ridge (Thorkelson and Taylor 1989, Haeussler et al 2003).

The last crustal thickening event, magmatic flare-up, and exhumation are best recorded in the central gneiss complex. The central gneiss complex is an orogen parallel belt of high-grade metamorphic rocks metamorphosed in the upper amphibolite to low-pressure granulite facies (Hollister and Andronicos 2000). Metamorphism occurred between the Late Cretaceous and Early Eocene during wide-spread intrusion of tonalites and granodiorites that make up a large portion of the Coast plutonic complex (Hollister 1982).

In this study we re-evaluate the exhumation history of the central gneiss complex and associated plutonic rocks, based on cooling ages and petrological and geochemical analysis. We add new data in the areas of Gardner Canal and the Kitlope Lake to better constrain the metamorphism and exhumation of these areas. P-T-paths have also been calculated in other areas of the Coast Mountains and core complexes in the Omineca belt, located to the east of the Coast belt. We compare these previous results with our data and examine differences and similarities between the different sectors of the mountain belt. Finally, we propose a model for the exhumation of metamorphic rocks in the Canadian Cordillera.

IV. Gardner Canal and Kitlope Lake areas

Here we focus on the exhumation history of the southern termination of the central gneiss complex (Figure 3.2). The tectonic history of the rocks is analyzed with respect to adjacent plutons. In this area there are three main plutons: the Kitlope pluton (61 Ma), the Quottoon pluton (60 Ma), and the Chief Matthew's pluton (57 Ma). The Tsaytis pluton (56 Ma) is also present in the

Figure 3.2: Geologic map of the southern termination of the central gneiss complex. Geographic features and sample names are also shown.

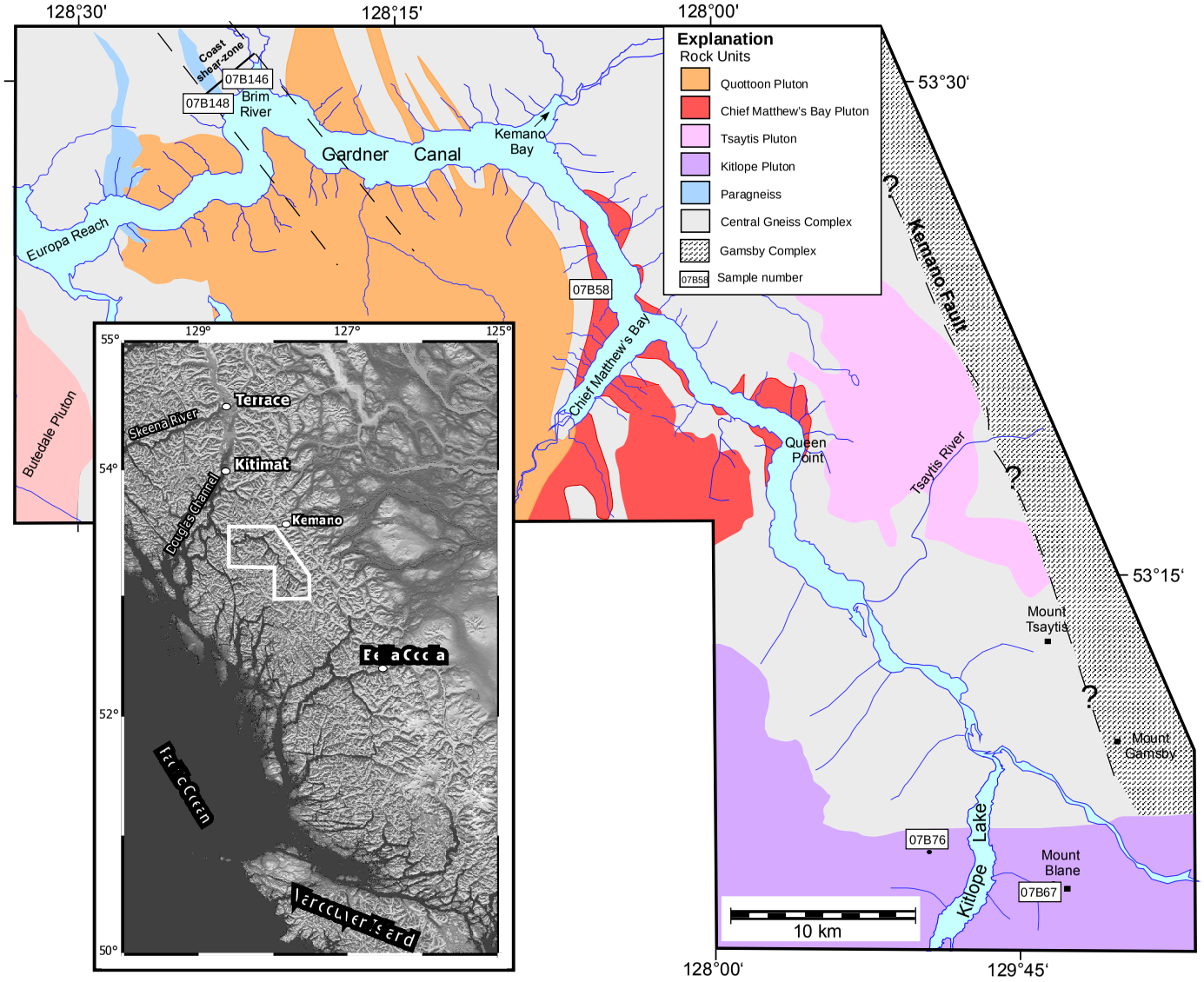
128°30'
128°15'
128°00'
53°30'
53°15'
128°00'
129°45'
Explanation
Rock Units
Quottoon Pluton
Chief Matthew's Bay Pluton
Tsaytis Pluton
Kitlope Pluton
Paragneiss
Central Gneiss Complex
Gamsby Complex
Sample number
07B58
Coast shear-zone
07B146
07B148
Brim River
Gardner Canal
Kemano Bay
Europa Reach
Butedale Pluton
Chief Matthew's Bay
Kemano Fault
Queen Point
Tsaytis River
Mount Tsaytis
Mount Gamsby
07B76
Lake
Kitlope
Mount Blane
07B67
10 km
129°
127°
125°
55°
54°
52°
50°
Terrace
Skeena River
Kitimat
Douglas Channel
Kemano

area. This pluton has been described by Van der Heyden (1989) as a gently to moderately dipping tonalite. We believe that the Tsaytis pluton can be linked to the Chief Matthew's pluton given the similar age, structure, cooling history and areal proximity. The country-rocks are part of the central gneiss complex and are metamorphosed to upper amphibolite grade.

The western flank of the central gneiss complex is a crustal-scale structure called the Coast shear-zone (Brew and Ford 1978, Hollister and Andronicos 2000). Rocks to the west of this structure are believed to have experienced a different tectonic history than the rocks to the east (Crawford and Hollister 1982). These rocks are metamorphosed to upper amphibolite facies, and also experienced widespread plutonism. However, no plutons younger than ~80 Ma are found west of the Coast shear-zone, and the rocks cooled to <300℃ by 73 Ma, then were partially rehe ated during the Eocene (Hollister et al 2004).

The eastern flank of the central gneiss complex at this latitude is defined by the Gamsby Complex, an early Late Jurassic magmatic and metamorphic belt with no evidence of major middle Cretaceous or younger orogenic episodes (Van der Heyden 1989). Zircon ages correlated to the Gamsby complex are also found in metamorphic rocks at Gardner Canal. This observation points to a common tectonic evolution for the two areas during the Late Jurassic and Early Cretaceous.

To the south, the central gneiss complex terminates. Rocks show a change in metamorphic grade which appears to correlate with the location of the Kitlope pluton. The rocks to the south are correlated with the Stikine terrane and are metamorphosed into green-schist facies (Rusmore et al 2001). The exact location and style of this transition is still unknown.

V. Petrology

V.A. Kitlope Pluton

The Kitlope pluton is a Paleocene (61.1± 1.2 Ma, Gehrels et al in revision) granodiorite that outcrops on the shores and high peaks around Kitlope Lake (Table 3.1). The pluton intruded as a series of discrete tabular intrusions. The Kitlope pluton is grey in outcrop, characterized by equigranular texture with grains as large as 1 cm, and varies from non-foliated to weakly foliated. The pluton is characterized by abundant mafic enclaves, streaks and mafic schlieren composed of mafic minerals, which suggest mingling between felsic and more mafic magmas (Vernon 1983), as has also found in the plutons at Skeena River (Hollister and Andronicos 2000).

The pluton contains subhedral plagioclase (An_{26}-Oligoclase) with polysynthetic twinning, sometimes zoning, and myrmekitic texture. K-Feldspar is subhedral. Biotite is pleochroic ranging from dark green to yellow. Hornblende, when present, has a pleochroism ranging from dark green to green and is spatially associated with biotite. The abundance of titanite in this metaluminous magma indicates relatively oxidized conditions (Tiepolo et al 2002), as it crystallizes during hydration reactions that convert clinopyroxene to amphibole or oxidation during post-magmatic re-equilibration (Frost et al 2001). Allanite is commonly present as a magmatic phase in the pluton and has thin rims of epidote which appear to be magmatic. The presence of allanite and epidote also indicates oxidizing magmatic conditions. Modifications from the magmatic texture include chessboard extinction in quartz and deformational twinning in plagioclase.

Table 3.1: Mineralogy of rocks at Gardner Canal and Kitlope Lake areas

Rock Type	Quartz	Plg	Kfs	Biotite	Hbl	Opq	Titanite	Epidote	Allanite	Apatite	Zircon	Garnet	CPX	Sill
Orthogneiss	x	x	x	x	±	x	±	x		±				
Amphibolite	x	x	±	x	x	x	±	x		x		±	±	
Paragneiss	x	x		x		x				x		x		±
Calc-silicate	x							x				x	x	
Quottoon Pluton	x	x	±	x	x	x	±			±				
Chief Matthew's Pluton	x	x	x	x	x	x	x			x				
Kitlope Pluton	x	x	x	x	±	x	x		±	x	x			

V.B. Quottoon Pluton

The Quottoon pluton (Table 3.1) is exposed at Gardener Canal from Europa Reach to Kemano Bay (Figure 3.2). The pluton is a tabular granodiorite that intruded along the Coast shear-zone. A zircon age indicates that the pluton intruded at 59.5 ± 1.6 Ma (Gehrles et al in revision). The plagioclase (An_{32}-Andesine) often shows zoning and twinning.

Modifications to the magmatic texture include bulging/sutured grain boundaries; undulouse extinction in quartz, and deformation twinning in plagioclase. These textures indicate high temperature deformation of the rocks while they were cooling.

V.C. Chief Matthew's Pluton

The Chief Matthew's Bay pluton is a granodiorite that intruded between 55.6 ± 0.9 and 58.2 ± 0.9 Ma (Gehrels et al in revision, Table 3.1). The pluton has a sill-like geometry and a thickness of ~6 km. The plagioclase (An_{34}-Andesine) is subhedral with tabular shape, is normally zoned and twinned. The quartz is anhedral and located in the interstices of the other minerals. The hornblende is subhedral and shows a pleochroism ranging from light-green to dark green; it is usually associated with biotite and titanite. The biotite is subhedral and has a pleochroism that varies from yellow to dark brown, and it is incipiently altered to chlorite. The K-feldspar becomes more abundant in the more felsic parts of the pluton.

Solid state transformations to the magmatic texture of the rock include chessboard extinction for quartz, development of deformation twinning in plagioclase and some times core and mantle structures. Also there is some

evidence for phase boundary migration. These observations also indicate high temperature deformation was occurring while the pluton was cooling.

V.D. Country-rocks

The country-rocks of the plutons occur either as screens in the plutons or in contact with the plutons. The lithologies include orthogneiss of tonalitic and granodioritic compositions, amphibolite, paragneiss, and calc-silicate rocks of the central gneiss complex (Table 3.1). The foliation in the country-rocks is generally concordant with the magmatic fabric in the plutons. Two orthogneiss rocks close to the Quottoon pluton have U/Pb zircon ages, one rock is 96.8 ± 2.1 Ma and the other one is 125.4 ± 3.3 Ma (Gehrels et al in revision).

In general, orthogneiss is grey in the field with a variable grain size smaller than ~1mm, and characterized by a prominent continuous foliation given by the orientation of mafic minerals. Amphibolite appears black with gneissic texture and varies from fine to medium grain size. Calc-silicate rocks are brown in color given by the garnet and green given by the epidote. They are internally layered, with the epidote located closer to the contact with the amphibolite, and the garnet-diopside-quartz layer located towards the core of the layers.

The paragneiss presents a wide range of mineralogies at the same outcrop, providing evidence for a sedimentary protolith. For example, associated with the Quottoon pluton is sample 07B148B (Figure 3.2), which is composed of biotite, apatite, plagioclase, quartz, garnet and opaques. Epidote, titanite and apatite appear clustered at the grain boundaries and are very fine grained. The garnet in this rock has inclusions of opaque minerals

that parallel the matrix foliation indicating that the growth of the garnet either occurred late during the deformation or postdates it. Sample 07B148A is from the same outcrop but the mineralogy is garnet, biotite, plagioclase, quartz, sillimanite, and opaque minerals. Also chlorite is present as a retrograde mineral, associated with garnet (Figure 3.3a). The garnet in this rock develops corona textures of plagioclase. The biotite present in the coronas is finer grained than in the matrix of the rock, indicating that it also participated in the reactions that made the corona.

Migmatitic rocks are widespread in the area except for east of Kitlope Lake. These rocks are characterized by a gneissic foliation with bands of different composition and grain size. The different bands of the rock show a change from magmatic texture, given by random distribution of euhedral plagioclase, quartz and hornblende grains, to solid-sate deformation given by foliated layers composed of fine grained quartz, plagioclase, hornblende, and biotite.

The rocks have a granular texture with felsic grains forming triple junctions at 120°, and mafic grains with 180° grain boundaries (Figure 3.3b). Some grains show interlobate grain boundaries (eg. sample 06B76, associated with the Kitlope pluton). This texture indicates that the rocks underwent recovery and recrystallization at high temperatures, with grain boundary migration and grain boundary area reduction. The hornblendes are usually poikiloblasts with inclusions of plagioclase and quartz that are distributed along cleavage planes. Plagioclase is generally andesine (An_{31-36}). Garnet, when present, shows irregular boundaries indicating dissolution into the matrix, sometimes accompanied by plagioclase corona reactions (Figure 3.3c) (e.g. sample 07B58, associated with the Chief Matthew's pluton). Garnet

Figure 3.3: Photomicrographs of thin sections from rocks from the southern termination of the central gneiss complex. (a) Garnet with chlorite and quartz in paragneiss (sample 07B148A). (b) Granular texture that characterizes most of the country-rocks of the central gneiss complex. (c) Plagioclase corona around garnet in sample 07B58. Also present in the corona is fine grained biotite. (d) Same as (c), except in crossed polarized light. (e) Mg x-ray map of garnet of sample 06B77 that shows inclusions of pyrite- epidote- quartz-chlorite. (f) Mn x-ray map of same garnet. (g) Backscatter image of inclusions in garnet.

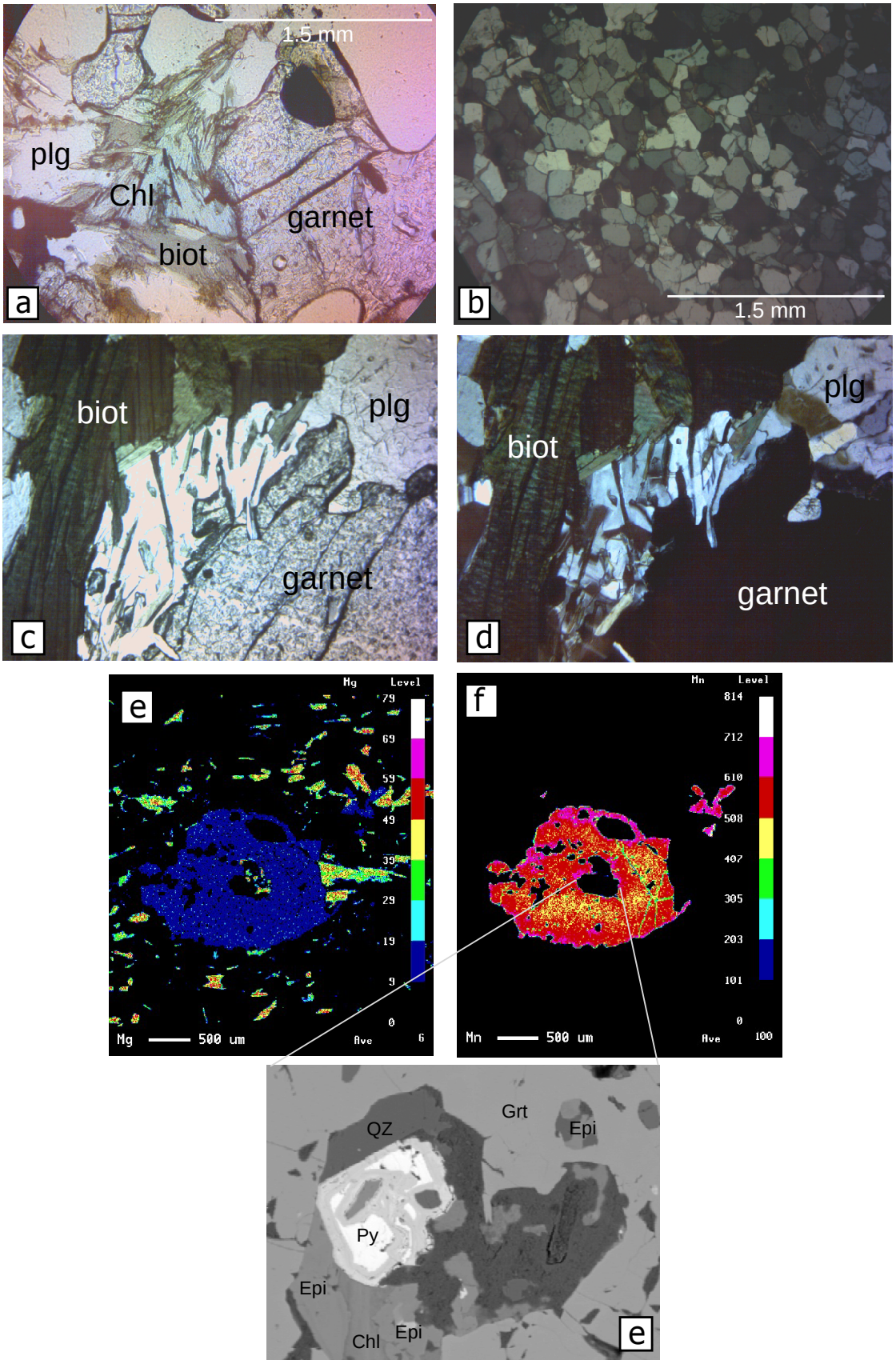
1.5 mm
plg
Chl
garnet
biot
a
b
1.5 mm
biot
plg
garnet
c
biot
plg
garnet
d
e
Mg
Level
79
69
59
49
39
29
19
9
0
Mg
500 um
Ave
6
f
Mn
Level
814
712
610
508
407
305
203
101
0
Mn
500 um
Ave
100
QZ
Grt
Epi
Py
Epi
Chl
Epi
e

can contain inclusions of epidote and pyrite (Figure 3.3e-g). The inclusions can be interpreted as indicators of the prograde path of the rock previous to the garnet growth.

VI. Pressure-Temperature calculations

VI.A. Methodology

Mineral compositional data and x-ray maps of minerals were collected using a Jeol 8900 electron microprobe at Cornell University. For quantitative analysis, the operating conditions were 15kv, 15-30 nA and a beam diameter of 1-5 μm. X-ray maps were collected to detect zoning of minerals using wavelength dispersive scanning (WDS). The operating conditions were 15kev of accelerating voltage, 100nA beam current, and a fixed beam with a diameter of 1 μm over a moving stage. The standards used to calibrate the microprobe were glass of basaltic composition (Si, Al, Fe), pyroxene (Mg, Ca), Albite (Na), Orthoclase (K), Rutile (Ti), Rhodonite (Mn), and Chromite (Cr). The standard block was prepared at Cornell University. The data obtained is presented in the Appendix, the sample location and P-T results are shown in Figure 3.4 and Table 3.2.

Pseudosections, or equilibrium phase diagrams, are also a means of obtaining information about peak metamorphic conditions as well as information about the metamorphic path followed by a specific rock. Pseudosections represent a phase diagram specific to the composition of the rock. The calculation relies on thermodynamic data for the minerals stable in a specific rock bulk composition at varying P-T conditions. The software package used to calculate the pseudosections is Theriak-Domino (De Capitani and Brown 1987), and gives similar results to software packages like Perplex

Table 3.2: Mineral assemblages and results of pressures and temperature calculations for selected samples

Igneous		Qz	KF	Plg	Bt	Hbl	Tita	Epi	All	Grt	Zir	Apt	Oq	Ms	Sill	P S	Hbl/ Pl	Grt/ Bi	T (°C)	Al in hbl	Gr/Pl/ Ms/Qz	Gr/Pl/ Bi/Qz	P (Gpa)
Kitlope pluton	06B18	X		X	X	X	X					X					X		643				
	06B19	X		X	X	X	X					X					X		701				
	06B22	X	X	X	X	X	X		X			X	X				X		709	X			0.68
	06B67	X	X	X						X				X					620-750		X		0.6-0.8
	06B68	X	X	X	X	X	X		X				X				X		716	X			0.71
	06B72	X	X	X	X	X	X				X	X	X				X		736	X			0.71
CMP	07B66	X	X	X	X	X	X					X					X		773	X			0.57
	07B93	X	X	X	X	X	X										X		746	X			0.61
QP	07B141	X	X	X	X	X	X	X									X		762	X			0.68
	07B146A	X	X	X	X					X			X					X	620			X	0.68-0.72
Metamorphic																							
Kitlope pluton	06B15	X		X		X	X	X			X						X		706				
	06B26	X		X	X	X	X						X				X		756				
	06B33	X		X	X	X		X					X				X		697				
	06B35	X		X	X	X	X										X		736				
	06B76	X		X	X	X			X		X		X				X		717				
QP	07B148A	X		X	X					X			X		X	X			630-710				0.55-0.77

QP: Quottoon Pluton
CMP: Chief Matthew's Pluton

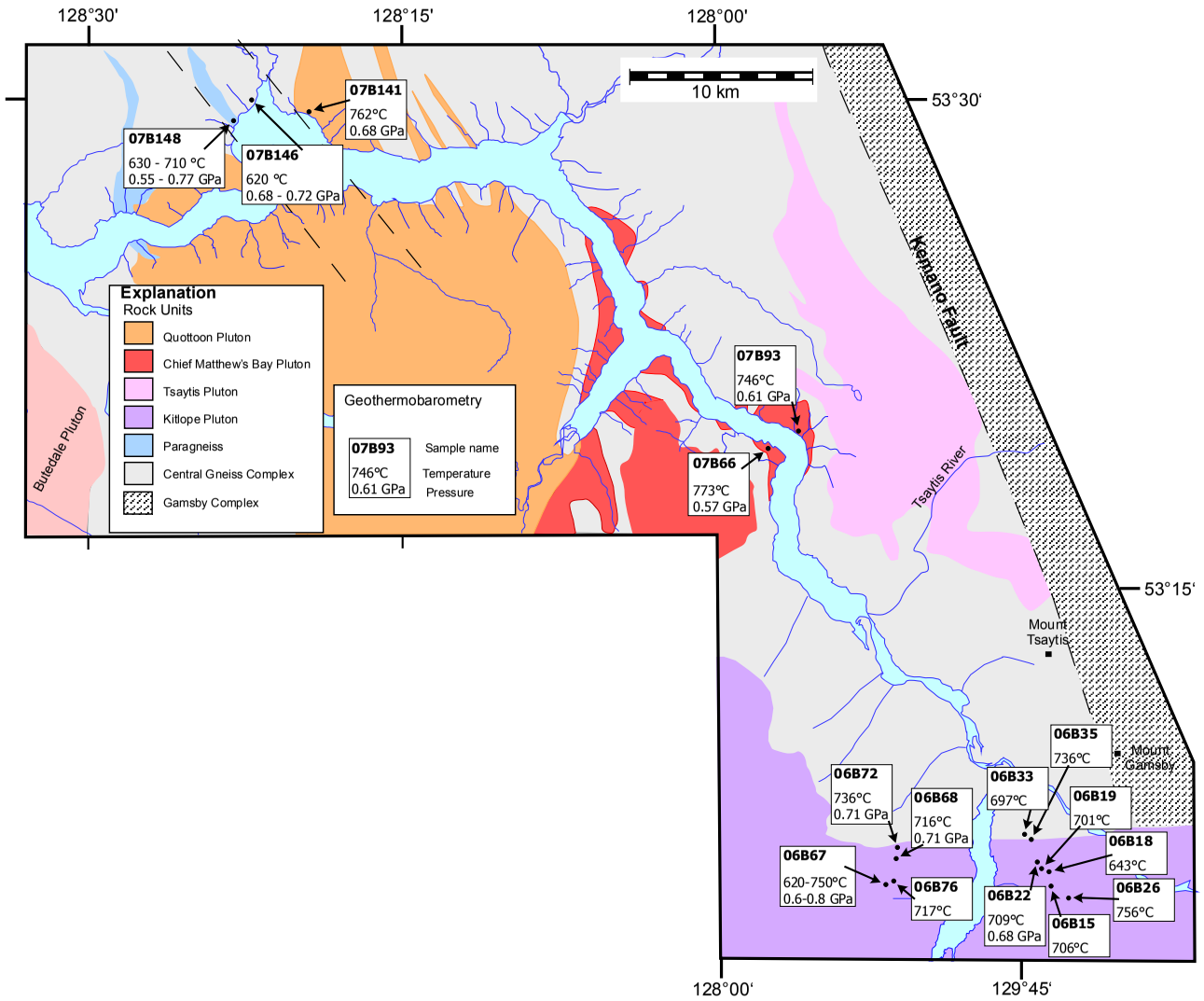

Figure 3.4: Location of samples used for geothermobarometry and the resulting pressure and temperature.

(Connolly and Kerrick 1987) and Thermocalc (Powell et al 1998). The database used is that of Holland and Powell (1998) updated to ds5.5 in 2003. We used the anhydrous whole rock chemical composition obtained through calculating the modal abundances of minerals and measuring its chemical composition with the electron microprobe. We did not apply any correction for Fe^{3+}. The water pressure was assumed to equal lithostatic pressure in one run and equal to 0.3 of the lithostatic pressure, in a second run, to set the boundaries of possible reactions.

Six plutonic rocks had the required mineral assemblage to apply the Al in hornblende barometer. The samples were selected making sure they preserved the magmatic texture. The composition of the hornblendes in the rocks was obtained by performing line scans of the minerals across the core and the rims. The hornblendes were not zoned; however we used the rim compositions to calculate pressure. Table 3.3 shows the pressures calculated using different calibrations (Hammarstrom and Zen, 1986, Hollister at al, 1987, Schmidt, 1992, and Anderson and Smith, 1995). The results are within 0.2 standard deviations from each other. The Schmidt calibration is experimental and reproduces the results of the previous empirically calibrated regressions. For this reason the Schmidt calibration is the preferred and will be used for the following analysis.

The plagioclase-hornblende thermometer (Holland and Blundy, 1990) was used in thirteen samples of the plutons and amphibolite; the results are shown in Figure 3.4 and 3.5. For silica-saturated rocks two thermometers were used simultaneously and the temperature was estimated to be where the two curves intercept. The compositional data was collected along line scans across hornblende-plagioclase boundaries to try to obtain compositions from

Table 3.3: Different calibrations of the Al in Hornblende Barometer

		Kitlope Pluton			Chief Matthew's Pluton		Quottoon
Calibration	**Error**	**06B68**	**06B22**	**06B72**	**07B66**	**07B93**	**07B141**
Hammerstrom and Zen (1986)	**(± 0.3 GPa)**	0.67	0.64	0.69	0.51	0.52	0.65
Hollister et al. (1987)	**(± 0.1 GPa)**	0.71	0.69	0.74	0.54	0.55	0.70
Anderson and Smith (1995)		0.64	0.63	0.62	0.43	0.54	0.53
Schmidt (1992)	**(± 0.06 GPa)**	0.70	0.68	0.72	0.56	0.56	0.69

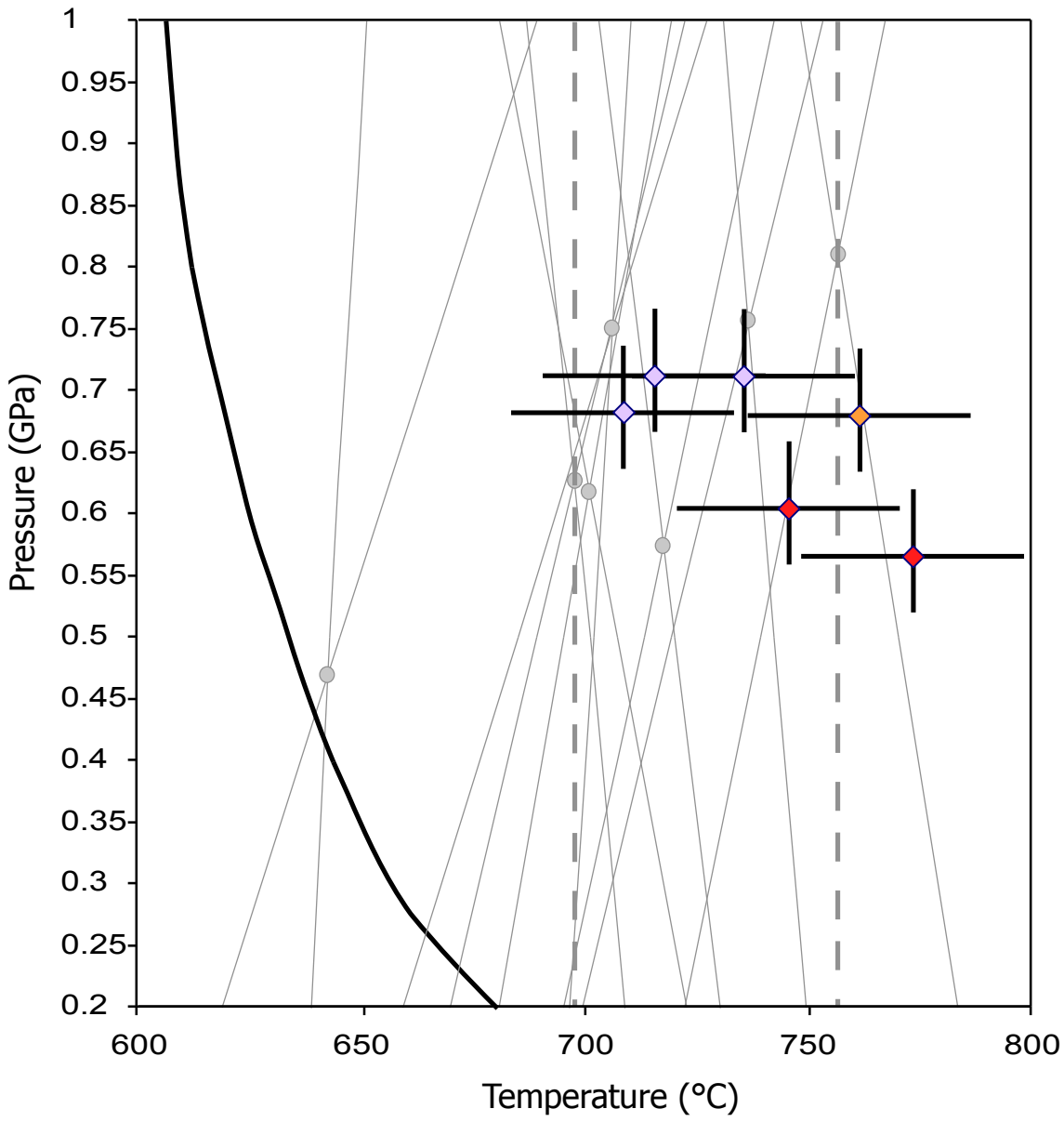

Figure 3.5: Pressure-temperature diagram showing the calculated values for the rocks. The crosses represent plutonic rocks with temperature and pressure values. The thin grey lines are the two independent hbl-plg thermometers; the interception of them is the calculated temperature for each sample, represented by a grey dot in the figure. The dashed grey lines bracket the temperatures calculated by the hbl-plg thermometer except for a low temperature value. The black line is for reference and is the water saturated solidus for granites.

grains which were in textural equilibrium. The minerals were rarely zoned, but when they were, rim compositions were used for the calculation of temperature. Combining the temperature estimates with the Al in Hornblende barometer allows us to estimate the P-T conditions during final crystallization of the plutons (Figure 3.5). The range in temperature calculated for all the rocks is between 640-760℃.

The garnet-biotite thermometer (Ferry and Spear 1978, Hodges and Spear 1982, Ganguly and Saxena 1984) is one of the most widely used in the literature, given that biotite and garnet are common assemblages in the middle and lower crust. Several country-rocks and pegmatitic dikes contain the assemblage garnet-biotite. However, most of them show strong evidence for retrograde diffusion, indicated by flat element zoning profiles in the garnet with thin rims that indicate retrograde diffusion. Additionally, even when garnet lacks a diffusional zoning profile, it shows evidence for participation in retrograde net transfer reactions as indicated by resorbed margins (Figure 3.6). Also, several samples show two generations of biotite, one biotite in the matrix and the other present in coronas around the garnet. For these reasons the thermometer was applied with care. Most samples gave unreasonably high or unreasonably low temperatures for the mineral assemblage in the rock. However a pegmatitic dike associated with the Quottoon pluton (sample 07B146A, Figure 3.2), where the garnet appeared euhedral and unzoned, gave a temperature which is consistent with the mineralogy of the sample, between 620 and 640℃, depending on the calibration of the thermometer.

We were also able to apply the garnet-plagioclase-muscovite-quartz barometer (Hoisch 1990, 1991) to a pegmatitic dike associated with the Kitlope pluton (sample 06B67, Figure 3.2). This sample is the only one with

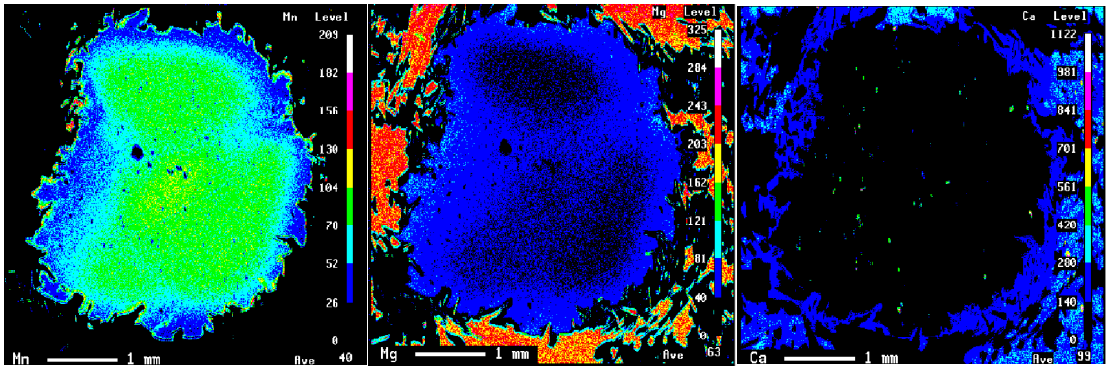

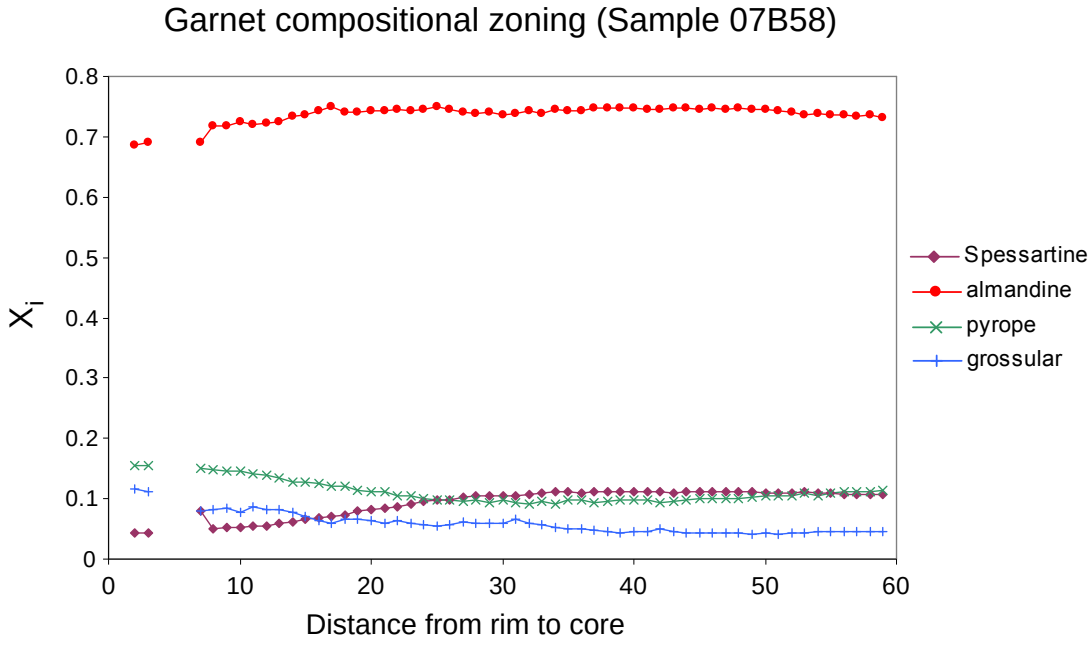

Figure 3.6: X-ray maps and zoning profiles of garnet with plagioclase corona in sample 07B58. X_i is the mole fraction of each garnet end-member. The profiles correspond to a zoned garnet that shows relative enrichment of pyrope and grossular end-members and relative depletion of almandine and spessartine end-members, at the rims . This zoning profile might be preserved from the time the garnet crystallized.

muscovite present in the region. Muscovite being stable is consistent with the intrusion of the pegmatitic dike during cooling, because peak temperatures for the central gneiss complex are hotter than the stability of this mineral in the presence of quartz. The pressure obtained for this sample was calculated by the intercept of the barometer with reaction curves (Figure 3.7a). The first curve is the water saturated granite solidus, the second curve is the reaction that constrains the stability of muscovite below 750℃ at 0.7 GPa. The pressure should be in between these two curves with a value of 0.63 to 0.8 GPa. The temperature is also calculated with the reactions and falls between 620 and 750℃. A variation of this barometer (garnet-plagioclase-biotite-quartz, Hoisch 1990, 1991) was applied to sample 07B146A. The pressure of the sample was calculated by the intercept of two calibrations of the garnet-biotite thermometer and reaction curves (Figure 3.7b), and it is between 0.68 and 0.72 GPa. The temperature is between 580 and 680℃ when applied the garnet-biotite thermometer.

Figure 3.8 and 3.9 are equilibrium phase diagrams calculated for sample 07B148A with water pressure equal to lithostatic pressure and water pressure equal to 0.3 of the lithostatic pressure respectively, from a paragneiss near the Quottoon pluton. The mineral assemblage of the rock is reproduced within the shaded area. For the same paragenesis, the two phase diagrams give a difference in temperature of 100℃ and a difference in pressure of ~0.4 GPa (compare Figure 3.8 and 3.9). However, if we assume that the rocks had k-feldspar that retrograded to biotite during decompression the differences in pressure and temperature between the phase diagrams is reduced. The modes of the minerals within the rock are only partly reproduced. Modes for most minerals generated by the calculation are within

A)

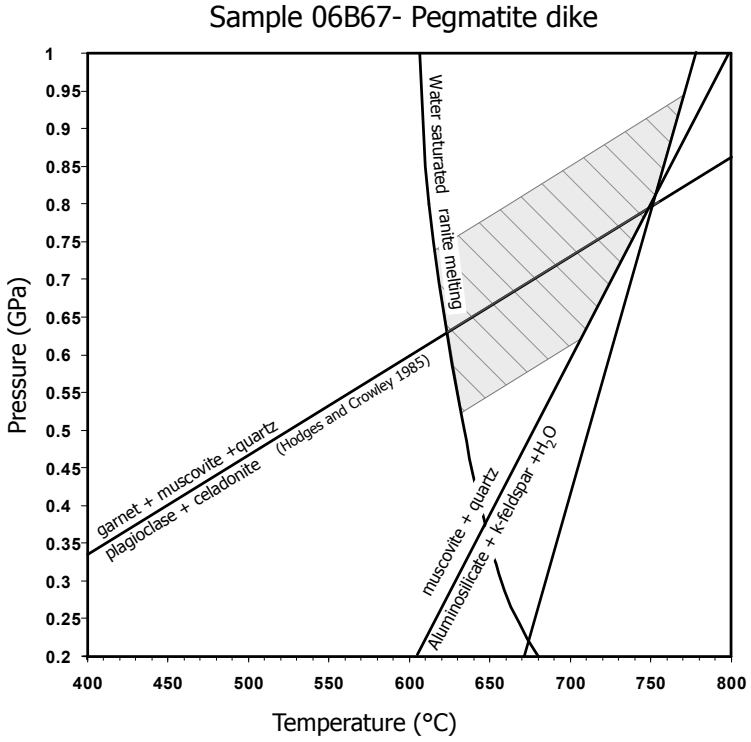

B)

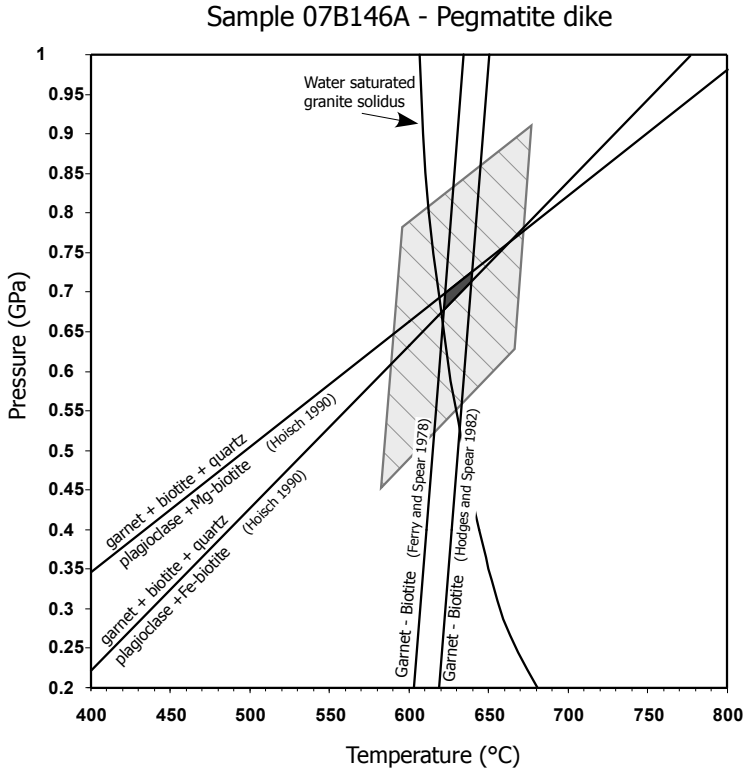

Figure 3.7: Pressure-temperature calculations for pegmatite dikes. The grey areas are the results assuming an error of ± 0.1GPa and ± 50°C. Sample 06B67 is within the Kitlope pluton; sample 07B146A is within the Quottoon pluton. See text for further explanation.

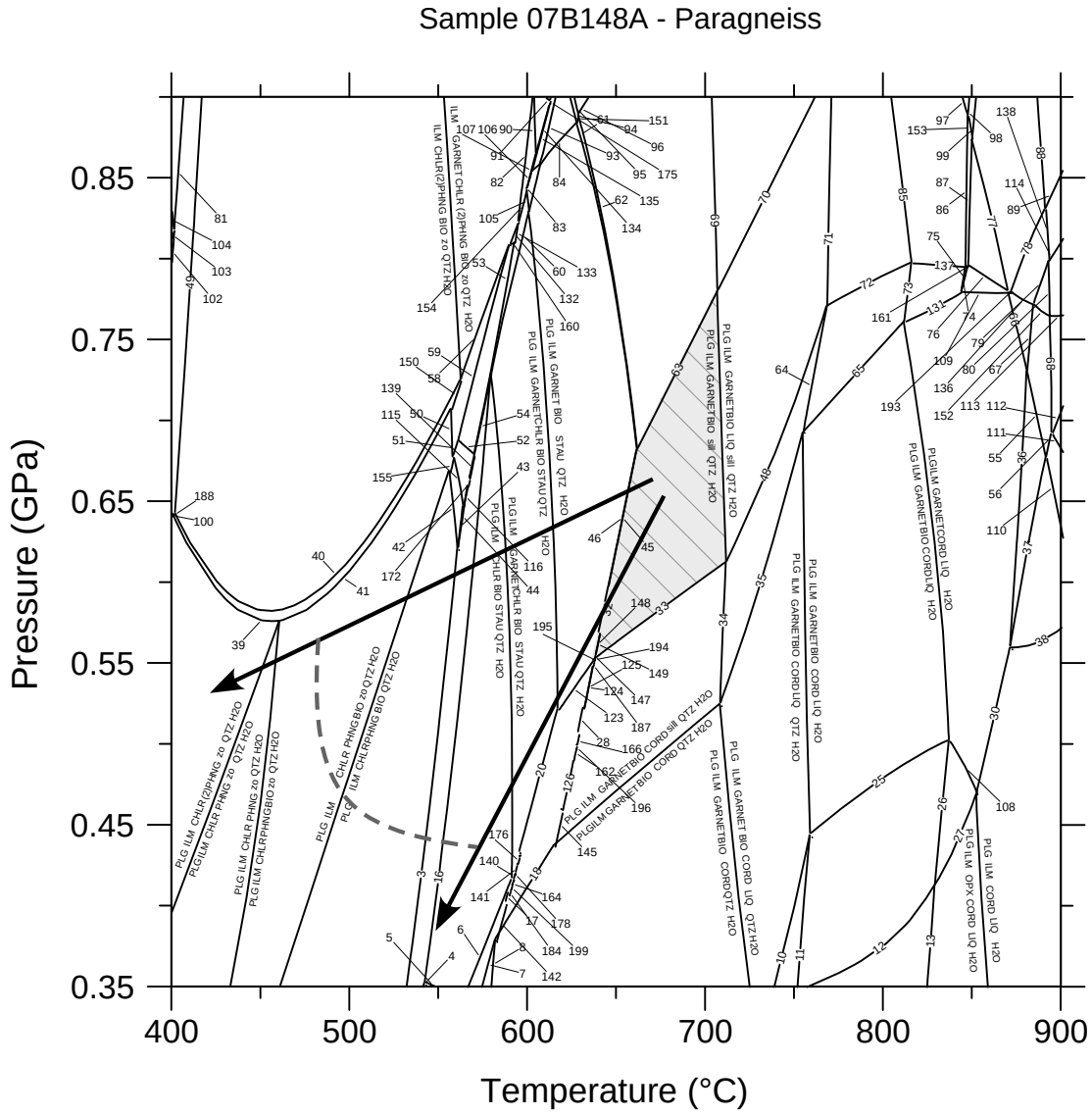

Figure 3.8: Pseudosection with water pressure equal lithostatic pressure of sample 07B148A. The numbers represent reactions described in next page. The grey field reproduces the mineralogy in the sample. The black arrows bracket the possible decompression paths for the rock. See text for discussion.

Figure 3.8 (Continued)

Reactions:

1) PLG ILM CHLR PHNG zo QTZ H2O = PLG ILM CHLR PHNG BIO zo QTZ H2O
2) PLG ILM CHLR PHNG BIO zo QTZ H2O = PLG ILM CHLR PHNG BIO QTZ H2O
3) PLG ILM CHLR PHNG BIO QTZ H2O = PLG ILM CHLR PHNG BIO STAU QTZ H2O
4) PLG ILM CHLR PHNG BIO STAU QTZ H2O = PLG ILM CHLR BIO STAU and QTZ H2O
5) PLG ILM CHLR BIO STAU and QTZ H2O = PLG ILM CHLR BIO STAU QTZ H2O
6) PLG ILM CHLR BIO STAU QTZ H2O = PLG ILM CHLR BIO STAU CORD QTZ H2O
7) PLG ILM CHLR BIO STAU CORD QTZ H2O = PLG ILM GARNET CHLR BIO CORD QTZ H2O
8) PLG ILM GARNET CHLR BIO CORD QTZ H2O = PLG ILM GARNET BIO CORD QTZ H2O
9) PLG ILM GARNET BIO CORD QTZ H2O = PLG ILM GARNET BIO CORD LIQ QTZ H2O
10) PLG ILM GARNET BIO CORD LIQ QTZ H2O = PLG ILM GARNET OPX BIO CORD LIQ QTZ H2O
11) PLG ILM GARNET OPX BIO CORD LIQ QTZ H2O = PLG ILM GARNET OPX BIO CORD LIQ H2O
12) PLG ILM GARNET OPX BIO CORD LIQ H2O = PLG ILM OPX BIO CORD LIQ H2O
13) PLG ILM OPX BIO CORD LIQ H2O = PLG ILM OPX CORD LIQ H2O
14) PLG ILM OPX CORD LIQ H2O = PLG ILM CORD LIQ H2O
15) PLG ILM CHLR (2)PHNG zo QTZ H2O = PLG ILM CHLR PHNG zo QTZ H2O
16) PLG ILM CHLR PHNG BIO STAU QTZ H2O = PLG ILM CHLR BIO STAU QTZ H2O
17) PLG ILM CHLR BIO STAU CORD QTZ H2O = PLG ILM GARNET BIO STAU CORD QTZ H2O
18) PLG ILM GARNET BIO STAU CORD QTZ H2O = PLG ILM GARNET BIO CORD QTZ H2O
19) PLG ILM CHLR BIO STAU QTZ H2O = PLG ILM GARNET CHLR BIO STAU QTZ H2O
20) PLG ILM GARNET CHLR BIO STAU QTZ H2O = PLG ILM GARNET BIO STAU CORD QTZ H2O
21) PLG ILM GARNET BIO STAU CORD QTZ H2O = PLG ILM GARNET BIO STAU CORD sill QTZ H2O
22) PLG ILM GARNET BIO STAU CORD sill QTZ H2O = PLG ILM GARNET BIO CORD sill QTZ H2O
23) PLG ILM GARNET BIO CORD sill QTZ H2O = PLG ILM GARNET BIO CORD QTZ H2O
24) PLG ILM GARNET BIO CORD LIQ QTZ H2O = PLG ILM GARNET BIO CORD LIQ H2O
25) PLG ILM GARNET BIO CORD LIQ H2O = PLG ILM GARNET OPX BIO CORD LIQ H2O
26) PLG ILM GARNET OPX BIO CORD LIQ H2O = PLG ILM GARNET OPX CORD LIQ H2O
27) PLG ILM GARNET OPX CORD LIQ H2O = PLG ILM OPX CORD LIQ H2O
28) PLG ILM GARNET BIO STAU CORD QTZ H2O = PLG ILM GARNET BIO CORD sill QTZ H2O
29) PLG ILM GARNET BIO CORD LIQ H2O = PLG ILM GARNET CORD LIQ H2O
30) PLG ILM GARNET CORD LIQ H2O = PLG ILM CORD LIQ H2O
31) PLG ILM GARNET CHLR BIO STAU QTZ H2O = PLG ILM GARNET BIO STAU QTZ H2O
32) PLG ILM GARNET BIO STAU QTZ H2O = PLG ILM GARNET BIO sill QTZ H2O
33) PLG ILM GARNET BIO sill QTZ H2O = PLG ILM GARNET BIO CORD sill QTZ H2O
34) PLG ILM GARNET BIO CORD sill QTZ H2O = PLG ILM GARNET BIO CORD LIQ sill QTZ H2O
35) PLG ILM GARNET BIO CORD LIQ sill QTZ H2O = PLG ILM GARNET BIO CORD LIQ QTZ H2O
36) PLG ILM GARNET CORD LIQ H2O = PLG ILM GARNET CORD SPIN LIQ H2O
37) PLG ILM GARNET CORD SPIN LIQ H2O = PLG ILM CORD SPIN LIQ H2O
38) PLG ILM CORD SPIN LIQ H2O = PLG ILM CORD LIQ H2O
39) PLG ILM CHLR (2)PHNG BIO zo QTZ H2O = PLG ILM CHLR (2)PHNG zo QTZ H2O
40) PLG ILM CHLR (2)PHNG BIO zo QTZ H2O = ILM CHLR (2)PHNG BIO zo QTZ H2O
41) PLG ILM CHLR (2)PHNG BIO zo QTZ H2O = PLG ILM CHLR PHNG BIO zo QTZ H2O
42) PLG ILM CHLR PHNG BIO QTZ H2O = PLG ILM CHLR PHNG BIO ma QTZ H2O
43) PLG ILM CHLR PHNG BIO ma QTZ H2O = PLG ILM CHLR PHNG BIO STAU ma QTZ H2O
44) PLG ILM CHLR PHNG BIO STAU ma QTZ H2O = PLG ILM CHLR PHNG BIO STAU QTZ H2O
45) PLG ILM GARNET BIO STAU QTZ H2O = PLG ILM GARNET BIO STAU sill QTZ H2O
46) PLG ILM GARNET BIO STAU sill QTZ H2O = PLG ILM GARNET BIO sill QTZ H2O
47) PLG ILM GARNET BIO sill QTZ H2O = PLG ILM GARNET BIO LIQ sill QTZ H2O
48) PLG ILM GARNET BIO LIQ sill QTZ H2O = PLG ILM GARNET BIO CORD LIQ sill QTZ H2O
49) ILM CHLR (2)PHNG BIO zo sph QTZ H2O = ILM CHLR (2)PHNG BIO zo QTZ H2O
50) PLG ILM CHLR PHNG BIO zo QTZ H2O = PLG ILM GARNET CHLR PHNG BIO zo QTZ H2O
51) PLG ILM GARNET CHLR PHNG BIO zo QTZ H2O = PLG ILM GARNET CHLR PHNG BIO ma QTZ H2O
52) PLG ILM GARNET CHLR PHNG BIO QTZ H2O = PLG ILM GARNET CHLR PHNG BIO ma QTZ H2O
53) PLG ILM GARNET CHLR PHNG BIO QTZ H2O = PLG ILM GARNET CHLR PHNG BIO STAU QTZ H2O
54) PLG ILM GARNET CHLR PHNG BIO STAU QTZ H2O = PLG ILM CHLR PHNG BIO STAU QTZ H2O
55) PLG ILM GARNET CORD SPIN LIQ H2O = ILM GARNET CORD SPIN LIQ H2O
56) ILM GARNET CORD SPIN LIQ H2O = ILM CORD SPIN LIQ H2O
57) ILM CHLR (2)PHNG BIO zo QTZ H2O = ILM GARNET CHLR (2)PHNG BIO zo QTZ H2O
58) ILM GARNET CHLR (2)PHNG BIO zo QTZ H2O = PLG ILM GARNET CHLR PHNG BIO zo QTZ H2O

59) PLG ILM GARNET CHLR PHNG BIO zo QTZ H2O = PLG ILM GARNET CHLR PHNG BIO QTZ H2O
60) PLG ILM GARNET CHLR PHNG BIO STAU QTZ H2O = PLG ILM GARNET CHLR BIO STAU QTZ H2O
61) PLG ILM GARNET BIO STAU QTZ H2O = PLG ILM GARNET BIO STAU ky QTZ H2O
62) PLG ILM GARNET BIO STAU ky QTZ H2O = PLG ILM GARNET BIO ky QTZ H2O
63) PLG ILM GARNET BIO ky QTZ H2O = PLG ILM GARNET BIO sill QTZ H2O
64) PLG ILM GARNET BIO CORD LIQ sill QTZ H2O = PLG ILM GARNET BIO CORD LIQ sill H2O
65) PLG ILM GARNET BIO CORD LIQ sill H2O = PLG ILM GARNET BIO CORD LIQ H2O
66) PLG ILM GARNET CORD LIQ H2O = ILM GARNET CORD LIQ H2O
67) ILM GARNET CORD LIQ H2O = ILM GARNET CORD SPIN LIQ H2O
68) ILM GARNET CORD SPIN LIQ H2O = ILM GARNET CORD SPIN LIQ
69) PLG ILM GARNET BIO ky QTZ H2O = PLG ILM GARNET BIO LIQ ky QTZ H2O
70) PLG ILM GARNET BIO LIQ ky QTZ H2O = PLG ILM GARNET BIO LIQ sill QTZ H2O
71) PLG ILM GARNET BIO LIQ sill QTZ H2O = PLG ILM GARNET BIO LIQ sill H2O
72) PLG ILM GARNET BIO LIQ sill H2O = PLG ILM GARNET BIO CORD LIQ sill H2O
73) PLG ILM GARNET BIO CORD LIQ sill H2O = PLG ILM GARNET CORD LIQ sill H2O
74) PLG ILM GARNET CORD LIQ sill H2O = PLG ILM GARNET CORD LIQ sill cor H2O
75) PLG ILM GARNET CORD LIQ sill cor H2O = PLG ILM GARNET CORD LIQ cor H2O
76) PLG ILM GARNET LIQ cor H2O = PLG ILM GARNET CORD LIQ cor H2O
77) PLG ILM GARNET LIQ cor H2O = ILM GARNET LIQ cor H2O
78) ILM GARNET LIQ cor H2O = ILM GARNET LIQ H2O
79) ILM GARNET LIQ H2O = ILM GARNET SPIN LIQ H2O
80) ILM GARNET SPIN LIQ H2O = ILM GARNET SPIN LIQ
81) ILM CHLR (2)PHNG zo sph QTZ H2O = ILM CHLR (2)PHNG BIO zo sph QTZ H2O
82) ILM GARNET CHLR (2)PHNG BIO zo QTZ H2O = ILM GARNET CHLR PHNG BIO STAU zo QTZ H2O
83) ILM GARNET CHLR PHNG BIO STAU zo QTZ H2O = PLG ILM GARNET PHNG BIO STAU QTZ H2O
84) PLG ILM GARNET PHNG BIO STAU QTZ H2O = PLG ILM GARNET BIO STAU QTZ H2O
85) PLG ILM GARNET BIO LIQ sill H2O = PLG ILM GARNET LIQ sill H2O
86) PLG ILM GARNET LIQ sill H2O = PLG ILM GARNET LIQ sill cor H2O
87) PLG ILM GARNET LIQ sill cor H2O = PLG ILM GARNET LIQ cor H2O
88) ILM GARNET LIQ cor H2O = ILM GARNET LIQ cor
89) ILM GARNET LIQ cor = ILM GARNET LIQ
90) ILM GARNET CHLR PHNG BIO STAU zo QTZ H2O = ILM GARNET PHNG BIO STAU zo QTZ H2O
91) ILM GARNET (2)PHNG BIO STAU zo QTZ H2O = ILM GARNET PHNG BIO STAU zo QTZ H2O
92) ILM GARNET (2)PHNG BIO STAU zo QTZ H2O = PLG ILM GARNET (2)PHNG BIO STAU QTZ H2O
93) PLG ILM GARNET (2)PHNG BIO STAU QTZ H2O = PLG ILM GARNET PHNG BIO STAU QTZ H2O
94) PLG ILM GARNET PHNG BIO STAU QTZ H2O = PLG ILM GARNET PHNG BIO STAU ky QTZ H2O
95) PLG ILM GARNET PHNG BIO STAU ky QTZ H2O = PLG ILM GARNET PHNG BIO ky QTZ H2O
96) PLG ILM GARNET PHNG BIO ky QTZ H2O = PLG ILM GARNET BIO ky QTZ H2O
97) PLG ILM GARNET LIQ sill H2O = ILM GARNET LIQ sill H2O
98) ILM GARNET LIQ sill H2O = ILM GARNET LIQ sill cor H2O
99) ILM GARNET LIQ sill cor H2O = ILM GARNET LIQ cor H2O
100) PLG ILM CHLR (2)PHNG zo sph QTZ H2O = PLG ILM CHLR (2)PHNG zo QTZ H2O
101) ILM CHLR (2)PHNG BIO zo sph QTZ H2O = PLG ILM CHLR (2)PHNG zo sph QTZ H2O
102) ILM CHLR (2)PHNG BIO sph QTZ H2O = ILM CHLR (2)PHNG BIO zo sph QTZ H2O
103) ILM CHLR (2)PHNG sph QTZ H2O = ILM CHLR (2)PHNG BIO sph QTZ H2O
104) ILM CHLR (2)PHNG zo sph QTZ H2O = ILM CHLR (2)PHNG sph QTZ H2O
105) PLG ILM GARNET CHLR PHNG BIO STAU QTZ H2O = PLG ILM GARNET PHNG BIO STAU QTZ H2O
106) PLG ILM GARNET PHNG BIO STAU zo QTZ H2O = PLG ILM GARNET PHNG BIO STAU QTZ H2O
107) ILM GARNET CHLR PHNG BIO STAU zo QTZ H2O = PLG ILM GARNET PHNG BIO STAU zo QTZ H2O
108) PLG ILM GARNET CORD LIQ H2O = PLG ILM GARNET OPX CORD LIQ H2O
109) PLG ILM GARNET CORD LIQ cor H2O = PLG ILM GARNET CORD LIQ H2O
110) PLG ILM CORD SPIN LIQ H2O = ILM CORD SPIN LIQ H2O
111) ILM CORD SPIN LIQ H2O = ILM CORD SPIN LIQ
112) ILM CORD SPIN LIQ = ILM GARNET CORD SPIN LIQ
113) ILM GARNET SPIN LIQ = ILM GARNET CORD SPIN LIQ
114) ILM GARNET LIQ = ILM GARNET SPIN LIQ
115) PLG ILM CHLR PHNG BIO ma QTZ H2O = PLG ILM GARNET CHLR PHNG BIO ma QTZ H2O
116) PLG ILM GARNET CHLR PHNG BIO ma QTZ H2O = PLG ILM CHLR PHNG BIO STAU ma QTZ H2O
117) PLG ILM GARNET CHLR BIO STAU QTZ H2O = PLG ILM GARNET CHLR BIO STAU CORD TZ H2O
118) PLG ILM GARNET CHLR BIO STAU QTZ H2O = PLG ILM GARNET CHLR BIO STAU CORD QTZ H2O
119) PLG ILM GARNET CHLR BIO STAU QTZ H2O = PLG ILM GARNET CHLR BIO STAU CORD QTZ H2O
120) PLG ILM GARNET CHLR BIO STAU CORD QTZ H2O = PLG ILM GARNET BIO STAU CORD QTZ H2O
121) PLG ILM GARNET CHLR BIO STAU CORD QTZ H2O = PLG ILM GARNET BIO STAU CORD QTZ H2O
122) PLG ILM GARNET CHLR BIO STAU CORD QTZ H2O = PLG ILM GARNET BIO STAU CORD QTZ H2O

123) PLG ILM GARNET BIO STAU QTZ H2O = PLG ILM GARNET BIO STAU CORD QTZ H2O
124) PLG ILM GARNET BIO STAU CORD QTZ H2O = PLG ILM GARNET BIO STAU CORD sill QTZ H2O
125) PLG ILM GARNET BIO STAU CORD sill QTZ H2O = PLG ILM GARNET BIO CORD sill QTZ H2O
126) PLG ILM GARNET BIO STAU CORD QTZ H2O = PLG ILM GARNET BIO CORD sill QTZ H2O
127) PLG ILM GARNET BIO STAU CORD sill QTZ H2O = PLG ILM GARNET BIO CORD sill QTZ H2O
128) PLG ILM GARNET BIO STAU CORD sill QTZ H2O = PLG ILM GARNET BIO CORD sill QTZ H2O
129) PLG ILM GARNET BIO STAU CORD QTZ H2O = PLG ILM GARNET BIO STAU CORD sill QTZ H2O
130) PLG ILM GARNET BIO STAU CORD QTZ H2O = PLG ILM GARNET BIO STAU CORD sill QTZ H2O
131) PLG ILM GARNET CORD LIQ sill H2O = PLG ILM GARNET CORD LIQ H2O
132) ILM GARNET CHLR (2)PHNG BIO zo QTZ H2O = PLG ILM GARNET CHLR (2)PHNG BIO QTZ H2O
133) PLG ILM GARNET CHLR (2)PHNG BIO QTZ H2O = PLG ILM GARNET CHLR PHNG BIO STAU QTZ H2O
134) ILM GARNET PHNG BIO STAU zo QTZ H2O = PLG ILM GARNET PHNG BIO STAU zo QTZ H2O
135) PLG ILM GARNET PHNG BIO STAU zo QTZ H2O = PLG ILM GARNET (2)PHNG BIO STAU QTZ H2O
136) ILM GARNET LIQ H2O = ILM GARNET CORD LIQ H2O
137) PLG ILM GARNET LIQ sill H2O = PLG ILM GARNET CORD LIQ sill H2O
138) ILM GARNET LIQ H2O = ILM GARNET LIQ
139) PLG ILM GARNET CHLR PHNG BIO ma QTZ H2O = PLG ILM GARNET CHLR PHNG BIO STAU QTZ H2O
140) PLG ILM GARNET CHLR BIO STAU QTZ H2O = PLG ILM GARNET BIO STAU CORD QTZ H2O
141) PLG ILM GARNET CHLR BIO STAU QTZ H2O = PLG ILM GARNET BIO STAU CORD QTZ H2O
142) PLG ILM CHLR BIO STAU CORD QTZ H2O = PLG ILM GARNET BIO STAU CORD QTZ H2O
143) PLG ILM GARNET CHLR BIO STAU CORD QTZ H2O = PLG ILM GARNET BIO STAU CORD QTZ H2O
144) PLG ILM GARNET CHLR BIO STAU CORD QTZ H2O = PLG ILM CHLR BIO STAU CORD QTZ H2O
145) PLG ILM GARNET BIO STAU CORD QTZ H2O = PLG ILM GARNET BIO CORD sill QTZ H2O
146) PLG ILM GARNET BIO CORD LIQ sill QTZ H2O = PLG ILM GARNET BIO CORD LIQ H2O
147) PLG ILM GARNET BIO STAU QTZ H2O = PLG ILM GARNET BIO sill QTZ H2O
148) PLG ILM GARNET BIO STAU sill QTZ H2O = PLG ILM GARNET BIO sill QTZ H2O
149) PLG ILM GARNET BIO STAU QTZ H2O = PLG ILM GARNET BIO STAU sill QTZ H2O
150) PLG ILM CHLR (2)PHNG BIO zo QTZ H2O = PLG ILM GARNET CHLR PHNG BIO zo QTZ H2O
151) PLG ILM GARNET PHNG BIO STAU ky QTZ H2O = PLG ILM GARNET BIO STAU ky QTZ H2O
152) ILM GARNET SPIN LIQ H2O = ILM GARNET CORD SPIN LIQ H2O
153) PLG ILM GARNET LIQ sill cor H2O = ILM GARNET LIQ sill cor H2O
154) ILM GARNET CHLR PHNG BIO STAU zo QTZ H2O = PLG ILM GARNET CHLR PHNG BIO STAU QTZ H2O
155) PLG ILM CHLR PHNG BIO zo QTZ H2O = PLG ILM CHLR PHNG BIO ma QTZ H2O
156) PLG ILM GARNET CHLR BIO STAU CORD QTZ H2O = PLG ILM CHLR BIO STAU CORD QTZ H2O
157) PLG ILM CHLR BIO STAU CORD QTZ H2O = PLG ILM GARNET CHLR BIO STAU CORD QTZ H2O
158) PLG ILM GARNET CHLR BIO STAU CORD QTZ H2O = PLG ILM GARNET BIO STAU CORD QTZ H2O
159) PLG ILM GARNET CHLR BIO STAU CORD QTZ H2O = PLG ILM GARNET BIO STAU CORD QTZ H2O
160) PLG ILM GARNET CHLR (2)PHNG BIO QTZ H2O = PLG ILM GARNET CHLR PHNG BIO QTZ H2O
161) PLG ILM GARNET LIQ sill cor H2O = PLG ILM GARNET CORD LIQ sill cor H2O
162) PLG ILM GARNET BIO STAU CORD QTZ H2O = PLG ILM GARNET BIO CORD sill QTZ H2O
163) PLG ILM CHLR PHNG BIO ma QTZ H2O = PLG ILM CHLR PHNG BIO STAU QTZ H2O
164) PLG ILM CHLR BIO STAU CORD QTZ H2O = PLG ILM GARNET BIO STAU CORD QTZ H2O
165) PLG ILM GARNET BIO CORD sill QTZ H2O = PLG ILM GARNET BIO CORD LIQ QTZ H2O
166) PLG ILM GARNET BIO STAU CORD QTZ H2O = PLG ILM GARNET BIO CORD sill QTZ H2O
167) PLG ILM GARNET BIO STAU CORD sill QTZ H2O = PLG ILM GARNET BIO CORD sill QTZ H2O
168) PLG ILM GARNET BIO STAU CORD sill QTZ H2O = PLG ILM GARNET BIO CORD sill QTZ H2O
169) PLG ILM GARNET BIO STAU CORD QTZ H2O = PLG ILM GARNET BIO STAU CORD sill QTZ H2O
170) PLG ILM GARNET BIO STAU CORD QTZ H2O = PLG ILM GARNET BIO STAU CORD sill QTZ H2O
171) PLG ILM GARNET BIO STAU CORD QTZ H2O = PLG ILM GARNET BIO sill QTZ H2O
172) PLG ILM GARNET CHLR PHNG BIO ma QTZ H2O = PLG ILM CHLR PHNG BIO STAU QTZ H2O
173) ILM GARNET CORD LIQ H2O = ILM GARNET SPIN LIQ H2O
174) ILM GARNET PHNG BIO STAU zo QTZ H2O = PLG ILM GARNET (2)PHNG BIO STAU QTZ H2O
175) ILM GARNET PHNG BIO STAU zo QTZ H2O = PLG ILM GARNET (2)PHNG BIO STAU QTZ H2O
176) PLG ILM GARNET CHLR BIO STAU QTZ H2O = PLG ILM GARNET BIO STAU CORD QTZ H2O
177) PLG ILM GARNET CHLR BIO STAU QTZ H2O = PLG ILM GARNET CHLR BIO STAU CORD QTZ H2O
178) PLG ILM GARNET CHLR BIO STAU CORD QTZ H2O = PLG ILM GARNET BIO STAU CORD QTZ H2O
179) PLG ILM CHLR PHNG BIO STAU and QTZ H2O = PLG ILM CHLR BIO STAU and QTZ H2O
180) PLG ILM CHLR PHNG BIO STAU QTZ H2O = PLG ILM CHLR PHNG BIO STAU and QTZ H2O
181) PLG ILM CHLR BIO STAU QTZ H2O = PLG ILM GARNET CHLR BIO STAU CORD QTZ H2O
182) PLG ILM GARNET CHLR BIO STAU CORD QTZ H2O = PLG ILM GARNET BIO STAU CORD QTZ H2O
183) PLG ILM GARNET BIO CORD LIQ QTZ H2O = PLG ILM GARNET OPX BIO CORD LIQ H2O

184) PLG ILM CHLR BIO STAU CORD QTZ H2O = PLG ILM GARNET BIO STAU CORD QTZ H2O
185) PLG ILM GARNET CHLR BIO STAU CORD QTZ H2O = PLG ILM GARNET BIO STAU CORD QTZ H2O
186) PLG ILM CHLR BIO STAU CORD QTZ H2O = PLG ILM GARNET CHLR BIO STAU CORD QTZ H2O
187) PLG ILM GARNET BIO STAU CORD QTZ H2O = PLG ILM GARNET BIO CORD sill QTZ H2O
188) ILM CHLR (2)PHNG BIO zo sph QTZ H2O = PLG ILM CHLR (2)PHNG BIO zo QTZ H2O
189) PLG ILM GARNET CHLR PHNG BIO zo QTZ H2O = PLG ILM CHLR PHNG BIO ma QTZ H2O
190) PLG ILM CHLR PHNG BIO zo ma QTZ H2O = PLG ILM CHLR PHNG BIO ma QTZ H2O
191) PLG ILM GARNET CHLR PHNG BIO zo QTZ H2O = PLG ILM CHLR PHNG BIO zo ma QTZ H2O
192) ILM GARNET CORD LIQ cor H2O = ILM GARNET CORD LIQ H2O
193) ILM GARNET LIQ cor H2O = ILM GARNET CORD LIQ cor H2O
194) PLG ILM GARNET BIO STAU QTZ H2O = PLG ILM GARNET BIO STAU sill QTZ H2O
195) PLG ILM GARNET BIO STAU sill QTZ H2O = PLG ILM GARNET BIO sill QTZ H2O
196) PLG ILM GARNET BIO STAU CORD QTZ H2O = PLG ILM GARNET BIO CORD sill QTZ H2O
197) PLG ILM GARNET BIO STAU CORD sill QTZ H2O = PLG ILM GARNET BIO CORD sill QTZ H2O
198) PLG ILM GARNET BIO STAU CORD QTZ H2O = PLG ILM GARNET BIO STAU CORD sill QTZ H2O
199) PLG ILM CHLR BIO STAU CORD QTZ H2O = PLG ILM GARNET BIO STAU CORD QTZ H2O
200) PLG ILM CHLR BIO STAU CORD QTZ H2O = PLG ILM GARNET BIO CORD QTZ H2O
201) PLG ILM GARNET CHLR BIO STAU QTZ H2O = PLG ILM GARNET BIO STAU CORD QTZ H2O
202) PLG ILM GARNET CHLR BIO STAU CORD QTZ H2O = PLG ILM GARNET BIO STAU CORD QTZ H2O
203) PLG ILM GARNET CHLR BIO STAU QTZ H2O = PLG ILM GARNET CHLR BIO STAU CORD QTZ H2O
204) PLG ILM GARNET CORD LIQ H2O = PLG ILM CORD SPIN LIQ H2O
205) PLG ILM GARNET BIO STAU CORD QTZ H2O = PLG ILM GARNET BIO STAU CORD sill QTZ H2O
206) PLG ILM GARNET BIO STAU CORD sill QTZ H2O = PLG ILM GARNET BIO CORD sill QTZ H2O
207) ILM GARNET CORD SPIN LIQ H2O = ILM CORD SPIN LIQ
208) ILM GARNET CHLR (2)PHNG BIO zo QTZ H2O = PLG ILM GARNET CHLR PHNG BIO QTZ H2O
209) ILM GARNET CORD LIQ cor H2O = PLG ILM GARNET CORD LIQ cor H2O
210) ILM GARNET CORD LIQ cor H2O = ILM GARNET LIQ H2O
211) ILM CHLR (2)PHNG sph QTZ H2O = ILM CHLR (2)PHNG BIO zo sph QTZ H2O
212) ILM GARNET CHLR (2)PHNG BIO zo QTZ H2O = PLG ILM GARNET CHLR PHNG BIO STAU QTZ H2O
213) PLG ILM GARNET CHLR BIO STAU QTZ H2O = PLG ILM GARNET BIO STAU CORD QTZ H2O
214) PLG ILM GARNET BIO STAU CORD QTZ H2O = PLG ILM GARNET BIO CORD sill QTZ H2O
215) PLG ILM GARNET PHNG BIO STAU zo QTZ H2O = PLG ILM GARNET (2)PHNG BIO STAU QTZ H2O
216) ILM GARNET PHNG BIO STAU zo QTZ H2O = PLG ILM GARNET PHNG BIO STAU zo QTZ H2O

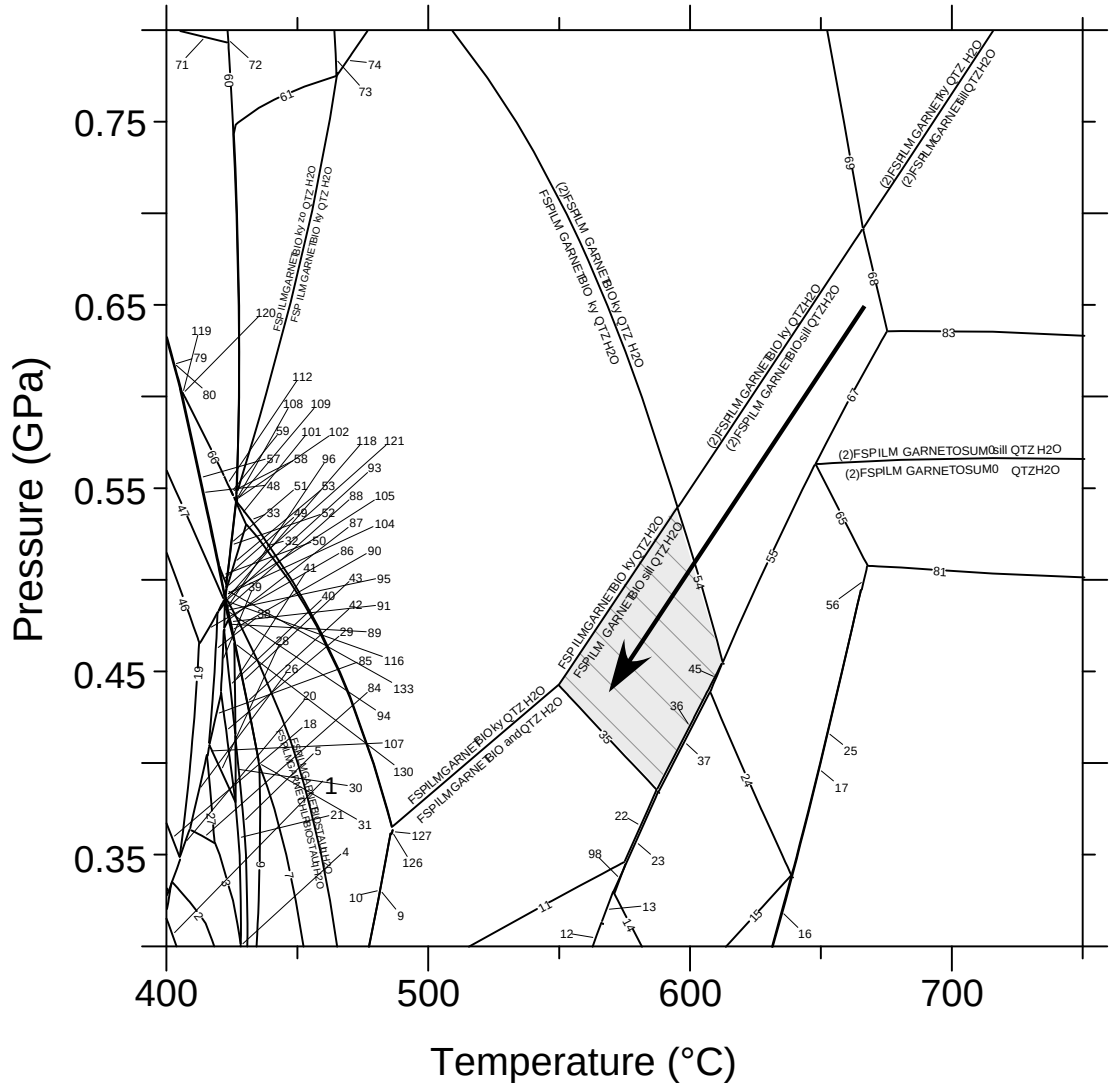

Figure 3.9: Pseudosection with water pressure equal to 0.3 of teh lithostatic pressure of sample 07B148A. The numbers
represent reactions described on next page. The grey field reproduces the mineralogy in the sample. The black arrow indicates a possible decompression paths for the rock. See text for discussion.

Figure 3.9 (Continued)

Reactions:

1) FSP ILM CHLR PHNG BIO QTZ H2O = FSP ILM CHTD CHLR PHNG BIO QTZ H2O
2) FSP ILM CHTD CHLR PHNG BIO QTZ H2O = FSP ILM CHTD CHLR (2)PHNG BIO QTZ H2O
3) FSP ILM CHTD CHLR PHNG BIO QTZ H2O = FSP ILM CHTD CHLR (2)PHNG BIO QTZ H2O
4) FSP ILM CHTD CHLR (2)PHNG BIO QTZ H2O = FSP ILM CHTD CHLR PHNG BIO STAU QTZ H2O
5) FSP ILM CHTD CHLR PHNG BIO STAU QTZ H2O = FSP ILM CHTD CHLR BIO STAU QTZ H2O
6) FSP ILM CHTD CHLR BIO STAU QTZ H2O = FSP ILM CHLR BIO STAU QTZ H2O
7) FSP ILM CHLR BIO STAU QTZ H2O = FSP ILM GARNET CHLR BIO STAU QTZ H2O
8) FSP ILM GARNET CHLR BIO STAU QTZ H2O = FSP ILM GARNET BIO STAU QTZ H2O
9) FSP ILM GARNET BIO STAU QTZ H2O = FSP ILM GARNET BIO STAU and QTZ H2O
10) FSP ILM GARNET BIO STAU and QTZ H2O = FSP ILM GARNET BIO and QTZ H2O
11) FSP ILM GARNET BIO and QTZ H2O = FSP ILM GARNET BIO CORD and QTZ H2O
12) FSP ILM GARNET BIO CORD and QTZ H2O = FSP ILM GARNET BIO CORD OSUM0 QTZ H2O
13) FSP ILM GARNET BIO CORD and QTZ H2O = FSP ILM GARNET BIO CORD OSUM0 QTZ H2O
14) FSP ILM GARNET BIO CORD OSUM0 QTZ H2O = FSP ILM GARNET BIO OSUM0 QTZ H2O
15) FSP ILM GARNET BIO OSUM0 QTZ H2O = FSP ILM GARNET OPX BIO OSUM0 QTZ H2O
16) FSP ILM GARNET OPX BIO OSUM0 QTZ H2O = (2)FSP ILM GARNET OPX BIO OSUM0 QTZ H2O
17) (2)FSP ILM GARNET OPX BIO OSUM0 QTZ H2O = (2)FSP ILM GARNET OPX OSUM0 QTZ H2O
18) ILM CHTD CHLR PHNG BIO zo QTZ H2O = ILM CHTD CHLR (2)PHNG BIO zo QTZ H2O
19) ILM CHTD CHLR PHNG BIO zo QTZ H2O = FSP ILM CHTD CHLR PHNG BIO zo QTZ H2O
20) FSP ILM CHTD CHLR PHNG BIO zo QTZ H2O = FSP ILM CHTD CHLR (2)PHNG BIO QTZ H2O
21) FSP ILM CHTD CHLR PHNG BIO QTZ H2O = FSP ILM CHTD CHLR PHNG BIO STAU QTZ H2O
22) FSP ILM GARNET BIO and QTZ H2O = FSP ILM GARNET BIO OSUM0 and QTZ H2O
23) FSP ILM GARNET BIO OSUM0 and QTZ H2O = FSP ILM GARNET BIO OSUM0 QTZ H2O
24) (2)FSP ILM GARNET BIO OSUM0 QTZ H2O = FSP ILM GARNET BIO OSUM0 QTZ H2O
25) (2)FSP ILM GARNET BIO OSUM0 QTZ H2O = (2)FSP ILM GARNET OPX BIO OSUM0 QTZ H2O
26) FSP ILM CHTD CHLR PHNG BIO zo QTZ H2O = FSP ILM CHTD CHLR PHNG BIO ma QTZ H2O
27) FSP ILM CHTD CHLR PHNG BIO ma QTZ H2O = FSP ILM CHTD CHLR PHNG BIO QTZ H2O
28) FSP ILM CHTD PHNG BIO QTZ H2O = FSP ILM CHTD CHLR PHNG BIO QTZ H2O
29) FSP ILM CHTD PHNG BIO STAU QTZ H2O = FSP ILM CHTD PHNG BIO QTZ H2O
30) FSP ILM CHTD PHNG BIO STAU QTZ H2O = FSP ILM CHTD CHLR PHNG BIO STAU QTZ H2O
31) FSP ILM CHTD CHLR BIO STAU QTZ H2O = FSP ILM GARNET CHLR BIO STAU QTZ H2O
32) FSP ILM GARNET BIO STAU QTZ H2O = FSP ILM GARNET BIO STAU ky QTZ H2O
33) FSP ILM GARNET BIO STAU ky QTZ H2O = FSP ILM GARNET BIO ky QTZ H2O
34) FSP ILM GARNET BIO ky QTZ H2O = FSP ILM GARNET BIO and QTZ H2O
35) FSP ILM GARNET BIO sill QTZ H2O = FSP ILM GARNET BIO and QTZ H2O
36) FSP ILM GARNET BIO sill QTZ H2O = FSP ILM GARNET BIO OSUM0 sill QTZ H2O
37) FSP ILM GARNET BIO OSUM0 sill QTZ H2O = FSP ILM GARNET BIO OSUM0 QTZ H2O
38) FSP ILM CHTD CHLR PHNG BIO zo QTZ H2O = FSP ILM CHTD PHNG BIO zo QTZ H2O
39) FSP ILM CHTD PHNG BIO zo QTZ H2O = FSP ILM CHTD PHNG BIO STAU QTZ H2O
40) FSP ILM CHTD PHNG BIO STAU QTZ H2O = FSP ILM CHTD BIO STAU QTZ H2O
41) FSP ILM CHTD BIO STAU QTZ H2O = FSP ILM CHTD CHLR BIO STAU QTZ H2O
42) FSP ILM GARNET CHTD CHLR BIO STAU QTZ H2O = FSP ILM CHTD CHLR BIO STAU QTZ H2O
43) FSP ILM GARNET CHLR BIO STAU QTZ H2O = FSP ILM GARNET CHTD CHLR BIO STAU QTZ H2O
44) FSP ILM GARNET BIO ky QTZ H2O = FSP ILM GARNET BIO sill QTZ H2O
45) FSP ILM GARNET BIO OSUM0 sill QTZ H2O = (2)FSP ILM GARNET BIO OSUM0 QTZ H2O
46) ILM CHTD CHLR PHNG BIO zo QTZ H2O = ILM GARNET CHTD CHLR PHNG BIO zo QTZ H2O
47) ILM GARNET CHTD CHLR PHNG BIO zo QTZ H2O = ILM GARNET CHTD PHNG BIO zo QTZ H2O
48) ILM GARNET CHTD PHNG BIO zo QTZ H2O = ILM GARNET CHTD PHNG BIO STAU zo QTZ H2O
49) ILM GARNET CHTD PHNG BIO STAU zo QTZ H2O = ILM GARNET CHLR PHNG BIO STAU zo QTZ H2O
50) ILM GARNET CHLR PHNG BIO STAU zo QTZ H2O = ILM GARNET PHNG BIO STAU zo QTZ H2O
51) ILM GARNET PHNG BIO STAU zo QTZ H2O = FSP ILM GARNET PHNG BIO STAU zo QTZ H2O
52) FSP ILM GARNET PHNG BIO STAU zo QTZ H2O = FSP ILM GARNET BIO STAU zo QTZ H2O
53) FSP ILM GARNET BIO STAU zo QTZ H2O = FSP ILM GARNET BIO STAU QTZ H2O
54) FSP ILM GARNET BIO sill QTZ H2O = (2)FSP ILM GARNET BIO sill QTZ H2O
55) (2)FSP ILM GARNET BIO sill QTZ H2O = (2)FSP ILM GARNET BIO OSUM0 QTZ H2O
56) (2)FSP ILM GARNET BIO OSUM0 QTZ H2O = (2)FSP ILM GARNET OPX OSUM0 QTZ H2O
57) ILM GARNET CHTD PHNG BIO STAU zo QTZ H2O = ILM GARNET PHNG BIO STAU zo QTZ H2O
58) ILM GARNET PHNG BIO STAU zo QTZ H2O = ILM GARNET PHNG BIO STAU ky zo QTZ H2O

59) ILM GARNET PHNG BIO STAU ky zo QTZ H2O = ILM GARNET PHNG BIO ky zo QTZ H2O
60) ILM GARNET PHNG BIO ky zo QTZ H2O = FSP ILM GARNET PHNG BIO ky zo QTZ H2O
61) FSP ILM GARNET PHNG BIO ky zo QTZ H2O = FSP ILM GARNET BIO ky zo QTZ H2O
62) FSP ILM GARNET BIO ky zo QTZ H2O = FSP ILM GARNET BIO ky QTZ H2O
63) FSP ILM GARNET BIO ky QTZ H2O = (2)FSP ILM GARNET BIO ky QTZ H2O
64) (2)FSP ILM GARNET BIO ky QTZ H2O = (2)FSP ILM GARNET BIO sill QTZ H2O
65) (2)FSP ILM GARNET BIO OSUM0 QTZ H2O = (2)FSP ILM GARNET OSUM0 QTZ H2O
66) ILM GARNET PHNG BIO STAU zo QTZ H2O = ILM GARNET PHNG BIO ky zo QTZ H2O
67) (2)FSP ILM GARNET BIO sill QTZ H2O = (2)FSP ILM GARNET OSUM0 sill QTZ H2O
68) (2)FSP ILM GARNET BIO sill QTZ H2O = (2)FSP ILM GARNET sill QTZ H2O
69) (2)FSP ILM GARNET BIO ky QTZ H2O = (2)FSP ILM GARNET ky QTZ H2O
70) (2)FSP ILM GARNET ky QTZ H2O = (2)FSP ILM GARNET sill QTZ H2O
71) ILM GARNET (2)PHNG BIO ky zo QTZ H2O = ILM GARNET PHNG BIO ky zo QTZ H2O
72) ILM GARNET (2)PHNG BIO ky zo QTZ H2O = FSP ILM GARNET PHNG BIO ky zo QTZ H2O
73) FSP ILM GARNET PHNG BIO ky zo QTZ H2O = FSP ILM GARNET PHNG BIO ky QTZ H2O
74) FSP ILM GARNET PHNG BIO ky QTZ H2O = FSP ILM GARNET BIO ky QTZ H2O
75) FSP ILM CHTD CHLR PHNG BIO zo QTZ H2O = FSP ILM CHTD CHLR PHNG BIO QTZ H2O
76) FSP ILM CHLR (2)PHNG BIO zo QTZ H2O = FSP ILM CHTD CHLR PHNG BIO zo QTZ H2O
77) ILM CHLR (2)PHNG BIO zo QTZ H2O = FSP ILM CHLR (2)PHNG BIO zo QTZ H2O
78) ILM CHTD CHLR (2)PHNG BIO zo QTZ H2O = ILM CHLR (2)PHNG BIO zo QTZ H2O
79) ILM GARNET CHTD PHNG BIO ky zo QTZ H2O = ILM GARNET CHTD PHNG BIO zo QTZ H2O
80) ILM GARNET PHNG BIO ky zo QTZ H2O = ILM GARNET CHTD PHNG BIO ky zo QTZ H2O
81) (2)FSP ILM GARNET OSUM0 QTZ H2O = (2)FSP ILM GARNET OPX OSUM0 QTZ H2O
82) (2)FSP ILM GARNET OSUM0 sill QTZ H2O = (2)FSP ILM GARNET OSUM0 QTZ H2O
83) (2)FSP ILM GARNET sill QTZ H2O = (2)FSP ILM GARNET OSUM0 sill QTZ H2O
84) FSP ILM CHTD CHLR PHNG BIO ma QTZ H2O = FSP ILM CHTD CHLR (2)PHNG BIO QTZ H2O
85) FSP ILM CHTD PHNG BIO zo QTZ H2O = FSP ILM CHTD PHNG BIO QTZ H2O
86) ILM GARNET CHTD CHLR PHNG BIO zo QTZ H2O = FSP ILM CHTD CHLR PHNG BIO zo QTZ H2O
87) FSP ILM CHTD PHNG BIO zo QTZ H2O = FSP ILM CHTD BIO STAU zo QTZ H2O
88) FSP ILM CHTD PHNG BIO zo QTZ H2O = FSP ILM CHTD BIO STAU zo QTZ H2O
89) FSP ILM CHTD BIO STAU zo QTZ H2O = FSP ILM CHTD BIO STAU QTZ H2O
90) FSP ILM CHTD BIO STAU QTZ H2O = FSP ILM GARNET CHTD BIO STAU QTZ H2O
91) FSP ILM GARNET CHTD BIO STAU QTZ H2O = FSP ILM GARNET CHTD CHLR BIO STAU QTZ H2O
92) ILM CHTD CHLR (2)PHNG BIO zo QTZ H2O = FSP ILM CHTD CHLR (2)PHNG BIO QTZ H2O
93) ILM GARNET CHTD CHLR PHNG BIO zo QTZ H2O = FSP ILM GARNET CHTD PHNG BIO zo QTZ H2O
94) FSP ILM GARNET CHTD PHNG BIO zo QTZ H2O = FSP ILM CHTD PHNG BIO zo QTZ H2O
95) FSP ILM CHTD BIO STAU zo QTZ H2O = FSP ILM GARNET CHTD BIO STAU zo QTZ H2O
96) FSP ILM GARNET CHTD BIO STAU zo QTZ H2O = FSP ILM GARNET CHTD BIO STAU QTZ H2O
97) FSP ILM GARNET BIO STAU QTZ H2O = FSP ILM GARNET BIO and QTZ H2O
98) FSP ILM GARNET BIO CORD and QTZ H2O = FSP ILM GARNET BIO OSUM0 and QTZ H2O
99) FSP ILM GARNET BIO CORD OSUM0 and QTZ H2O = FSP ILM GARNET BIO CORD OSUM0 QTZ H2O
100) FSP ILM GARNET BIO CORD and QTZ H2O = FSP ILM GARNET BIO CORD OSUM0 and QTZ H2O
101) FSP ILM GARNET BIO STAU zo QTZ H2O = FSP ILM GARNET BIO STAU ky QTZ H2O
102) ILM GARNET PHNG BIO STAU zo QTZ H2O = ILM GARNET PHNG BIO ky zo QTZ H2O
103) ILM CHTD CHLR (2)PHNG BIO zo QTZ H2O = FSP ILM CHTD CHLR PHNG BIO zo QTZ H2O
104) ILM GARNET CHLR PHNG BIO STAU zo QTZ H2O = FSP ILM GARNET PHNG BIO STAU QTZ H2O
105) FSP ILM GARNET PHNG BIO STAU QTZ H2O = FSP ILM GARNET BIO STAU QTZ H2O
106) ILM GARNET CHTD PHNG BIO zo QTZ H2O = FSP ILM GARNET CHTD PHNG BIO zo QTZ H2O
107) FSP ILM CHTD CHLR PHNG BIO QTZ H2O = FSP ILM CHTD CHLR PHNG BIO zo QTZ H2O
108) FSP ILM GARNET PHNG BIO ky zo QTZ H2O = FSP ILM GARNET PHNG BIO ky QTZ H2O
109) FSP ILM GARNET PHNG BIO ky QTZ H2O = FSP ILM GARNET BIO ky QTZ H2O
110) FSP ILM CHTD PHNG BIO STAU zo QTZ H2O = FSP ILM CHTD BIO STAU zo QTZ H2O
111) FSP ILM CHTD PHNG BIO zo QTZ H2O = FSP ILM CHTD PHNG BIO STAU zo QTZ H2O
112) ILM GARNET PHNG BIO STAU zo QTZ H2O = ILM GARNET PHNG BIO ky zo QTZ H2O
113) ILM GARNET PHNG BIO STAU zo QTZ H2O = ILM GARNET PHNG BIO STAU ky zo QTZ H2O
114) ILM GARNET PHNG BIO ky zo QTZ H2O = ILM GARNET PHNG BIO STAU ky zo QTZ H2O
115) FSP ILM CHTD PHNG BIO STAU QTZ H2O = FSP ILM CHTD CHLR BIO STAU QTZ H2O
116) FSP ILM GARNET CHTD PHNG BIO zo QTZ H2O = FSP ILM GARNET CHTD BIO STAU zo QTZ H2O
117) FSP ILM GARNET CHTD BIO STAU QTZ H2O = FSP ILM GARNET CHLR BIO STAU QTZ H2O
118) FSP ILM GARNET CHTD BIO STAU QTZ H2O = FSP ILM GARNET CHLR BIO STAU QTZ H2O
119) ILM GARNET PHNG BIO STAU zo QTZ H2O = ILM GARNET PHNG BIO STAU ky zo QTZ H2O
120) ILM GARNET PHNG BIO STAU ky zo QTZ H2O = ILM GARNET PHNG BIO ky zo QTZ H2O
121) ILM GARNET CHLR PHNG BIO STAU zo QTZ H2O = FSP ILM GARNET PHNG BIO STAU zo QTZ H2O
122) FSP ILM GARNET PHNG BIO ky zo QTZ H2O = FSP ILM GARNET BIO ky QTZ H2O

123) FSP ILM GARNET BIO OSUM0 QTZ H2O = (2)FSP ILM GARNET OPX BIO OSUM0 QTZ H2O
124) FSP ILM GARNET BIO and QTZ H2O = FSP ILM GARNET BIO OSUM0 sill QTZ H2O
125) FSP ILM CHTD CHLR PHNG BIO zo QTZ H2O = FSP ILM CHTD PHNG BIO QTZ H2O
126) FSP ILM GARNET BIO STAU QTZ H2O = FSP ILM GARNET BIO STAU and QTZ H2O
127) FSP ILM GARNET BIO STAU and QTZ H2O = FSP ILM GARNET BIO and QTZ H2O
128) FSP ILM CHTD PHNG BIO STAU zo QTZ H2O = FSP ILM CHTD PHNG BIO zo QTZ H2O
129) FSP ILM CHTD PHNG BIO STAU zo QTZ H2O = FSP ILM CHTD PHNG BIO STAU QTZ H2O
130) FSP ILM CHTD BIO STAU QTZ H2O = FSP ILM GARNET CHTD CHLR BIO STAU QTZ H2O
131) ILM GARNET CHTD PHNG BIO STAU zo QTZ H2O = ILM GARNET CHTD PHNG BIO ky zo QTZ H2O
132) ILM GARNET PHNG BIO ky zo QTZ H2O = ILM GARNET PHNG BIO STAU zo QTZ H2O
133) ILM GARNET CHLR PHNG BIO STAU zo QTZ H2O = FSP ILM GARNET BIO STAU zo QTZ H2O
134) (2)FSP ILM GARNET BIO ky QTZ H2O = (2)FSP ILM GARNET sill QTZ H2O
135) FSP ILM CHTD BIO STAU zo QTZ H2O = FSP ILM GARNET CHTD BIO STAU QTZ H2O
136) ILM GARNET CHTD PHNG BIO STAU zo QTZ H2O = FSP ILM GARNET CHLR PHNG BIO STAU QTZ H2O
137) FSP ILM GARNET CHLR PHNG BIO STAU QTZ H2O = FSP ILM GARNET PHNG BIO STAU QTZ H2O
138) FSP ILM GARNET BIO OSUM0 and QTZ H2O = FSP ILM GARNET BIO OSUM0 sill QTZ H2O
139) FSP ILM GARNET PHNG BIO STAU zo QTZ H2O = FSP ILM GARNET PHNG BIO ky QTZ H2O
140) FSP ILM GARNET PHNG BIO ky QTZ H2O = FSP ILM GARNET BIO STAU ky QTZ H2O
141) FSP ILM GARNET BIO sill QTZ H2O = (2)FSP ILM GARNET BIO OSUM0 QTZ H2O
142) ILM GARNET CHTD CHLR PHNG BIO zo QTZ H2O = FSP ILM CHTD PHNG BIO zo QTZ H2O
143) FSP ILM CHTD PHNG BIO zo QTZ H2O = FSP ILM CHTD BIO STAU QTZ H2O
144) ILM GARNET CHLR PHNG BIO STAU zo QTZ H2O = FSP ILM GARNET BIO STAU zo QTZ H2O
145) FSP ILM GARNET PHNG BIO STAU zo QTZ H2O = FSP ILM GARNET BIO STAU zo QTZ H2O
146) ILM GARNET CHLR PHNG BIO STAU zo QTZ H2O = FSP ILM GARNET PHNG BIO STAU zo QTZ H2O
147) ILM GARNET PHNG BIO STAU zo QTZ H2O = ILM GARNET PHNG BIO ky zo QTZ H2O
148) ILM GARNET PHNG BIO STAU ky zo QTZ H2O = ILM GARNET PHNG BIO STAU zo QTZ H2O
149) ILM GARNET PHNG BIO ky zo QTZ H2O = ILM GARNET PHNG BIO STAU ky zo QTZ H2O
150) FSP ILM GARNET CHTD CHLR BIO STAU QTZ H2O = FSP ILM GARNET CHTD BIO STAU QTZ H2O
151) FSP ILM GARNET CHLR BIO STAU QTZ H2O = FSP ILM GARNET CHTD CHLR BIO STAU QTZ H2O

5-25% when compared to the modes in the actual rock. Quartz and garnet have the largest difference and are off by more than 25% of the actual mode for quartz and garnet. The composition of the minerals obtained by the program in the field of equilibrium does not reproduce the compositions of the minerals obtained with the electron microprobe. The discrepancies can be explained by a combination of errors in the mixing models of the minerals; the presence of more variables not introduced in the calculations, such as Mn within the garnet; non-equilibrium composition of the minerals in the rock; composition of minerals in the rock affected by retrograde reactions. There is also error in the estimation of the bulk composition of the rock when using microprobe data of individual minerals.

VI.B. Summary and discussion of geothermobarometry

The resulting pressures obtained for the intrusion of the Kitlope and Quottoon plutons is between 0.75 to 0.65 GPa (Figure 3.5). These pressure differences are within the calibration error of the barometers used and suggest little pressure difference between the two areas. The Chief Matthew's pluton records lower pressures ranging from 0.65-0.5 GPa. This result shows that ~0.2 GPa decompression occurred between the intrusion of the plutons at a rate of 2-3 mm/yr.

The country-rocks give peak temperatures consistent with those obtained from the plutons, which either indicates efficient heating by the plutons or that the rocks were already hot at the time the plutons were emplaced. We favor the second argument for the country rocks at Gardner Canal, given that the mineralogy and textures of the rocks indicates hot conditions were present for long enough times to completely recrystallize the

rocks. Also, rocks showing amphibolite grade metamorphism are widespread in the central gneiss complex, and record a long-lived history of plutonism as indicated by the abundance of orthogneiss and zircon ages which span 100 Ma. This argues for a regional long-lived thermal pulse, instead of contact metamorphism associated with individual plutonic intrusions. A regional thermal pulse can be achieved by overlapping aureoles in area with widespread magmatism (Den Tex 1963), producing a “regional aureole” metamorphism.

The pegmatitic dikes intruded late in the cooling history of the plutons. Of the two analyzed dikes, one intrudes the Kitlope pluton and the other intrudes the Quottoon pluton. Both dikes show lower temperature but the same pressure of the plutons that they are associated with. This indicates some cooling of the plutons prior to the intrusion of the pegmatitic dikes. It also correlates with the fact that one dike contains muscovite.

Sample 07B148A gives important information about the possible decompression paths followed by the rocks (Figure 3.8 and 3.9). The rock has neither cordierite nor andalusite implying that the post peak decompression path involved significant cooling before the rocks got below 0.4 GPa. A higher rate of cooling relative to decompression is confirmed by the fact that there are no rocks with textural evidence for rapid isothermal decompression. This contrasts strongly with rocks found in other parts of the central gneiss complex to the north which contain abundant cordierite coronas around garnet, orthopyroxene and plagioclase symplectites rimming garnet, sillimanite replacing kyanite, and veins which contain andalusite (Selverstone and Hollister 1980, Hollister 1982, Kenah and Hollister 1983, Whitney et al 1999). These observations suggest the decompression path at Gardner Canal could

not have been steeper than ~8^{o}C/km. However, several samples in the area show plagioclase rimming garnet (e.g. Figure 3.3c). This texture has been frequently related to decompression (Wernike and Getty 1997, Whitney 1992). However, Stowell and Stein (2005) described similar textures as indicators of progressive metamorphism. In their study in the Cascade ranges they interpret the rimming plagioclase as a relic of primary igneous plagioclase, based on zoning profiles, and growth of garnet by the consumption of chlorite in a prograde path. At Gardner Canal, the rocks that show plagioclase coronas around garnet have both igneous and sedimentary protoliths. We were unable to obtain precise calculations of pressure or temperature for these samples due to disequilibrium in the mineral assemblages. Therefore, we are unable to unravel how the textures were formed.

VII. Cooling ages

Cooling ages were compiled from the literature. We also include unpublished ages from work in preparation (Wanless 1970-1979, Van der Heyden 1989, Friedman and Ullrich, 2007, Friedman 2007, Gehrels et al in revision, Chang and Andronicos in revision).

New ^{40}Ar/^{39}Ar geochronology analyses were obtained at the New Mexico Geochronology Research Laboratory, New Mexico Bureau of Geology and Mineral Resources, Socorro New Mexico under the direction of Matt Heizler. All samples were analyzed using the incremental step-heating approach using either a double-vacuum Mo resistance furnace or a CO_2 laser to heat the samples. Table 3.4 shows the compiled data and the references. Table 3.5 presents the closure temperature used for the different minerals. Figure 3.10 shows the distribution of the ages in the map. The ages were

Table 3.4: Cooling Ages

Sample	Latitude	Longitude	Lithology	Age	Error	Mineral	Method	Ref
Mount Gamsby								
			Diorite	188.1	3.3	ZIRCON	U-PB	6
			Tonalite	155.3	2.7	ZIRCON	U-PB	6
34-JBM-06	53.1702	-127.673	Diorite	138	1.8	ZIRCON	U-PB	4
05B13B			Schist	63.93	0.1	MUSC	AR-AR	7
60-JBM-05	53.2298	-127.734	Granite	61.87	0.34	BIOTITE	AR-AR	3
05B65				54.45	0.12	BIOTITE	AR-AR	7
Kitlope Lake								
MT05-137	53.0852	-127.795	Granodiorite	61.1	1.2	ZIRCON	U-PB	2
MT05-137	53.0852	-127.795	Granodiorite	62.5	1.3	TITANITE	MC-ICP-MS	2
06B38			Granodiorite	55.53	0.12	HBL	AR-AR	7
06B38			Granodiorite	51.23	0.12	BIOTITE	AR-AR	7
06B69			Granodiorite	52.76	0.11	BIOTITE	AR-AR	7
77-WV-340	53.0540	-127.719		52.7	2.3	BIOTITE	K/Ar	5
05MR06				51.6	0.1	BIOTITE	AR-AR	7
Tsaytis Pluton								
84-JBM-06	53.3683	-127.879	Megacryst	56.8	3.4	ZIRCON	U-PB	1
84-V-98	53.3424	-127.797	Granodiorite	54.9	0.2	ZIRCON	U-PB	1
77-WV-261	53.3442	-127.795	Granodiorite	50	2.9	HBL	AR-AR	5
GSC78-66	53.3424	-127.797		50	1.5	HBL		5
GSC78-66	53.3424	-127.797		51.4	1.2	BIOTITE		5
Chief Matthew's Pluton								
MT05-136	53.3744	128.020	Tonalite	58.2	0.9	ZIRCON		2
GJP-77	53.4133	-128.091	Granodiorite	55.6	0.9	ZIRCON	MC-ICP-MS	2
GJP-77	53.4133	-128.091	Granodiorite	53	2.2	TITANITE	MC-ICP-MS	2
79-WV-654	53.3367	-127.946	Granodiorite	53	1.9	HBL	AR-AR	1
79-WV-654	53.3367	-127.946	Granodiorite	49.9	1.7	BIOTITE		1
Quottoon Pluton								
GJP-79	53.4702	-128.234	Tonalite	59.5	1.6	ZIRCON	MC-ICP-MS	2
GJP-79	53.4702	-128.234	Tonalite	59.6	3.5	TITANITE	MC-ICP-MS	2
GSC67-25				50	2	BIOTITE		5
Kemano Bay								
GJP-78	53.4777	-128.168	Orthogneiss	57.6	2.8	ZIRCON	MC-ICP-MS	2
GJP-78	53.4777	-128.168	Orthogneiss	96.8	2.1	ZIRCON	MC-ICP-MS	2
MT05-135	53.4367	128.087	Orthogneiss	52.6	1.4	ZIRCON	MC-ICP-MS	2
MT05-135	53.4367	128.087	Orthogneiss	125.4	3.3	ZIRCON	MC-ICP-MS	2
GJP-78	53.4777	-128.168	Orthogneiss	52.4	2.1	TITANITE	MC-ICP-MS	2
MT05-135	53.4367	128.087	Orthogneiss	49.9	1.4	TITANITE	MC-ICP-MS	2
78-WV-348	53.5656	-127.960	Diorite	52	1.8	BIOTITE	AR-AR	1
78-WV-342	53.5712	-128.009	Granodiorite	51.3	1.8	BIOTITE	AR-AR	1

Table 3.4 (Continued)

References:

1 .Van de Heyden 1989
2 .Gehrels 2008
3 .Friedman and Ullrich 2007
4 .Friedman 2007
5 .Wanless 1970-79
6 .Chang and Andronicos in revision
7 .This study

Table 3.5: Closure temperatures of minerals

Mineral	Cooling temperature (℃)	Reference
Zircon	750 - 800	Spear 1992
Titanite	660	Frost et al 2001
Hornblende	550	Harrison 1981
Muscovite	350	Hames and Bowring 1994
Biotite	300	Dunlap 2000

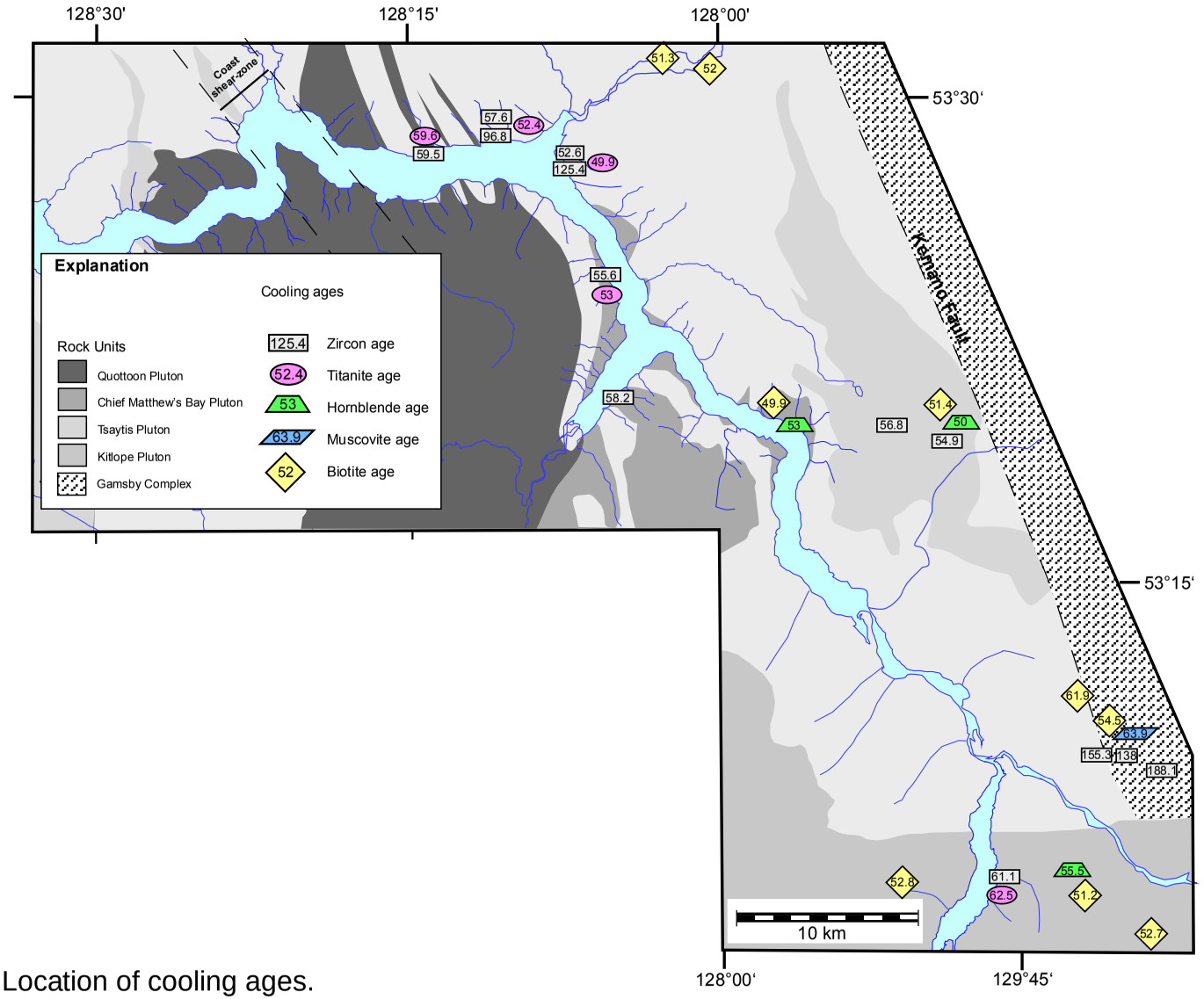

Figure 3.10: Location of cooling ages.

separated into five groups representing different plutons, including the Tsaytis pluton and associated country-rocks.

Figure 3.11 shows the cooling curves associated with the different plutons. The cooling history for rocks in the Gamsby Complex is older (Early Cretaceous, Van der Heyden 1989) when compared to the other plutons. The young muscovite and biotite ages in the area are explained by reheating the Gamsby Complex by the later Paleocene intrusions (Van der Heyden 1989). Mt. Gamsby is part of the Gamsby Complex and cooled following an isobaric cooling trend in the Cretaceous (Chang and Andronicos in revision).

The other plutons of the central gneiss complex show a complex cooling history as observed in Figure 3.11. If we assume a linear trend, the Kitlope and Quottoon plutons show slightly slower cooling rates of ~40℃/Ma. The Chief Matthew's and Tsaytis plutons have cooling rates of ~60℃/Ma. The Kitlope pluton is the oldest pluton and also the one with the oldest cooling ages. By ~52 Ma, this pluton was already at 300℃. The Quottoon, Chief Matthew's and Tsaytis plutons all cooled down to 300℃ by ~51 Ma.

Kitlope and Quottoon plutons have titanite ages that are older than the zircon ages. Titanite is a very reactive mineral during high temperature metamorphism; the ages are susceptible to be reset by growth of new titanite, rather than by diffusion (Frost et al 2001). For this reason we believe that the zircon/hornblende ages are more robust than zircon/titanite ages for inferring cooling rates.

VIII. Geochemistry

Table 3.6 shows the geochemistry for twelve samples of the Kitlope pluton; four samples of the Quottoon pluton; four samples of the Chief

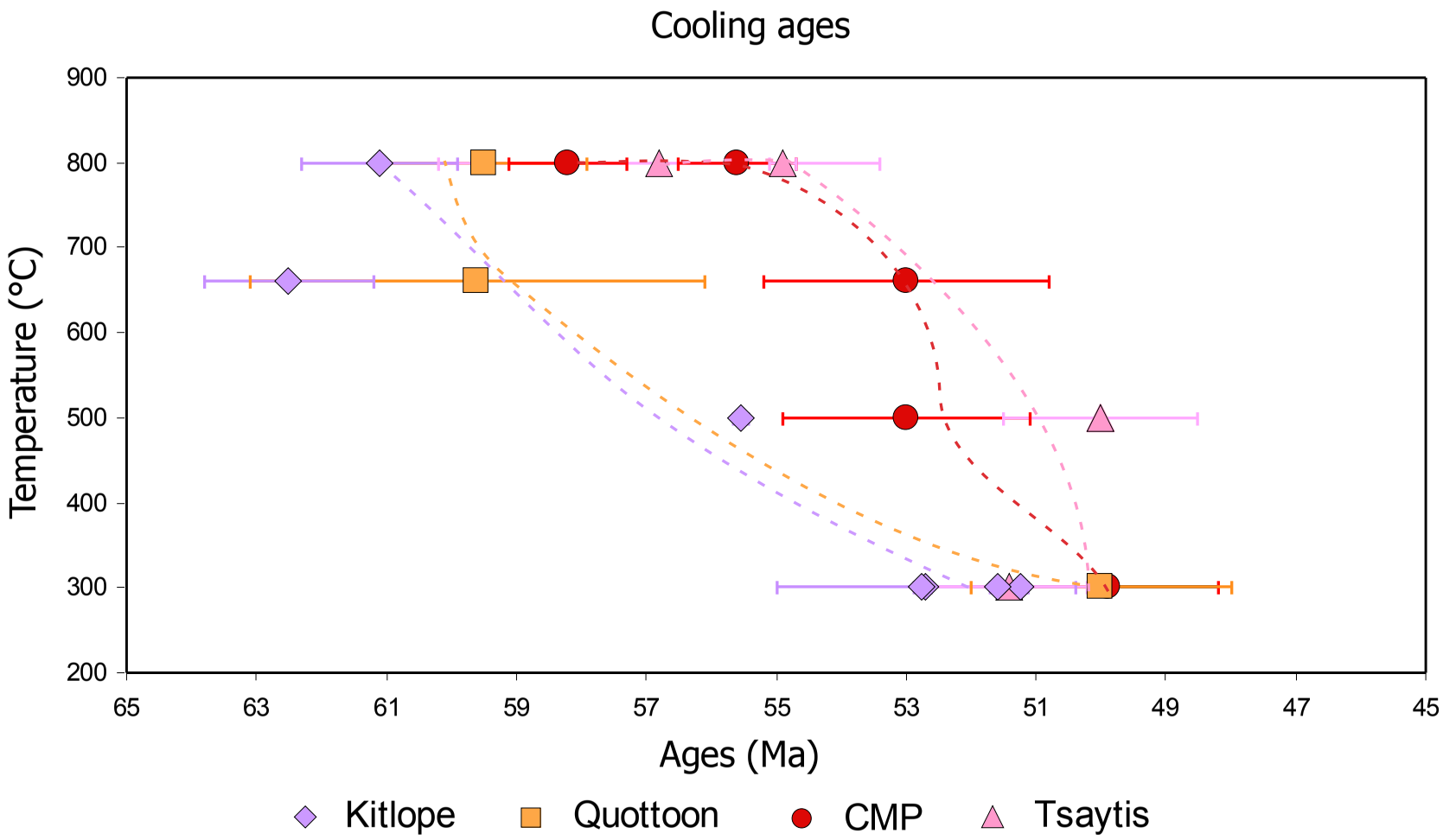

Figure 3.11: Cooling ages for samples at the southern termination of the central gneiss complex. The cooling history is complex, as shown by the dashed lines. However, a linear approximation for cooling rate would give a ~40°C/Ma for the Quottoon and Kitlope plutons, and ~60°C/Ma for the Chief Matthew's and Tsaytis plutons.

Table 3.6: Geochemical data

	Tonalite- Gamsby			Diorite-Gamsby			Kitlope Pluton									
	05B11	**05B27**	**05B30A**	**05B65**	**05B70C**	**05B72**	**06B21**	**06B22**	**06B23**	**06B30**	**06B39**	**06B66**	**06B69**	**06B72**	**06B73**	**06B74**
SiO2	63.29	64.05	61.98	56.48	54.25	52.02	59.71	63.53	66.88	71.74	72.93	72.02	55.03	62.02	72.42	68.98
TiO2	0.490	0.455	0.496	1.005	1.013	1.025	1.057	0.922	0.588	0.398	0.245	0.237	1.392	1.364	0.238	0.481
Al2O3	17.23	17.30	17.90	17.78	18.54	19.01	19.41	17.57	16.74	15.22	14.74	15.60	17.13	17.39	15.36	16.35
FeO	5.17	4.73	5.52	8.84	8.54	8.91	4.97	4.46	3.77	2.10	1.72	1.44	7.79	4.97	1.54	3.18
MnO	0.143	0.137	0.187	0.163	0.183	0.183	0.056	0.063	0.067	0.040	0.058	0.022	0.100	0.060	0.032	0.045
MgO	2.47	2.20	2.39	2.85	3.96	4.67	1.96	1.69	1.28	0.63	0.49	0.39	5.33	1.88	0.36	1.09
CaO	6.10	5.71	6.34	8.44	8.27	9.40	4.62	4.20	3.69	2.55	2.10	1.99	7.07	5.17	2.03	3.83
Na2O	3.29	3.59	3.55	3.19	3.86	3.67	5.13	4.77	4.47	4.38	4.06	4.30	3.66	4.47	4.53	4.25
K2O	1.55	1.59	1.35	0.94	1.07	0.77	2.72	2.48	2.30	2.83	3.58	3.93	2.19	2.26	3.42	1.62
P2O5	0.262	0.241	0.292	0.306	0.316	0.329	0.356	0.310	0.214	0.121	0.084	0.069	0.311	0.433	0.070	0.180
TOTAL	100	100	100	100	100	100	100	100	100	100	100	100	100	100	100	100
Ba	529.9	576.2	510.8	445.1	749.0	573.8	1722.7	1545.3	1329.8	1209.8	1202.1	2301.8	1281.5	1496.3	1830.1	1452.6
Rb	54.4	56.3	50.0	18.0	19.5	9.3	66.2	56.8	50.4	54.1	80.1	59.6	56.2	55.0	67.9	38.1
Sr	577.3	586.6	626.5	314.6	736.6	856.9	1022.3	856.7	674.9	548.4	400.4	807.4	853.5	967.8	740.3	870.9
Zr	88.1	81.4	82.2	100.5	91.5	56.9	269.7	226.3	157.0	121.0	88.4	113.5	195.8	141.9	115.7	155.4
Nb	5.0	5.1	4.6	2.2	4.0	3.2	9.7	10.1	6.5	4.1	6.5	2.0	7.1	10.2	2.7	3.2
Ni	10.0	8.0	4.7	11.5	12.3	16.1	7.3	5.8	5.5	4.3	3.7	3.0	27.6	7.2	4.0	5.0
Zn	54.4	52.7	70.6	88.3	81.6	80.9	104.8	117.3	98.1	58.1	56.2	54.6	132.1	114.7	54.3	81.9
Cr	12.8	10.9	5.0	12.7	15.6	27.1	8.4	6.9	5.2	3.4	4.2	2.4	66.0	5.1	1.3	5.7
La	7.9	50.7	17.0	9.4	14.8	12.6	40.6	31.3	30.0	21.8	17.3	15.1	19.2	27.3	21.9	38.1
Ce	17.2	91.3	33.8	22.5	31.3	27.1	81.5	69.3	57.5	40.5	32.8	28.4	47.5	60.9	41.1	67.1
Pr	2.6	10.6	4.6	3.3	4.4	3.9	10.2	9.2	6.8	4.7	3.8	3.3	6.7	8.0	4.8	7.2
Nd	11.9	36.4	19.1	15.7	19.4	17.4	39.7	36.9	25.4	17.3	14.2	12.1	29.2	33.7	17.8	24.3
Sm	3.0	5.2	4.3	4.5	4.6	4.3	7.6	7.4	4.6	3.0	2.7	1.9	6.5	7.1	2.8	3.1
Eu	1.1	1.4	1.3	1.4	1.6	1.5	2.1	2.0	1.3	0.8	0.7	0.8	2.0	2.1	0.8	1.1
Gd	2.9	3.6	3.9	5.0	4.4	4.0	5.4	5.5	3.4	2.0	2.0	1.1	5.4	5.5	1.6	1.7
Tb	0.4	0.5	0.6	0.9	0.7	0.6	0.7	0.7	0.4	0.2	0.3	0.1	0.7	0.7	0.2	0.2
Dy	2.7	2.7	3.6	5.8	4.0	3.6	3.2	3.3	2.1	1.0	1.4	0.5	3.4	3.0	0.7	0.7
Ho	0.5	0.5	0.7	1.2	0.8	0.7	0.5	0.5	0.3	0.2	0.2	0.1	0.6	0.5	0.1	0.1
Er	1.5	1.5	2.0	3.5	2.2	1.9	1.2	1.2	0.7	0.4	0.5	0.2	1.2	1.0	0.3	0.3
Tm	0.2	0.2	0.3	0.5	0.3	0.3	0.2	0.2	0.1	0.0	0.1	0.0	0.2	0.1	0.0	0.0
Yb	1.5	1.4	2.0	3.2	1.9	1.7	0.9	0.9	0.5	0.3	0.5	0.2	0.8	0.7	0.3	0.2
Lu	0.3	0.2	0.3	0.5	0.3	0.3	0.1	0.1	0.1	0.0	0.1	0.0	0.1	0.1	0.0	0.0
Y	14.9	14.3	19.8	31.7	21.1	18.5	14.0	14.0	8.7	4.3	6.7	2.2	14.1	12.0	3.3	3.2
Cs	1.8	1.3	1.1	0.9	0.8	0.5	3.4	1.2	0.8	0.9	0.8	0.9	1.3	0.8	1.4	0.6
Ta	0.4	0.4	0.2	0.2	0.2	0.2	0.7	0.7	0.5	0.3	0.5	0.1	0.4	0.6	0.2	0.1
Hf	2.5	2.3	2.2	2.9	2.4	1.6	6.8	5.7	4.2	3.5	2.8	3.4	4.8	3.8	3.6	3.5
Sc	11.6	10.2	12.2	29.9	21.8	23.7	2.7	5.7	3.4	3.2	2.4	1.7	13.9	4.8	1.6	1.8
V	92.6	78.7	86.1	268.8	212.8	229.1	100.1	91.8	62.6	38.6	24.3	22.8	234.4	132.0	20.6	52.2
Ga	15.8	15.1	16.0	17.6	19.1	17.8	23.4	22.9	20.5	20.0	18.8	18.8	23.5	24.2	19.4	19.1
Cu	14.6	10.6	20.3	33.4	45.6	21.8	25.2	17.1	4.9	4.3	2.2	1.9	5.2	17.8	2.5	2.7
Zn	54.4	52.7	70.6	88.3	81.6	80.9	104.8	117.3	98.1	58.1	56.2	54.6	132.1	114.7	54.3	81.9
Pb	3.0	2.9	2.6	4.1	3.3	2.8	9.1	8.5	8.0	10.5	15.2	19.4	7.0	8.9	18.7	6.8
Th	1.2	10.3	2.5	1.4	1.4	0.7	5.1	4.1	5.3	6.6	4.9	2.1	1.6	2.9	3.7	5.7
U	1.5	1.4	0.5	0.8	0.6	0.3	1.6	1.2	1.1	1.0	1.3	0.7	1.1	2.1	0.9	0.9

Table 3.6 (Continued)

	Kitlope Pluton		CMP		Quottoon Pluton		
	06B75	**06B80**	**07B66**	**07B118**	**07B159**	**07B149**	**07B136**
SiO2	73.81	62.71	62.84	60.47	60.22	58.85	62.73
TiO2	0.225	0.781	0.753	0.562	0.843	0.855	0.727
Al2O3	14.72	18.27	17.59	19.69	17.86	17.74	17.13
FeO	1.41	4.64	4.34	4.64	6.22	6.78	4.96
MnO	0.042	0.061	0.074	0.094	0.095	0.122	0.079
MgO	0.36	1.64	2.52	2.00	3.21	3.67	2.64
CaO	1.96	4.96	5.59	5.82	5.53	6.43	5.43
Na2O	4.23	4.71	4.19	5.08	3.76	3.66	4.20
K2O	3.17	1.94	1.87	1.37	2.04	1.68	1.86
P2O5	0.064	0.290	0.234	0.280	0.211	0.217	0.243
TOTAL	100	100	100	100	100	100	100
Ba	1682.7	1113.3	842.3	869.0	852.5	593.6	995.1
Rb	56.6	51.0	49.3	25.0	48.2	39.0	34.7
Sr	686.9	941.6	825.7	975.0	515.8	513.1	786.7
Zr	111.3	191.1	105.8	122.4	143.4	104.0	131.3
Nb	3.8	5.5	4.0	2.8	4.5	3.8	3.7
Ni	3.9	6.2	0.0	1.7	11.7	18.0	2.9
Zn	55.3	105.6	83.1	86.6	93.9	98.8	94.3
Cr	2.6	6.3	17.5	10.5	56.1	71.2	25.8
La	17.1	36.5	15.5	9.7	7.3	12.5	16.6
Ce	32.0	68.2	29.0	21.9	19.6	26.6	30.2
Pr	3.7	8.0	3.5	3.2	3.2	3.5	3.6
Nd	14.0	30.3	13.5	14.9	15.8	15.2	14.0
Sm	2.3	5.4	2.6	3.7	4.4	3.6	2.8
Eu	0.7	1.5	0.9	1.2	1.1	1.1	0.9
Gd	1.4	3.7	2.1	3.1	4.3	3.4	2.2
Tb	0.2	0.4	0.3	0.4	0.7	0.5	0.3
Dy	0.8	2.1	1.5	2.3	3.9	3.0	1.6
Ho	0.1	0.3	0.3	0.4	0.7	0.6	0.3
Er	0.4	0.7	0.7	1.0	1.9	1.6	0.7
Tm	0.1	0.1	0.1	0.2	0.3	0.2	0.1
Yb	0.4	0.5	0.6	0.9	1.6	1.5	0.6
Lu	0.1	0.1	0.1	0.1	0.2	0.2	0.1
Y	4.1	8.0	8.0	10.6	18.1	15.0	7.1
Cs	0.9	0.8	1.6	0.4	1.6	1.5	0.8
Ta	0.2	0.3	0.4	0.2	0.3	0.3	0.3
Hf	3.5	4.9	2.9	3.2	3.7	2.9	3.3
Sc	2.5	4.5	9.4	10.3	14.7	15.4	10.4
V	17.3	78.2	104.8	89.5	141.2	153.1	117.7
Ga	18.8	21.6	19.5	22.0	19.1	17.8	19.3
Cu	1.3	26.5	1.9	5.0	21.1	34.8	16.4
Zn	55.3	105.6	107.3	124.4	137.5	106.2	129.8
Pb	19.4	8.2	10.3	6.8	5.8	7.1	10.2
Th	2.2	4.6	3.5	0.8	0.4	2.0	2.6
U	0.9	1.0	2.6	0.5	0.5	0.9	0.8

Matthew's pluton; three samples of a tonalite in the Gambsy Complex (155 Ma); and three samples of a diorite in the Gamsby complex (188 Ma). The analyses were done at the geoanalytical lab at Washington State University using XRF and ICP-MS. The samples of the different plutons are associated with different ages ranging from Early Jurassic to Paleocene.

The Kitlope pluton has SiO_2 values ranging from 55.03 to 73.81 wt%. When using the feldspar triangle for classification of plutons most of the samples classify as granodiorite but older units of the pluton fall in the granite field (Figure 3.12a). The pluton is metaluminous and contains medium K, as also indicated by the presence of hornblende, magnetite and titanite. Older units of the pluton are peraluminous, and contain high K. The Quottoon pluton ranges in SiO_2 content between 58.85 and 62.73 wt%. The rocks classify as granodiorite when using the feldspar triangle for classification of plutons. The Chief Matthew's pluton ranges in SiO_2 content between 70.02 and 60.47 wt%, the rocks classify as granodiorites when using the feldspar triangle of classification of plutons. The Quottoon, Chief Matthew's and the plutons of the Gamsby Complex are metaluminous (Figure 3.12b) and contain medium K (Figure 3.12c).

Binary diagrams were used to compare the different plutons. All the units show a negative correlation between SiO_2 and TiO_2, Al_2O_3, MgO, CaO, P_2O_5, FeOt, Ni, Cr, and Mg#; and a positive correlation for A/CNK. The rocks of the Quottoon pluton show enrichment in Cr and Ni when compared to the other plutons for the same SiO_2 content (Figure 3.13). This enrichment is also found in the Mg# of these rocks. This observation indicates a stronger mantle component for the Quottoon pluton and Gamsby diorite.

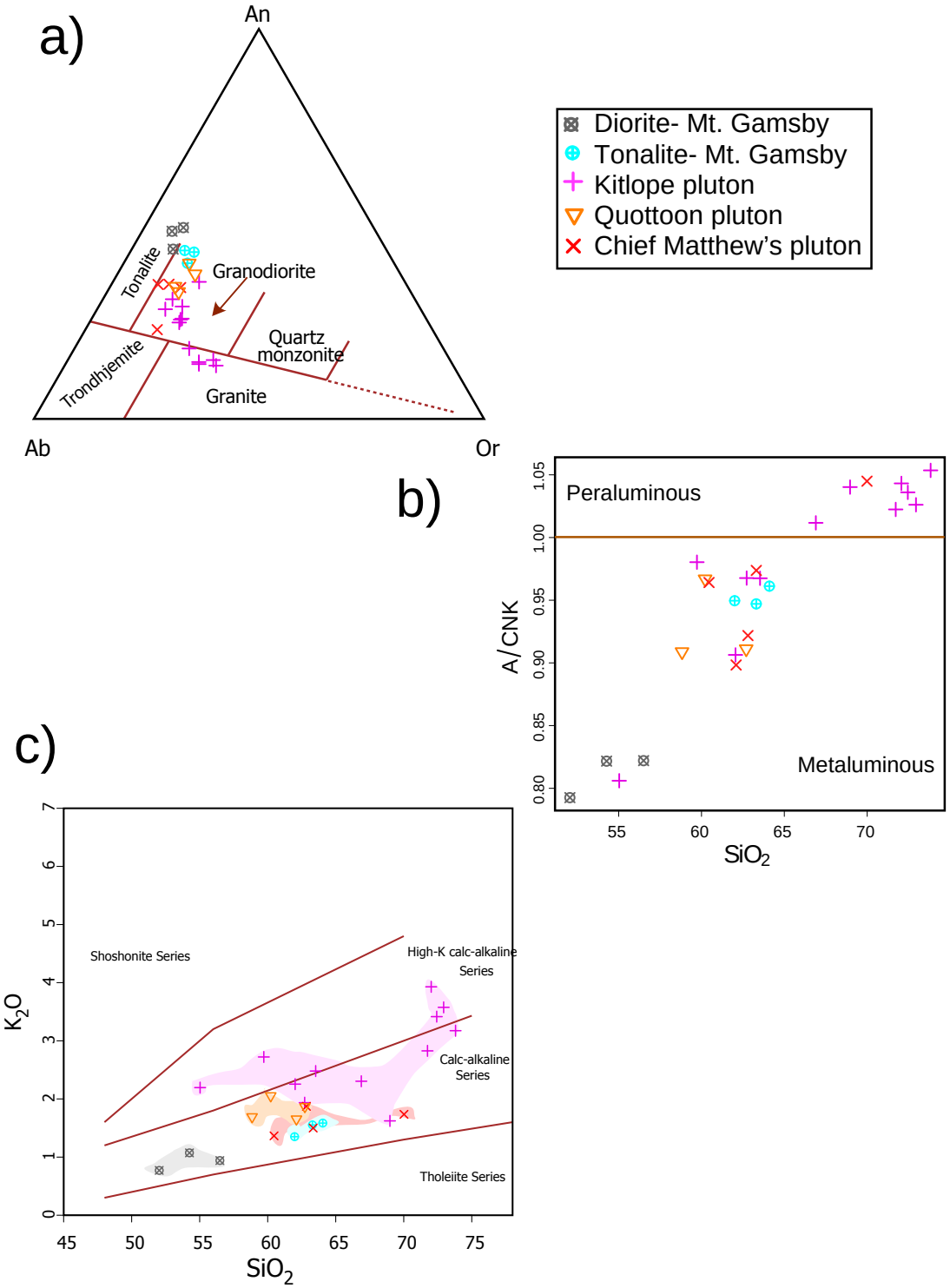

Figure 3.12: Geochemical classification diagrams for plutons. (a) Feldspar triangle for classifying plutons. (b) Aluminum/ Alkalis with respect to silica content indicates that the plutons are mainly metaluminous. (c) Potassium with respect to silica classifies most of the rocks as medium K content typical of calc-alkaline series.

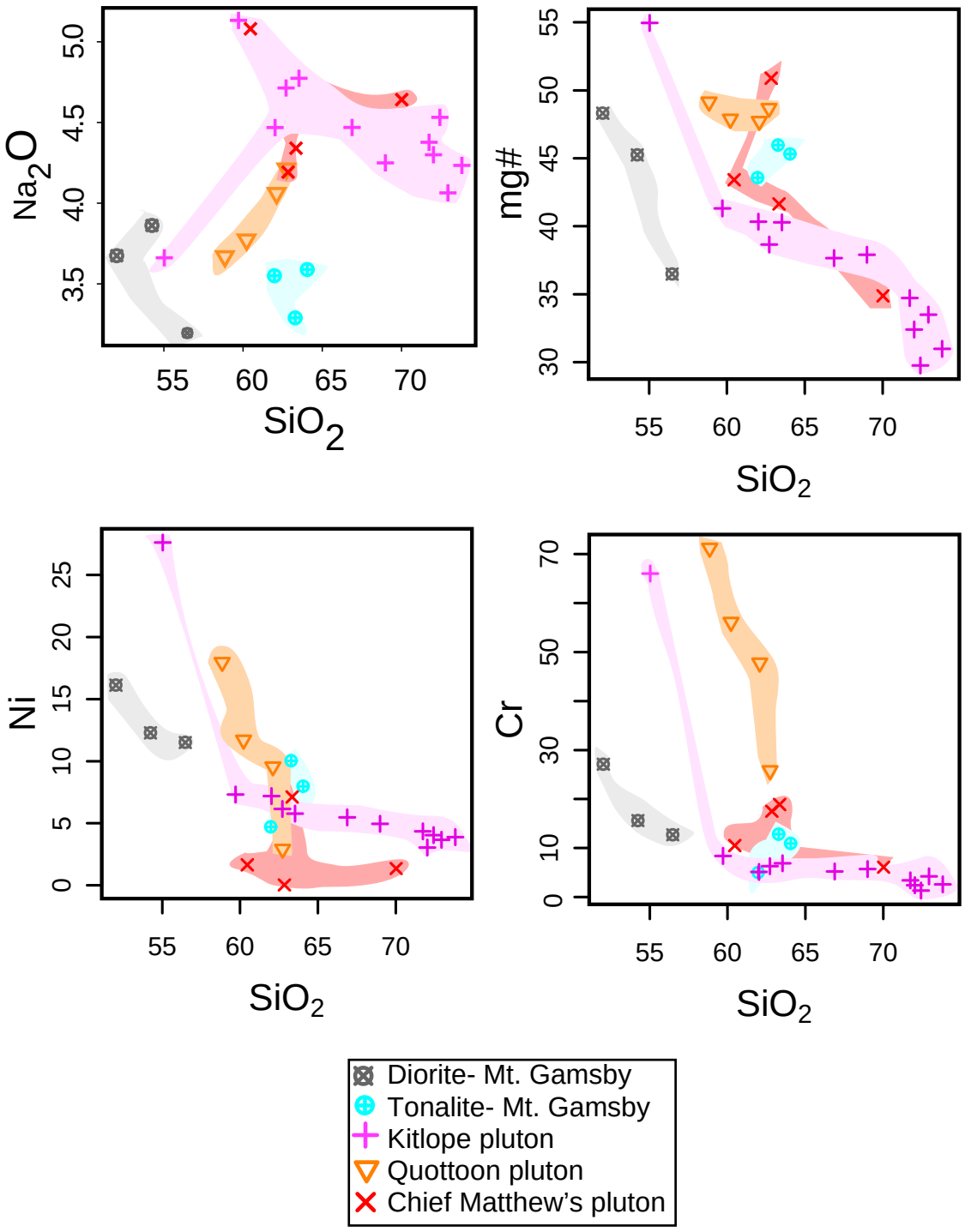

Figure 3.13: Variation diagrams with respect to silica content. See text for discussion.

All the analyzed plutons are subduction-related intrusions. The arc signature is indicated by the major elements and by peaks in Ba relative to the LREE; and depletion in the High field strength elements, as seen on spider diagrams (Figure 3.14).

A graph of variation of Pb/Ce with SiO_2 is presented to track crustal contamination of the magmas (Figure 3.15a). Typically Pb/Ce ratios greater than 0.3 are found in sediments; and <0.04 ratios characterize MORB. Figure 3.15a shows that most of the rocks have values of the ratio between 0.1 and 0.3. These values are explained by interaction of magmas with the crust. This is also supported by negative anomalies in P_2O_5 accompanied by positive anomalies in Sr (Figure 3.14).

The plutons at Gardner Canal have affinities more like the Aleutian plutons, typical of oceanic origin, than the Peruvian Batholith of continental origin (Figure 3.15b). This is consistent with an amphibolite composition rock as the source for the pluton (Thomas and Sinha 1999). The underplated Insular Superterrane has been suggested as the source crust of amphibolitic composition melting together with mantle-derived basaltic intrusions to generate the magmas of the Coast Plutonic complex (Hollister and Andronicos 2006). The Insular Superterrane is a Triassic ocean island-arc with juvenile isotopes and chemistry. Melting these kinds of rocks will not imprint a strong continental crust signature to the derived magmas, but it would explain the crustal/melt interactions seen in Figure 3.15a.

When looking at the REE spider plots (Firgure 3.16) some samples of the Kitlope and Chief Matthew's plutons show a positive Eu anomaly and

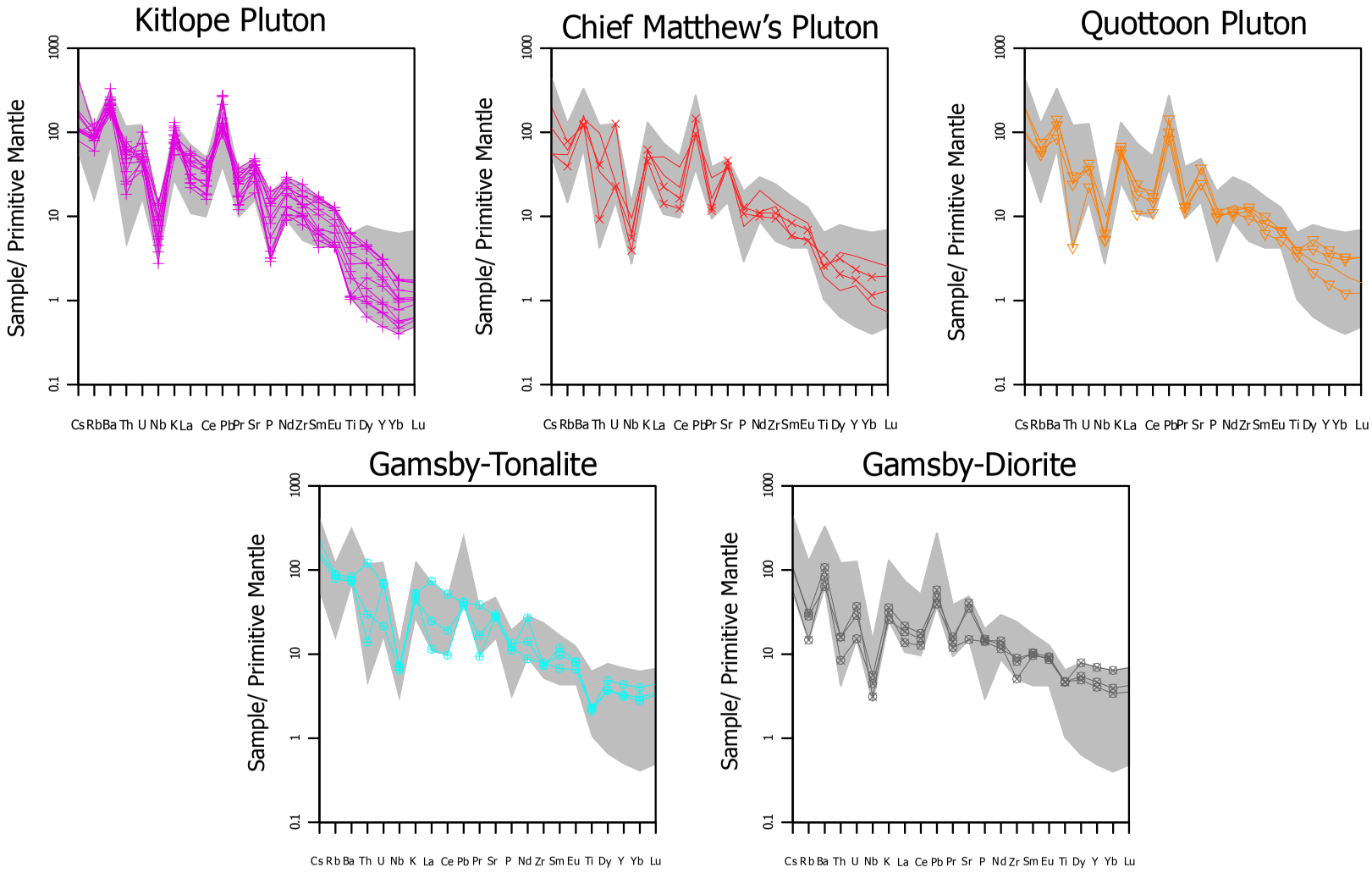

Figure 3.14: Spider diagram for each pluton normalized to primitive mantle (Sun and McDonough 1989). The grey field represents all the samples for reference.

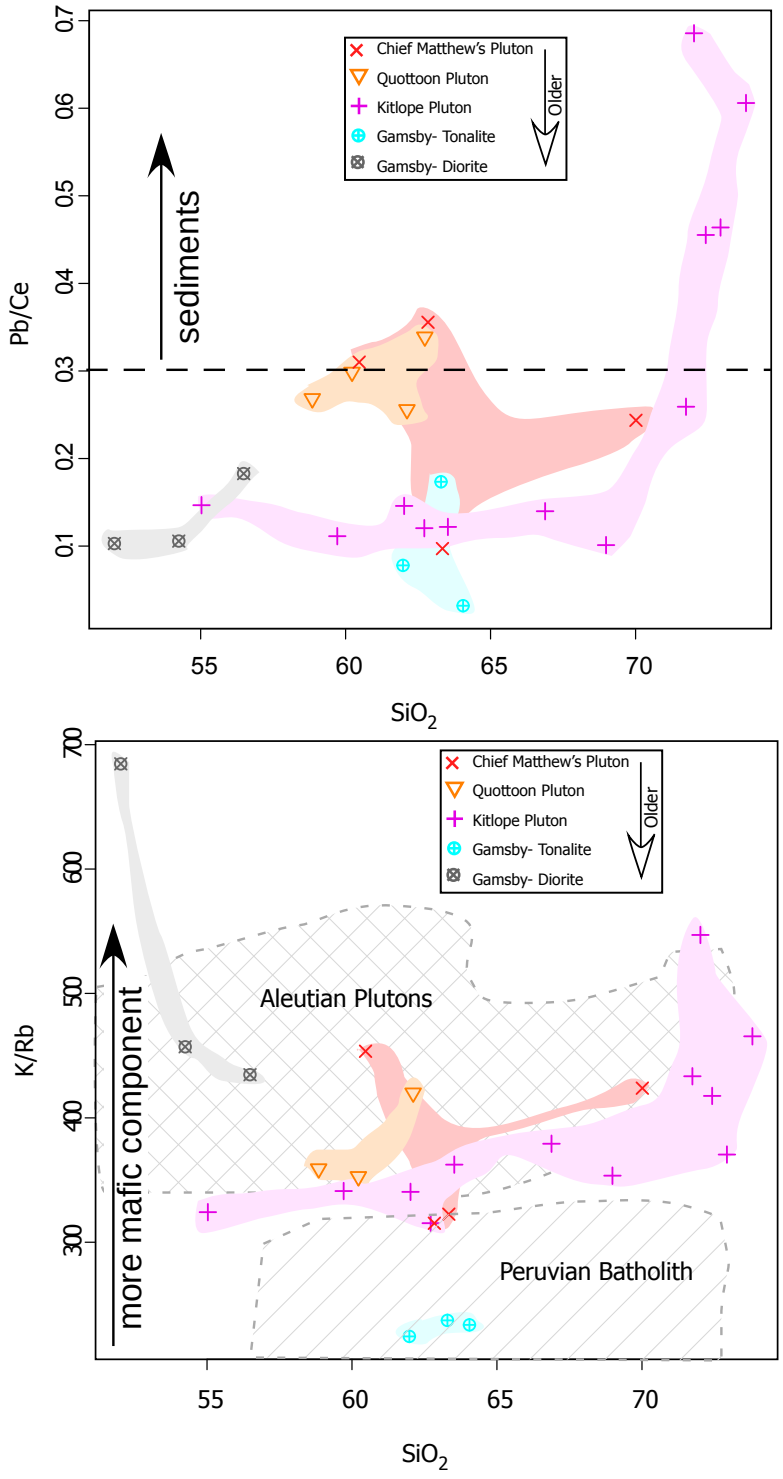

Figure 3.15: Discrimination diagrams. (a) Pb/Ce variation with silica is used to track crustal contamination in the magmas. (b) K/Rb with silica is used to track oceanic versus continental components for the magmas. For reference we compare our values with plutons in the Aleutians and Peru from Kay et al 1990.

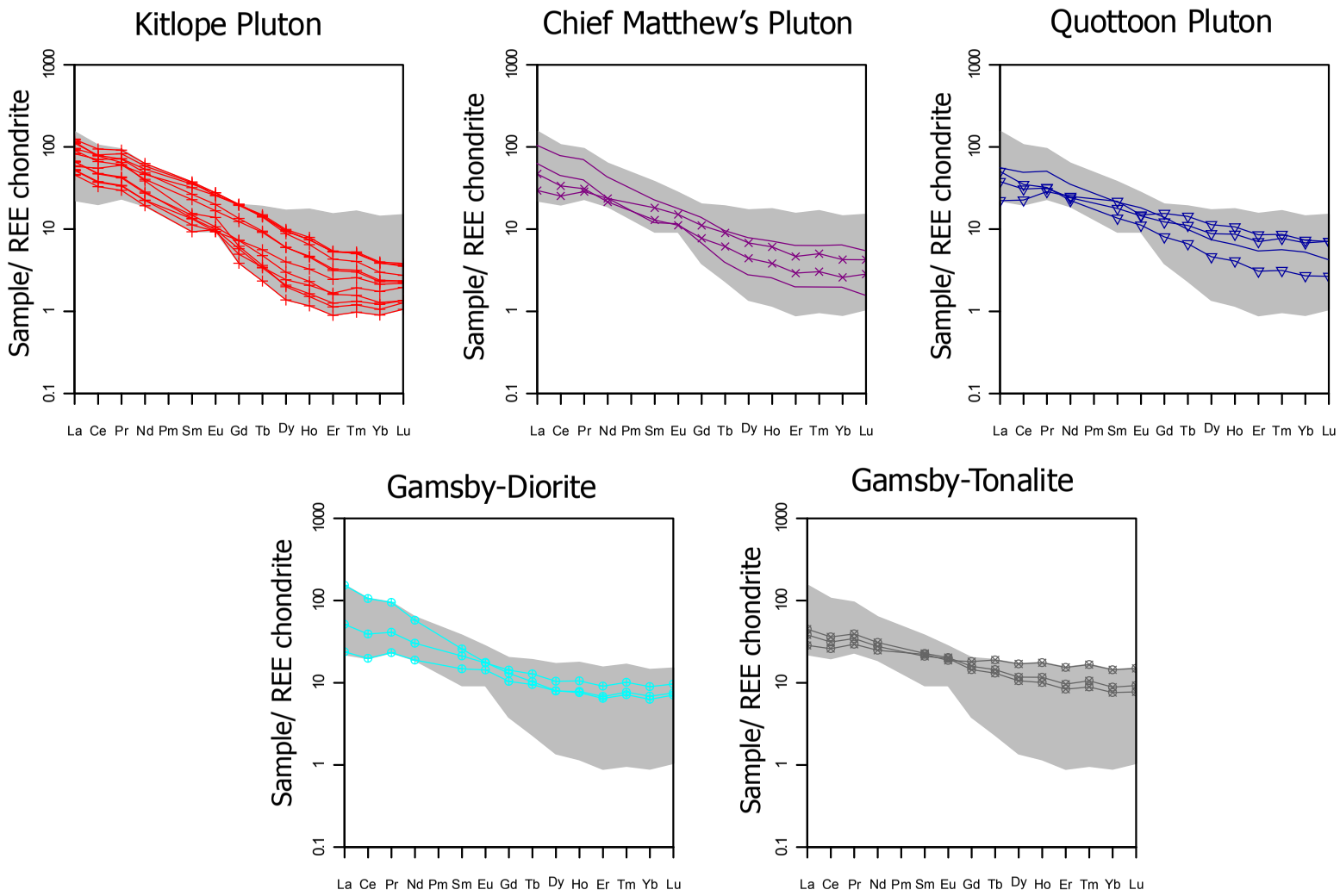

Figure 3.16: Rare Earth elements plots normalized to chondrite values (Nakamura 1974) for the samples. The grey area is the whole range for reference.

depletion in the middle REE. This is consistent with the rocks representing cumulates, instead of true magmas.

The plutons at Mt. Gamsby show consistently flatter patterns in the REE (Figure 3.16-3.17a). This is also evident when compared rocks from Mt Gamsby with the same SiO_2 content than rocks from the Kitlope pluton (Figure 3.17b). The Kitlope, Quottoon, and Chief Matthew's plutons also show a peak in Na_2O and Sr concentrations, as well as a lack of a Eu anomaly (Figure 3.13-3.14), which indicates that plagioclase was not being fractionated in the residue, but garnet and/or hornblende were in equilibrium and segregated from the melts depleting the plutons in HREE. The increase in the slope of the REE with increasing age of the rocks is consistent with an increase in crustal thickness where garnet became stable at the source region of the plutons. This is seen very strongly in the Kitlope pluton (Figure 3.17a-b). This result is consistent with previous results for the region (e.g. Thomas and Sinha 1999; Crawford et al 2005; Hollister and Andronicos 2006). The Quottoon and Chief Matthew's pluton do not show garnet signature, and are more consistent with fractionation of hornblende in the source region. This could be either because garnet did not fractionate at the source, or that the melts were generated above the stability of garnet, at shallower depths. The implications of this last case are an amphibolite crust that was generating magmas at different depths above and below the stability of garnet, consistent with an isothermal geotherm for the crust. This conclusion is also supported by geochemical analysis in other parts of the coast plutonic complex that show some plutons that intruded during the magmatic flare-up have garnet signature and others lack it (Crawford et al 2005).

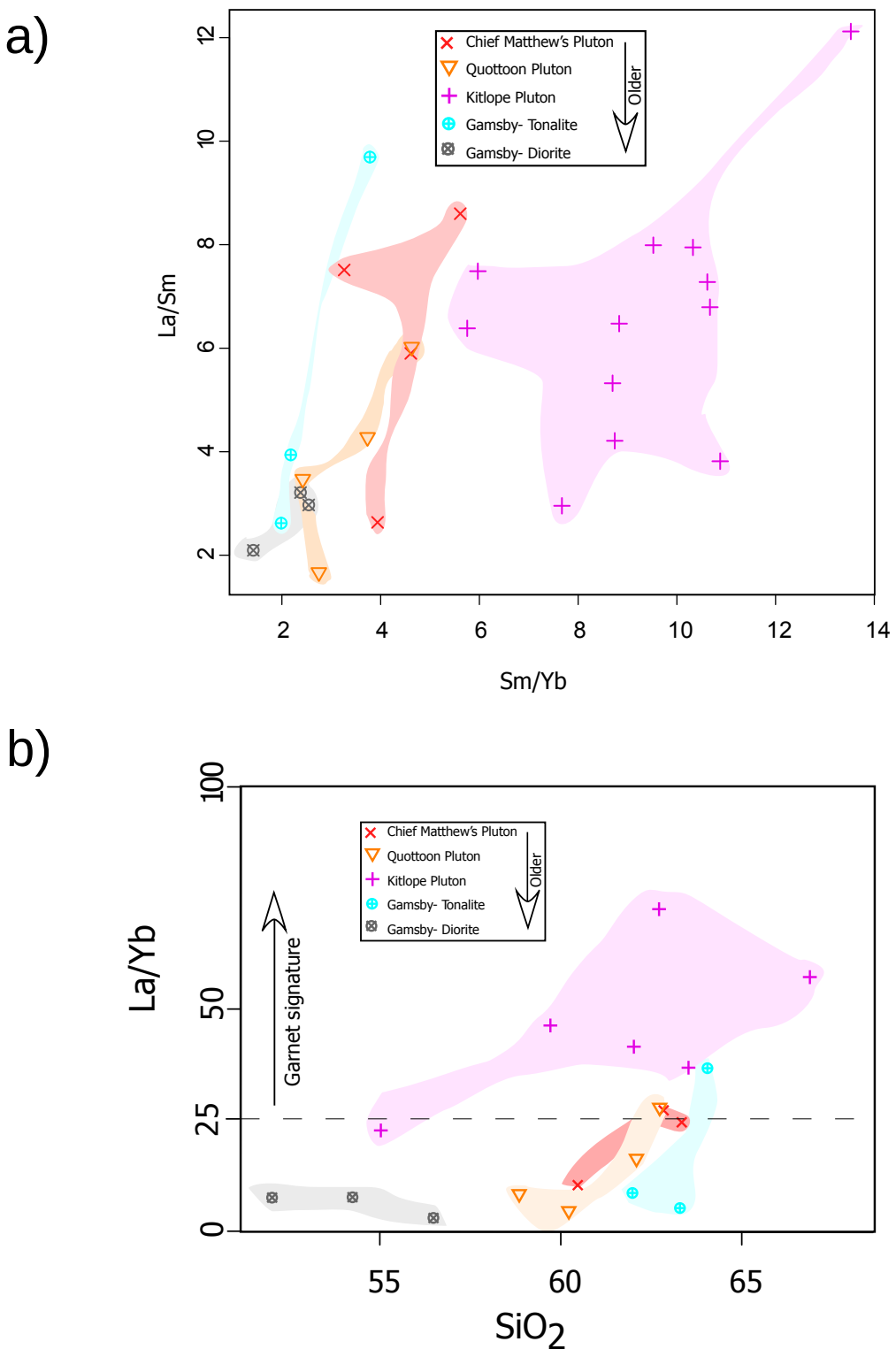

Figure 3.17: (a) Variation of light rare-earth elements with respect to heavy rare earth elements. (b) Variation of the slope of the rare earth elements with respect to the silica content.

IX. Results and discussion

Based on petrological observations, the rocks at the southern termination of the central gneiss complex show evidence of a long-lived history of metamorphism at high temperatures (~750℃) in th e upper amphibolite facies. This is indicated by granular textures, abundance of migmatized amphibolites, diffusional zoning profiles in garnet, and the mineral assemblages in the rocks. The abundance of orthogneiss in the area indicates a long history of plutonic intrusion in the area. Some zircon ages in some of these rocks are Early and Late Cretaceous, and adjacent areas have Late Jurassic ages (Van der Heyden 1989). The last pulse of magmatic activity in the area occurred between 61-57 Ma and is represented by the Quottoon, Kitlope, Chief Matthew's and Tsaytis plutons.

The Kitlope, Quottoon, and Chief Matthew's plutons are calc-alkaline granodiorites that intruded in a thick crust of ~55 km (Hollister and Andronicos 2006). The magmas were generated by interactions between mantle-derived melts and partial melt of amphibolitic crust at different depths in the crust, consistent with an isothermal profile for the crust. The Kitlope and Quottoon plutons intruded as vertical sheets during crustal shortening (eg. Ingram and Hutton 1994, Chapter 2, this thesis) at 0.65-0.75 GPa. The Chief Matthew's pluton intruded as a tabular body (Chapter 2, this thesis) at a pressure of 0.55-0.6 GPa, after 3 Ma of isothermal decompression of the rocks at a rate of ~3 mm/yr. We rule out the possibility of different emplacement depths for the plutons during constant crustal thickness, given that the three studied plutons are exposed at the same elevation today, and the Chief Matthew's pluton is located in between the two older plutons (the Kitlope and Quottoon) discouraging the presence of a tilted section. The P-T path followed after the

plutonic events appears to be dominated by cooling rather than decompression, as indicated by the minerals, textures and P-T calculations. From the equilibrium diagram we obtained a minimum cooling path of ~8℃/km.

The cooling rate for the Kitlope and Quottoon plutons is ~40℃/Ma, slower than the cooling rate of ~60℃/Ma recorded f or the younger plutons (Chief Matthew's and Tsaytis plutons). These values are not as high as what is found in active orogens, which values range between 100-350℃/Ma. Dunlap (2000) explains this discrepancy between rates in active versus ancient orogens by stating that the post-orogenic history in ancient orogens usually involves periods of rocks at isothermal conditions where the K/Ar system remains open to diffusion, at temperatures as low as 180℃ if the rocks are kept for long periods of time. According to Dunlap (2000), an orogen of 50 Ma, if it experienced rapid cooling, should then record a cooling rate of 50℃/Ma, which is exactly what we obtained for the central gneiss complex at Gardner Canal and Kitlope Lake areas. All the plutons and country-rocks at the southern termination of the central gneiss complex cooled under the biotite closure temperature by ~51Ma.

The rocks at Mount Gamsby (Early to Late Jurassic) record a different exhumation and cooling history than rocks to the west and north. Peak temperatures are 600-750℃ and the peak pressures a re 0.8-1 GPa (Hamblock 2006). The deduced P-T-path is isobaric cooling of the rocks at high pressures, also indicated by the presence of muscovite throughout the tectonic evolution (Hamblock 2006). Mount Gamsby does not belong to the central gneiss complex; given that it was already in the green-schist facies by the time the rocks of the central gneiss complex were experiencing their peak

metamorphic conditions. It also lacks the intrusion of voluminous Late Cretaceous to Eocene age plutons, only Eocene dikes with chilled margins are reported to occur in the area (Hamblock 2006).

IX.A. Comparison with other areas in the central gneiss complex:

Surface rocks at Douglas Channel (Figure 3.2) were ~25 km deep at 90 Ma, as indicated by kyanite inclusions in garnet. These rocks experienced isothermal decompression from 70 Ma to 59 Ma at a rate of ~0.5 mm/yr, which is attributed to thickening and erosion of the crust (Rusmore et al 2005). At 59 Ma, the exhumation rate doubled until 52 Ma, assisted by motion along a normal east-dipping detachment fault (Rusmore 2005). These rocks passed through biotite closure temperature by 48.7 Ma (Rusmore 2005). At Douglas Channel, the Quottoon pluton intruded at 58.6 Ma at a pressure of 0.65 GPa (Rusmore et al 2005). Peak temperatures in the area were ~750℃.

The rocks of the central gneiss complex in southeast Alaska record high-temperature moderate pressure metamorphism, with peak pressures of 0.56 GPa and temperatures of 710℃ (Stowell and Cra wford 2000, Kleipes et al 1999). This peak condition is overprinted by lower pressure and similar temperature assemblages, which include cordierite rims around garnet. Here exhumation was assisted by extension across normal shear-zones between 65 and 57 Ma (Kleipeis and Crawford 1999). A N-S orientation of extension is inferred from the structures.

At the Skeena River, Hollister (1982) proposed exhumation of ~30 km of rock between 62 and 48 Ma, at a rate of 2 mm/yr. Based on cooling ages, the cooling rate of the rocks was ~100℃/Ma between 51 and 49 Ma (Hollister 1993). This rapid cooling occurred when the rocks were at depths between 5-

10 km (Hollister 1982). The rocks passed through the closure temperature of biotite by 48 Ma (Andronicos et al 2003). The rocks experienced granulite facies metamorphism with peak temperature of ~800℃ , and pressures of 0.4 to 0.7 GPa (Hollister 1982). The Quottoon pluton at this latitude intruded at pressures between 0.4 and 0.6 GPa (Kenah and Hollister 1983) at 58.6 Ma (Gehrels et al 1991). The last phase of exhumation of the rocks is linked to a shallowly dipping detachment called the Shames River mylonite, which was active between 54 and 48 Ma (Andronicos et al 2003). The extension on this structure is E-W. However, a tabular pluton associated with the structure, the Kasiks sill complex, shows N-S displacement directions consistent with extension in a N-S direction.

In summary, rocks of the central gneiss complex north of the studied area show peak metamorphic conditions in the upper amphibolite facies similar to what we observe at Gardner Canal. The exceptions are the areas around the Skeena River that experienced granulite facies metamorphism. The large areal distribution of rocks at high metamorphic grade attests to long-lived peak conditions.

Fast exhumation rates of 1-2 mm/yr found at the Skeena River and Douglas Channel are comparable to the maximum value calculated at Gardner Canal of 2-3 mm/yr. These fast rates only occurred after ~100 Ma, which is the time interval of the formation of the plutons in this study. Cooling rates are also comparable along the orogen. However, there is a discrepancy in the timing when rocks cooled under the biotite cooling temperature. Areas to the north consistently give an age of 48 Ma, while Gardner Canal and Kitlope Lake areas cooled by 51 Ma.

The studied area shows no evidence for the isothermal decompression found in other parts of the central gneiss complex, this could either be because we still have not found the evidence for it or because the rocks followed a different decompression path.

A last discrepancy in the studied area is that the last pulse of decompression from ~60 to 52 Ma is assisted by large shallow detachments in the areas to the north. We have yet to find such structures at the southern termination of the central gneiss complex. However, the discrepancy in cooling histories, age of rocks and metamorphism between rocks at Mt. Gamsby and rocks to the west point to the presence of a structure separating the different blocks. Based on the abrupt discrepancy in the cooling ages Van der Heyden (1989) proposed the presence of an unmapped crustal crustal structure, the Kemano fault, separating the Gamsby complex from the central gneiss complex. We agree with his interpretation for the position of this structure for the Tsaytis pluton, however, the contact of the Kitlope pluton with the Gamsby complex seems to be continuous following a normal thermal gradient between the rocks. The character of the Kemano fault is unknown, but if we assume that it represents the southern continuation of the Shames River mylonite (Andronicos et al 2003), also called east-side detachment (Rusmore et al 2005), then this structure should be a low-angle detachment, with the Gamsby complex located in the hanging wall, and would have assisted the Early Eocene exhumation of the orogen.

The Chief Matthew's pluton is associated with extension and shows sub-vertical flattening (Chapter 2, this thesis), consistent with stretching parallel and perpendicular to the orogen.

IX.B. Comparison with other areas in the Canadian Cordillera:

The North Cascades represent the southernmost extension of the >1500 km long Coast Mountains. Peak metamorphic conditions of 0.9-1.2 GPa and 650-750℃ (Valley et al 2003) were developed during a history of thickening by thrusting during intra-arc contraction (Whitney et al 1999) between 96 to 73 Ma (Patterson et al 2004). More evidence for a more than 55-60 km thick crust in the Cascades in the Cretaceous is indicated by the trace element chemistry in calc-alkaline plutons (DeBari 1999), and by seismic evidence that shows a normal thickness crust present today, and when coupled with geothermobarometry results gives a thick crust for the Early Tertiary.

Isothermal decompression during dextral transpression is responsible for exhuming the Cascades between 73 and 55 Ma followed by dextral transtension and rapid cooling (Patterson et al 2004). This last phase of exhumation was assisted by dextral-normal faulting on a bounding fault (Miller and Bowring 1990). Rapid exhumation of ~1.6 mm/yr occurred both in N-S and E-W directions (Patterson et al 2004). A major difference between the Cascades and the central gneiss complex is that when the central gneiss complex is experiencing its highest magmatic flux between~60-50 Ma, the Cascades experience a lull in magmatism (Wernicke and Getty 1997). This variation in the timing could be tracking a migration of a heating source (e.g. slab window).

The Shuswap metamorphic core complex is the largest core complex that developed in the Omineca belt as a result of distributed extension during the Early Eocene (Figure 3.18). The exhumation of the complex is assisted by a low-angle detachment that thinned the previously thickened crust (Brown

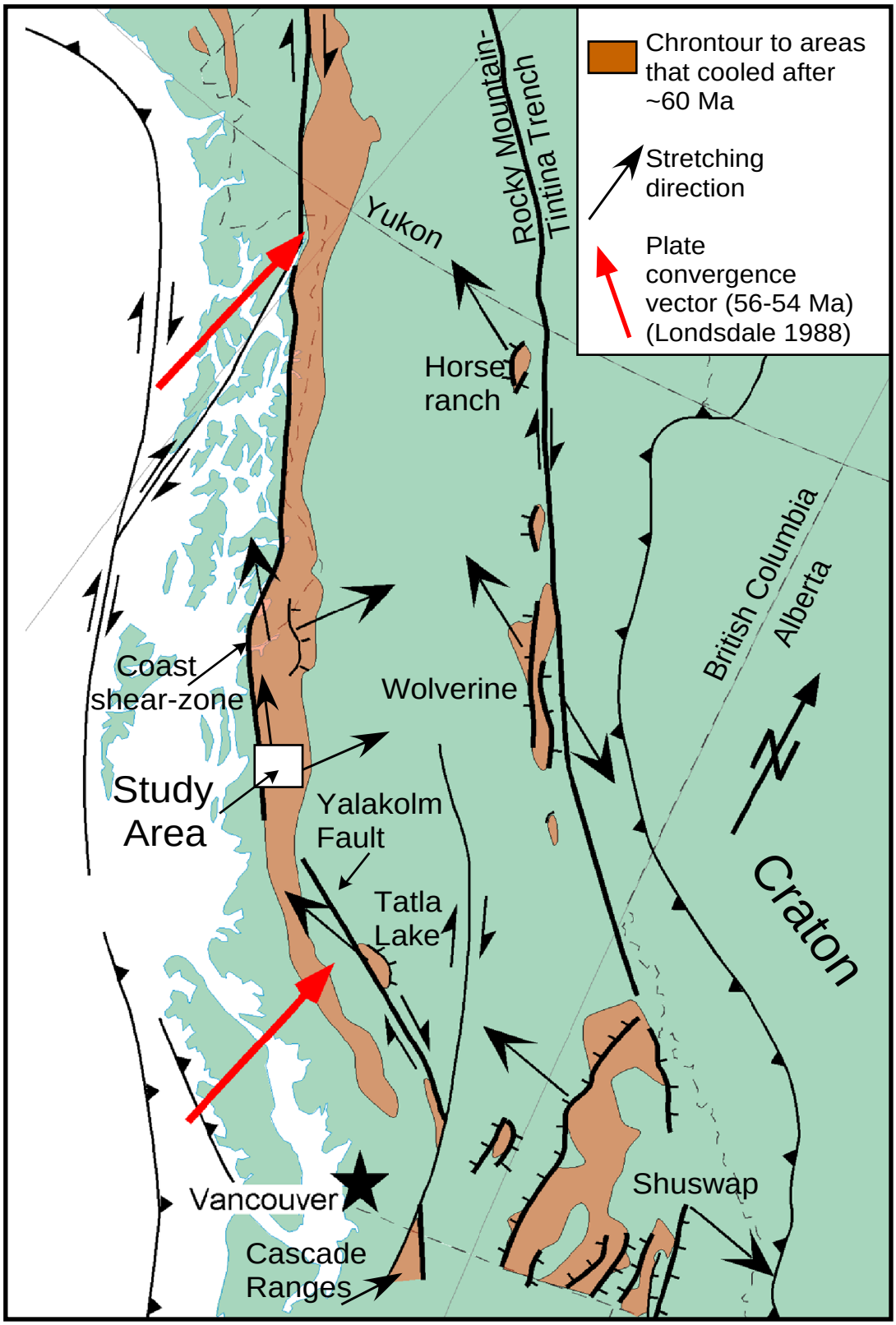

Figure 3.18: Map of western Canada showing the Eocene metamorphic core-complexes and associated faults. Modified from Andronicos et al 2003.

and Journeay 1987). Oxygen isotopes studies, consistent with fossil flora studies, show that the paleoaltimetry of the Shuswap core complex was > 4000 m by 49 Ma and decreased ~1000 m with the formation of the detachments in the Eocene (Mulch et al 2007). The first stage of exhumation was in the Paleocene between ~60-50 Ma when the still thick crust was partially molten. The cooling rate for this period is 65℃/ Ma, and it was assisted by a low-angle detachment. Thermal re-equilibration was achieved by 48 Ma. The second stage occurred at ~45 Ma during regional extension (Vanderhaeghe et al 2003, Ewing 1981). Extension was oriented E-W in the Shuswap core-complex.

Other metamorphic core-complexes in the Canadian Cordillera are the Horseranch Range (Figure 3.18) that exposes rocks with peak metamorphic conditions of 650℃ and 0.5-0.7 GPa achieved during the Late Cretaceous and Early Tertiary. The exhumation was accompanied by the intrusion of plutons and occurred between 53-41 Ma based on cooling ages and fission tracks in apatite (Plint et al 1992). Exhumation was assisted by a normal strike-slip fault on its western margin. The Wolverine Complex was also exhumed in the Early Eocene during extension (Figure 3.18). It is bounded by two faults that delimit a crustal pull-apart region. The Tatla Lake Metamorphic Complex has a similar history but the exhumation was assisted by another major structure, the Yalakom fault, between 53 to 46 Ma (Friedman and Armstrong 1988).

As a summary, all the metamorphic core complexes of northwestern North America (Figure 3.18) share a very similar tectonic evolution to the central gneiss complex. This observation suggests a common integrative tectonic evolution for the core-complexes. Exhumation was assisted by long

strike-slip faults in all the core-complexes. All the ranges also have widespread magmatism associated with exhumation. The extension direction tracked in the Shuswap core complex is E-W, and NW-SE for the Horseranch. The extension direction in the Cascade ranges is E-W and N-S, similar to the central gneiss complex. A change in the style of exhumation (e.i. change in exhumation rate, change in compression to extension, etc) is tracked across the Canadian Cordillera within ~5 Ma.

Suggested causes of extension and exhumation of high-grade metamorphic rocks along the Canadian Cordillera have been: 1) Gravitational collapse of a thickened and partially molten crust (Parrish et al 1988, Klepeis and Crawford 1999, Vanderhaeghe et al 2003, Paterson et al 2004); 2) release of horizontal stress by changes in plate motion (Engebretson et al 1985, Parrish et al 1988, Andronicos et al 2003, Rusmore et al 2005); 3) Uplift of the crust related to asthenospheric upwelling due to delamination of lithosphere (Bardoux and Mareschal 1994), or rise of a mantle plume (Gough 1986); 4) Softening of the lithosphere above a slab window by differential traction between North America-Kula and North America-Farallon on opposite sides of the triple junction (Breitsprecher et al 2003); 5) Heterogeneous underthrusting of buoyant materials combined with differential tectonic thickening/stretching and erosion (Paterson et al 2004); 6) Intracrustal subduction (Wernicke and Getty 1997). However, an integrative orogen-scale model accounting for a unique exhumation mechanics that includes all the metamorphic core-complexes has not been suggested yet.

IX.C. Exhumation mechanics

The model for exhumation of the northwestern North American margin that we propose combines both intrinsic (gravitational spreading) and extrinsic (change in plate motion) causes. The period of acceleration in the exhumation rate and extension in the Coast and Omineca belts occurred during oblique convergence at the plate boundary. For this reason, a change in rheology of the rocks that form the orogen is required to explain the extension tracked in the continental interior. However, the fact that the extension is tracked simultaneously with a change in the convergence angle of the oceanic plates suggests that extrinsic reasons are also important (Parrish et al 1988).

IX.C.A. *Local causes*

Gravitational collapse of the orogen after thickening has been argued to have occurred in the Canadian Cordillera. The collapse of an orogen is dependent on the strength of the lithosphere, which is modified by the presence of melts and the thermal profile; and on the contrasts in potential energy between thickened and a normal thickness lithosphere (Molnar and Lyon-Caen 1988, Sonder et al 1987). Thickening of the crust to at least ~55 km is reported in most of the core-complexes. The thickening is attributed to terrane collision during the Mesozoic. The internal plateau located in between the Omineca and Coast belts was probably high topographically and the locus of thickening.

Long-lived magmatism in the Canadian Cordillera is tracked by igneous rocks since the Jurassic (Armstrong 1988). Pervasive magmatism creates a special geothermal state of the crust; essentially the rocks arrive to a constant equilibrium temperature which is buffered by the solidus temperature of the

country-rocks and the temperature at the Moho (Depine et al 2008). The geotherm is isothermal from the lower crust to the depth at which plutons intrude (15-25 km in the Coast Mountains). This thermal structure of the crust creates a weak middle and lower crust. We postulate that the Coast Mountains of British Columbia were characterized by an isothermal geotherm in thick crust induced by widespread intrusion of plutons. This thermal profile set the ground for the uplift and exhumation of ~20 km of the orogen from the Paleocene to the Early Eocene.

IX.C.B. Far-field causes

Plate restorations show an abrupt change in the convergence angle of the Kula/Farallon plates between 57 and 55 Ma (Lonsdale 1988). Late Cretaceous and early Tertiary are characterized by dextral oblique convergence, after the plate reorganization subduction became more oblique with a NE direction.

Structural analysis along the Coast Mountains show evidences for dextral transpression as the tectonic regime in the region before the plate reorganization event (Andronicos et al 1999, Chardon et al 1999). The Coast shear-zone was the focus of the strike-slip motion in the orogenic belt. The structural analyses are corroborated by the metamorphic history of the central gneiss complex characterized by long-lived metamorphism and migmatization of the middle and lower crust, and the generation of granulites, as it would be expected in a transpressive regime (Thompson et al 1997). In the Omineca and interior plateau there are major faults with displacements as much as 900 km, which track dextral transcurrence during the middle Cretaceous to the Eocene (Gabrielse 1985, Struik 1993, Price and Charmical 1986).

Exhumation is usually assisted by major structures, large detachments or thrusts reactivated with normal displacements (Armstrong 1982, Coney 1980, Vanderhaeghe et al 2003). The dextral faults in the Canadian Cordillera assisted most of the Early Eocene exhumation. Most of the major faults cease their transcurrent motion by the time of the exhumation and only track normal displacements.

IX.C.C. *Model*

In the Late Cretaceous (90-70 Ma) the region in between the Coast shear-zone and the Tintina-Rocky Mount trench was experiencing transpression (Figure 3.19). The deformation was partitioned into orogen perpendicular compressive deformation represented by the Skeena fold belt in the interior plateau that ceased to be active by the end of the Cretaceous (Evenchick 2001), and widespread folding in the Coast and Omineca belts. Orogen parallel deformation was accommodated by the major strike-slip faults. The orogen experienced its maximum thickness during this time period. Magmatism mainly occurred in the Coast belt, however isolated plutonic bodies are also found in the Omineca belt (Armstrong 1988). Migmatization of the crust was also occurring, and related to igneous intrusions.

In the time period between 60 and 50 Ma (Figure 3.19), field studies show a change in the deformation regime in both the Coast and Omineca belts. The strike-slip faults stop showing dextral motion at this time. A release in the convergence forces relaxed the horizontal compression in the orogenic belt, which allowed the already weakened lower and middle crust to flow and extrude. This is tracked by acceleration in the exhumation rates tracked in the orogenic belts. We envision the collapse as a consequence of the rigid upper

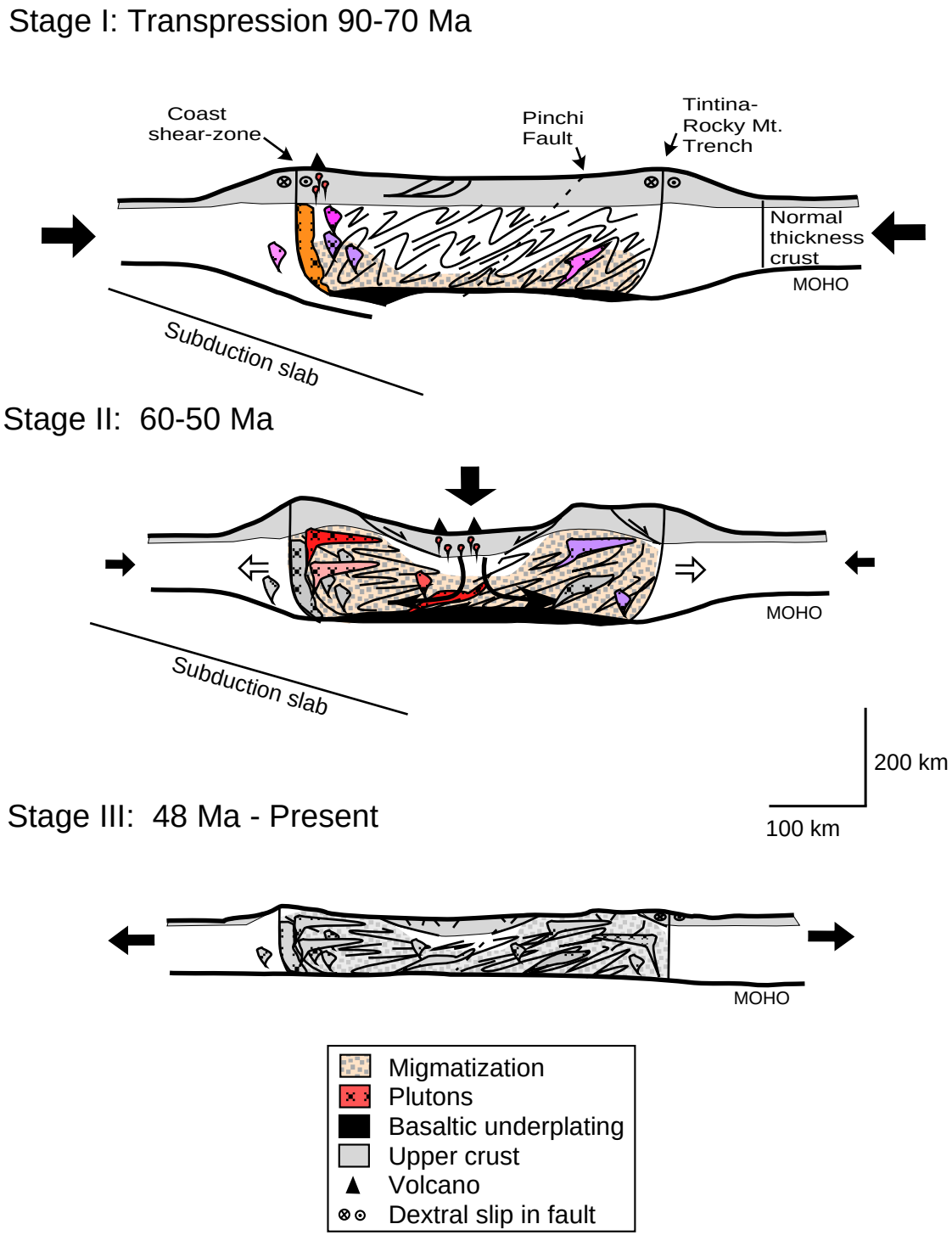

Figure 3.19: Cartoon of tectonic model for the Canadian Cordillera since the Late Cretaceous. The abundant terrane sutures present in the region are not shown on the cartoons. See text for discussion.

crust acting as a piston falling downwards generating horizontal flow away form the center of the plateau to the sides. This mechanism requires decoupling of the upper crust from the middle and lower crust, as well as decoupling of the deep crust from the mantle. The lateral flow encountered a thermal and rheological boundary when approaching the Coast shear-zone to the NW and the Tintina-Rocky Mountain trench to the NE. As a consequence the ductile rocks flowed upwards along these faults, encouraged by buoyancy forces. The lateral flow was accompanied by widespread magmatism across the whole orogen. Melting was intensified by decompression and upwelling of the asthenosphere due to crustal thinning below the interior plateau. These areas possibly represented topographic highs, supported by isostatic equilibration as a result of displacing hot material towards the sides of the orogen. New detachments (e.g. Shames River mylonite) and normally reactivated preexisting faults (e.g. Pinchi Fault) partially assisted the collapse of the orogen. N-S as well as E-W directed stretching directions, as seen in the Cascade ranges and the Coast Mountains to the north, are required to accommodate regional oblique convergence. The gravitational collapse of the orogen was responsible for orogen perpendicular stretching that resulted in SW-NE lineations, like the ones found in Wolverine, Horseranch and Shuswap ranges. At the plate margin, there is still a dextral component to the deformation that needs to be accommodated. The dextral component before the collapse of the orogen was being focused in discrete strike-slip faults, however, with a thermally softened partially-melted middle and lower crust strain should be focused into these weaker regions. This would result in orogen parallel stretching.

This model can also explain why there is a gap in high grade rocks south of the Kitlope Pluton. If the trigger for the exhumation is the collapse of the internal plateau, and crustal scale structures act as barriers to lateral extrusion by deep crustal flow, then the presence of a major structure like the Yalakolm fault in the interior plateau (Figure 3.19) would have inhibited deep crustal flow to the west. Also, as the model would predict the Tatla Lake core complex is present west of the Yalakolm fault.

Subduction stopped by 47 Ma (Haeussler et al 2003, Figure 3.19). The present thickness of the crust across the Coast to Omineca belts is ~32 km. The Moho is flatter as a consequence of lower crustal flow during the exhumation. The heat flow is high (100 mW/m^2) below the Omineca belt (Hyndman and Lewis 1999). This contrasts with a cratonic crust to the east with typical cratonic crustal heat flow of 40 mW/ m^2, 40 km of thickness and similar elevation.

X. Conclusions

The southern termination of the central gneiss complex is characterized by a long history of magmatic intrusions and upper amphibolite facies metamorphism. The exhumation of the three youngest plutonic intrusions in the area was studied: the Kitlope (61 Ma), the Quottoon (60 Ma), and the Chief Matthew's Pluton (57 Ma). Isothermal decompression of 0.2 GPa occurred between 61 and 58 Ma, at a rate of ~2-3 mm/yr. After this event, the rocks decompressed during cooling and were below the closure temperature of biotite by 51 Ma, which is an older decompression than is observed further north in the central gneiss complex.

The similarities in exhumation history found along the Coast Mountains from Cascadia to southeast Alaska, as well as coincident exhumation timing for the core complexes in the Omineca belt and Idaho batholith, support a regional tectonic cause for the distributed dextral transtension and exhumation that lead to the exposure of the middle crust. We propose that the internal plateau was a high plateau that sank into a ductile middle and lower crust. This resulted in extrusion of material at both sides because the flow found crustal-scale boundaries that prevented further lateral extrusion. To the west, the central gneiss complex is bounded by the Coast-shear zone. To the east, the core complexes abruptly end at the Tintina-Rocky Mountain trench. These two structures probably acted as barriers for the material to further flow in a NE-SW direction, this led to extrusion of the deep crust, at the these margins, at the same time material was flowing in a NW-SE direction, which accommodates the dextral component of plate-scale deformation.

REFERENCES

Anderson, J.L., Smith, D.R., 1995. The effects of temperature and fO2 on the Al-in-hornblende barometer. American Mineralogist, 80: 549-559.

Andronicos, C.L., Hollister, L.S., Davidson, C. and Chardon, D. 1999. Kinematics and tectonic significance of transpressive structures within the Coast Plutonic Complex, British Columbia. Journal of Structural Geology, 21: 229–243.

Andronicos, C.L., Chardon, D.H., Hollister, L.S., Gehrels, G.E., and Woodsworth, G.J., 2003. Strain partitioning in an obliquely convergent orogen, plutonism, and synorogenic collapse: Coast Mountains Batholith, British Columbia, Canada. Tectonics, 22(2): 1012.

Armstrong, R.L., 1982. Cordilleran metamorphic core complexes - from Arizona to southern Canada. Annual Reviews of Earth and Planetary Sciences, 10: 129-154.

Armstrong, R.L., 1988. Mesozoic and early Cenozoic magmatic evolution of the Canadian Cordillera. In: S.C. Clark, B.C. Burchfiel, J. Suppe (Eds.), Processes in Continental Lithospheric Deformation, Geological Society of America Special Paper 18: 55–91.

Bardoux, M. and Mareschal, J.C., 1994. Extension in south-central British Columbia: mechanical and thermal controls. Tectonophysics, 238: 451–470.

Bogue, S.W., Gromme, S. and Millhouse, J.W., 1995. Paleomagnetic anisotropy and mid-: Cretaceous Paleolatitude of the Outer Island (Alaska) Ultramafic complex. Tectonics, 14: 1133-1152.

Breitsprecher, Thorkelson, D.J., Groome, W.G. and Dostal, J., 2003. Geochemical confirmation of the Kula-Farallon slab window beneath the Pacific Northwest in Eocene time. Geology, 31: 351–354.

Brew, D.A. and Ford, A.B., 1978. Megalineament in southeastern Alaska marks southwest edge of coast Range batholithic complex. Canadian Journal of Earth Sciences, 15: 1763–1772.

Brown, R.L. and Journeay, J.M., 1987. Tectonic denudation of the Shuswap metamorphic terrane of southeastern British Columbia. Geology 15:142-146.

Chardon, D., Andronicos, C.L. and Hollister, L.S., 1999. Large-scale transpressive shear zone patterns and displacements within magmatic arcs: the coast plutonic complex, British Columbia. Tectonics 18, 278–292.

Cook, F.A., Varsek, J.L., Clowes, R.M., Kanasewich, E.R., Spencer, C.S., Parrish, R.R., Brown, R.L., Carr, S.D., Johnson, B.J. and Price, R.A., 1992. Lithoprobe crustal reflection cross section of the southern Canadian Cordillera, I. Foreland thrust and fold belt to Fraser River fault. Tectonics, 11: 12–35.

Coney, P.J., 1980. Cordilleran metamorphic core complexes. In: Crittenden, M.D., Coney, P.J., and Davis, G.H., (Eds.), Cordilleran Metamorphic Core Complexes, Geological Society of America Memoir, 153: 7-34.

Coney, P.J, Jones, D.L and Monger, J.W.H., 1980. Cordilleran suspect terranes. Nature, 288: 329-333.

Connolly, J.A.D. and Kerrick, D.M., 1987. An algorithm and computer program for calculating composition phase diagrams. CALPHAD 11: 1-55.

Crawford, M.L. and Hollister, L.S., 1982. Contrast of metamorphic and structural histories across the work channel lineament, coast plutonic complex, British Columbia. Journal of Geophysical Research, 87(B5): 3849-3860.

Crawford, M.L., Klepeis, K.A., Gehrels, G. and Isachsen, C., 1999. Batholith emplacement at mid-crustal levels and its exhumation within an obliquely convergent margin: The influence of granite emplacement on tectonics. Tectonophysics, 312: 57–78.

Crawford, M.L., Crawford, W.A. and Lindline, J., 2005. 105 Million years of igneous activity, Wrangell, Alaska, to Prince Rupert, British Columbia. Canadian Journal of Earth Sciences, 42: 1097–1116.

DeBari, S.M. (1999), Production of dioritic to tonalitic plutons in Cordilleran magmatic arcs by mixing of mantle-derived basaltic magmas with melts of amphibolitic lower crust. Geological Society of American, Abstracts and Programs, 18: 100–101.

Debiche, M.G., Cox, A. and Engebretson, D., 1987. The motion of allochthonous terranes across the North Pacific basin. Geological Society of America Special Paper, 207: 49.

De Capitani, B. and Brown, T.H., 1987. The computation of chemical equilibrium in complex systems containing non-ideal solutions. Geochimica et Cosmochimica Acta 51: 2639-2652.

Den Tex, E., 1963. A commentary on the correlation of metamorphism and deformation in space and time. Geology Mijnbouw, 42: 17176.

Depine, G.V., Andronicos, C.L. and Phipps-Morgan, J., 2008. Near-isothermal conditions in the middle and lower crust induced by melt migration. Nature 452: 80-83.

Ducea, M. and Barton, M.D., 2007. Igniting flare-up events in Cordilleran arcs. Geology, 35 (11): 1047-1050.

Dunlap, W.J., 2000. Nature's diffusion experiment: The cooling-rate cooling-age correlation. Geology, 28(2): 139–142.

Engebretson, D.C., Cox, A. and Gordon, R.G., 1985. Relative motions between oceanic and continental plates in the Pacific basins. Geological Society of America Special Paper, 206: 1–59.

Evenchick, C.A., 2001. Northeast-trending folds in the western Skeena Fold Belt, northern Canadian Cordillera: a record of Early Cretaceous sinistral plate convergence. Journal of Structural Geology, 23: 1123–1140.

Ewing, T.E., 1981. Regional stratigraphy and structural setting of the Kamloops Group, south-central British Columbia. Canadian Journal of Earth Sciences, 18: 1464–1477.

Ferry, J.M. and Spear, F.S., 1978. Experimental calibration of the partitioning of Fe and Mg between biotite and garnet. Contributions to Mineralogy and Petrology, 66: 113–117.

Friedman 2007. NAVDAT: http://matisse.kgs.ku.edu/navdat/NavdatSearch/OutputData.cfm?Form.pkey=4682.

Friedman and Ullrich 2007. NAVDAT: http://matisse.kgs.ku.edu/navdat/NavdatSearch/OutputData.cfm?Form.pkey=4682.

Friedman, R.M. and Armstrong, R.L., 1988. Tatla Lake metamorphic complex: An Eocene metamorphic core complex on the southwestern edge of the Intermontane Belt of British Columbia. Tectonics, 7: 1141–1166.

Frost, B.R., Chamberlain, K.R. and Schumacher, J.C., 2001. Sphene (titanite): phase relations and role as a geochronometer. Chemical Geology, 172: 131–148.

Gabrielse, H., 1985. Major dextral transcurrent displacements along the Northern Rocky Mountain Trench and related lineaments in north-central British Columbia. Geology of the Society of America Bulletin, 96: 1–14.

Ganguly, J. and Saxena, S.K., 1984. Mixing properties of aluminosilicate garnets: constraints from natural and experimental data, and applications to geothermobarometry. American Mineralogist, 69 (1–2): 88–97.

Gehrels, G.E., McClelland, W.C., Samson, S.D., Patchett, P.J. and Brew, D.A., 1991. U-Pb geochronology of Late Cretaceous and early Tertiary plutons in the northern Coast Mountains Batholith. Canadian Journal of Earth Sciences, 28: 899–911.

Gough, D.I., 1986. Mantle upflow tectonics in the Canadian Cordillera. Journal of Geophysical Research, 91: 1909–1919.

Haeussler, P.J., Bradley, D.C., Wells, R.E. and Miller, M.L. 2003. Life and death of the Resurrection plate: Evidence for its existence and subduction in the northeastern Pacific in Paleocene–Eocene time. Geological Society of America Bulletin, 115(7): 867-880.

Hamblock, J.M. 2006. Understanding the composition, origin, and evolution of the continental crust: Case studies in the southern Rio Grande rift, New Mexico, United States of Americaand the Coast Plutonic Complex, British Columbia, Canada. Doctorate dissertation, ETD Collection for University of Texas, El Paso. Paper AAI3242135.

Hames, W.E and Bowring, S.A., 1994. An empirical evaluation of the argon diffusion geometry in muscovite. Earth and Planetary Science Letters, 124: 161-167.

Hammarstrom, J.M. and Zen, E., 1986. Aluminum in hornblende: An empirical igneous geobarometer. American Mineralogist, 71: 1297-1313.

Harrison, T.M., 1981. Diffusion of ^{40}Ar in Hornblende. Contributions to Mineralogy and Petrology, 78: 324-331.

Heah, T.S.T., 1991. Mesozoic ductile shear and Paleogene extension along the eastern margin of the central gneiss complex, Coast belt, Shames River area, near Terrace, British Columbia [MS Dissertation]: University of British Columbia, BC.

Hodges, K.V. and Spear, F.S., 1982. Geothermometry, geobarometry and the Al2SiO5 triple point at Mt. Moosilauke, New Hampshire. American Mineralogist, 67: 1118–1134.

Hoisch, T.D., 1990. Empirical calibration of six geobarometers for the mineral assemblage quartz + muscovite + biotite + plagioclase + garnet. Contributions to Mineralogy and Petrology, 104: 225–234.

Hoisch, T.D., 1991. Equilibria within the mineral assemblage quartz + muscovite + biotite + garnet + plagioclase, and implications for the

mixing properties of octahedrally-coordinated cations in muscovite and biotite. Contributions to Mineralogy and Petrology, 108: 43–54.

Holland, T. and Blundy, J.D., 1990. Non-ideal interactions in calcic amphiboles and their bearing on amphibole-plagioclase thermometry. Contributions to Mineralogy and Petrology, 116: 433-447.

Holland, T. and Powell, R., 1998. An internally-consistent thermodynamic data set for phases of petrological interest. Journal of Metamorphic Geology, 16: 309–343.

Hollister, L.S., 1982. Metamorphic evidence for rapid (2 mm/yr) uplift of a portion of the Central Gneiss Complex, Coast Mountains, B.C. The Canadian Mineralogist, 20(3): 319-332.

Hollister, L.S., 1993. The role of melt in the uplift and exhumation of orogenic belts. Chemical Geology, 108(1-4): 31-48.

Hollister, L.S., Grissom, G.C., Peters, E.K., Stowell, H.H. and Sisson, V.B., 1987. Confirmation of the empirical correlation of Al in hornblende with pressure of solidification of calc-alkaline plutons. American Mineralogist, 72: 231-239.

Hollister, L.S. and Andronicos, C.L., 1997. A candidate for the Baja British Columbia Fault system in the Coast Plutonic Complex. Geological Society of America Today 7:1–7.

Hollister, L.S. and Andronicos, C.L. 2000. The Central Gneiss Complex, Coast Orogen, British Columbia. Special Paper Geological Society of America, 343: 45–59.

Hollister, L.S., Hargraves, R.B., James, T.S. and Renne, P.R., 2004. The paleomagnetic effects of reheating the Ecstall pluton, British Columbia. Earth and Planetary Science Letters, 221 (1-4): 397-407.

Hollister, L.S. and Andronicos, C.L., 2006. Formation of new continental crust in Western British Columbia during transpression and transtension. Earth and Planetary Science Letters, 249(1-2): 29-38.

Hyndman, R.D. and Lewis, T.J.,1999. Geophysical consequences of the Cordillera-Craton thermal transition. Tectonophysics, 306: 397–422.

Ingram, G.M., and Hutton, D.H.W., 1994. The Great Tonalite Sill: Emplacement into a contractional shear zone and implications for Late Cretaceous to early Eocene tectonics in southeastern Alaska and British Columbia. Geological Society of America Bulletin, 106(5): 715-728.

Irving, E., Wynne, P.J., Thorkelson, D.J. and Schiarizza, P. 1996. Large (1000 to 4000 km) northward movements of tectonic domains in the northern Cordillera, 83 to 45 Ma. Journal of Geophysical Research, 101: 901–916.

Kay, S.M., Kay, R.W., Citron, G.P. and Perfit, M.R., 1990. Calc-alkaline plutonism in the intra-oceanic Aletian arc, Alaska. In: Kay, S.M. and Rapela, C.W. (eds.), Plutonism from Antartica to Alaska, Geological Society of America Special Paper, 241: 233-255.

Kenah, C. and Hollister, L.S. 1983. Anatexis in the Central Gneiss Complex, British Columbia. In Migmatites, Melting and Metamorphism; Proceedings of Meeting on High Grade Metamorphism, Migmatites and Melting of the Geochemical Group of the Mineralogical Society of the University of Glasgow, edited by M. P. Atherton and C. D. Gribble: 142–162, Shiva, Nantwich, U.K.

Klepeis, K.A., Crawford, M.L. and Gehrels, G., 1998. Structural history of the crustal-scale Coast shear zone north of Portland Canal, southeast Alaska and British Columbia. Journal of Structural Geology, 20: 883–904.

Klepeis, K.A. and Crawford, M.L., 1999. High-temperature arc-parallel normal faulting and transtension at the roots of an obliquely convergent orogen. Geology, 27(7–10).

Lonsdale, P. 1988. Paleogene history of the Kula plate: Offshore evidence and onshore implications. Geological Society America Bulletin, 100: 733–754.

Miller, R.B. and Bowring, S.A., 1990. Structure and chronology of the Oval Peak batholith and adjacent rocks: Implications for the Ross Lake fault zone, North Cascades, Washington. Geological Society of America Bulletin, 102: 1361–1377.

Molnar, P. and Lyon-Caen, H., 1988. Some simple physical aspects of the support, structure, and evolution of mountain belts. Geological Society of America Special Paper, 218: 179-207.

Monger, J.W.H., Price, R.A. and Tempelman-Kluit, D.J., 1982. Tectonic accretion and the origin of the two major metamorphic and plutonic welts in the Canadian Cordillera. Geology 10: 70–75.

Morozov, I.B., Smithson, S.B., Chen, J. and Hollister, L.S., 2001. Generation of new continental crust and terrane accretion in southeastern Alaska and western British Columbia: constraints from P- and S-wave wide-angle seismic data (ACCRETE). Tectonophysics, 341: 49–67.

Mulch, A., Teyssier, C., Cosca, M.A., and Chamberlain, C.P., 2007. Stable isotope paleoaltimetry of Eocene Core Complexes in the North American Cordillera. Tectonics: doi:10.1029/2006TC001995.

Nakamura N. 1974. Determination of REE, Ba, Fe, Mg, Na and K in carbonaceous and ordinary chondrites. Geochemica et Cosmochimica Acta, 38: 757 775.

Powell, R., Holland, T.J.B. and Worley, B., 1998. Calculating phase diagrams with THERMOCALC: methods and examples. Journal of Metamorphic Geology, 16: 577–588.

Paterson, S.R., Miller, R.B., Alsleben, H., Whitney, D.L., Valley, P.M. and Hurlow, H., 2004. Driving mechanisms for >40 km of exhumation during contraction and extension in a continental arc, Cascades core, Washington, Tectonics 23: TC3005.

Parrish, R.R., Carr, S.D. and Parkinson, D.L. 1988. Eocene Extensional Tectonics and Geochronology of the southern Omineca Belt, British Columbia and Washington. Tectonics, 7: 181–212.

Plint, H.E., Erdmer, P., Reynolds, P.H. and Grist, A.M. 1992. Eocene tectonics in the Omineca Belt, northern British Columbia, Canada: Field, 40Ar/39Ar, and fission track data from the Horseranch Range. Geological Society of America Bulletin, 104: 106–116.

Price, R.A. and Carmichael, D.M., 1986. Geometric test for Late Cretaceous-Paleogene intracontinental transform faulting in the Canadian Cordillera. Geology, 14: 468–471.

Rusmore, M.E., Gehrels, G., Woodsworth, G.J., 2001. Southern continuation of the Coast shear zone and Paleocene strain partitioning in British Columbia–southeast Alaska. Geological Society America Bulletin, 113(8): 961-975.

Rusmore, M. E., Woodsworth, G. J. and Gehrels, G. E. 2005. Two-stage exhumation of midcrustal arc rocks, Coast Mountains, British Columbia. Tectonics, 24: TC5013.

Selverstone, J. and Hollister, L.S., 1980. Cordierite-bearing granulites from the Coast Ranges, British Columbia; P-T conditions of metamorphism. Canadian Mineralogist, 18: 119–129.

Schmidt, M.W., 1992. Amphibole composition in tonalite as a function of pressure: An experimental calibration of the Al-in-hornblende barometer. Contributions to Mineralogy and Petrology, 110: 304-310.

Sonder, L.J., England, P.C., Wernicke, B.P. and Christiansen, R.L., 1987. A physical model for Cenozoic extension of western North America. In: Conward, M.P., Dewey, J.F., Hancock, P.L. (Eds.). Continental Extensional Tectonics, Geological Society of London Special Publication, 28: 187–201.

Spear, F.S., 1993. Metamorphic Phase Equilibria and Pressure-Temperature-Time Paths. Mineralogical Society of America, Washington, D. C.

Stowell, H.H. and Stein, E., 2005. The significance of plagioclase-dominant coronas on garnet, Wenatchee block, northern Cascades, Washington, USA. The Canadian Mineralogist, 43: 367-385.

Stowell, H.H. and Crawford, M.L., 2000. Metamorphic history of the Coast Mountains orogen, western British Columbia and southeastern Alaska. In Tectonics of the Coast Mountains, Southeastern Alaska and British Columbia, Stowell, H.H. and McClelland, W.C. (eds.), Special Paper of the Geological Society of America, 343: 257–284.

Struik, L.C., 1992. Intersecting intracontinental Tertiary transform fault systems in the North American Cordillera. Canadian Journal of Earth Sciences, 30: 1262–1274.

Sun, S.S., McDonough, W.F. and Ewart, A., 1989. Four component dynamic model for East Australian basalts. In: R.W. Johnson (ed.), Intraplate Volcanism in Eastern Australia and New Zealand, Cambridge University Press: 333–347.

Tiepolo, M., Oberti, R. and Vannucci, R., 2002. Trace-element incorporation in titanite: constraints from experimentally determined solid/liquid partition coefficients. Chemical Geology, 191: 103–117.

Thomas, J.B. and Sinha, A.K. 1999. Field, geochemical, and isotopic evidence for magma mixing and assimilation and fractional crystallization processes in the Quottoon igneous complex, northwestern British Columbia and southeastern Alaska. Canadian Journal of Earth Science, 36: 819–831.

Thompson, A.B., Schulman, K. and Jezek, J., 1997. Extrusion tectonics and elevation of lower crustal metamorphic rocks in convergent orogens. Geology, 25(6): 491-494.

Thorkelson, D.J., Taylor, R.P., 1989. Cordilleran slab windows. Geology, 17: 833-836.

Valley, P.M., Whitney, D.L., Paterson, S.R., Miller, R.B. and Alsleben, H., 2003. Metamorphism of deepest exposed rocks in the Cretaceous and Paleogene Cascades belt, Washington: Evidence for large-scale vertical motion in a continental margin arc. Journal of Metamorphic Geology, 21: 203–220.

Vanderhaeghe, O., Teyssier, C., McDougall, I. and Dunlap, W.J. 2003. Cooling and exhumation of the Shuswap Metamorphic Core Complex constrained by $^{40}Ar/^{39}Ar$ thermochronology. Geological Society Society of America Bulletin, 115(2): 200-216.

Van der Heyden, P., 1989. U-Pb and K-Ar geochronometry of the Coast Plutonic complex, 53°N to 54°N, British Columbia, and implications for the Insular-Intermontane Superterrane boundary. Doctoral thesis, University of British Columbia, Canada.

Vernon, R.H. 1983. Restite, xenoliths and microgranitoid enclaves in granites. Journal and Proceedings, Royal Society of New South Wales, 116(3-4): 77-103.

Wanless, R.K., Stevens, R.D., Lachance, G.R. and Delabio, R.N. 1970. Age determinations and geological studies: K-Ar isotopic ages. Report 9, Geological Survey of Canada, Paper 69-2.

Wanless, R.K., Stevens, R.D., Lachance, G.R. and Delabio, R.N. 1973. Age determinations and geological studies: K-Ar isotopic ages. Report 11, Geological Survey of Canada, Paper 73-2.

Wanless, R.K., Stevens, R.D., Lachance, G.R. and Delabio, R.N. 1978. Age determinations and geological studies: K-Ar isotopic ages. Report 13, Geological Survey of Canada, Paper 77-2.

Wanless, R.K., Stevens, R.D., Lachance, G.R. and Delabio, R.N. 1979. Age determinations and geological studies: K-Ar isotopic ages. Report 9, Geological Survey of Canada, Paper 79-2.

Whitney, D.L., 1992. High-pressure metamorphism in the western Cordillera of North America: An example from the Skagit Gneiss, North Cascades. Journal of Metamorphic Geology, 10: 71–85.

Whitney, D.L., Miller, R.B. and Paterson, S.R., 1999. P-T-t evidence for mechanisms of vertical tectonic motion in a contractional orogen; north-western US and Canadian Cordillera. Journal of Metamorphic Geology, 17: 75-90.

Wernicke, B. and Getty, S.R., 1997. Intracrustal subduction and gravity currents in the deep crust: Sm-Nd, Ar-Ar, and thermobarometric constraints from the Skagit Gneiss Complex, Washington. Geological Society of America Bulletin, 109: 1149-1166.

APPENDIX: Mineral composition of sample 06B18.

	Hornblende									Plagioclase						
	Core								Rim	Rim						
SiO2	43.57	43.43	42.68	43.00	42.96	43.63	43.67	43.73	44.08	62.52	62.34	62.41	63.66	62.14	62.27	62.02
Al2O3	13.57	12.09	12.72	11.09	10.94	11.01	10.85	10.73	11.33	24.95	25.72	25.28	25.53	25.11	24.82	24.80
K2O	1.45	1.28	1.47	1.24	1.22	1.21	1.19	1.14	0.99	0.21	0.23	0.24	0.26	0.25	0.22	0.23
FeO	18.09	18.08	18.79	20.03	20.58	20.31	19.82	19.95	19.53	0.43	0.42	0.38	0.29	0.24	0.22	0.19
MgO	9.35	9.59	9.21	9.26	9.30	9.34	9.40	9.49	8.59	0.02	0.02	0.00	0.02	0.00	0.00	0.00
CaO	11.46	11.74	11.61	11.62	11.44	11.49	11.50	11.59	11.14	5.74	5.73	5.70	5.63	5.74	5.74	5.71
Na2O	1.23	1.24	1.35	1.32	1.39	1.36	1.33	1.43	1.54	7.79	7.64	8.06	7.66	7.63	7.43	7.78
TiO2	0.66	0.60	0.69	0.68	0.66	0.65	0.62	0.61	0.50	0.00	0.01	0.01	0.01	0.01	0.01	0.00
Total	99.38	98.04	98.51	98.25	98.49	98.99	98.37	98.65	97.69	101.65	102.12	102.08	103.05	101.12	100.70	100.73

	Plagioclase							Hornblende							Plag
							Core	Core						Rim	Rim
SiO2	62.18	62.39	62.26	62.15	61.83	62.06	62.21	42.30	43.46	42.76	43.13	42.70	43.03	43.17	42.73	65.96
Al2O3	24.99	24.86	24.94	25.04	25.00	25.10	25.09	10.14	11.03	10.70	11.02	10.86	11.05	10.96	10.56	22.73
K2O	0.24	0.24	0.20	0.18	0.16	0.19	0.19	1.16	1.23	1.23	1.25	1.24	1.25	1.25	1.17	0.11
FeO	0.21	0.18	0.18	0.24	0.17	0.18	0.15	19.45	20.61	19.98	20.14	20.39	20.16	20.07	19.70	0.33
MgO	0.00	0.00	0.00	0.02	0.00	0.00	0.00	9.80	9.54	9.52	9.36	9.32	9.32	9.25	9.43	0.01
CaO	5.81	5.73	5.73	5.64	5.74	5.77	5.67	11.46	11.59	11.55	11.55	11.57	11.43	11.56	11.54	3.06
Na2O	7.44	7.53	7.76	7.75	7.69	7.74	7.65	1.41	1.45	1.40	1.43	1.48	1.41	1.32	1.32	8.88
TiO2	0.01	0.02	0.02	0.00	0.01	0.01	0.01	0.62	0.65	0.65	0.65	0.66	0.65	0.64	0.56	0.01
Total	100.88	100.94	101.09	101.02	100.60	101.04	100.97	96.34	99.55	97.79	98.53	98.22	98.30	98.21	97.01	101.08

	Plagioclase									Hornblende					Plag
									Core	Core				Rim	Rim
SiO2	62.62	62.17	61.95	62.10	62.35	62.31	62.76	61.75	62.11	61.95	42.69	35.63	41.81	44.83	29.73	59.66
Al2O3	24.57	24.33	24.48	24.69	24.44	24.76	24.42	24.31	24.61	24.43	11.48	9.04	10.96	11.46	2.11	24.16
K2O	0.18	0.24	0.29	0.29	0.30	0.31	0.30	0.27	0.26	0.22	1.23	1.12	1.20	1.03	0.01	0.19
FeO	0.33	0.28	0.22	0.24	0.18	0.23	0.20	0.13	0.11	0.15	20.64	19.11	20.26	19.51	1.32	0.15
MgO	0.00	0.01	0.00	0.00	0.01	0.01	0.00	0.00	0.00	0.01	9.60	8.90	9.59	10.16	0.01	0.00
CaO	5.32	5.25	5.33	5.22	5.33	5.31	5.32	5.29	5.30	5.32	11.56	11.39	11.70	11.06	28.24	6.01
Na2O	7.82	7.84	7.86	7.64	7.71	7.78	7.75	7.51	7.72	7.87	1.31	1.13	1.37	1.45	0.03	7.58
TiO2	0.00	0.00	0.01	0.01	0.00	0.02	0.01	0.00	0.00	0.00	0.68	0.63	0.70	0.84	35.52	0.14
Total	100.83	100.12	100.15	100.19	100.33	100.71	100.75	99.26	100.12	99.96	99.18	86.96	97.59	100.34	96.97	97.89

APPENDIX: Mineral composition of sample 06B18.

	Plagioclase		Core	Hornblende				Rim	Rim	Plagioclase						
SiO2	59.78	59.33	59.43	41.84	42.27	41.20	39.94	52.13	60.25	61.08	60.97	60.18	60.68	60.85	60.60	60.04
Al2O3	24.40	24.20	24.46	11.27	11.36	11.48	11.69	20.92	24.73	24.36	24.36	24.23	24.31	24.64	24.27	24.33
K2O	0.21	0.22	0.22	1.17	1.15	1.21	1.30	0.64	0.36	0.21	0.21	0.22	0.24	0.26	0.27	0.25
FeO	0.15	0.07	0.13	20.58	20.50	20.88	20.70	5.71	0.54	0.41	0.36	0.32	0.34	0.28	0.23	0.20
MgO	0.01	0.01	0.00	8.81	9.20	8.60	7.81	1.48	0.03	0.01	0.00	0.01	0.01	0.00	0.01	0.01
CaO	5.98	5.90	5.84	11.69	11.69	11.69	11.33	5.56	6.30	5.67	5.64	5.59	5.52	5.55	5.61	5.72
Na2O	7.58	7.40	7.55	1.19	1.22	1.27	1.16	6.64	7.63	7.86	8.01	7.90	7.87	8.01	7.85	7.64
TiO2	0.07	0.03	0.01	0.49	0.48	0.44	0.47	0.16	0.01	0.00	0.01	0.03	0.01	0.00	0.02	0.00
Total	98.17	97.14	97.63	97.04	97.88	96.76	94.40	93.22	99.84	99.60	99.56	98.46	98.97	99.59	98.84	98.19

	Plagioclase						Core	Biotite								
SiO2	60.70	60.05	60.28	60.20	60.35	60.04	58.90	36.57	36.25	30.45	32.99	36.85	36.14	36.02	36.38	37.69
Al2O3	24.64	24.05	24.33	24.36	24.32	24.70	23.97	15.13	15.26	15.37	15.93	15.79	15.54	15.47	14.92	17.11
K2O	0.25	0.25	0.26	0.25	0.24	0.23	0.24	9.63	9.42	6.34	7.05	9.01	7.14	8.72	7.84	7.88
FeO	0.21	0.26	0.26	0.30	0.32	0.40	0.37	20.51	20.38	17.51	19.03	20.08	19.57	20.23	18.62	20.08
MgO	0.01	0.00	0.01	0.00	0.02	0.00	0.01	10.66	11.24	8.24	10.79	11.83	11.06	11.56	10.07	11.91
CaO	5.78	5.67	5.73	5.83	5.75	5.68	5.67	0.06	0.05	0.65	0.43	0.16	2.23	0.22	3.47	0.22
Na2O	7.62	7.61	7.84	7.84	7.88	7.64	7.69	0.06	0.07	0.13	0.14	0.09	0.08	0.04	0.07	0.07
TiO2	0.00	0.01	0.00	0.00	0.00	0.01	0.01	2.65	2.61	12.16	10.07	2.66	5.18	2.55	5.10	2.66
Total	99.20	97.90	98.71	98.79	98.87	98.71	96.85	95.26	95.28	90.86	96.41	96.47	96.93	94.82	96.46	97.62

	Biotite										
SiO2	37.45	36.64	37.37	36.92	36.33	35.95	36.82	36.88	37.02	36.72	38.41
Al2O3	15.61	15.33	15.63	14.88	14.91	14.57	15.11	15.56	15.43	15.24	15.90
K2O	9.82	9.75	9.74	9.75	9.77	9.69	9.67	9.49	9.61	9.60	9.61
FeO	20.11	20.51	20.80	20.75	20.83	19.99	20.47	19.76	20.23	19.86	20.84
MgO	11.66	11.22	11.25	11.56	11.17	11.47	11.89	11.82	11.62	11.25	12.68
CaO	0.06	0.05	0.07	0.06	0.08	0.07	0.10	0.07	0.06	0.30	0.09
Na2O	0.09	0.06	0.07	0.08	0.07	0.06	0.08	0.06	0.07	0.08	0.08
TiO2	2.72	2.64	2.56	2.50	2.48	2.45	2.36	2.31	2.30	2.54	2.35
Total	97.52	96.19	97.48	96.50	95.64	94.24	96.51	95.95	96.34	95.59	99.96

APPENDIX: Mineral Composition of sample 06B19.

	Hornblende									Plagioclase						
	Core								Rim	Rim						
SiO2	43.66	43.80	44.24	44.59	44.84	44.41	44.50	44.08	43.93	61.67	60.29	62.17	61.51	61.51	59.20	60.94
Al2O3	11.29	11.28	10.87	10.30	10.27	10.22	9.93	9.91	9.79	25.53	24.50	25.39	25.33	25.43	24.32	25.58
K2O	1.21	1.19	1.10	1.02	1.01	0.97	0.95	0.92	0.90	0.20	0.75	0.25	0.25	0.26	0.28	0.26
FeO	18.36	18.62	18.49	17.69	17.57	17.71	17.91	17.73	17.66	0.47	1.44	0.45	0.45	0.33	0.81	0.20
MgO	10.11	10.04	10.30	10.67	10.57	10.74	10.75	10.79	10.87	0.02	0.61	0.01	0.00	0.01	0.36	0.01
CaO	11.67	11.60	11.67	11.76	11.75	11.61	11.78	11.68	11.30	6.24	5.64	5.94	6.08	6.06	6.98	6.10
Na2O	1.31	1.25	1.26	1.24	1.17	1.16	1.13	1.22	1.28	7.78	7.20	7.67	7.41	7.70	7.25	7.71
TiO2	0.66	0.65	0.60	0.58	0.56	0.58	0.57	0.53	0.44	0.03	0.02	0.01	0.02	0.02	0.02	0.01
Total	98.26	98.43	98.54	97.84	97.75	97.40	97.52	96.86	96.16	101.94	100.44	101.88	101.04	101.30	99.22	100.80

	Plagioclase		Hornblende									Plagioclase				
		Core	Core								Rim	Rim				
SiO2	61.16	61.50	44.42	44.55	45.70	45.80	43.46	44.77	43.98	46.23	45.81	46.95	60.57	61.01	61.24	61.34
Al2O3	25.46	25.49	10.10	10.21	9.11	9.25	10.64	9.65	9.13	8.56	9.07	11.01	24.83	25.26	25.10	25.16
K2O	0.27	0.29	0.92	0.98	0.82	0.80	1.19	0.94	0.79	0.71	0.71	0.88	0.26	0.26	0.27	0.27
FeO	0.22	0.20	17.94	18.01	17.67	17.55	18.00	18.05	17.55	17.20	17.63	17.94	0.18	0.10	0.12	0.15
MgO	0.01	0.00	10.74	10.61	11.25	11.39	10.25	10.70	10.45	11.55	11.17	10.07	0.01	0.00	0.01	0.01
CaO	6.09	5.92	11.63	11.79	11.74	11.81	11.68	11.75	11.59	11.85	11.73	11.08	6.18	6.06	6.05	6.07
Na2O	7.54	7.53	1.27	1.21	1.04	0.98	1.14	1.11	0.91	0.94	1.04	1.06	7.69	7.51	7.71	7.72
TiO2	0.01	0.00	0.50	0.52	0.46	0.48	0.66	0.49	0.45	0.40	0.41	0.51	0.01	0.00	0.01	0.01
Total	100.75	100.94	97.52	97.86	97.79	98.03	97.01	97.46	94.85	97.43	97.55	99.49	99.72	100.20	100.51	100.72

	Plagioclase						Hornblende					Plagioclase				
						Core	Core				Rim	Rim				Core
SiO2	61.17	61.13	60.89	61.28	61.04	62.11	45.98	43.51	43.16	42.50	42.20	60.31	60.51	60.46	60.34	61.29
Al2O3	25.32	25.14	25.17	25.13	25.22	25.62	11.52	10.61	10.57	10.53	10.74	24.70	24.91	24.85	25.00	24.96
K2O	0.27	0.27	0.27	0.27	0.25	0.22	1.04	1.06	1.11	1.09	1.09	0.28	0.28	0.29	0.16	0.20
FeO	0.13	0.11	0.19	0.12	0.23	0.23	18.70	19.08	19.16	19.40	19.44	0.20	0.14	0.16	0.07	0.08
MgO	0.00	0.00	0.00	0.00	0.00	0.01	11.57	10.25	10.16	10.03	9.96	0.00	0.00	0.00	0.00	0.00
CaO	6.12	6.07	6.15	5.96	6.05	6.08	11.26	11.65	11.74	11.72	11.67	5.99	5.92	5.95	6.24	5.99
Na2O	7.63	7.55	7.66	7.75	7.79	8.00	1.43	1.21	1.22	1.13	1.15	7.73	7.54	7.61	7.58	7.80
TiO2	0.01	0.00	0.00	0.00	0.00	0.00	0.61	0.59	0.62	0.61	0.62	0.00	0.00	0.02	0.01	0.00
Total	100.66	100.27	100.33	100.50	100.58	102.26	102.10	97.94	97.73	97.02	96.87	99.20	99.30	99.34	99.40	100.32

APPENDIX: Mineral Composition of sample 06B19.

	Biotite															
SiO2	37.56	37.38	36.99	37.00	37.52	36.84	37.81	37.37	37.21	37.23	37.18	37.35	37.29	36.80	36.93	37.27
Al2O3	15.99	15.57	15.58	15.53	15.72	15.68	15.82	15.62	15.51	15.47	15.47	15.57	15.59	15.35	15.43	15.98
K2O	9.78	9.67	9.68	9.78	9.75	9.68	9.73	9.72	9.67	9.68	9.68	9.72	9.66	9.71	9.71	9.48
FeO	18.89	19.08	19.11	19.33	19.11	19.37	19.46	19.58	19.46	19.47	19.67	19.74	19.65	19.54	19.26	19.05
MgO	11.97	12.06	12.29	12.19	11.87	11.94	12.09	12.09	12.47	12.20	12.20	12.11	12.14	11.89	11.99	12.10
CaO	0.06	0.07	0.04	0.03	0.05	0.04	0.05	0.02	0.05	0.03	0.06	0.04	0.04	0.06	0.04	0.10
Na2O	0.12	0.09	0.10	0.08	0.11	0.09	0.10	0.09	0.08	0.09	0.06	0.09	0.10	0.08	0.11	0.12
TiO2	2.81	2.84	2.80	2.81	2.78	2.82	2.73	2.76	2.72	2.73	2.76	2.72	2.73	2.74	2.73	2.77
Total	97.18	96.76	96.57	96.75	96.91	96.46	97.78	97.25	97.15	96.89	97.07	97.34	97.19	96.16	96.20	96.87

	Biotite			
SiO2	36.95	36.72	37.36	37.02
Al2O3	15.69	15.79	15.81	15.89
K2O	9.70	9.63	9.73	9.39
FeO	19.25	19.64	19.12	19.07
MgO	11.92	12.14	12.04	12.31
CaO	0.06	0.04	0.01	0.11
Na2O	0.09	0.09	0.08	0.12
TiO2	2.77	2.69	2.72	2.68
Total	96.43	96.74	96.86	96.58

APPENDIX: Mineral Composition of sample 06B15.

	Hornblende												Plagioclase			
	Core											Rim	Rim			
SiO2	43.57	43.43	42.68	42.18	41.68	41.92	42.33	42.18	42.33	42.64	42.01	42.26	61.23	62.05	61.75	61.71
Al2O3	13.57	12.09	12.72	12.86	13.05	12.80	12.97	12.77	12.55	12.45	12.91	12.90	25.03	25.51	25.89	25.88
K2O	1.45	1.28	1.47	1.53	1.57	1.58	1.58	1.58	1.53	1.48	1.53	1.50	0.26	0.25	0.24	0.24
FeO	18.09	18.08	18.79	18.40	19.12	18.89	19.33	18.79	19.03	18.72	19.17	19.19	0.23	0.20	0.18	0.22
MgO	9.35	9.59	9.21	9.09	8.95	8.85	9.07	8.74	8.90	9.17	8.89	8.75	0.01	0.01	0.00	0.00
CaO	11.46	11.74	11.61	11.59	11.63	11.62	11.54	11.75	11.65	11.64	11.71	11.69	6.24	6.38	6.65	6.84
Na2O	1.23	1.24	1.35	1.37	1.37	1.35	1.40	1.32	1.30	1.30	1.39	1.28	8.07	7.74	7.43	7.10
TiO2	0.66	0.60	0.69	0.74	0.72	0.73	0.70	0.67	0.64	0.58	0.55	0.42	0.01	0.00	0.00	0.00
Total	99.38	98.04	98.51	97.75	98.10	97.74	98.92	97.80	97.92	97.97	98.15	97.99	101.07	102.14	102.13	101.99

	Plagioclase			Hornblende									Plagioclase			
	Core			Core								Rim	Rim			
SiO2	61.29	61.60	61.36	41.87	42.14	42.35	42.05	42.33	42.28	42.45	42.99	54.04	60.23	60.34	60.41	61.03
Al2O3	25.95	26.03	25.32	12.45	12.85	12.74	12.53	12.73	12.60	12.59	12.17	23.48	27.06	26.95	26.42	26.39
K2O	0.24	0.27	1.73	1.56	1.56	1.57	1.54	1.57	1.54	1.51	1.39	0.39	0.24	0.27	0.25	0.29
FeO	0.19	0.20	0.19	18.68	18.74	18.98	19.54	18.85	18.61	18.32	18.09	3.34	0.34	0.24	0.18	0.21
MgO	0.00	0.00	0.00	8.82	8.80	8.83	8.75	8.85	8.89	8.76	9.00	1.19	0.01	0.02	0.01	0.01
CaO	6.93	6.87	6.39	11.61	11.68	11.74	11.50	11.65	11.55	11.66	11.67	8.33	7.78	7.81	7.18	7.33
Na2O	7.46	7.41	6.69	1.27	1.36	1.31	1.34	1.33	1.30	1.33	1.33	6.00	6.97	6.98	6.59	7.20
TiO2	0.01	0.01	0.01	0.74	0.73	0.75	0.72	0.72	0.71	0.69	0.63	0.09	0.01	0.00	0.01	0.01
Total	102.08	102.38	101.67	96.99	97.86	98.27	97.96	98.03	97.48	97.30	97.29	96.85	102.63	102.61	101.04	102.48

	Plagioclase															Core
SiO2	61.44	61.66	61.12	61.01	60.86	60.78	61.47	61.65	62.08	62.03	62.29	62.62	61.91	62.33	62.71	62.23
Al2O3	26.26	26.35	26.42	26.47	26.62	26.71	26.85	25.47	25.59	25.65	25.44	25.77	25.55	25.50	25.83	25.87
K2O	0.23	0.29	0.28	0.26	0.27	0.30	0.30	0.26	0.28	0.28	0.27	0.27	0.29	0.28	0.26	0.26
FeO	0.17	0.12	0.16	0.14	0.14	0.15	0.11	0.09	0.16	0.16	0.20	0.11	0.17	0.17	0.25	0.27
MgO	0.01	0.00	0.00	0.01	0.00	0.01	0.00	0.01	0.00	0.00	0.00	0.00	0.00	0.02	0.00	0.01
CaO	7.03	7.02	7.10	7.16	7.18	7.27	7.30	6.32	6.35	6.18	6.24	6.30	6.36	6.25	6.30	6.36
Na2O	7.17	7.30	7.20	7.14	6.92	7.09	7.17	7.71	7.53	7.50	7.47	7.52	7.62	7.82	7.63	7.65
TiO2	0.00	0.00	0.00	0.00	0.00	0.00	0.00	0.00	0.01	0.00	0.00	0.01	0.00	0.00	0.01	0.00
Total	102.31	102.74	102.29	102.20	102.00	102.30	103.19	101.51	101.99	101.81	101.91	102.59	101.90	102.37	103.00	102.65

APPENDIX: Mineral Composition of sample 06B22.

	Hornblende															
	Core															
SiO2	42.66	42.01	39.03	41.64	41.70	43.09	42.38	42.25	42.47	42.50	42.29	42.23	42.18	41.91	42.68	42.37
Al2O3	10.79	11.62	11.56	11.56	11.63	11.96	11.35	11.64	11.53	11.54	11.58	11.55	11.53	11.52	11.91	11.84
K2O	1.38	1.61	1.54	1.60	1.56	1.58	1.57	1.55	1.55	1.53	1.57	1.55	1.54	1.55	1.56	1.58
FeO	22.25	21.59	21.00	21.69	21.90	21.79	22.11	21.83	21.93	22.21	21.62	21.98	21.68	21.49	21.42	22.09
MgO	8.17	7.60	8.44	7.70	7.76	7.94	7.71	7.66	7.78	7.64	7.72	7.83	7.54	7.59	7.73	7.59
CaO	11.45	11.41	10.99	11.41	11.30	11.40	11.33	11.36	11.33	11.49	11.27	11.38	11.26	11.29	11.22	11.43
Na2O	1.38	1.37	1.63	1.43	1.36	1.40	1.45	1.42	1.36	1.45	1.40	1.48	1.44	1.38	1.45	1.43
TiO2	1.20	1.17	1.12	1.18	1.21	1.22	1.20	1.22	1.23	1.21	1.23	1.24	1.23	1.24	1.25	1.24
Total	99.28	98.38	95.31	98.21	98.42	100.39	99.08	98.93	99.16	99.56	98.69	99.24	98.40	97.97	99.22	99.57

	Hornblende															
																Rim
SiO2	42.64	42.72	42.61	42.61	42.65	41.54	42.21	41.71	41.98	42.14	42.52	41.90	41.46	41.77	41.10	42.90
Al2O3	11.79	11.63	11.75	11.81	11.80	12.15	11.52	11.43	11.65	11.58	11.04	11.72	11.81	11.72	11.72	12.58
K2O	1.58	1.57	1.59	1.60	1.62	1.49	1.47	1.48	1.46	1.50	1.38	1.49	1.47	1.43	1.35	1.39
FeO	22.31	21.82	22.16	22.05	22.22	21.61	21.88	22.23	22.23	22.03	22.46	22.57	22.20	22.51	21.07	21.78
MgO	7.73	7.60	7.76	7.62	7.65	7.55	7.92	7.83	7.97	7.96	8.05	7.75	7.56	7.68	7.49	6.94
CaO	11.30	11.21	11.35	11.24	11.27	11.21	11.46	11.46	11.58	11.51	11.54	11.47	11.61	11.56	11.46	11.26
Na2O	1.46	1.45	1.44	1.48	1.50	1.26	1.26	1.20	1.24	1.32	1.30	1.32	1.26	1.28	1.23	1.41
TiO2	1.25	1.25	1.24	1.24	1.24	0.95	1.01	0.98	1.00	1.00	0.92	0.92	0.87	0.78	0.77	0.70
Total	100.05	99.24	99.89	99.65	99.96	97.75	98.73	98.32	99.11	99.05	99.20	99.13	98.25	98.72	96.18	98.96

	Plagioclase															
SiO2	62.16	62.77	62.86	62.78	62.24	62.14	62.27	62.20	62.55	62.17	62.25	62.27	62.14	62.54	62.14	62.28
Al2O3	24.59	24.67	24.42	24.19	24.31	24.33	24.28	24.44	24.25	24.10	24.26	24.27	23.96	24.02	23.98	24.16
K2O	0.16	0.23	0.22	0.21	0.21	0.25	0.26	0.28	0.16	0.22	0.23	0.11	0.10	0.14	0.12	0.25
FeO	0.28	0.18	0.15	0.07	0.09	0.14	0.17	0.11	0.10	0.09	0.14	0.09	0.07	0.11	0.14	0.12
MgO	0.01	0.00	0.00	0.00	0.01	0.00	0.00	0.00	0.01	0.00	0.01	0.00	0.00	0.00	0.02	0.00
CaO	5.40	5.38	5.30	5.34	5.27	5.28	5.25	5.38	5.33	5.37	5.31	5.38	4.91	5.23	5.29	5.34
Na2O	8.01	8.36	8.11	8.40	8.04	8.29	8.15	8.28	8.16	8.19	8.43	8.02	6.99	8.22	8.15	8.21
TiO2	0.02	0.01	0.00	0.00	0.02	0.01	0.00	0.00	0.01	0.00	0.01	0.00	0.01	0.01	0.00	0.01
Total	100.61	101.59	101.07	100.99	100.19	100.44	100.37	100.68	100.57	100.14	100.64	100.13	98.19	100.26	99.83	100.37

APPENDIX: Mineral Composition of sample 06B22.

	Plagioclase		K-Feldspar						Biotite							
SiO2	62.02	61.95	64.96	65.48	65.11	65.18	64.97	64.94	36.58	37.91	37.13	36.84	36.85	35.86	36.92	32.45
Al2O3	24.48	24.04	19.42	19.21	19.56	19.41	19.30	19.45	15.26	15.99	15.47	15.55	15.40	14.90	15.51	13.44
K2O	0.24	0.26	14.65	14.99	14.28	15.02	15.03	14.73	9.84	9.88	9.82	9.55	9.72	9.60	9.57	8.67
FeO	0.11	0.10	0.04	0.04	0.04	0.02	0.09	0.19	22.29	22.01	21.76	22.02	21.89	21.51	21.53	20.26
MgO	0.01	0.01	0.00	0.00	0.00	0.00	0.00	0.00	10.00	10.26	10.23	10.22	10.29	10.08	10.13	9.14
CaO	5.34	5.36	0.01	0.02	0.05	0.02	0.03	0.03	0.08	0.08	0.10	0.11	0.07	0.10	0.10	0.13
Na2O	7.19	7.90	0.88	1.23	1.39	1.26	1.08	1.02	0.11	0.12	0.12	0.11	0.10	0.13	0.12	0.12
TiO2	0.00	0.01	0.02	0.01	0.03	0.03	0.02	0.02	1.90	2.02	2.07	2.12	2.19	2.21	2.22	2.09
Total	99.38	99.62	99.98	100.98	100.46	100.95	100.52	100.36	96.06	98.25	96.69	96.52	96.51	94.39	96.09	86.29

	Biotite											
SiO2	33.06	32.84	34.17	36.21	36.31	37.02	36.76	37.17	36.94	36.99	36.55	37.47
Al2O3	14.18	14.00	14.42	15.28	15.43	15.86	15.26	15.63	15.53	15.44	15.52	15.90
K2O	8.61	8.45	9.10	9.85	9.36	9.71	9.87	10.01	9.92	9.88	9.74	9.92
FeO	21.01	21.86	20.46	22.20	21.99	23.20	21.96	22.06	22.51	22.20	22.01	22.03
MgO	9.17	9.25	9.59	10.06	9.79	10.16	9.86	10.12	10.07	10.06	9.75	10.28
CaO	0.18	0.12	0.10	0.03	0.14	0.08	0.10	0.03	0.05	0.06	0.13	0.08
Na2O	0.10	0.10	0.08	0.10	0.09	0.09	0.12	0.10	0.08	0.09	0.11	0.10
TiO2	2.12	2.06	2.24	2.34	2.32	2.34	2.40	2.41	2.42	2.42	2.48	2.56
Total	88.42	88.67	90.16	96.05	95.44	98.45	96.31	97.53	97.53	97.14	96.28	98.33

APPENDIX: Mineral Composition of sample 06B26.

	Hornblende						Plagioclase							
	Core					Rim	Rim							Core
SiO2	43.22	43.32	43.55	43.60	44.07	43.84	58.51	57.87	57.59	57.26	57.14	57.35	56.64	56.18
Al2O3	11.71	11.94	11.53	11.38	11.18	11.14	25.62	26.30	26.19	26.52	26.55	26.45	26.56	26.99
K2O	0.93	0.96	0.88	0.91	0.92	0.93	0.15	0.15	0.15	0.14	0.14	0.15	0.15	0.13
FeO	15.59	16.03	15.67	15.76	15.65	15.58	0.28	0.21	0.17	0.14	0.14	0.23	0.15	0.13
MnO	0.60	0.61	0.60	0.61	0.61	0.63	0.00	0.01	0.00	0.02	0.00	0.01	0.00	0.00
MgO	11.26	11.32	11.56	11.41	11.55	11.73	0.01	0.00	0.00	0.00	0.00	0.00	0.00	0.00
CaO	11.89	11.85	12.03	11.91	11.99	12.04	7.98	8.68	8.75	8.98	9.12	8.91	9.16	9.67
Na2O	1.47	1.45	1.37	1.42	1.37	1.37	6.91	6.53	6.53	6.50	6.33	6.49	6.33	5.99
TiO2	0.76	0.75	0.68	0.67	0.63	0.60	0.01	0.00	0.00	0.00	0.00	0.01	0.00	0.00
Total	97.44	98.22	97.87	97.67	97.97	97.86	99.46	99.74	99.39	99.55	99.43	99.60	99.00	99.10

APPENDIX: Mineral Composition of sample 06B33.

	Plagioclase						Hornblende			
	Core					Rim	Rim			Core
SiO2	55.61	55.43	55.54	55.84	54.63	53.86	46.39	46.38	46.35	46.04
Al2O3	26.66	27.07	26.78	26.76	22.79	27.63	10.35	9.69	9.86	9.84
K2O	0.13	0.12	0.14	0.12	0.11	0.09	0.65	0.59	0.61	0.62
FeO	0.01	0.00	0.00	0.01	0.02	0.00	13.55	13.67	13.76	13.65
MnO	0.00	0.00	0.01	0.00	0.00	0.02	0.33	0.30	0.28	0.31
MgO	0.11	0.13	0.18	0.24	0.26	0.36	13.19	12.45	12.91	13.03
CaO	9.91	10.05	9.79	9.76	9.94	10.98	12.20	12.13	12.24	12.24
Na2O	5.82	5.72	5.79	5.92	5.80	5.30	1.04	0.94	1.00	1.01
TiO2	0.00	0.00	0.01	0.00	0.01	0.00	0.58	0.50	0.43	0.39
Total	98.25	98.51	98.23	98.64	93.56	98.24	98.28	96.65	97.44	97.12

APPENDIX: Mineral Composition of sample 06B35.

	Plagioclase							Hornblende								
SiO2	56.34	55.67	55.59	56.10	55.66	56.18	56.03	44.68	46.08	48.81	49.78	48.11	48.17	46.18	44.84	44.73
Al2O3	27.53	27.71	27.44	27.58	27.33	27.33	27.25	10.39	9.24	5.89	5.26	6.75	6.97	8.47	10.26	10.63
K2O	0.12	0.11	0.11	0.11	0.12	0.12	0.12	0.55	0.44	0.21	0.20	0.27	0.28	0.37	0.48	0.49
FeO	0.17	0.23	0.08	0.10	0.12	0.10	0.09	15.19	15.15	13.18	12.65	12.97	12.73	13.65	14.56	14.36
MgO	0.00	0.02	0.00	0.00	0.00	0.00	0.00	12.60	12.97	14.92	15.64	14.84	14.99	13.86	12.89	12.66
CaO	10.05	10.32	10.15	10.11	10.07	9.89	9.87	11.94	12.15	12.27	12.33	12.19	12.22	12.01	11.99	11.97
Na2O	5.90	5.87	5.86	5.85	5.86	5.98	6.06	1.02	0.89	0.57	0.46	0.69	0.69	0.88	1.07	1.07
TiO2	0.00	0.00	0.01	0.01	0.00	0.01	0.02	0.56	0.46	0.25	0.20	0.30	0.31	0.43	0.58	0.62
Total	100.11	99.94	99.24	99.86	99.16	99.60	99.43	96.91	97.38	96.10	96.52	96.12	96.38	95.84	96.67	96.52

	Hornblende															
SiO2	44.76	44.57	44.23	44.41	44.25	45.35	45.18	45.26	44.70	45.18	46.89	48.43	45.82	45.79	45.79	45.61
Al2O3	10.72	10.93	11.31	11.27	10.89	9.96	10.09	10.06	9.76	10.12	8.05	7.04	10.75	11.28	11.03	10.75
K2O	0.48	0.52	0.58	0.58	0.57	0.53	0.50	0.49	0.49	0.51	0.36	0.28	0.35	0.37	0.35	0.33
FeO	14.07	14.08	14.17	14.11	13.88	14.10	14.28	14.24	14.53	14.57	13.66	13.29	13.23	13.50	13.43	13.09
MgO	12.74	12.85	12.63	12.84	12.79	13.22	13.24	12.96	12.90	12.95	13.95	14.72	13.23	12.84	12.92	13.11
CaO	12.00	11.79	11.87	11.87	11.92	12.00	11.97	11.98	12.08	11.96	12.18	12.15	12.29	12.12	12.17	12.08
Na2O	1.08	1.15	1.23	1.22	1.15	1.03	1.02	1.00	0.97	1.04	0.70	0.73	1.10	1.17	1.20	1.15
TiO2	0.65	0.65	0.69	0.65	0.61	0.56	0.54	0.51	0.49	0.52	0.40	0.31	0.60	0.67	0.65	0.62
Total	96.50	96.52	96.71	96.93	96.06	96.74	96.81	96.49	95.93	96.86	96.20	96.96	97.36	97.73	97.53	96.73

	Hbl
SiO2	45.91
Al2O3	10.69
K2O	0.53
FeO	13.32
MgO	13.02
CaO	12.18
Na2O	1.08
TiO2	0.55
Total	97.27

APPENDIX: Mineral Composition of sample 06B67.

	Garnet															
SiO2	37.71	37.63	37.72	37.44	37.30	37.07	36.99	36.84	37.31	36.77	36.97	37.04	37.05	36.95	36.92	37.22
Al2O3	21.96	21.76	21.32	21.30	21.18	21.27	21.04	21.27	21.03	20.93	20.90	21.07	21.05	20.91	20.93	20.89
K2O	0.02	0.00	0.01	0.00	0.00	0.00	0.00	0.01	0.00	0.01	0.00	0.00	0.01	0.00	0.00	0.00
FeO	22.46	22.49	22.59	17.93	17.47	17.41	17.38	17.21	17.13	17.08	16.97	17.24	17.21	17.51	17.37	17.60
MnO	22.97	23.24	23.46	23.81	23.87	23.86	23.75	23.55	23.62	23.77	23.57	23.61	23.72	23.61	23.56	23.77
MgO	0.98	0.98	0.91	0.92	0.89	0.89	0.91	0.95	0.96	0.91	0.94	0.94	0.90	0.90	0.95	0.89
CaO	0.71	0.59	0.56	0.63	0.66	0.62	0.70	0.71	0.66	0.68	0.66	0.64	0.64	0.76	0.77	0.82
Na2O	0.00	0.13	0.20	0.16	0.10	0.46	0.15	0.24	0.00	0.17	0.18	0.11	0.04	0.00	0.00	0.19
TiO2	0.15	0.13	0.10	0.15	0.18	0.18	0.20	0.22	0.19	0.22	0.22	0.21	0.19	0.22	0.21	0.21
Total	106.95	106.93	106.87	102.33	101.65	101.74	101.12	101.00	100.89	100.53	100.41	100.87	100.81	100.86	100.71	101.58

	Garnet							Muscovite								
SiO2	37.36	36.98	37.27	37.25	37.49	37.44	37.92	47.55	47.20	46.28	46.02	46.16	46.25	46.34	46.60	46.24
Al2O3	20.97	21.02	21.22	21.16	21.11	21.49	21.71	29.25	33.74	33.84	33.68	33.49	33.77	33.82	33.75	33.54
K2O	0.00	0.00	0.00	0.00	0.00	0.00	0.00	7.86	10.59	10.54	10.42	10.37	10.41	10.33	10.36	10.39
FeO	17.96	17.75	17.51	17.94	17.79	17.97	17.66	4.70	5.17	4.58	4.63	4.63	4.77	4.61	4.59	4.76
MnO	23.59	23.60	23.19	23.26	23.20	23.31	22.79	0.12	0.10	0.07	0.07	0.07	0.10	0.04	0.09	0.08
MgO	0.90	0.95	0.99	1.00	1.00	0.95	1.02	0.74	0.83	0.78	0.75	0.72	0.74	0.68	0.69	0.69
CaO	0.77	0.66	0.63	0.68	0.61	0.57	0.64	0.30	0.02	0.01	0.00	0.02	0.00	0.04	0.03	0.02
Na2O	0.00	0.00	0.00	0.08	0.07	0.09	0.08	2.39	0.46	0.28	0.56	0.62	0.62	0.64	0.53	0.56
TiO2	0.16	0.19	0.22	0.20	0.14	0.04	0.04	0.19	0.56	0.50	0.53	0.53	0.56	0.51	0.55	0.55
Total	101.71	101.14	101.04	101.55	101.42	101.87	101.85	93.09	98.65	96.87	96.66	96.60	97.22	97.03	97.19	96.83

APPENDIX: Mineral Composition of sample 06B67.

	Muscovite															
SiO2	46.07	45.74	46.19	45.93	45.82	46.16	45.57	45.61	45.49	46.17	46.30	46.20	46.55	45.53	45.94	45.98
Al2O3	33.93	33.69	33.66	33.78	33.74	33.78	33.33	33.29	33.04	33.16	32.78	32.70	33.17	33.60	33.51	33.37
K2O	10.33	10.31	10.41	10.38	10.35	10.40	10.39	10.44	10.57	10.56	10.50	10.44	10.48	10.41	10.44	10.47
FeO	4.85	4.75	4.91	4.90	4.79	4.95	4.84	4.75	4.95	4.94	4.67	4.94	4.72	4.71	4.87	4.69
MnO	0.08	0.09	0.10	0.07	0.08	0.08	0.08	0.09	0.10	0.08	0.10	0.10	0.09	0.04	0.08	0.07
MgO	0.64	0.65	0.63	0.66	0.67	0.63	0.64	0.68	0.72	0.84	0.78	0.86	0.87	0.66	0.67	0.72
CaO	0.00	0.02	0.00	0.00	0.01	0.00	0.00	0.04	0.03	0.00	0.00	0.00	0.00	0.00	0.01	0.01
Na2O	0.69	0.54	0.64	0.47	0.36	0.76	0.53	0.41	0.23	0.29	0.32	0.32	0.39	0.61	0.65	0.50
TiO2	0.55	0.56	0.55	0.55	0.55	0.59	0.58	0.60	0.69	0.69	0.59	0.55	0.55	0.61	0.64	0.56
Total	97.13	96.35	97.09	96.72	96.37	97.33	95.94	95.89	95.82	96.71	96.03	96.10	96.82	96.17	96.82	96.35

	Muscovite			Plagioclase												
SiO2	46.13	46.13	46.17	67.29	66.46	67.22	67.20	66.86	66.20	66.67	66.32	66.89	66.71	66.71	67.37	66.90
Al2O3	33.64	33.08	33.26	21.31	20.77	20.79	20.97	20.89	20.47	20.67	20.45	20.85	20.70	21.16	20.88	20.03
K2O	10.45	10.37	10.45	0.13	0.15	0.24	0.25	0.26	0.27	0.28	0.29	0.16	0.27	0.25	0.24	0.20
FeO	4.67	4.80	4.66	0.02	0.00	0.06	0.00	0.07	0.05	0.07	0.07	0.04	0.04	0.05	0.02	0.00
MnO	0.04	0.05	0.07	0.00	0.00	0.00	0.00	0.00	0.00	0.00	0.00	0.00	0.00	0.00	0.00	0.00
MgO	0.72	0.64	0.73	0.00	0.00	0.00	0.00	0.00	0.00	0.00	0.00	0.00	0.00	0.00	0.00	0.00
CaO	0.00	0.03	0.00	1.57	1.52	1.52	1.52	1.52	1.55	1.49	1.49	1.56	1.73	1.58	1.51	1.03
Na2O	0.63	0.43	0.68	10.95	10.50	10.00	10.91	10.54	10.23	10.45	10.60	10.47	9.83	10.88	10.02	11.02
TiO2	0.51	0.51	0.51	0.00	0.00	0.00	0.00	0.00	0.00	0.00	0.00	0.00	0.00	0.00	0.00	0.00
Total	96.78	96.04	96.52	101.26	99.40	99.83	100.85	100.14	98.77	99.62	99.21	99.97	99.28	100.63	100.03	99.18

APPENDIX: Mineral Composition of sample 06B67.

	K-Feldspar															
SiO2	65.41	65.67	65.05	65.07	65.32	64.40	64.33	65.70	65.16	65.42	65.60	65.77	65.44	65.18	65.11	60.92
Al2O3	18.52	18.53	18.34	18.44	18.34	18.25	18.04	18.47	18.54	18.43	18.41	18.62	18.47	18.58	18.66	18.57
K2O	15.46	15.29	15.10	15.26	15.91	15.95	15.89	15.61	15.30	15.25	15.21	15.22	15.14	15.11	15.17	14.80
FeO	0.02	0.00	0.03	0.03	0.07	0.05	0.02	0.00	0.08	0.01	0.00	0.00	0.03	0.00	0.00	0.09
MnO	0.00	0.00	0.00	0.00	0.00	0.00	0.00	0.00	0.00	0.00	0.00	0.00	0.00	0.00	0.00	0.00
MgO	0.00	0.00	0.00	0.00	0.00	0.00	0.00	0.00	0.00	0.00	0.00	0.00	0.00	0.00	0.00	0.00
CaO	0.00	0.00	0.04	0.03	0.02	0.02	0.01	0.00	0.01	0.03	0.02	0.01	0.00	0.05	0.00	0.04
Na2O	0.78	1.12	1.03	0.93	0.49	0.22	0.33	0.99	0.72	1.19	1.13	1.36	1.18	1.23	1.09	1.03
TiO2	0.00	0.00	0.00	0.00	0.00	0.00	0.00	0.00	0.00	0.00	0.00	0.00	0.00	0.00	0.00	0.00
Total	100.19	100.62	99.59	99.76	100.14	98.89	98.63	100.78	99.82	100.31	100.38	100.97	100.25	100.14	100.04	95.45

	K-Feldspar													Plagioclase		
SiO2	65.47	65.29	65.31	65.13	65.31	65.23	65.38	65.26	65.22	64.96	64.55	64.10	64.95	68.64	68.00	67.66
Al2O3	18.40	18.52	18.40	18.25	18.40	18.54	18.61	18.67	18.57	18.56	18.20	18.21	18.34	19.73	20.12	20.63
K2O	15.07	15.07	15.06	15.06	15.02	15.00	14.83	15.05	15.13	15.05	14.81	14.81	15.20	0.24	0.19	0.23
FeO	0.00	0.06	0.00	0.02	0.01	0.02	0.02	0.02	0.04	0.03	0.06	0.06	0.00	0.02	0.02	0.11
MnO	0.00	0.00	0.00	0.00	0.00	0.00	0.00	0.00	0.00	0.00	0.00	0.00	0.00	0.00	0.00	0.00
MgO	0.00	0.00	0.00	0.00	0.00	0.00	0.00	0.00	0.00	0.00	0.00	0.00	0.00	0.00	0.00	0.00
CaO	0.00	0.02	0.02	0.03	0.01	0.02	0.04	0.02	0.06	0.05	0.04	0.11	0.06	0.50	0.85	1.17
Na2O	1.09	1.32	1.10	1.17	1.34	1.47	1.29	1.11	1.14	1.32	0.99	1.12	1.14	10.90	10.94	10.74
TiO2	0.00	0.00	0.00	0.00	0.00	0.00	0.00	0.00	0.00	0.00	0.00	0.00	0.00	0.00	0.00	0.00
Total	100.02	100.27	99.88	99.66	100.10	100.28	100.17	100.12	100.16	99.96	98.65	98.40	99.68	100.03	100.13	100.54

APPENDIX: Mineral Composition of sample 06B67.

	Plagioclase			
SiO2	67.46	69.57	83.69	67.75
Al2O3	20.79	19.20	6.73	19.73
K2O	0.26	0.19	0.08	1.04
FeO	0.02	0.04	0.11	0.06
MnO	0.00	0.00	0.00	0.00
MgO	0.00	0.00	0.00	0.00
CaO	1.39	1.17	0.28	0.65
Na2O	11.06	10.72	4.03	11.01
TiO2	0.00	0.00	0.00	0.00
Total	100.98	100.89	94.91	100.24

APPENDIX: Mineral Composition of sample 06B68.

	Plagioclase								Hornblende							
	Core							Rim	Rim							
SiO2	61.19	61.23	61.25	56.65	61.60	61.75	62.16	61.01	42.83	42.19	42.05	42.69	42.40	43.01	42.21	42.60
Al2O3	24.71	25.15	25.02	22.95	25.32	25.25	23.06	25.05	12.33	11.96	11.92	12.19	12.06	12.31	12.03	12.01
K2O	0.23	0.28	0.28	0.27	0.24	0.24	6.02	0.19	1.43	1.45	1.48	1.43	1.44	1.44	1.46	1.47
FeO	0.10	0.13	0.13	0.14	0.15	0.13	0.17	0.43	22.79	22.23	22.75	23.15	22.99	22.56	22.06	22.70
MgO	0.00	0.01	0.00	0.00	0.00	0.00	0.00	0.02	7.32	7.32	7.24	7.50	7.48	7.55	7.40	7.80
CaO	6.19	6.33	6.30	6.11	6.32	6.22	4.08	6.70	11.41	11.31	11.36	11.40	11.39	11.36	11.35	11.31
Na2O	7.07	7.08	7.35	6.71	7.41	7.51	4.70	7.29	1.26	1.27	1.21	1.27	1.33	1.37	1.33	1.45
TiO2	0.01	0.00	0.01	0.00	0.01	0.01	0.03	0.00	0.70	0.74	0.74	0.65	0.72	0.73	0.73	0.75
Total	99.50	100.21	100.34	92.84	101.04	101.11	100.20	100.69	100.08	98.47	98.75	100.28	99.82	100.33	98.58	100.10

	Hornblende															
														Core	Core	
SiO2	42.77	42.74	42.34	42.23	42.35	42.79	42.65	42.62	42.81	42.71	42.85	42.81	42.89	42.58	62.30	62.40
Al2O3	11.98	11.94	11.70	11.90	11.78	12.09	11.99	11.99	11.82	11.94	12.06	12.05	12.00	12.01	25.36	25.64
K2O	1.48	1.48	1.49	1.50	1.50	1.52	1.53	1.53	1.51	1.53	1.53	1.52	1.54	1.53	0.23	0.16
FeO	22.69	22.89	22.94	22.68	22.60	22.57	22.16	21.71	22.01	22.03	22.02	22.74	22.59	22.35	0.07	0.12
MgO	7.55	7.52	7.44	7.43	7.49	7.26	7.54	7.53	7.42	7.44	7.43	7.68	7.45	7.55	0.00	0.01
CaO	11.31	11.36	11.40	11.32	11.37	11.38	11.25	11.26	11.29	11.35	11.25	11.31	11.33	11.35	6.45	6.37
Na2O	1.40	1.37	1.43	1.47	1.35	1.42	1.38	1.40	1.39	1.31	1.24	1.36	1.30	1.33	7.45	7.37
TiO2	0.78	0.74	0.79	0.80	0.80	0.82	0.86	0.87	0.86	0.88	0.87	0.89	0.89	0.90	0.03	0.00
Total	99.95	100.04	99.53	99.33	99.25	99.85	99.36	98.89	99.11	99.19	99.24	100.36	99.98	99.60	101.89	102.06

	Plagioclase								Hornblende							
								Rim	Rim							Core
SiO2	62.19	62.37	62.14	62.48	62.30	62.31	61.68	61.30	42.28	41.75	41.91	42.62	42.04	42.28	42.16	41.80
Al2O3	25.30	25.29	25.41	25.13	25.29	25.51	25.11	25.39	12.31	12.20	12.21	10.38	12.04	12.10	12.22	12.24
K2O	0.23	0.27	0.23	0.26	0.26	0.22	0.24	0.22	1.40	1.48	1.49	1.27	1.54	1.54	1.56	1.59
FeO	0.11	0.20	0.16	0.07	0.17	0.21	0.22	0.33	22.34	22.88	22.58	22.39	22.42	22.61	22.37	22.39
MgO	0.00	0.00	0.00	0.00	0.00	0.00	0.00	0.00	7.36	7.46	7.58	7.34	7.52	7.55	7.50	7.41
CaO	6.36	6.35	6.33	6.41	6.40	6.27	6.31	6.44	11.48	11.43	11.44	11.40	11.54	11.45	11.37	11.47
Na2O	7.54	7.27	7.41	7.15	7.18	7.46	7.48	7.49	1.19	1.27	1.18	1.08	1.24	1.25	1.36	1.33
TiO2	0.00	0.01	0.00	0.01	0.03	0.00	0.00	0.00	0.85	0.90	0.85	0.71	0.84	0.82	0.85	0.88
Total	101.72	101.75	101.69	101.52	101.63	101.97	101.04	101.17	99.21	99.36	99.24	97.18	99.18	99.59	99.39	99.09

APPENDIX: Mineral Composition of sample 06B68.

	Hornblende			Biotite												
SiO2	41.83	41.63	41.75	37.60	38.02	37.54	37.38	37.78	37.47	36.19	36.63	32.28	36.37	38.04	37.58	37.97
Al2O3	12.18	12.18	12.11	15.76	16.01	15.69	15.60	15.61	15.56	15.18	15.33	15.18	16.26	15.91	15.84	15.73
K2O	1.60	1.58	1.59	9.97	10.01	10.02	9.89	9.98	9.77	9.53	9.51	6.23	6.06	9.82	9.78	10.04
FeO	22.32	22.14	22.45	22.34	22.43	22.21	22.20	22.06	22.17	21.90	21.91	20.87	19.64	21.81	22.11	22.07
MgO	7.45	7.36	7.29	9.58	9.70	9.44	9.69	9.68	9.18	9.86	10.02	9.35	8.85	9.17	9.43	9.04
CaO	11.36	11.46	11.32	0.00	0.01	0.00	0.01	0.02	0.09	0.03	0.07	0.51	0.89	0.15	0.04	0.05
Na2O	1.30	1.35	1.28	0.11	0.10	0.11	0.10	0.09	0.10	0.09	0.12	0.10	0.07	0.09	0.11	0.09
TiO2	0.88	0.88	0.87	2.90	2.90	2.88	2.88	2.87	2.90	2.89	2.89	7.27	5.67	3.19	2.83	2.84
Total	98.92	98.59	98.66	98.27	99.19	97.89	97.74	98.08	97.23	95.66	96.48	91.79	93.81	98.17	97.72	97.82

	Biotite						
SiO2	38.36	38.01	38.10	36.71	38.24	38.30	37.91
Al2O3	16.18	15.89	16.12	15.11	16.31	16.18	15.99
K2O	10.08	10.10	9.66	9.58	10.05	9.94	9.95
FeO	22.39	22.63	21.95	22.52	22.30	22.17	22.26
MgO	9.56	9.86	9.76	9.26	9.58	9.89	9.67
CaO	0.01	0.04	0.06	0.10	0.02	0.01	0.04
Na2O	0.12	0.10	0.13	0.12	0.11	0.13	0.12
TiO2	2.84	2.84	2.81	2.81	2.95	2.92	2.89
Total	99.54	99.47	98.58	96.19	99.56	99.53	98.83

APPENDIX: Mineral Composition of sample 06B72.

	Plagioclase							Hornblende								
	Core						Rim	Rim								Core
SiO2	59.33	59.79	59.55	59.44	59.64	59.65	59.65	40.31	40.08	40.13	39.96	39.96	40.27	40.26	40.12	40.34
Al2O3	24.75	24.63	24.69	24.83	24.97	25.00	24.82	12.21	11.76	11.84	11.82	11.80	11.71	11.87	11.73	11.64
K2O	0.19	0.21	0.21	0.23	0.22	0.20	0.17	1.47	1.52	1.53	1.54	1.53	1.36	1.51	1.51	1.46
FeO	0.14	0.13	0.14	0.15	0.24	0.21	0.34	21.99	22.02	22.54	22.18	22.15	22.48	22.07	22.40	22.21
MgO	0.00	0.00	0.01	0.00	0.00	0.00	0.00	7.17	7.30	7.34	7.40	7.38	7.40	7.42	7.37	7.41
CaO	6.24	6.22	6.26	6.36	6.40	6.45	6.29	11.44	11.36	11.39	11.27	11.47	11.72	11.37	11.33	11.43
Na2O	7.89	7.85	7.82	7.74	7.79	7.27	7.89	1.32	1.27	1.34	1.35	1.32	1.14	1.34	1.38	1.26
TiO2	0.00	0.00	0.00	0.00	0.01	0.00	0.00	0.69	0.77	0.81	0.81	0.78	0.72	0.79	0.76	0.70
Total	98.52	98.82	98.68	98.76	99.26	98.78	99.15	96.59	96.08	96.91	96.32	96.39	96.80	96.63	96.60	96.46

	Plagioclase													Hornblende		
	Core												Rim	Rim		
SiO2	61.99	62.37	60.73	60.87	61.28	61.25	61.12	60.79	60.88	59.32	59.11	59.01	59.07	40.10	39.89	40.01
Al2O3	23.60	23.71	24.40	24.18	23.01	24.15	24.30	23.89	23.95	24.53	24.64	24.68	24.05	12.42	12.07	12.04
K2O	0.23	0.25	0.31	0.33	3.96	0.37	0.36	0.36	0.39	0.19	0.19	0.17	0.19	1.27	1.35	1.37
FeO	0.25	0.17	0.17	0.13	0.09	0.10	0.14	0.14	0.10	0.19	0.23	0.31	0.53	22.12	21.90	21.96
MgO	0.01	0.00	0.01	0.00	0.00	0.00	0.00	0.00	0.00	0.00	0.01	0.03	0.18	6.70	6.88	7.09
CaO	4.35	3.99	5.44	5.41	4.20	5.40	5.27	5.45	5.44	6.45	6.39	6.36	6.26	11.54	11.51	11.50
Na2O	7.78	7.06	8.12	8.18	6.55	8.04	8.05	8.26	8.09	7.76	7.69	7.78	7.69	1.35	1.23	1.24
TiO2	0.00	0.02	0.00	0.00	0.01	0.00	0.01	0.00	0.00	0.00	0.01	0.01	0.02	0.47	0.57	0.63
Total	98.21	97.56	99.19	99.09	99.10	99.31	99.24	98.90	98.85	98.45	98.25	98.35	98.00	95.97	95.40	95.82

	Hornblende								Core	Plagioclase Core						
SiO2	40.04	39.77	39.94	40.24	40.20	40.42	40.56	40.46	38.99	60.40	60.50	60.39	60.30	60.73	60.79	60.73
Al2O3	11.99	11.84	11.91	11.65	11.64	11.58	11.51	11.43	11.57	23.73	24.46	24.21	24.12	24.38	24.33	23.73
K2O	1.39	1.58	1.58	1.54	1.54	1.50	1.49	1.45	1.38	1.70	0.26	0.23	0.25	0.25	0.27	1.20
FeO	21.97	21.95	22.23	22.24	21.92	21.71	21.84	21.71	21.51	0.29	0.21	0.20	0.20	0.17	0.14	0.10
MgO	7.23	7.48	7.43	7.58	7.51	7.54	7.62	7.57	7.42	0.01	0.00	0.00	0.00	0.01	0.01	0.00
CaO	11.52	11.36	11.41	11.42	11.41	11.33	11.33	11.30	11.22	5.41	5.61	5.60	5.53	5.46	5.52	5.07
Na2O	1.30	1.37	1.36	1.33	1.37	1.37	1.36	1.38	1.46	7.59	8.16	8.33	8.23	7.60	8.34	7.83
TiO2	0.65	0.84	0.84	0.81	0.81	0.80	0.80	0.78	0.72	0.01	0.01	0.01	0.00	0.00	0.00	0.01
Total	96.08	96.19	96.71	96.80	96.39	96.24	96.52	96.08	94.27	99.13	99.20	98.96	98.62	98.60	99.40	98.67

APPENDIX: Mineral Composition of sample 06B72.

	Plagioclase															
SiO2	60.69	60.60	60.66	60.90	60.22	60.06	60.38	60.17	59.89	59.92	59.72	59.93	59.85	59.92	60.28	60.16
Al2O3	24.15	24.00	24.06	23.86	24.72	24.54	24.28	24.39	24.31	24.26	24.21	24.11	24.32	24.18	24.19	24.16
K2O	0.25	0.25	0.25	0.24	0.19	0.21	0.21	0.21	0.19	0.20	0.20	0.21	0.24	0.23	0.24	0.25
FeO	0.12	0.14	0.12	0.12	0.31	0.33	0.25	0.22	0.18	0.16	0.14	0.30	0.34	0.36	0.32	0.43
MgO	0.00	0.02	0.01	0.01	0.00	0.00	0.00	0.00	0.00	0.01	0.00	0.00	0.00	0.00	0.00	0.00
CaO	5.55	5.46	5.34	5.21	5.90	6.14	5.83	5.89	5.96	5.88	5.94	5.94	5.90	5.90	5.87	5.77
Na2O	8.28	8.24	8.35	8.38	8.45	8.15	8.04	8.07	8.09	8.16	8.12	7.99	8.15	8.09	7.98	8.20
TiO2	0.01	0.00	0.00	0.00	0.00	0.01	0.00	0.02	0.00	0.01	0.01	0.00	0.01	0.00	0.00	0.02
Total	99.05	98.72	98.79	98.72	99.80	99.43	98.99	98.95	98.62	98.59	98.33	98.48	98.79	98.68	98.89	98.98

	Plagioclase		K-Feldspar										Hornblende			
SiO2	60.09	60.64	62.66	63.10	62.83	62.76	62.55	62.56	62.89	63.16	62.96	62.90	40.18	43.79	46.16	46.51
Al2O3	23.72	24.47	18.51	18.54	18.62	18.50	18.46	18.49	18.55	18.48	18.43	18.38	11.64	11.15	7.03	9.67
K2O	0.47	0.23	15.23	14.98	14.79	14.87	14.92	15.11	15.02	14.90	15.13	14.63	1.42	1.16	0.63	1.04
FeO	0.45	0.10	0.09	0.03	0.07	0.10	0.04	0.11	0.07	0.10	0.11	0.09	22.37	21.54	16.58	19.05
MgO	0.02	0.00	0.00	0.00	0.00	0.00	0.00	0.00	0.00	0.00	0.00	0.00	7.40	7.12	5.54	6.11
CaO	5.75	5.73	0.00	0.01	0.02	0.01	0.03	0.01	0.01	0.01	0.01	0.02	11.52	10.88	7.69	9.46
Na2O	7.86	7.91	1.04	1.03	1.03	1.06	1.05	1.07	1.04	1.05	1.04	1.07	1.26	1.07	0.59	1.01
TiO2	0.00	0.00	0.02	0.01	0.02	0.02	0.03	0.02	0.01	0.02	0.01	0.03	0.66	0.55	0.35	0.47
Total	98.35	99.09	97.55	97.69	97.37	97.33	97.08	97.36	97.59	97.73	97.69	97.13	96.46	97.25	84.56	93.30

	Hornblende							Biotite								
SiO2	40.65	40.46	40.49	40.20	40.17	39.92	39.60	35.18	35.17	35.31	35.78	35.83	35.49	35.92	35.84	36.35
Al2O3	11.65	11.57	11.70	11.54	11.57	11.77	13.05	14.69	14.80	14.85	14.81	14.96	14.92	14.87	15.05	15.22
K2O	1.39	1.44	1.46	1.45	1.43	1.42	1.48	9.78	9.84	9.80	9.82	9.65	9.74	9.85	9.83	9.90
FeO	21.63	21.96	22.46	22.20	22.24	21.75	23.11	22.72	22.31	22.66	22.55	22.38	22.40	22.38	22.37	21.97
MgO	7.46	7.40	7.52	7.42	7.51	7.41	6.40	9.51	9.62	9.66	9.76	9.78	9.74	9.68	9.78	9.57
CaO	11.40	11.36	11.42	11.33	11.35	11.43	11.42	0.01	0.00	0.00	0.00	0.02	0.00	0.01	0.00	0.01
Na2O	1.24	1.34	1.40	1.35	1.33	1.30	1.19	0.09	0.08	0.09	0.08	0.08	0.09	0.09	0.09	0.11
TiO2	0.63	0.67	0.70	0.66	0.65	0.66	0.38	2.99	3.00	2.98	3.01	3.00	2.98	3.01	3.01	3.03
Total	96.04	96.20	97.16	96.13	96.25	95.65	96.62	94.97	94.81	95.36	95.81	95.69	95.36	95.79	95.97	96.16

APPENDIX: Mineral Composition of sample 06B76.

	Plagioclase									Hornblende						
	Core								Rim	Rim						
SiO2	61.80	60.88	60.87	59.87	61.03	60.94	60.62	60.72	60.55	42.64	42.63	42.62	42.28	42.76	42.22	42.68
Al2O3	26.22	25.95	25.80	24.94	26.05	25.84	25.46	25.96	25.71	11.95	11.85	11.99	11.81	11.63	11.75	11.87
K2O	0.28	0.34	0.34	0.33	0.56	0.31	0.31	0.29	0.26	1.31	1.34	1.32	1.35	1.31	1.32	1.33
FeO	0.11	0.11	0.18	0.18	0.20	0.21	0.19	0.21	0.27	19.89	20.36	20.34	20.82	20.42	20.50	20.67
MgO	0.01	0.00	0.01	0.01	0.00	0.02	0.00	0.00	0.00	8.76	8.82	8.75	8.70	8.78	8.83	8.80
CaO	6.71	6.70	6.75	6.39	6.58	6.66	6.73	6.69	6.79	11.54	11.48	11.52	11.56	11.51	11.49	11.53
Na2O	7.64	7.37	7.39	6.66	7.25	7.46	7.35	7.43	7.31	1.17	1.27	1.28	1.35	1.28	1.29	1.26
TiO2	0.00	0.00	0.00	0.00	0.00	0.01	0.00	0.01	0.01	0.99	0.96	0.90	0.90	0.86	0.87	0.87
Total	98.52	98.82	98.68	98.76	99.26	98.78	99.15	101.31	100.91	98.25	98.70	98.71	98.77	98.54	98.26	99.00

	Hornbelnde										Core	Plagioclase Core				
SiO2	42.50	42.54	42.60	42.76	43.10	43.01	43.16	42.99	42.86	43.03	42.87	60.88	60.77	60.58	60.90	60.93
Al2O3	11.68	11.74	11.82	11.70	11.43	11.46	11.49	11.55	11.48	11.72	11.72	25.80	25.83	25.70	25.78	25.70
K2O	1.31	1.34	1.33	1.27	1.27	1.28	1.27	1.27	1.25	1.28	1.25	0.30	0.31	0.32	0.30	0.31
FeO	20.67	19.93	20.19	20.35	19.89	20.04	20.05	20.72	20.17	20.41	20.40	0.35	0.28	0.24	0.21	0.20
MgO	8.92	8.88	8.91	9.10	9.18	9.29	9.06	9.06	9.10	9.03	8.95	0.00	0.01	0.01	0.00	0.01
CaO	11.54	11.54	11.37	11.49	11.34	11.32	11.37	11.30	11.39	11.42	11.45	6.75	6.78	6.62	6.73	6.71
Na2O	1.18	1.24	1.26	1.24	1.31	1.31	1.30	1.29	1.28	1.26	1.25	7.32	7.33	7.52	7.12	7.35
TiO2	0.87	0.85	0.85	0.85	0.83	0.86	0.86	0.83	0.85	0.84	0.85	0.01	0.02	0.01	0.00	0.01
Total	98.67	98.07	98.34	98.75	98.35	98.57	98.56	99.00	98.38	98.99	98.74	101.40	101.32	101.00	101.04	101.23

	Plagioclase													Rim	Hornblende Rim	
SiO2	60.73	60.81	60.25	60.68	61.09	60.57	60.16	60.20	60.08	60.12	60.25	60.28	60.60	60.54	42.76	42.60
Al2O3	25.54	25.84	25.53	25.83	25.86	25.90	25.46	25.36	25.63	25.51	25.66	25.58	25.88	25.63	11.65	11.56
K2O	0.33	0.34	0.34	0.33	0.34	0.34	0.32	0.27	0.33	0.28	0.26	0.32	0.31	0.30	1.24	1.27
FeO	0.21	0.16	0.12	0.19	0.14	0.16	0.20	0.16	0.18	0.18	0.19	0.26	0.21	0.34	20.45	20.35
MgO	0.00	0.00	0.00	0.01	0.00	0.02	0.00	0.00	0.00	0.00	0.00	0.01	0.01	0.00	8.79	8.84
CaO	6.64	6.67	6.71	6.70	6.75	6.72	6.74	6.72	6.69	6.72	6.72	6.69	6.75	6.73	11.52	11.46
Na2O	7.53	7.38	7.34	7.51	7.29	7.30	7.33	7.31	7.26	7.48	7.30	7.41	7.27	7.16	1.19	1.24
TiO2	0.00	0.00	0.00	0.01	0.01	0.00	0.01	0.01	0.01	0.00	0.00	0.00	0.01	0.02	0.79	0.81
Total	100.97	101.19	100.28	101.24	101.48	101.01	100.22	100.02	100.18	100.29	100.37	100.55	101.04	100.71	98.38	98.13

APPENDIX: Mineral Composition of sample 06B76.

	Hornblende			Core	Biotite											
SiO2	42.82	42.62	42.89	42.95	36.57	38.47	37.14	36.56	37.51	37.34	37.01	37.20	37.60	36.95	37.74	37.99
Al2O3	11.59	11.56	11.68	11.57	15.95	16.95	16.56	16.49	16.85	16.52	16.22	16.34	16.43	16.10	16.25	16.44
K2O	1.27	1.26	1.27	1.26	9.87	10.03	9.87	9.96	9.92	9.82	10.01	9.79	9.84	9.84	9.85	9.81
FeO	20.26	19.98	20.40	20.05	19.47	19.84	19.43	19.59	20.29	19.70	19.60	19.48	19.74	19.84	19.63	19.77
MgO	8.90	9.01	9.02	9.04	10.14	10.07	10.13	10.79	10.34	10.55	10.02	10.09	10.34	10.30	10.27	10.61
CaO	11.41	11.48	11.42	11.52	0.07	0.03	0.07	0.04	0.06	0.05	0.03	0.07	0.05	0.09	0.08	0.10
Na2O	1.25	1.22	1.23	1.24	0.04	0.04	0.04	0.05	0.05	0.06	0.04	0.05	0.06	0.05	0.07	0.10
TiO2	0.83	0.82	0.83	0.83	3.13	3.26	3.23	3.18	3.27	3.26	3.28	3.25	3.23	3.22	3.24	3.23
Total	98.31	97.95	98.74	98.45	95.22	98.68	96.47	96.66	98.28	97.31	96.19	96.28	97.29	96.39	97.13	98.04

	Biotite		
SiO2	36.87	37.74	36.51
Al2O3	16.13	16.42	15.64
K2O	9.79	9.77	9.83
FeO	19.82	19.85	19.82
MgO	10.39	10.62	10.56
CaO	0.11	0.08	0.06
Na2O	0.05	0.06	0.07
TiO2	3.22	3.23	3.22
Total	96.37	97.78	95.70

APPENDIX: Mineral Composition of sample 07B66.

	Hornblende															
	Core															
SiO2	42.92	42.62	42.86	43.32	43.63	43.55	43.44	43.49	43.52	42.95	43.92	43.81	44.17	43.77	44.49	44.62
Al2O3	11.64	10.86	10.57	10.75	10.50	10.49	10.38	10.54	10.55	10.08	10.10	9.45	9.65	9.54	9.66	9.59
K2O	1.24	1.23	1.21	1.19	1.15	1.15	1.15	1.13	1.16	1.13	1.11	1.03	1.04	1.03	1.03	1.05
FeO	17.92	17.74	17.96	18.31	17.97	18.07	17.77	17.96	18.11	18.23	17.68	17.67	17.73	17.32	17.24	17.57
MnO	0.37	0.40	0.40	0.43	0.36	0.40	0.42	0.41	0.39	0.42	0.36	0.38	0.42	0.39	0.37	0.38
MgO	10.15	10.30	10.57	10.49	10.52	10.49	10.48	10.62	10.57	10.79	10.84	10.80	11.14	10.81	11.08	10.95
CaO	11.53	11.64	11.69	11.66	11.65	11.54	11.67	11.67	11.60	11.61	11.76	11.76	11.81	11.64	11.71	11.71
Na2O	1.53	1.56	1.49	1.50	1.43	1.45	1.33	1.37	1.39	1.41	1.37	1.31	1.29	1.36	1.32	1.33
TiO2	1.29	1.28	1.25	1.24	1.24	1.25	1.22	1.19	1.20	1.15	1.13	1.00	1.01	0.97	0.98	0.99
Total	98.60	97.62	97.98	98.89	98.46	98.39	97.85	98.38	98.49	97.77	98.27	97.20	98.27	96.83	97.88	98.21

	Hornblende												Plagioclase			
													Rim	Rim		
SiO2	44.19	44.29	44.29	44.35	44.26	44.14	43.89	43.75	43.59	44.26	44.02	44.19	44.90	59.16	59.81	59.17
Al2O3	9.75	9.65	9.70	9.82	9.90	9.80	9.72	9.93	9.80	9.92	9.66	9.67	9.85	25.25	25.72	25.42
K2O	1.04	1.08	1.05	1.10	1.08	1.09	1.11	1.08	1.09	1.10	1.05	1.09	1.09	0.13	0.20	0.27
FeO	17.21	17.77	17.62	17.64	17.88	17.61	17.81	17.61	17.56	17.60	17.51	17.47	17.97	0.34	0.28	0.22
MnO	0.37	0.41	0.45	0.40	0.37	0.39	0.34	0.41	0.39	0.45	0.38	0.41	0.41	0.00	0.02	0.01
MgO	10.94	11.20	11.18	11.01	11.03	10.89	10.89	10.95	11.06	10.97	11.09	10.97	11.25	0.05	0.00	0.02
CaO	11.65	11.70	11.75	11.59	11.60	11.64	11.69	11.67	11.55	11.62	11.75	11.64	11.55	6.77	6.97	6.85
Na2O	1.37	1.38	1.36	1.42	1.36	1.41	1.38	1.37	1.38	1.32	1.35	1.41	1.37	7.51	7.73	7.49
TiO2	1.01	1.01	1.03	1.02	1.03	1.03	1.03	1.03	1.02	1.01	1.02	1.04	1.01	0.01	0.02	0.02
Total	97.52	98.49	98.44	98.36	98.51	98.01	97.85	97.80	97.45	98.24	97.84	97.87	99.40	99.20	100.74	99.47

APPENDIX: Mineral Composition of sample 07B66.

	Plagioclase														Core	Hbl Core
SiO2	59.67	59.85	60.24	59.82	59.78	59.66	59.56	59.67	59.95	60.08	59.84	59.76	60.06	59.76	59.63	42.43
Al2O3	25.14	25.22	25.02	25.17	25.45	25.27	25.56	25.17	25.30	25.21	25.26	25.28	25.17	25.31	25.25	11.28
K2O	0.31	0.28	0.29	0.33	0.36	0.35	0.35	0.34	0.33	0.32	0.33	0.29	0.28	0.27	0.23	1.35
FeO	0.24	0.14	0.22	0.16	0.17	0.13	0.20	0.13	0.15	0.12	0.12	0.16	0.13	0.16	0.20	18.56
MnO	0.01	0.00	0.00	0.00	0.02	0.01	0.00	0.00	0.00	0.00	0.00	0.01	0.00	0.02	0.01	0.37
MgO	0.00	0.00	0.02	0.01	0.01	0.01	0.01	0.01	0.00	0.00	0.01	0.00	0.00	0.00	0.01	10.09
CaO	6.79	6.66	6.52	6.78	6.66	6.77	6.64	6.70	6.73	6.62	6.68	6.67	6.60	6.72	6.68	11.50
Na2O	7.52	7.50	7.85	7.57	7.48	7.60	7.51	7.50	7.58	7.72	7.56	7.55	7.49	7.47	7.69	1.47
TiO2	0.01	0.00	0.02	0.00	0.00	0.03	0.01	0.00	0.01	0.00	0.01	0.00	0.01	0.01	0.00	1.10
Total	99.70	99.66	100.16	99.83	99.94	99.83	99.83	99.51	100.03	100.06	99.81	99.72	99.73	99.72	99.69	98.15

	Hornblende											Rim	Plagioclase Rim			
SiO2	41.96	42.20	42.02	42.31	42.13	41.87	41.86	42.75	41.72	40.68	42.68	43.73	59.38	59.93	59.72	59.67
Al2O3	11.35	11.58	11.72	11.76	11.83	11.82	11.72	11.64	11.64	11.59	11.29	10.38	25.34	25.63	25.25	25.23
K2O	1.35	1.38	1.37	1.40	1.41	1.37	1.40	1.39	1.38	1.40	1.35	1.19	0.19	0.15	0.19	0.15
FeO	18.31	18.44	18.72	18.75	18.76	18.71	18.61	18.68	18.99	18.97	19.39	17.92	0.34	0.21	0.21	0.17
MnO	0.38	0.40	0.42	0.42	0.40	0.41	0.40	0.41	0.43	0.42	0.39	0.40	0.00	0.01	0.01	0.02
MgO	9.97	9.79	9.83	9.91	9.83	9.78	9.83	9.87	9.62	9.47	9.59	10.48	0.00	0.00	0.00	0.04
CaO	11.48	11.76	11.55	11.53	11.42	11.60	11.59	11.48	11.49	11.45	11.67	11.80	6.79	6.83	6.81	6.72
Na2O	1.47	1.48	1.52	1.50	1.55	1.52	1.52	1.54	1.49	1.37	1.35	1.13	7.45	7.74	7.65	7.55
TiO2	1.13	1.08	1.08	1.08	1.05	1.08	1.07	1.12	1.11	1.15	1.11	1.01	0.00	0.00	0.01	0.00
Total	97.39	98.10	98.23	98.67	98.37	98.15	98.00	98.88	97.88	96.50	98.81	98.04	99.49	100.50	99.83	99.55

APPENDIX: Mineral Composition of sample 07B66.

	Plagioclase															
SiO2	59.81	59.68	60.02	59.52	59.77	59.76	59.65	59.72	59.65	59.64	59.20	59.12	59.78	59.54	59.41	59.55
Al2O3	25.12	25.49	24.87	25.15	25.57	25.33	25.45	25.34	25.50	25.37	25.55	25.58	25.63	25.44	25.39	25.68
K2O	0.20	0.16	0.27	0.21	0.22	0.36	0.38	0.38	0.32	0.34	0.35	0.34	0.32	0.32	0.25	0.28
FeO	0.18	0.25	0.21	0.10	0.14	0.19	0.20	0.18	0.19	0.16	0.15	0.17	0.19	0.08	0.12	0.15
MnO	0.03	0.00	0.00	0.01	0.01	0.00	0.01	0.03	0.00	0.01	0.01	0.00	0.01	0.00	0.00	0.00
MgO	0.00	0.00	0.00	0.02	0.00	0.01	0.00	0.00	0.00	0.01	0.02	0.02	0.00	0.02	0.03	0.00
CaO	6.85	6.79	6.74	6.94	6.86	6.93	6.84	6.92	6.91	6.97	7.06	7.12	7.18	7.26	7.20	7.13
Na2O	7.60	7.68	7.53	7.51	7.47	7.33	7.44	7.34	7.50	7.32	7.40	7.31	7.41	7.28	7.35	7.33
TiO2	0.01	0.00	0.01	0.00	0.00	0.00	0.02	0.01	0.02	0.01	0.00	0.00	0.01	0.00	0.02	0.01
Total	99.81	100.04	99.64	99.47	100.04	99.91	99.99	99.91	100.09	99.83	99.74	99.64	100.52	99.93	99.75	100.13

	Plagioclase												
													Core
SiO2	59.53	59.24	59.16	59.55	58.68	58.97	59.32	59.59	59.05	58.91	59.13	58.77	59.06
Al2O3	25.49	25.34	25.27	25.58	25.42	25.72	25.90	25.68	25.88	25.51	25.63	25.71	25.59
K2O	0.32	0.31	0.31	0.29	0.28	0.25	0.26	0.21	0.27	0.28	0.29	0.29	0.29
FeO	0.16	0.18	0.12	0.16	0.13	0.10	0.16	0.19	0.16	0.15	0.13	0.10	0.19
MnO	0.01	0.04	0.01	0.02	0.02	0.00	0.02	0.01	0.02	0.00	0.00	0.00	0.00
MgO	0.02	0.00	0.00	0.00	0.00	0.00	0.02	0.00	0.00	0.02	0.00	0.00	0.01
CaO	7.17	7.26	7.22	7.26	7.29	7.30	7.14	7.12	7.16	7.28	7.30	7.47	7.42
Na2O	7.35	7.33	7.38	7.14	7.23	7.35	7.46	7.36	7.38	7.27	7.22	6.94	7.22
TiO2	0.00	0.00	0.00	0.00	0.03	0.00	0.01	0.00	0.00	0.00	0.02	0.00	0.02
Total	100.05	99.70	99.46	99.99	99.08	99.67	100.29	100.17	99.91	99.42	99.71	99.28	99.81

APPENDIX: Mineral Composition of sample 07B93.

	Hornblende														Plagioclase	
	Core													Rim	Rim	
SiO2	42.51	42.86	42.64	42.91	42.31	42.44	42.33	42.45	42.55	42.00	42.07	43.11	43.76	43.44	63.85	62.89
Al2O3	10.87	10.87	10.91	10.87	11.08	10.85	11.42	11.19	11.69	11.55	11.51	10.29	9.79	10.47	22.81	18.67
K2O	1.43	1.42	1.42	1.44	1.44	1.43	1.49	1.50	1.54	1.53	1.54	1.24	1.16	1.25	0.53	14.79
FeO	19.02	18.75	19.22	19.09	19.23	19.32	19.43	19.15	19.43	19.09	19.40	18.82	18.22	18.61	0.19	0.13
MnO	0.41	0.39	0.38	0.42	0.42	0.38	0.42	0.45	0.41	0.40	0.38	0.39	0.40	0.39	0.02	0.00
MgO	9.78	9.71	9.79	9.75	9.70	9.60	9.57	9.47	9.67	9.46	9.39	10.18	10.47	10.33	0.02	0.00
CaO	11.46	11.41	11.32	11.29	11.53	11.43	11.35	11.38	11.42	11.53	11.48	11.45	11.65	11.56	4.36	0.00
Na2O	1.59	1.65	1.59	1.61	1.58	1.55	1.64	1.52	1.59	1.58	1.58	1.48	1.37	1.41	8.47	0.87
TiO2	1.42	1.39	1.43	1.34	1.31	1.31	1.25	1.29	1.25	1.22	1.15	1.15	1.09	1.18	0.00	0.05
Total	98.50	98.46	98.69	98.73	98.60	98.31	98.89	98.40	99.54	98.34	98.50	98.11	97.91	98.64	100.25	97.39

	Plagioclase															Core
SiO2	62.88	62.41	63.05	63.66	63.11	63.37	62.35	63.46	63.18	63.48	62.91	63.18	63.46	63.34	62.91	62.86
Al2O3	18.76	18.72	18.93	18.46	18.76	18.96	19.50	18.68	18.85	18.69	18.93	18.79	18.73	18.89	18.95	18.92
K2O	14.41	14.39	14.40	14.68	14.29	14.15	14.32	14.32	15.00	14.19	14.00	13.95	14.23	13.87	13.87	13.88
FeO	0.08	0.06	0.09	0.06	0.06	0.07	0.04	0.07	0.11	0.08	0.03	0.12	0.06	0.11	0.11	0.07
MnO	0.02	0.00	0.00	0.01	0.01	0.02	0.02	0.02	0.00	0.01	0.00	0.00	0.00	0.03	0.02	0.00
MgO	0.00	0.00	0.00	0.00	0.00	0.00	0.00	0.00	0.00	0.00	0.00	0.00	0.00	0.00	0.00	0.00
CaO	0.01	0.02	0.04	0.02	0.04	0.04	0.06	0.01	0.02	0.03	0.07	0.09	0.02	0.08	0.10	0.12
Na2O	1.16	1.21	1.20	1.15	1.34	1.36	1.11	1.36	0.91	1.25	1.43	1.42	1.40	1.49	1.45	1.45
TiO2	0.03	0.02	0.06	0.03	0.04	0.01	0.04	0.03	0.00	0.03	0.00	0.00	0.02	0.02	0.02	0.04
Total	97.34	96.82	97.77	98.07	97.63	97.97	97.44	97.95	98.07	97.76	97.38	97.54	97.92	97.82	97.43	97.33

	K-Feldspar								
SiO2	62.79	63.85	62.58	63.74	63.35	63.70	64.27	63.40	63.89
Al2O3	18.68	22.49	18.87	18.92	18.33	18.62	18.66	18.72	18.71
K2O	13.94	1.23	14.10	14.27	14.54	14.63	12.63	14.32	12.99
FeO	0.12	0.10	0.04	0.05	0.06	0.13	0.07	0.03	0.10
CaO	0.10	3.18	0.01	0.07	0.04	0.06	0.09	0.09	0.11
Na2O	1.43	8.87	1.32	1.32	1.22	1.21	2.37	1.46	2.15
TiO2	0.02	0.00	0.03	0.03	0.01	0.02	0.03	0.01	0.02
Total	97.08	99.72	96.94	98.39	97.55	98.38	98.14	98.02	97.99

APPENDIX: Mineral Composition of sample 07B141.

	Hornblende															
	Core															
SiO2	41.50	41.74	41.79	41.58	41.65	41.63	41.69	41.20	41.51	41.81	41.80	41.41	41.42	41.75	41.67	41.89
Al2O3	11.51	11.61	11.74	11.60	11.62	11.83	11.59	11.69	11.40	11.73	11.51	11.74	11.56	11.48	11.54	11.32
K2O	1.49	1.49	1.51	1.49	1.51	1.46	1.51	1.47	1.47	1.45	1.44	1.47	1.45	1.44	1.45	1.36
FeO	18.62	18.50	19.02	18.19	18.78	18.77	18.62	18.96	18.63	18.83	18.12	18.43	18.15	18.29	18.61	18.20
MnO	0.39	0.42	0.39	0.42	0.44	0.43	0.45	0.37	0.44	0.41	0.39	0.48	0.43	0.41	0.39	0.40
MgO	9.72	9.77	9.70	9.45	9.60	9.58	9.55	9.51	9.69	9.54	9.60	9.49	9.55	9.51	9.56	9.72
CaO	11.51	11.67	11.51	11.48	11.68	11.44	11.22	11.54	11.50	11.70	11.45	11.49	11.49	11.62	11.65	11.65
Na2O	1.49	1.65	1.62	1.56	1.52	1.49	1.56	1.51	1.45	1.49	1.44	1.45	1.47	1.41	1.46	1.44
TiO2	1.06	1.10	1.09	1.11	1.11	1.09	1.10	1.10	1.09	1.09	1.10	1.12	1.11	1.10	1.10	1.07
Total	97.29	97.96	98.35	96.92	97.89	97.75	97.28	97.34	97.21	98.07	96.85	97.06	96.62	97.02	97.48	97.07

	Hornblende		Plagioclase													
	Core		Rim													
SiO2	41.42	41.97	60.37	60.46	60.18	59.55	60.12	59.52	59.56	60.07	60.00	60.35	60.12	60.23	60.13	58.99
Al2O3	11.49	11.53	24.61	24.37	24.71	24.19	24.57	24.99	24.83	24.77	24.69	24.87	24.68	24.83	24.77	24.04
K2O	1.43	1.29	0.21	0.21	0.20	0.40	0.22	0.24	0.24	0.22	0.20	0.16	0.12	0.16	0.18	0.21
FeO	18.49	18.05	0.37	0.22	0.24	0.21	0.08	0.08	0.13	0.16	0.10	0.14	0.11	0.11	0.14	0.12
MnO	0.41	0.43	0.00	0.02	0.02	0.00	0.00	0.00	0.00	0.01	0.02	0.01	0.00	0.00	0.01	0.00
MgO	9.63	9.62	0.01	0.00	0.00	0.00	0.01	0.01	0.00	0.00	0.01	0.01	0.01	0.00	0.00	0.03
CaO	11.60	11.44	6.05	6.15	6.36	6.09	6.61	6.78	6.57	6.70	6.59	6.58	6.47	6.43	6.24	5.93
Na2O	1.26	1.35	7.89	7.76	7.83	7.59	7.73	7.62	7.75	7.43	7.71	7.84	7.67	7.86	7.62	7.53
TiO2	1.07	1.05	0.00	0.00	0.00	0.00	0.00	0.00	0.00	0.01	0.00	0.00	0.00	0.00	0.04	0.02
Total	96.81	96.74	99.52	99.18	99.55	98.05	99.33	99.23	99.08	99.39	99.32	99.94	99.17	99.61	99.14	96.89

APPENDIX: Mineral Composition of sample 07B141.

	Plagioclase						Core	Hornblende Core								
SiO2	60.32	60.38	60.54	60.14	60.36	60.39	60.59	42.94	42.70	42.58	42.32	42.62	42.44	42.59	42.77	43.38
Al2O3	24.85	24.60	24.81	24.85	24.74	24.73	24.65	10.97	10.92	11.11	11.01	11.04	10.96	10.80	10.51	10.12
K2O	0.13	0.17	0.16	0.16	0.18	0.14	0.14	1.28	1.32	1.28	1.29	1.25	1.24	1.21	1.18	1.11
FeO	0.08	0.11	0.08	0.08	0.13	0.04	0.14	18.29	18.12	18.53	18.44	18.37	18.31	18.29	18.15	17.77
MnO	0.01	0.00	0.00	0.02	0.03	0.01	0.00	0.41	0.42	0.44	0.44	0.46	0.41	0.44	0.39	0.40
MgO	0.00	0.00	0.01	0.01	0.00	0.00	0.01	9.86	10.23	10.12	10.04	10.05	10.55	10.37	10.35	10.50
CaO	6.28	6.34	6.23	6.39	6.30	6.31	6.24	11.39	11.41	11.33	11.49	11.52	11.60	11.52	11.73	11.55
Na2O	7.76	7.82	7.78	7.88	7.85	7.89	7.86	1.46	1.51	1.50	1.45	1.36	1.59	1.48	1.55	1.32
TiO2	0.01	0.00	0.00	0.03	0.00	0.00	0.00	1.04	1.03	1.02	1.01	1.01	0.99	0.97	0.90	0.91
Total	99.45	99.42	99.61	99.59	99.58	99.52	99.64	97.64	97.68	97.93	97.50	97.71	98.14	97.65	97.56	97.06

	Hornblende			Rim	Rim			Plagioclase								Core
SiO2	43.65	43.23	43.73	44.42	62.26	65.16	60.58	57.72	60.76	62.44	60.30	60.58	60.19	60.17	59.94	59.84
Al2O3	10.17	10.44	10.32	9.43	24.26	21.50	24.55	24.18	25.15	23.66	24.69	24.85	25.10	23.71	24.85	24.82
K2O	1.05	1.07	0.98	0.90	0.15	0.60	0.32	0.22	0.28	0.70	0.22	0.36	0.18	0.35	0.25	0.21
FeO	17.79	17.85	17.55	17.42	0.13	0.02	0.13	0.17	0.06	0.14	0.18	0.13	0.14	0.07	0.08	0.08
MnO	0.44	0.36	0.37	0.40	0.00	0.01	0.00	0.03	0.02	0.00	0.00	0.00	0.00	0.00	0.00	0.01
MgO	10.58	10.46	10.80	10.93	0.00	0.00	0.03	0.12	0.00	0.01	0.00	0.00	0.00	0.01	0.00	0.01
CaO	11.95	11.71	11.75	11.67	5.24	2.24	6.12	6.55	6.36	4.83	6.26	6.25	6.32	5.48	6.47	6.63
Na2O	1.29	1.18	1.14	1.02	8.69	9.84	8.10	7.49	7.95	8.25	7.88	7.95	7.79	7.99	7.60	7.67
TiO2	0.86	0.86	0.78	0.63	0.02	0.01	0.00	0.00	0.00	0.03	0.01	0.01	0.00	0.00	0.00	0.02
Total	97.81	97.17	97.44	96.81	100.76	99.38	99.84	96.50	100.57	100.06	99.56	100.13	99.72	97.80	99.21	99.29

APPENDIX: Mineral Composition of sample 07B141.

	Plagioclase Core				Biotite											
SiO2	59.84	59.95	59.82	58.50	36.64	36.58	36.95	36.92	32.55	36.11	36.73	36.47	36.89	36.83	36.27	36.32
Al2O3	24.92	24.90	25.21	24.52	15.11	15.44	15.38	15.25	17.06	15.39	15.30	15.20	15.37	15.33	14.86	15.91
K2O	0.23	0.27	0.26	0.28	8.70	8.91	9.07	8.89	6.07	8.55	9.08	8.93	9.07	8.94	8.84	8.72
FeO	0.12	0.11	0.11	0.10	17.77	17.97	18.59	17.83	19.72	17.73	17.78	17.93	18.27	17.77	18.14	17.49
MnO	0.00	0.00	0.00	0.00	0.29	0.26	0.31	0.28	0.23	0.26	0.26	0.27	0.25	0.29	0.28	0.29
MgO	0.00	0.01	0.00	0.00	11.80	11.71	11.95	11.02	9.44	11.91	11.67	11.83	11.82	11.37	11.84	11.64
CaO	6.67	6.61	6.78	6.61	0.12	0.12	0.08	0.27	0.46	0.15	0.05	0.11	0.09	0.12	0.10	0.02
Na2O	7.43	7.57	7.48	7.32	0.14	0.10	0.12	0.09	0.18	0.12	0.13	0.11	0.11	0.10	0.12	0.11
TiO2	0.00	0.00	0.00	0.01	2.61	2.77	2.82	2.85	2.05	3.05	3.04	3.01	3.05	3.05	3.11	3.10
Total	99.21	99.44	99.72	97.33	93.16	93.86	95.26	93.39	87.76	93.28	94.08	93.86	94.95	93.81	93.55	93.63

	Biotite					Illmenite				
SiO2	36.04	36.93	36.89	36.86	36.68	0.02	0.22	0.04	0.03	0.08
Al2O3	15.17	15.49	15.15	15.05	15.18	0.12	0.17	0.16	0.13	0.13
K2O	8.75	8.86	8.95	8.94	9.08	0.00	0.01	0.00	0.00	0.00
FeO	17.50	17.98	17.44	17.37	18.14	79.72	77.56	76.97	78.53	78.14
MnO	0.26	0.24	0.27	0.25	0.26	0.10	0.17	0.19	0.11	0.13
MgO	11.52	12.20	11.85	11.66	11.90	0.10	0.13	0.09	0.09	0.09
CaO	0.10	0.03	0.00	0.03	0.04	0.00	0.00	0.00	0.00	0.00
Na2O	0.11	0.15	0.06	0.13	0.14	0.00	0.04	0.03	0.00	0.03
TiO2	3.17	3.16	3.23	3.18	3.30	14.39	15.71	15.91	15.07	14.73
Cr2O3	0.00	0.00	0.00	0.00	0.00	0.08	0.10	0.05	0.12	0.05
Total	92.69	95.04	93.90	93.49	94.73	94.53	94.11	93.43	94.07	93.36

APPENDIX: Mineral Composition of sample 07B146A.

	Garnet															
	Core															
SiO2	37.33	37.28	35.99	37.43	37.36	37.35	37.16	37.32	37.21	37.73	37.41	37.53	37.39	37.14	36.28	37.11
Al2O3	20.48	20.58	22.71	20.42	20.49	20.83	20.56	20.47	20.39	20.59	20.63	20.56	20.61	20.44	22.72	20.66
K2O	0.01	0.00	0.00	0.00	0.00	0.00	0.00	0.00	0.01	0.00	0.00	0.00	0.00	0.00	0.00	0.00
FeO	21.64	21.85	21.23	21.80	21.86	21.98	22.07	21.84	22.00	22.06	22.09	21.96	22.01	22.39	20.95	21.55
MnO	19.24	19.30	18.86	19.34	19.43	19.48	19.44	19.24	19.25	19.17	19.17	19.18	19.27	19.15	18.88	19.25
MgO	1.49	1.49	1.42	1.48	1.41	1.38	1.43	1.41	1.48	1.47	1.44	1.48	1.40	1.47	1.45	1.53
CaO	1.35	1.36	1.43	1.37	1.38	1.34	1.32	1.37	1.37	1.39	1.36	1.45	1.42	1.35	1.34	1.42
Na2O	0.04	0.04	0.08	0.07	0.06	0.03	0.03	0.04	0.04	0.05	0.05	0.07	0.00	0.02	0.03	0.02
TiO2	0.10	0.08	0.09	0.08	0.08	0.08	0.09	0.08	0.08	0.09	0.07	0.06	0.07	0.04	0.00	0.06
Total	101.68	101.97	101.80	102.00	102.08	102.47	102.10	101.77	101.83	102.55	102.21	102.27	102.17	102.00	101.67	101.60

	Garnet		Feldspar													
	Rim		Rim													
SiO2	37.28	37.03	66.23	65.40	64.85	64.57	98.11	90.92	63.80	64.28	64.67	64.74	64.03	64.20	64.79	64.53
Al2O3	20.38	20.92	19.87	20.39	22.06	21.39	0.07	4.75	22.59	22.60	22.47	22.17	18.62	22.12	21.70	22.19
K2O	0.00	0.02	4.61	7.55	0.11	3.31	0.02	0.03	0.14	0.15	0.11	0.66	15.54	0.13	0.12	0.10
FeO	21.79	20.46	0.42	0.13	0.08	0.07	0.04	0.00	0.09	0.04	0.07	0.04	0.03	0.03	0.00	0.00
MnO	19.46	20.03	0.27	0.11	0.07	0.07	0.03	0.03	0.01	0.03	0.01	0.02	0.01	0.01	0.02	0.02
MgO	1.48	1.33	0.00	0.00	0.00	0.00	0.00	0.00	0.00	0.00	0.01	0.01	0.00	0.00	0.00	0.00
CaO	1.45	1.98	0.77	1.30	2.94	2.23	0.05	0.58	3.41	3.35	3.41	3.08	0.04	3.21	2.67	2.92
Na2O	0.03	0.02	7.85	5.62	9.82	8.12	0.02	2.40	9.70	9.72	9.56	9.44	0.74	9.78	9.91	10.11
TiO2	0.10	0.00	0.00	0.00	0.00	0.01	0.01	0.00	0.01	0.00	0.00	0.02	0.00	0.00	0.00	0.00
Total	101.97	101.77	100.02	100.50	99.93	99.77	98.34	98.73	99.74	100.17	100.30	100.18	99.00	99.48	99.20	99.88

APPENDIX: Mineral Composition of sample 07B146A.

	Feldspar															
SiO2	64.46	71.69	64.88	63.98	63.42	64.53	63.41	65.11	63.78	65.01	64.13	65.05	64.06	63.96	63.50	63.43
Al2O3	22.79	17.95	21.98	18.58	20.38	18.51	19.25	18.77	17.67	22.19	21.85	22.02	21.59	19.51	22.32	22.58
K2O	0.12	0.07	0.10	15.71	7.48	15.86	11.59	15.78	14.11	0.20	0.14	0.11	3.48	10.50	0.29	0.30
FeO	0.10	0.02	0.01	0.00	0.02	0.00	0.05	0.00	0.04	0.02	0.03	0.00	0.04	0.06	0.08	0.07
MnO	0.00	0.01	0.00	0.00	0.01	0.01	0.00	0.01	0.03	0.00	0.00	0.02	0.01	0.00	0.02	0.01
MgO	0.00	0.02	0.01	0.00	0.00	0.00	0.00	0.00	0.00	0.00	0.02	0.00	0.01	0.00	0.04	0.01
CaO	3.35	2.65	2.62	0.05	1.60	0.01	0.64	0.07	0.20	3.05	3.36	2.93	2.67	1.02	3.08	3.29
Na2O	9.48	8.08	10.61	0.54	5.53	0.59	3.13	0.67	1.17	9.66	9.46	10.39	7.18	3.82	9.48	9.53
TiO2	0.03	0.01	0.01	0.01	0.00	0.01	0.02	0.00	0.01	0.00	0.00	0.00	0.01	0.01	0.00	0.00
Total	100.32	100.49	100.21	98.86	98.44	99.51	98.09	100.41	97.00	100.13	98.99	100.53	99.04	98.87	98.80	99.21

	Feldspar															Core
SiO2	64.67	63.66	65.38	63.67	64.42	63.88	64.08	63.90	64.52	62.87	63.98	64.14	64.26	64.06	64.01	64.56
Al2O3	22.57	22.58	22.89	22.61	22.82	22.54	22.75	22.83	22.82	22.29	22.84	22.24	22.71	22.75	22.24	22.45
K2O	0.08	0.10	0.09	0.11	0.12	0.13	0.12	0.15	0.16	0.19	0.17	0.19	0.17	0.19	0.17	0.16
FeO	0.09	0.02	0.03	0.03	0.06	0.00	0.08	0.00	0.00	0.07	0.02	0.00	0.03	0.00	0.08	0.05
MnO	0.00	0.00	0.00	0.00	0.00	0.00	0.00	0.02	0.02	0.00	0.01	0.00	0.00	0.00	0.01	0.00
MgO	0.00	0.02	0.00	0.00	0.00	0.01	0.00	0.00	0.00	0.01	0.00	0.00	0.00	0.00	0.01	0.00
CaO	3.52	3.49	3.44	3.44	3.36	3.55	3.62	3.55	3.52	3.50	3.45	3.48	3.60	3.59	3.42	3.45
Na2O	9.74	9.59	9.91	9.47	9.73	9.61	9.61	9.65	9.56	9.51	9.56	9.58	9.54	9.66	9.66	9.53
TiO2	0.00	0.01	0.00	0.01	0.01	0.01	0.01	0.00	0.00	0.02	0.00	0.00	0.00	0.01	0.00	0.00
Total	100.67	99.47	101.74	99.34	100.52	99.72	100.26	100.09	100.60	98.45	100.03	99.63	100.32	100.27	99.59	100.20

APPENDIX: Mineral Composition of sample 07B146A.

	Biotite							K-Feldspar								
	Core						Rim	Rim								Core
SiO2	35.64	36.03	35.48	35.49	34.32	35.52	35.24	63.86	64.80	63.91	64.03	64.28	64.15	64.26	64.76	64.39
Al2O3	17.27	17.68	17.41	17.25	17.06	17.10	17.29	18.39	18.47	18.58	18.48	18.57	18.78	18.51	18.49	18.38
K2O	9.47	9.60	9.52	9.54	8.51	9.55	9.63	15.69	15.57	15.70	16.05	15.57	15.57	15.65	15.88	15.96
FeO	22.36	22.16	21.69	22.34	23.24	22.17	21.78	0.24	0.08	0.05	0.00	0.00	0.04	0.01	0.03	0.04
MnO	1.11	1.17	1.12	1.11	1.18	1.09	1.10	0.00	0.01	0.00	0.01	0.03	0.00	0.00	0.00	0.00
MgO	7.39	7.32	7.35	7.36	7.83	7.33	7.25	0.00	0.00	0.00	0.00	0.00	0.00	0.00	0.00	0.00
CaO	0.12	0.03	0.05	0.04	0.07	0.02	0.01	0.00	0.02	0.00	0.02	0.00	0.00	0.00	0.00	0.00
Na2O	0.06	0.05	0.04	0.06	0.04	0.05	0.04	0.73	0.81	0.70	0.40	0.81	0.77	0.70	0.53	0.49
TiO2	2.38	2.52	2.53	2.76	2.54	2.98	3.08	0.02	0.02	0.00	0.00	0.00	0.00	0.00	0.01	0.01
Total	95.81	96.55	95.18	95.96	94.78	95.82	95.41	98.92	99.76	98.94	98.98	99.26	99.31	99.13	99.70	99.27

	K-Feldspar								Garnet						
	Core						Rim	Rim							Core
SiO2	64.48	65.32	64.30	64.80	64.36	64.69	64.37	64.47	64.22	37.72	37.03	37.00	37.67	37.26	37.84	37.74
Al2O3	18.33	18.85	18.81	18.62	18.67	18.62	18.60	18.85	18.36	20.73	20.64	21.06	20.95	20.63	20.76	21.05
K2O	15.21	15.29	15.26	15.38	15.67	15.36	15.13	15.06	15.44	0.02	0.01	0.00	0.00	0.02	0.01	0.01
FeO	0.06	0.01	0.01	0.02	0.00	0.11	0.06	0.00	0.11	21.28	21.87	21.71	21.76	21.55	21.93	21.82
MnO	0.00	0.02	0.00	0.03	0.00	0.00	0.05	0.04	0.10	19.06	18.80	19.18	19.52	19.40	19.41	19.35
MgO	0.00	0.00	0.00	0.00	0.00	0.00	0.00	0.00	0.00	1.48	1.49	1.47	1.48	1.50	1.48	1.54
CaO	0.03	0.03	0.01	0.00	0.01	0.00	0.01	0.01	0.00	1.72	1.64	1.44	1.35	1.28	1.23	1.38
Na2O	1.08	0.97	0.98	0.94	0.71	0.94	1.11	1.17	0.87	0.01	0.01	0.02	0.00	0.04	0.06	0.04
TiO2	0.00	0.00	0.01	0.00	0.00	0.01	0.00	0.00	0.01	0.01	0.02	0.03	0.02	0.05	0.06	0.04
Total	99.18	100.49	99.38	99.80	99.41	99.74	99.32	99.60	99.11	102.02	101.51	101.91	102.76	101.73	102.75	102.98

APPENDIX: Mineral Composition of sample 07B148A.

	Biotite						Plagioclase									
	Core					Rim	Rim				Core					
SiO2	35.85	35.46	36.48	36.95	36.20	36.91	58.14	58.44	58.83	58.41	59.65	59.73	60.07	59.78	59.38	59.44
Al2O3	19.05	19.07	19.33	19.15	19.31	19.14	25.79	25.81	25.74	26.14	24.98	25.04	25.14	25.10	25.58	25.20
K2O	8.25	8.17	8.37	8.57	8.40	8.43	0.07	0.06	0.06	0.07	0.08	0.08	0.08	0.07	0.05	0.05
FeO	17.84	17.52	17.89	17.11	16.79	17.07	0.26	0.18	0.15	0.16	0.09	0.05	0.02	0.09	0.04	0.08
MnO	0.08	0.09	0.08	0.04	0.07	0.05	0.04	0.01	0.00	0.00	0.02	0.00	0.03	0.00	0.02	0.00
MgO	12.38	11.88	11.92	11.83	11.75	11.89	0.01	0.01	0.00	0.01	0.00	0.01	0.02	0.00	0.00	0.01
CaO	0.04	0.12	0.03	0.06	0.13	0.07	7.42	7.19	7.36	7.48	6.45	6.55	6.45	6.54	7.01	6.81
Na2O	0.28	0.28	0.29	0.35	0.31	0.30	7.61	7.56	7.31	7.39	7.89	7.97	7.78	7.76	7.44	7.70
TiO2	1.60	1.79	1.65	1.85	1.91	1.77	0.07	0.16	0.02	0.00	0.02	0.01	0.01	0.00	0.01	0.00
Total	95.37	94.38	96.04	95.90	94.87	95.62	99.39	99.40	99.47	99.66	99.18	99.44	99.61	99.34	99.53	99.29

	Plagioclase		Garnet													
	Rim		Rim													
SiO2	59.92	57.89	37.89	38.30	38.55	38.58	38.65	38.47	38.58	38.97	38.72	38.65	38.84	38.63	38.76	38.43
Al2O3	25.57	26.47	21.62	21.87	22.00	22.26	22.12	22.09	21.91	22.17	22.14	22.10	22.14	22.09	22.20	22.21
K2O	0.04	0.06	0.01	0.00	0.00	0.00	0.00	0.00	0.00	0.00	0.00	0.00	0.00	0.00	0.00	0.00
FeO	0.15	0.36	33.20	33.71	33.00	32.68	31.77	31.72	31.87	31.81	31.59	31.67	32.04	31.77	32.19	31.54
MnO	0.02	0.01	3.49	2.04	1.55	1.37	1.40	1.36	1.36	1.36	1.36	1.28	1.26	1.29	1.30	1.27
MgO	0.00	0.00	4.08	5.12	6.01	6.33	6.40	6.72	6.59	6.80	6.74	6.72	6.69	6.95	7.08	6.95
CaO	6.94	8.05	1.68	1.67	1.69	1.73	1.69	1.67	1.58	1.59	1.62	1.52	1.52	1.45	1.39	1.40
Na2O	7.67	7.04	0.04	0.02	0.03	0.01	0.01	0.02	0.00	0.00	0.00	0.00	0.04	0.01	0.01	0.01
TiO2	0.00	0.02	0.00	0.02	0.03	0.01	0.00	0.02	0.00	0.03	0.02	0.02	0.01	0.02	0.00	0.01
Total	100.32	99.89	101.99	102.76	102.87	102.97	102.05	102.08	101.90	102.71	102.19	101.96	102.54	102.19	102.91	101.82

APPENDIX: Mineral Composition of sample 07B148A.

	Garnet			Garnet							Illmenite		
SiO2	38.76	38.94	38.79	38.85	38.83	38.95	38.59	38.80	38.53	39.02	0.19	0.17	0.24
Al2O3	22.39	21.91	22.01	22.41	22.01	22.23	22.21	22.29	22.19	22.07	0.08	0.05	0.12
K2O	0.00	0.00	0.01	0.00	0.00	0.00	0.00	0.00	0.00	0.00	0.08	0.03	0.06
FeO	31.84	31.30	31.80	31.38	30.57	30.89	31.75	31.26	31.12	30.91	47.45	47.46	47.16
MnO	1.28	1.30	1.27	1.14	1.18	1.19	1.19	1.15	1.17	1.14	1.24	1.33	1.34
MgO	7.00	7.01	6.98	7.39	7.16	7.25	7.31	7.34	7.35	7.26	0.25	0.23	0.23
CaO	1.46	1.41	1.39	1.52	1.52	1.50	1.52	1.45	1.47	1.45	0.00	0.02	0.03
Na2O	0.01	0.02	0.01	0.02	0.02	0.03	0.00	0.02	0.05	0.02	0.00	0.00	0.02
TiO2	0.00	0.00	0.02	0.02	0.01	0.01	0.02	0.02	0.03	0.01	53.58	53.78	53.74
Total	102.73	101.88	102.27	102.72	101.29	102.04	102.58	102.33	101.91	101.87	102.88	103.06	102.93